The molecular pathology of infant gliomas

Matthew Thomas Clarke

Submitted to the University of London/The Institute of
Cancer Research for the Degree of Doctor of Philosophy

2021

Declaration

I hereby declare that this thesis reports on my own original work. Any contribution made by others with whom I have worked is explicitly acknowledged in the thesis.

Matthew Thomas Clarke

Abstract

Infant high grade gliomas appear clinically distinct from their counterparts in older children, indicating that histopathologic grading may not accurately reflect the biology of these tumours. I have collected 241 cases under 4 years of age, and carried out histological review, methylation profiling, custom DNA fusion panel and whole genome/exome sequencing. After excluding tumours representing other established biological entities or subgroups, I identified 130 cases to be part of an intrinsic spectrum of disease specific to the infant population (~80% aged <1 year), the majority of which represented a relatively new tumour currently called ‘infantile hemispheric glioma’ (IHG). These tumours were found to be enriched for the presence of targetable MAP-kinase alterations, with nearly two-thirds of remaining cases harbouring gene fusions targeting *ALK*, *NTRK1/2/3*, *ROS1* and *MET* as their sole driving alterations. For the most part, these could be identified by small intragenic DNA copy number variants detectable in the methylation array data, and a review of publicly available methylation datasets (n=5660, half paediatric) showed that gene fusions were also present in gliomas outside of the infant population but at lower frequency. Novel *NTRK2* fusions were introduced into brain progenitor cells to explore their functional consequences, and patient-derived cell cultures of infant glioma harbouring various *NTRK* fusions were found to show differential efficacy for NTRK inhibitors. I further describe multiple cases of fusion-positive patients treated clinically with ALK or NTRK inhibitors who have responded to the drugs, even after progressing on standard chemotherapies. I have additionally profiled a series of cases for which longitudinal samples are available, exploring copy number and mutational differences post-therapy. Overall, the intrinsic group of infant glioma cases were found to have a significantly improved outcome compared to cases classified as high grade gliomas, with a median overall survival similar to those considered as low grade gliomas. These data strongly supports that infant gliomas require a change in both their diagnostic practice and management.

Statement of Impact

In March 2020, I was contacted by Health Education England (HEE) to ask if I would suspend my research and return to clinical practice in response to the COVID-19 pandemic. An ‘interruption to studies’ was implemented and my research paused; I was re-deployed to the NHS Nightingale Hospital, London as the Deputy Mortuary Manager until the 15th May 2020 at which time I returned to the ICR and restarted my studies. The ICR laboratories remained closed and after discussion with my supervisor Professor Chris Jones, it was decided that my focus should be the composition of my thesis and so the following experiments could not be completed.

***NTRK* modelling:** As described in chapter 6, using CRISPR/Cas9 and cloning techniques, I attempted to create *NTRK* fusion models using *ETV6:NTRK3* and *KCTD16:NTRK2* fusions in mouse neural stem cells (mNSC) using a PB-CAG plasmid, to explore the function of *NTRK* fusions in infant HGG. The mNSCs had been electroporated, expanded, and sorted for GFP positivity using the BeckmanCoulter MoFlo Astrios. At this point, the cultures were cryopreserved due to impending lockdown measures. Further work would have included DNA extraction and Sanger sequencing to confirm the successful integration of fusion constructs, RNA sequencing to confirm expression, cell proliferation assays, drug assays using Trk inhibitors with western blot analysis for pathway modulation, and *in vivo* studies with intracranial injections to assess tumourigenicity.

CXJ-020 liquid biopsies and cfDNA samples: An infant with a *KCTD16:NTRK2* positive HGG was being treated as part of a larotrectinib trial; blood samples were taken from the patient at review. DNA was extracted and sent for cfDNA panel sequencing at the CMP. We also planned to perform a ddPCR to detect the *KCTD16:NTRK2* fusion and monitor changes in response to treatment; this could not be completed due to the pandemic.

CXJ-020 resistance study: This study aimed to identify resistance mutations in the CXJ-020 cell culture in response to treatment with entrectinib, with possible benefit to the child currently in trial. The experiment involved adding media containing entrectinib (at IC80 concentration) to the cells three times per week (with control flasks using DMS0 and normal media). Pellets of cells were collected for DNA extraction and sequencing, and western blot analysis. This experiment could not be completed and all cells had to be cryopreserved before lockdown.

Single cell sequencing: In collaboration with Dr Mariella Filbin (DFCI, Boston, US) we sent *NTRK* (n=3) and *ALK* (n=1) fusion-positive frozen tumour samples for single nucleus RNA sequencing. As the DFCI labs were also closed due to the pandemic, data did not arrive until late August 2020. This enabled only a highly limited analysis (described in chapter 4). Further work would have included exploring the lineages and hierarchies of the malignant cell populations of each tumour, identifying the proportion of cells expressing the fusion, comparisons with the *ALK* fusion case (when the data arrives), and exploring in greater detail the differences in gene expression seen between the three cases and other pHGG.

Signed,

Dr Matthew Thomas Clarke | **Professor Chris Jones**

Student | **Supervisor**

Acknowledgements

There are many people who I would like to thank who have contributed and supported me in this project culminating in the production of this thesis. Firstly, I would like to thank my supervisor Professor Chris Jones for welcoming someone who had no research experience into the team; thank you for your teaching, support, guidance, always being available, the huge opportunities and the encouragement. I have achieved more than I could ever have hoped; my oral presentation at ISPNO 2018 and the publication of my paper in Cancer Discovery 2020 being two of the proudest moments of my career. As a result of your leadership, I have seen first-hand how research performed by such a dedicated team can make a difference to children with brain tumours. I look forward to our continuing ventures together. I would like to thank Dr Diana Carvalho, my assistant supervisor for teaching me from scratch the lab techniques (both theoretical and practical) that have allowed me to work independently. As a result of her tireless commitment, training, guidance, passion, encouragement and always being available when I need to ask a question, I now feel I can confidently talk about science. You have both been inspirational.

Thank you to Alan Mackay who has been instrumental in helping me with the bioinformatical elements of this project, and for teaching me basic skills to analyse my data. I have always enjoyed our coffee breaks talking through endless hypotheses that my data has created; I look forward to many more! A huge thank you to all of my funders; the financial support you provided has allowed this project to grow and has made a real difference to our knowledge of this disease. Thank you to Professor Thomas Jacques, my clinical supervisor for teaching me the basics of diagnostic neuropathology and for all of your guidance. Thank you very much to the other members of the Glioma Team; Elisa, Sara, Ketty, Rebecca, Valeria, Anna, Lynn, Haider and Yura for being such incredible colleagues and people I also consider good friends. I would like to thank my parents, brothers and family for their endless support and patience; I promise one day I will finish my training! Lastly to my partner, Fraser; thank you for your constant support, interest, patience, love and encouragement which has helped me to keep positive, focussed and feel proud of all I have achieved.

Table of contents

List of figures and tables

CHAPTER 1 - General introduction

1.1 Childhood cancer

Childhood malignancies remain a complex and challenging problem facing clinicians, pathologists, clinical scientists and researchers. An estimated 11,050 new cases of cancer in children aged 0-15 years were expected in 2020 in the US, alongside an estimated 1,190 deaths from cancer (1). It is the second most frequent cause of death in children, superseded only by deaths from accidents (2). There are reportedly 15.3 new cases per 100,000 children in the US each year (3).

Diagnosis of cancer in children is difficult as many of the symptoms are non-specific and can overlap with common childhood conditions (4). The most frequent type of childhood cancer is leukaemia representing 30% of cases, followed by brain and central nervous system tumours which represent 26%. Other cancers seen in childhood include neuroblastoma (6%), Wilms tumour (5%), lymphoma (8%), rhabdomyosarcoma (3%), osteosarcoma (2%), retinoblastoma (2%), and Ewing sarcoma (1%) (**figure 1-1**) (2). Treatment is dependent on the tumour type but generally consists of surgery, radiotherapy, and/or chemotherapy (5). The advent of ‘precision’ or ‘personalised’ medicine has seen the use of more targeted therapies based on the mutation profile of the tumour (6).

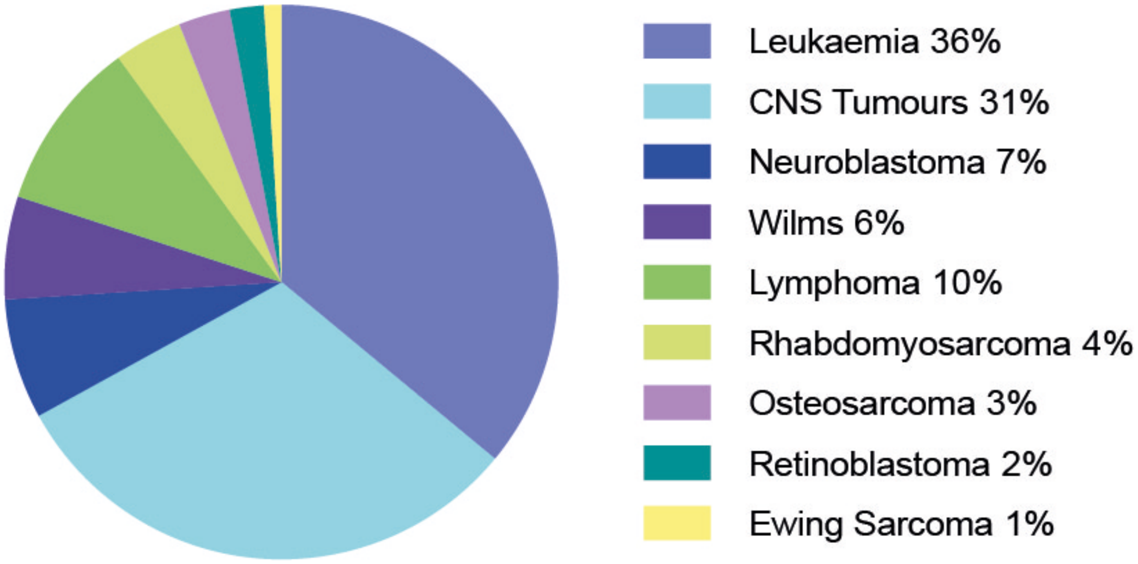

Figure 1-1. Childhood cancer. Pie chart showing the types and frequencies of the main subgroups of cancer seen in childhood (2).

Overall, the survival of childhood cancer has improved over the past 30 years with the 5-year survival rate increasing to 83% (2005-2011) from 58% in the mid-1970’s. The survival rate has considerable variation depending on type of tumour and age of the patient (2).

1.2 Paediatric brain tumours

Brain tumours are the most frequent solid tumour type in the paediatric population accounting for 20% of cases. Of these, astrocytic tumours represent the most frequent diagnosis accounting for 47%, followed by medulloblastomas which account for 19% (2). Other common tumours also seen include ependymomas and germ cell tumours (7). From 2012-2016, there were 5.74 cases per 100,000 children in the US (aged 0-14), with a slightly higher rate seen in male children (5.97 versus 5.51 PR 100,0000) (8). This gave a total of 17,540 new cases diagnosed across this period with a further 3540 new cases expected to be diagnosed in 2020 (8). Overall 5 year survival rates for 0-19 year olds in the US is 74.5% declining to 65.1% for those aged 20-44 years (8).

Low grade gliomas (LGG) are the most frequent tumour type seen in paediatrics. They can occur in both hemispheric and midline locations and comprise many different subtypes including pilocytic astrocytomas and gangliogliomas. They also have a very different mutation spectrum compared to adults, with most paediatric LGG being driven by a RAS/MAPK pathway activation frequently involving the *BRAF* gene, either a fusion or a mutation. In contrast, this is a rare finding in adults (9).

16.9% of brain tumour diagnoses in children aged 0-14 are glioblastomas or other malignant gliomas (8). A further 7.6% of this age group are diagnosed with other astrocytoma variants including diffuse astrocytoma and anaplastic astrocytoma (8). The most frequent CNS location for paediatric brain tumours is the cerebellum (15.2%), with 13.3% occurring in the brainstem. 15.3% of tumours occur within the cerebral hemispheres (frontal, parietal, temporal and occipital lobes combined) and 4.9% are found in the cauda equina or spinal cord (8). Although high-grade gliomas (HGG) are more frequently seen within the adult population, HGGs in adults and children are regarded as distinct clinical and biological entities (2). HGGs in adults tend to occur in the cerebral hemispheres whereas in children, they occur throughout the central nervous system with around 50% occurring in midline locations, especially the thalamus (13%) or pons (10). Midline or brainstem located tumours make surgical resection less amenable in these children due to the increased clinical risk; therefore chemotherapeutic or radiation remains the mainstay of treatment with limited success (11). However, where surgically accessible subtotal resection and gross total resection are associated with a 3-4 fold improved survival compared to biopsy alone (12). However, the prognosis remains dismal with less than 20% survival rate post-diagnosis for paediatric HGG (pHGG), providing motivation to better understand their molecular characteristics and how this relates to the clinical behaviour to significantly improve the outcome for these children (11). The cause or risk factors for their development remain unconfirmed, although changes in the local environment linked to age of the child, and exposure to ionising radiation are thought to have a role (7). Inherited syndromes can sometimes be associated with the appearance of a paediatric brain tumour; type 1 neurofibromatosis is associated with optic nerve gliomas and other astrocytomas, and Turcot's syndrome is associated with medulloblastomas and astrocytomas (2).

Paediatric brain tumours are graded from I – IV according to the guidelines issued by the World Health Organisation (WHO) and are decided by the histological features of the tumour. Grade I tumours show little atypia and are considered benign, whereas grade IV tumours show marked pleomorphism, microvascular proliferation and necrosis and are predicted to be aggressive. Gliomas are classified into two clinical categories of lower-grade gliomas (LGG, grade I and II) and HGG (grade III and IV) (13). Tumour location also influences the overall prognosis, influencing whether the tumour is surgically resectable. A complete surgical resection remains the gold standard treatment for all brain tumours and thus influences prognosis. This thesis will focus on high-grade gliomas occurring in the infant population.

1.3 Paediatric and adult gliomas

1.3.1 Clinical features

The clinical features of brain tumours can vary between individual patients and are dependent on the location of the tumour. In adults, up to 70% of patients report headaches during the clinical course (14), with 23-56% at diagnosis (15). In younger patients, seizures are frequently seen and may occur at times distant to the diagnosis (16), and 9% of patients will have a hospital admission due to a seizure before the diagnosis is made (16). Other signs and symptoms include motor weakness, confusion, dysphasia, memory loss and personality changes. However, due to their non-specific nature and association with many other conditions, it can be difficult for clinicians to decide when to investigate a patient for a possible brain tumour (2).

Studies have shown that other frequent presenting symptoms in paediatric cases are headache and vomiting (41% and 12% respectively), unsteadiness (11%) visual difficulties (10%), and educational or behavioural problems (10%) (**figure 1-2A**). Neurological signs are present at diagnosis in 88% of cases with 49% showing cranial nerve abnormalities, 48% with cerebellar signs, 38% show papilloedema, 27% with long tract signs, 12% have a reduced level of consciousness and 11% with somatosensory abnormalities (**figure 1-2B**). Therefore, a very broad approach to symptom questioning needs to be taken at the time of diagnosis (17).

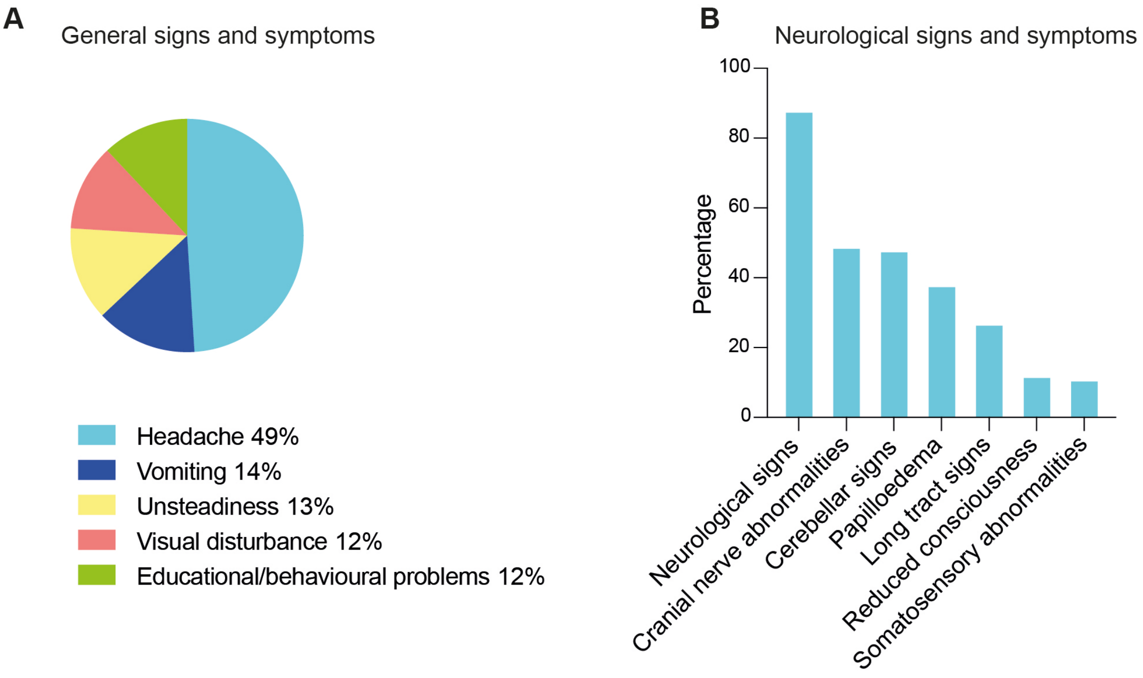

Figure 1-2. Signs and symptoms associated with paediatric brain tumours. **A,** Pie chart showing the percentage of cases that present with general non-specific signs and symptoms that can be associated with brain tumours. **B,** Bar chart showing the frequency of reported neurological signs and symptoms associated with the presentation of brain tumours (17).

The clinical presentation of diffuse intrinsic pontine glioma (DIPG, a class of paediatric HGG) is brainstem dysfunction or cerebrospinal fluid obstruction which develops over 1-2 months, with particular molecular characteristics conferring a worse prognosis, with a <10% 2-year survival (18). If located in the thalamus, a tumour with high-grade histology will have a worse prognosis regardless of the mutation status (18).

Types of pHGG are associated with particular anatomical locations; 50% of malignant paediatric gliomas arise in the brainstem with over 80% of these consistent with DIPG (19). Only 1-2% of cases will occur in the cerebellum, with 50% of those occurring in the supratentorial compartment of the brain, specifically in the cerebral hemispheres (20). Studies have shown that pHGG have an association of anatomical location and the age of diagnosis (**figure 1-3A**); midline tumours are diagnosed at a median of 10.0 years, DIPG at 6.5 years and hemispheric tumours at 13.0 years (**figure 1-3B**) (21). Clinical outcome is poor with a 20.8% 5-year survival for glioblastomas diagnosed in children aged 0-19 years, but is considerably better than for adults; those aged 45-54 and 55-64 years have a 5 year survival of 9.3% and 5.9% respectively (8). Clinical outcome is also in part dependent on location with hemispheric tumours having a median overall survival of 18.0 months, midline tumours 13.5 months (**figure 1-3C**) (21) and DIPG a median of 9 months (19).

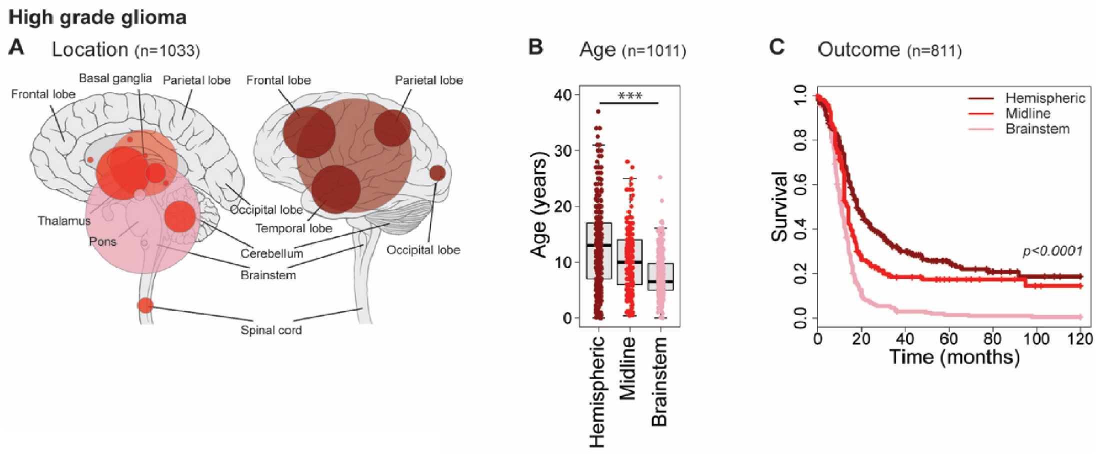

Figure 1-3. Clinicopathological and molecular subgroups of paediatric HGG. **A,** Anatomical location of all high-grade glioma cases included in this study, taken from original publications (n=1,033). Left, sagittal section showing internal structures; right, external view highlighting cerebral lobes. Hemispheric, dark red; non-brainstem midline structures, red; pons, pink. Radius of circle is proportional to the number of cases. Lighter shaded circles represent a non-specific designation of hemispheric, midline, or brainstem. **B,** Boxplot showing age at diagnosis of included cases, separated by anatomical location (n=1,011). The thick line within the box is the median, the lower and upper limits of the boxes represent the first and third quartiles, and the whiskers the interquartile range. ***Adjusted p < 0.0001 for all pairwise comparisons, t test. **C,** Kaplan-Meier plot of overall survival of cases separated by anatomical location, p value calculated by the log rank test (n=811) The label 'midline' does not include brainstem tumours which are considered separately (21).

Glioblastoma WHO grade IV has a median survival of 14.6 months with standard therapy including surgery, chemo- and radiotherapy (22). O6-methylguanine-DNA methyl-transferase (MGMT) methylation status is also used to predict response to alkylating agents such as temozolomide (22), which is important for both IDH-mutant astrocytomas/glioblastomas which are seen most frequently in younger and middle-aged adults (18). The use of metformin as part of the treatment regimen of grade III gliomas has also been shown to improve outcome with an HR for OS of 0.30 compared to an HR for OS of 0.80 for grade IV tumours (22).

In adults, the mean length of the clinical history for patients with glioblastoma is 6.3 months (23). However, *IDH1/2* mutations prolong this to 15 months whereas *IDH1/2*-wild type have a mean length of 3.9 months (23). The median overall survival with surgery and radiotherapy is 9.9 months for IDH-wild type and 24 months for IDH-mutant glioblastoma (23). The median overall survival with surgery, radiotherapy and chemotherapy for IDH- wild type is 15 months and 31 months for IDH-mutant (23).

However, we are still far behind where we need to be in terms of treatment. Studies have looked at the benefit of different treatment strategies on overall survival in recurrent pHGG with only marginal improvements noted; median age of 10 years cumulative OS of 5.6 months, 4.0 months for standard chemotherapy, 9.3 months using targeted therapies, 6.9 months using immunotherapy, and 14 months using re-irradiation (24). Greater extent of resection is a key component of this, and a great appreciation of the plasticity of the brain, advancing techniques and the use of staged operations will help to improve this further (25).

1.3.2 Classification and pathological features of the glioma subtypes

Adult and paediatric HGGs and their different subtypes have histological features in common (**figure 1-4**); they are cellular, contain pleomorphic (**figure 1-4C**) and atypical cells with brisk mitoses (**figure 1-4B)**. Essential diagnostic criteria are the presence of microvascular proliferation and/or necrosis (**figure 1-4D**). However, histological appearances vary considerably between tumours; some show a high degree of atypia and others can show frequent tumour giant cells (**figure 1-4A**). Focally, areas of lower grade features are observed, and bipolar/spindle cells which form bundles and fascicles (2). There are different cellular morphologies seen in glioblastoma including small cells, primitive neuronal cells, oligodendroglial components, multinucleated giant cells, gemistocytes, granular cells, lipidised cells, and metaplasia (11). Small cells are very monomorphic with slightly elongated nuclei that are surrounded by sparse cytoplasm. Very little nuclear atypia is seen but brisk mitoses are often present. Identifying tumour cells with minimal atypia can be challenging. Primitive neuronal components show nodules with neuronal differentiation, are easily distinguished from the background tumour and lose GFAP expression by immunohistochemistry (IHC) (13). Oligodendroglial components are very similar to features of an oligodendroglioma (a tumour most frequently seen in adults); cells showing the characteristic white halo surrounding a central nucleus, and these tumours have a better prognosis. Multinucleated giant cells vary in size and degree of pleomorphism. They are considered a regressive change, and if they predominate then the tumour is described as giant cell glioblastoma, with giant cells being positive for GFAP and S100 (26). Granular cells are large with a granular eosinophilic cytoplasm which is PAS stain positive. Their quantities vary and in rare cases they can be dominant. Most are negative for GFAP but some may be reactive for CD68. The term ‘granular cell astrocytoma/glioblastoma’ is used for tumours showing a predominance of granular cells; these have a worse prognosis irrespective of age or extent of granular cell morphology (27). Lipidised cells are large and contain a foamy cytoplasm; increased frequency can cause diagnostic overlap with pleomorphic xanthoastrocytoma (13). Metaplasia is defined as change from one differentiated cell type to another. In the context of glioblastomas, it refers to the presence of epithelial whorls, keratin pearls with associated cytokeratin expression, features normally associated with squamous cell carcinoma; these are called adenoid glioblastomas (13). They are very rare and the extent of these features varies with some showing the cells arranged in cords or nests with some pseudoglandular/cribriform spaces also occasionally seen (28).

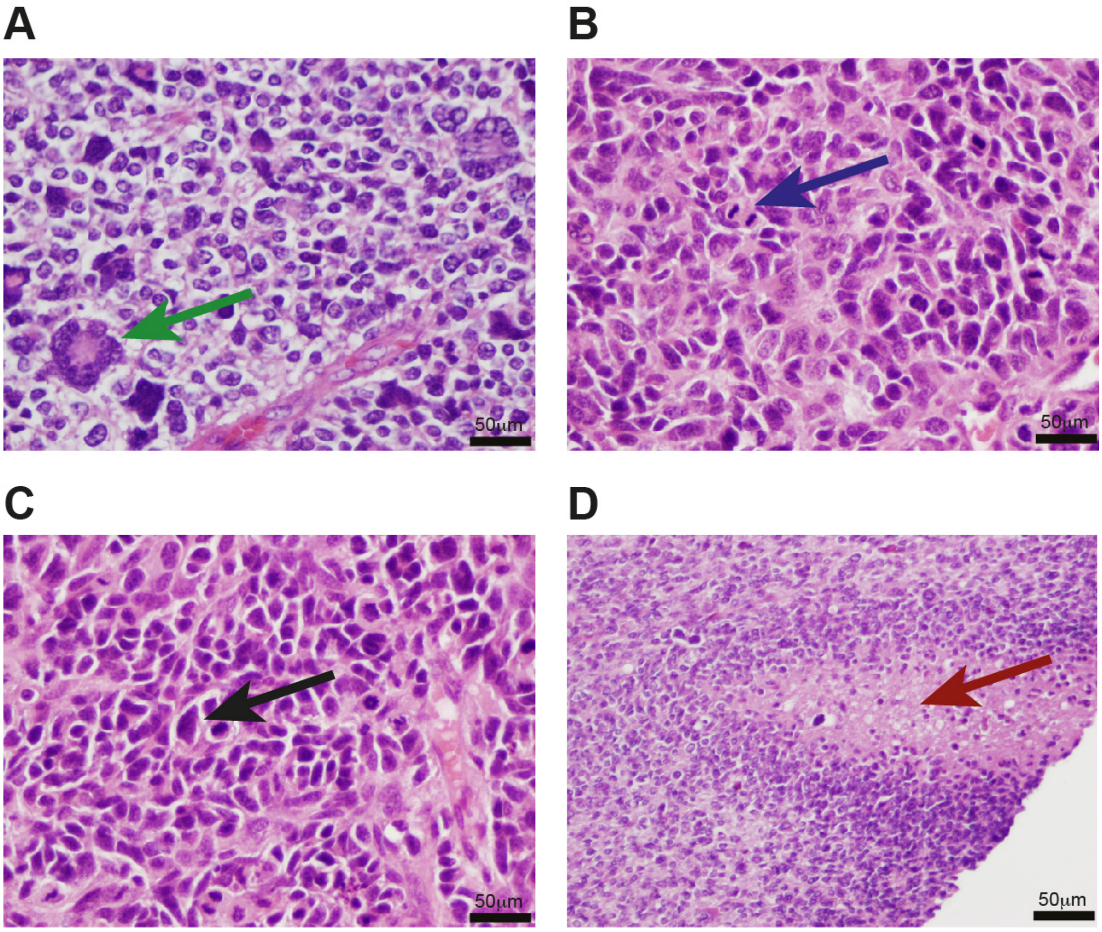

Figure 1-4. Histological features of high grade gliomas. **A,** Different cytological features can be observed with giant cells (green arrow) occasional seen. **B,** Mitotic activity is frequently seen in HGG (blue arrow). **C,** Moderate to severe nuclear pleomorphism is also a cytological feature of HGG. **D,** Palisading necrosis (red arrow) is a feature of high grade tumours in general but also seen in HGG.

Infiltration is a key feature of HGGs and is apparent when the interaction with host brain structures are observed; satellitosis applies to tumour cells surrounding normal neurons, and cells also accumulate in the cortex subpial zone. Extensive involvement of the cerebral cortex can be observed. Many cases show proliferative activity but the extent can vary, with most showing a proliferative index (measured by Ki67) of 15-20% but others show significantly more (13). Extensive vascularisation is confirmed by hypertrophic and hyperplastic endothelial cells (positive for CD31 and CD34) and some areas show a glomeruloid vascular pattern. This angiogenesis is driven by hypoxia. The presence of intravascular thrombosis is thought to be one of the factors that contribute to cause the pseudopallisading appearance, where the tumour cells begin to migrate away from the central area of necrosis (29).

1.3.3 WHO Classification of CNS tumours

In May 2016, the WHO published an updated version of the 'Classification of Tumours of the Central Nervous System', the first since 2007 (**figure 1-5**). A key feature of the updated version were the recommendations made about the construction of a histopathology report, adopting a 4-tiered approach comprising:

- Histological diagnosis
- WHO grade
- Molecular information
- Integrated diagnosis (13,18)

As a result, different tumour subtypes are characterised by their molecular biology; a glioblastoma can be classified as glioblastoma, IDH-wild type, (including giant cell glioblastoma, gliosarcoma, epitheliod glioblastoma), IDH-mutant, or glioblastoma NOS (13).

The specific changes included the addition of newly recognised entities, variants and patterns including diffuse midline glioma H3 K27M-mutant (entity), embryonal tumour with multilayered rosettes C19MC-altered (entity), ependymoma *RELA* fusion-positive (entity), anaplastic PXA (entity), epithelioid glioblastoma (variant) and glioblastoma with primitive neuronal component (pattern). There were deletions of former entities, variants and terms including gliomatosis cerebri, protoplasmic and fibrillary astrocytoma variants, and "primitive neuroectodermal tumour (PNET)" terminology (13).

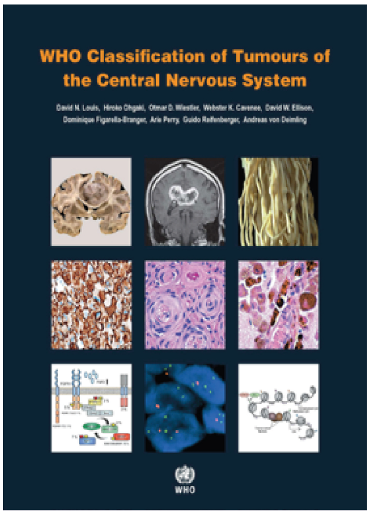

Diffuse astrocytic and oligodendroglial tumours	
Diffuse astrocytoma, IDH-mutant	9400/3
Gemistocytic astrocytoma, IDH-mutant	9411/3
Diffuse astrocytoma, IDH-wildtype	*9400/3*
Diffuse astrocytoma, NOS	9400/3
Anaplastic astrocytoma, IDH-mutant	9401/3
Anaplastic astrocytoma, IDH-wildtype	*9401/3*
Anaplastic astrocytoma, NOS	9401/3
Glioblastoma, IDH-wildtype	9440/3
Giant cell glioblastoma	9441/3
Gliosarcoma	9442/3
Epithelioid glioblastoma	*9440/3*
Glioblastoma, IDH-mutant	9445/3*
Glioblastoma, NOS	9440/3
Diffuse midline glioma, H3 K27M–mutant	9385/3*
Oligodendroglioma, IDH-mutant and 1p/19q-codeleted	9450/3
Oligodendroglioma, NOS	9450/3
Anaplastic oligodendroglioma, IDH-mutant and 1p/19q-codeleted	9451/3
Anaplastic oligodendroglioma, NOS	*9451/3*
Oligoastrocytoma, NOS	*9382/3*
Anaplastic oligoastrocytoma, NOS	*9382/3*

Embryonal tumours	
Medulloblastomas, genetically defined	
Medulloblastoma, WNT-activated	9475/3*
Medulloblastoma, SHH-activated and *TP53*-mutant	9476/3*
Medulloblastoma, SHH-activated and *TP53*-wildtype	9471/3
Medulloblastoma, non-WNT/non-SHH	9477/3*
Medulloblastoma, group 3	
Medulloblastoma, group 4	
Medulloblastomas, histologically defined	
Medulloblastoma, classic	9470/3
Medulloblastoma, desmoplastic/nodular	9471/3
Medulloblastoma with extensive nodularity	9471/3
Medulloblastoma, large cell / anaplastic	9474/3
Medulloblastoma, NOS	9470/3

Ependymal tumours	
Subependymoma	9383/1
Myxopapillary ependymoma	9394/1
Ependymoma	9391/3
Papillary ependymoma	9393/3
Clear cell ependymoma	9391/3
Tanycytic ependymoma	9391/3
Ependymoma, *RELA* fusion–positive	9396/3*
Anaplastic ependymoma	9392/3

Figure 1-5. The WHO blue book. The WHO classification of tumours of the central nervous system 2016 provides information on the histology, genetic profile and prognosis for the different tumour subtypes. Examples of the classifications for diffuse astrocytic and oligodendroglial tumours, embryonal tumours and ependymal tumours are shown (13).

1.3.3.1 Paediatric and adult high grade gliomas

The assignment of HGG to a tumour in a child compared to adults is different; in children, gliomas graded WHO grade II – IV can be considered higher grade and WHO grade I gliomas are low grade. In adults, those that are WHO grade III – IV are considered to be high grade and WHO grade I – II gliomas are lower grade (13,18) This reflects differences in survival with low grade gliomas known to do worse in children although still better than their HGG counterparts (9,30), with <10% 5-year survival for WHO grade IV tumours and <1% for DIPG (31). However, there are variations in survival between tumours of the same grade due to differing genetic markers (31).

Gliomas occurring in adults and children form different subgroups characterised by different molecular features. Diffuse astrocytomas (either *IDH*-mutant or wild type) are characterised by a diffusely infiltrating architecture with moderately pleomorphic nuclei, a high degree of cellular differentiation (13). They are frequently reported as low grade, with low to moderate cellularity and no mitotic activity (32). The IDH-mutant group are more frequently seen in adults. Gliomas harbouring an *IDH1* R132H mutation do occur in children, are located in the forebrain with a median age at diagnosis of 17 years, and have a 2-year survival of 59%, and thus have a better outcome than other subtypes of pHGG (21).

Anaplastic astrocytomas (IDH-mutant, IDH-wild type, NOS) are diffusely infiltrating tumours seen in both paediatric and adult cases with focal or dispersed anaplasia (increasing nuclear size, shape, coarseness, the dispersion of chromatin and the presence of nucleoli). IDH-mutant cases are most frequently seen in adult cases. Histologically, they correspond to WHO grade III (13). They can be hypercellular with prominent mitoses (33).

Oligodendroglioma IDH-mutant and 1p/19q-codeleted is an infiltrative tumour composed of cells with rounded nuclei and artefactually swollen clear cytoplasm. Microcalcifications and branching capillary networks are seen. It corresponds to WHO grade II (13). There is an anaplastic variant featuring microvascular proliferation and/or brisk mitotic activity (33). Oligodendrogliomas are rare in childhood and are mostly seen in adulthood (13).

Anaplastic gangliogliomas represent 1-5% of all gangliogliomas and are assigned a WHO grade of III. They are most frequently seen in children and young adults and are frequently found supratentorially in the temporal lobes although cases in the spinal cord are seen (34). They are characterised by the high-grade features seen in HGG including increased mitotic activity, necrosis, atypia and microvascular proliferation (35). Studies report 39% are associated with *BRAF* V600E mutations, sometimes coexistent with *ATRX* and *hTERT* mutations (70% of which are adults), and *H3F3A* K27M mutations (paediatric midline tumours) (35).

'Diffuse midline glioma, H3 K27M-mutant' is an infiltrative glioma located in the midline and characterised by a K27M mutation in the H3.1 (*HIST1H3B/C*) or H3.3 (*H3F3A*) histones. It is a diagnosis mainly seen in children, with a median age of 5-11 years, and with pontine tumours arising slightly earlier than thalamic counterparts. Whereas diffuse midline gliomas can occur in different midline locations, diffuse intrinsic pontine gliomas (DIPG) are confined to the pons, representing an expansile infiltrative tumour which may not have a K27M mutation. H3 K27-mutant tumours also show a global decrease in H3K27 tri-methylation, which is usually mediated by EZH2 (a H3K27M-specific histone methyltransferase) which is part of the polycomb repressive complex 2 (PRC2); K27M mutant H3.3 binds to this PRC2 and interferes with its enzymatic activity, leading to the loss of both di and trimethylation (36). Recently, a cofactor of PRC2 called EZH1/2 inhibitory protein (EZHIP) has been shown to limit the activity of PRC2 in germ cells, providing a potential mechanism for chromatin regulation in gametes, and for tri-methylation loss in non-H3K27M tumours (37,38). Histologically, the tumour cells are generally small and monomorphic but can be large and pleomorphic. 10% of DIPGs lack necrosis, microvascular proliferation and mitotic figures (features usually characteristic of a high-grade tumour) and therefore correspond to a WHO grade II tumour based on the histological appearance. The remainder correspond to WHO grade IV. Diffuse midline gliomas are automatically assigned WHO grade IV, with the presence of the mutation conferring a worse prognosis compared to other HGG (21).

1.3.3.2 Paediatric and adult low grade gliomas

Pilocytic astrocytomas (WHO grade I) occur frequently in childhood but also occur in adults, and are characterised by varying degrees of compact bipolar cells with Rosenthal fibres, microcysts and occasional granular bodies. They account for 5.4% of all gliomas and show different tissue patterns within the same tumour, including biphasic compact and microcystic areas (39). They are typically slow-growing with a favourable prognosis. Almost all cases are characterised by a single abnormality in the MAPK pathway, most frequently a *KIAA1549:BRAF* fusion (>70%), but also mutations in *BRAF* (usually V600E)*, FGFR1, KRAS* and *NF1* are seen (40). Other *BRAF* fusion partners in rare cases include *QKI, FZR1, MKRN1, FAM131B, CLCN6, GNA11, MACF1*, and *RNF13* (40).

Pilomyxoid astrocytomas are a variant of pilocytic astrocytomas. They have an angiocentric arrangement of bipolar tumour cells, with a myxoid background. They have been previously been assigned WHO grade II, but a definite grade assignment is not recommended due to existing uncertainty. They are more aggressive, and more prone to local recurrence and cerebrospinal spread than pilocytic astrocytomas but there is a lot of variation (13).

Pleomorphic xanthoastrocytoma (PXA) is a glioma seen in both adults and children characterised by large pleomorphic and frequently multinucleated cells, spindle and lipidised cells, a dense reticulin network and prominent eosinophilic granular bodies (13,41). Mitotic activity is low, and a *BRAF* V600E mutation is commonly found. It is superficially located in the cerebral hemispheres and corresponds histologically to WHO grade II. An anaplastic variant exists which corresponds to WHO grade III (13). Increased mitotic activity and necrosis are associated with a worse outcome (41).

Desmoplastic infantile astrocytoma and ganglioglioma (DIGG/DIA) are benign glioneuronal tumours that contain prominent desmoplastic stroma and neuroepithelial population of either neoplastic astrocytes or a mature neuronal component, typically seen in the infant population (42). They are characteristically large cystic lesions involving the superficial cerebral cortex and leptomeninges (42). Histologically, the desmoplastic component shows a mixture of fibroblast-like spindle shaped cells with a wavy pattern and abundant connective tissue. They correspond histologically to WHO grade I. Most studies indicate that gross resection of the tumours will result in long-term survival (13).

1.3.4 Imaging, diagnosis and treatment

When a brain tumour is suspected at clinical presentation, imaging modalities are used to detect a lesion. Radiological appearances of these tumours can vary; glioblastomas are often irregularly shaped with a dark central area of necrosis which is surrounded by a ring of contrast enhancement, extending into adjacent lobes, into the contralateral hemisphere or the brain stem (13). DIPGs are best imaged using MRI and are hypointense on T1 and hyperintense on T2 images. They typically show an asymmetrical expansile mass, but can also extend into the cerebellar peduncles, cerebellar hemispheres, midbrain and medulla (**figure 1-6**). Contrast enhancement is seen but rarely involves >25% of the tumour volume (13).

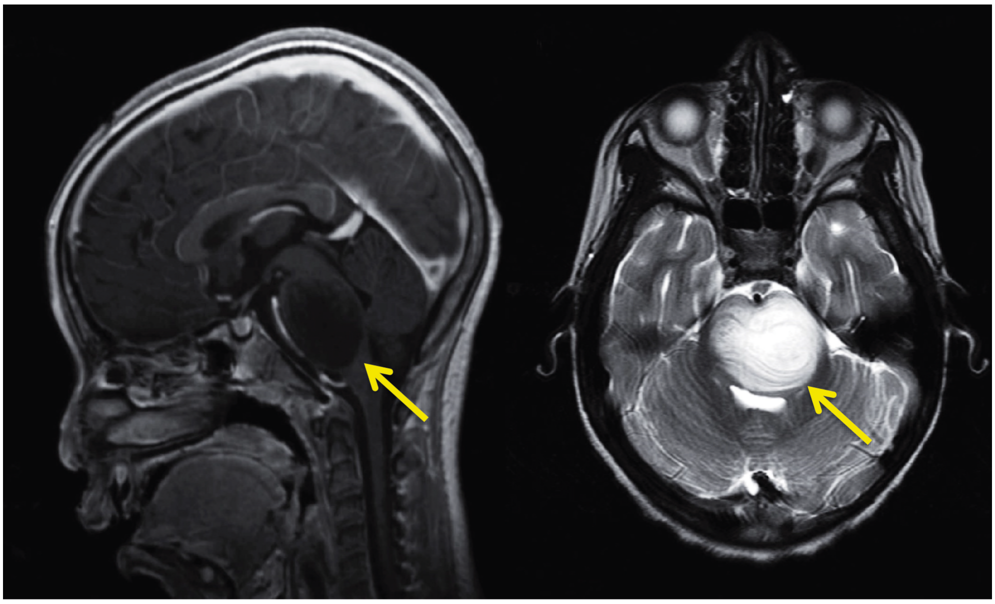

Figure 1-6. MRI images of paediatric patient with DIPG. Sagittal and axial T2 weighted MRI images demonstrating an expansile lesion located in the pons consistent with a radiological diagnosis of DIPG (yellow arrow). Images provided by Lynley Marshall.

Anaplastic astrocytomas show a poorly defined mass with a low intensity. Partial tumour enhancement is seen but usually lacking the ring enhancement and central necrosis seen in glioblastomas. Mass shifts and signs of raised intracranial pressure are observed with rapid tumour growth and peri-tumoural oedema (13). Low-grade tumours are well demarcated with a round to oval shape and smooth margins. Pilocytic astrocytomas can contain calcifications and cyst-like areas. Surrounding oedema is much less marked than higher-grade tumours due to the low biological activity (13).

Functional imaging modalities are increasingly used in the diagnostic work-up; diffusion imaging more accurately assesses the tissue structure, and perfusion imaging and magnetic resonance spectroscopy can measure the tissue metabolite profiles with characteristic features for each tumour type (43).

Accurate diagnosis of tumours requires a tissue sample for histological review and molecular studies, either via surgical resection or biopsy. However, the ability to access the tumour is very dependent on the location. Due to local infiltration and location, brainstem lesions are not generally amenable to surgical resection so these children have poorer outcomes. Routine biopsy of DIPGs was discontinued in the 1990's due to significant morbidity and limited therapeutic options (44). Biopsy of brainstem lesions is now more frequent as a result of a study which showed that the morbidity was similar to that reported for other brain locations, and that sufficient material could be obtained for the required analysis (45); such data has helped in the development of trials such as BIOMEDE, where biopsy is required as one of the criteria for trial entry (46). The importance of longitudinal sampling of gliomas to identify changes with time or in response to treatment is now recognised (47). For tumours where accessibility is challenging, autopsy is helpful to acquire multi-region samples, and has been essential to the discovery of the histone alterations (48) and to investigate heterogeneity within tumours (49), but has also been essential in the identification of novel molecular characteristics such as the H3K27M mutation. It has been utilised for clinical research to correlate radiological interpretation, and has a positive impact on families who derive comfort from the research that is being performed from the autopsy sampling for the benefit of others (50).

Maximal safe surgical resection is the primary objective for most HGG cases due to the positive impact on prognosis. A complete resection radiologically and surgically is often the case microscopically due to extensive infiltration of high-grade lesions. A careful balance between achieving a clear margin versus causing significant morbidity in the long-term is important. Diffuse midline gliomas H3K27M-mutant are usually unresectable in non-brainstem locations and always unresectable when located in the brainstem (51).

Children frequently require adjuvant treatment after surgery to prevent recurrence, including chemotherapy and radiotherapy. Younger children (<3 years) are very susceptible to deleterious effects of this and so it is often avoided. A child with a newly diagnosed HGG will typically receive a dose of 50-60 Gy given over a 6-week period in daily fractions of 180-200 cGy (51).

Chemotherapy was first introduced in the 1970s for the treatment of HGG but there remains very little improvement in overall survival. Several clinical trials have investigated possible benefits; the first occurred in 1989 by the Children's Cancer Study Group and compared strategies of using radiotherapy alone, or radiotherapy followed by pCV chemotherapy (includes prednisolone, chloroethyl-cyclohexyl nitrosourea (CCNU) and vincristine). Initially, an increased 5-year progression-free survival with the addition of chemotherapy was observed, increasing from 16% to 46%. However, subsequent reviews discovered that a large proportion of cases included were low grade gliomas which accounted for the surprising results (52). The results of the Children's Oncology Group (COG) single-arm study ACNS0126 showed no improved outcome when patients were given single agent temozolomide when given during and after radiotherapy, the opposite of that seen in adults (53). The *MGMT* gene promoter methylation status helps to predict prognosis and treatment response to temozolomide in glioblastoma. Methylation at this site silences the gene, therefore leading to inefficient DNA repair of DNA alkylation and then predicting an enhanced response to temozolomide (54). Most recently, the COG HGG trial ACNS0822 included two experimental arms; the first featured vorinostat with radiotherapy, and the second bevacizumab with radiotherapy, with temozolomide and radiotherapy as the control arm. No clear survival advantage was seen with any arm so it failed to advance into phase III testing (55).

1.3.5 Molecular biology

1.3.5.1 Genome wide DNA methylation

Gene activity is regulated by epigenetic mechanisms in spatio-temporal programmes across the course of development. CpG islands are located throughout the genome in a biased pattern, frequently associated with gene promotors; they are a key regulator of gene expression (56). DNA methyltransferases cause the methylation of the cytosine base to 5-methylcytosine which prevents DNA transcription factors gaining access to DNA (57). DNA methylation can therefore lead to many changes involved in the development of a cancer; tumour suppressors can be transcriptionally inactivated, and oncogenes can be activated by decreased levels of methylation (58). Recruitment of chromatin modifiers are also initiated leading to histone modification, and the development of heterochromatin (57).

Each different tumour entity (and normal brain tissue classes) have a distinct methylation profile which means that the methylation profile of a case can be compared to the known profiles to determine its classification (59). The publication of the Heidelberg brain tumour classifier (**figure 1-7**) (59) has provided a very useful tool for the exploration of brain tumour subgroups via methylation profiling. It is used for classifying a case against the existing reference set of tumour entities, and novel class discovery (**figure 1-7A**) (59).

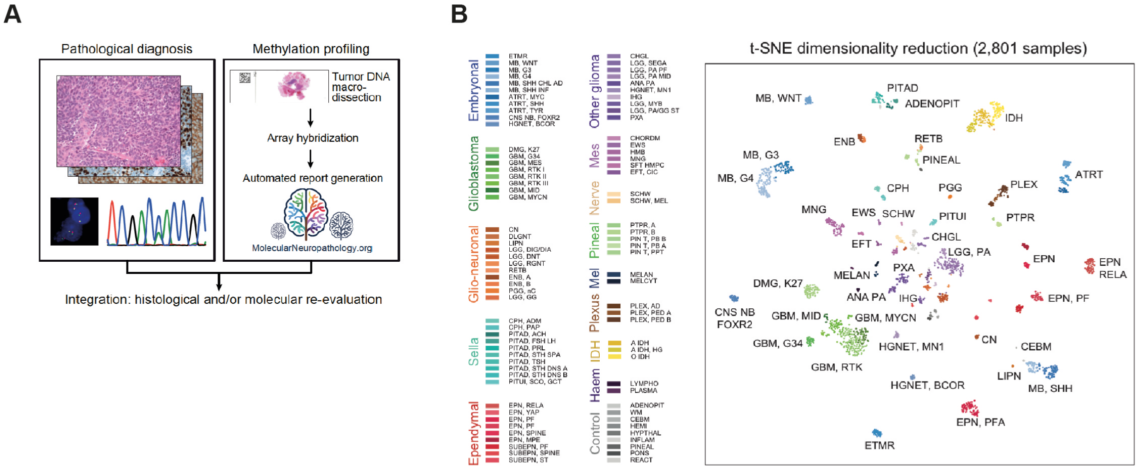

Figure 1-7. The Heidelberg brain tumour classifier. **A,** The classifier was validated using an independent prospective cohort, applying standard pathological diagnosis and then comparing with methylation profiling. **B,** A t-SNE demonstrating the reference cohort; composed of 82 CNS tumour methylation classes and 9 control tissue methylation classes (59).

The classifier is built using a reference set of cases for 91 different classes (82 tumour and 9 control tissue methylation classes). These reference cases are the most representative samples of each particular class (minimum of 9 cases in each class), giving a total of 2,801 reference cases (59). When plotted using a t-distributed stochastic neighbor embedding (t-SNE) dimensionality reduction (a technique that allows high-dimensional data to be visualised by allocating a location to each datapoint within either a two or three dimensional map (59,60)) these reference cases within a particular class cluster with similar cases based on their methylation profiles (**figure 1-7C**). The classifier assigns a calibrated score of 0.0 – 1.0 for each that is processed, providing a confidence level for the assigned classification (59). Therefore, observing where a case projects on the t-SNE, and the calibrated score (a score of >0.9 is considered to be diagnostic) can be used to classify individual cases. It is a diagnostic tool that has significant value in clinical practice in both paediatrics and adults, with 25% of diagnoses changed, 48% refined and 25% confirmed in some adult centres (61), and changing conventional management in 4% of cases and helping to solve 17% of difficult-to diagnose cases in paediatric centres (62).

The assigned methylation subgroups of HGG show differences in the overall survival, the anatomical location and also the age at diagnosis. An integrated meta-analysis featuring 1000 paediatric HGG cases showed that methylation profiling (n=441) assigns them to novel subgroups such as PXA-like (n=43) or LGG-like (n=27) (hemispheric tumours characterised by *BRAF* or *FGFR1* mutations or RTK fusions, which classify alongside other entities but have a better overall outcome), or other more established entities defined by their mutations such as IDH1 (n=36), HGG wild-type (n=156), H3G34R/V (n=51), H3K27M mutant (n=119) and 'other' (n=9) (21). The PXA-like group have a higher frequency of *BRAF*-V600E mutations (19/34) with an improved 2-year survival of 56%. Interestingly, and relevant to this project, the LGG-like group represented a younger group of patients with an excellent prognosis (median age of 4 years, and 74% 2-year survival) (21).

Trials have also evaluated different treatment methods and the impact on clinical outcome; the HERBY trial was a phase II randomised multicentre trial looking at the effect of bevacizumab compared to either temozolomide or radiotherapy (63). It showed that there was no difference in the event free survival (EFS) between different treatment modalities, but also showed that the non-brainstem midline gliomas had a shorter EFS compared to hemispheric tumours (8.0 versus 14.7 months median). The histone mutations also conferred a worse prognosis; *H3F3A* K27M mutation tumours showed a median EFS of 7.9 months, *H3F3A* G34R/V 8.3 months, and wildtype tumours showing a median EFS of 11.3 months (63). Methylation profiling has also helped to define clinical outcomes in pHGG; as mentioned previously, some tumours diagnosed as GBM have methylation profiles similar to PXA (associated with *BRAF* V600E mutations) or LGG, and are associated with a better prognosis (64). Also, when analysing tumours which are not histone mutated or oncogene amplified, these cases show a more favourable prognosis with a 3 year survival of around 70% (64). pHGG therefore represent a very diverse group of subgroups, characterised by both their methylation profiles and somatic mutations.

1.3.5.2 Histone and somatic mutations

A characteristic difference between paediatric and adult HGGs are the presence of histone mutations in pHGG. Histones are a component protein of chromatin; this is composed of nucleosomes which are made up of two copies of the H3, H4, H2A and H2B histones forming an octamer. DNA is wrapped around this within chromosomes (65). Histone mutations define approximately 50% of pHGG cases, and are very rare in adult HGG (66). A landmark study featuring 48 pHGG identified somatic mutations in the H3.3-ATRX-DAXX chromatin remodelling pathway in 44% of cases; 31% of these mutations were in the *H3F3A* gene consisting of two substitutions (K27M, G34R/V) (67). They were also associated with tumour location; the mutations in the *H3F3A* gene coding for the H3.3 histone (H3.3 G34R/V) were found in tumours located in the cerebral hemispheres (**figure 1-8A**) (68,69). However, mutations in a second gene (*HIST1H3B)* were also discovered to feature in a subset of DIPG (48), mutations in *HIST1H3B* and *H3F3A* genes coding for the H3.1 and H3.3 histones respectively (H3.1 or H3.3 K27M) are associated with brainstem or other midline tumours (**figure 1-8A**) (68,70).

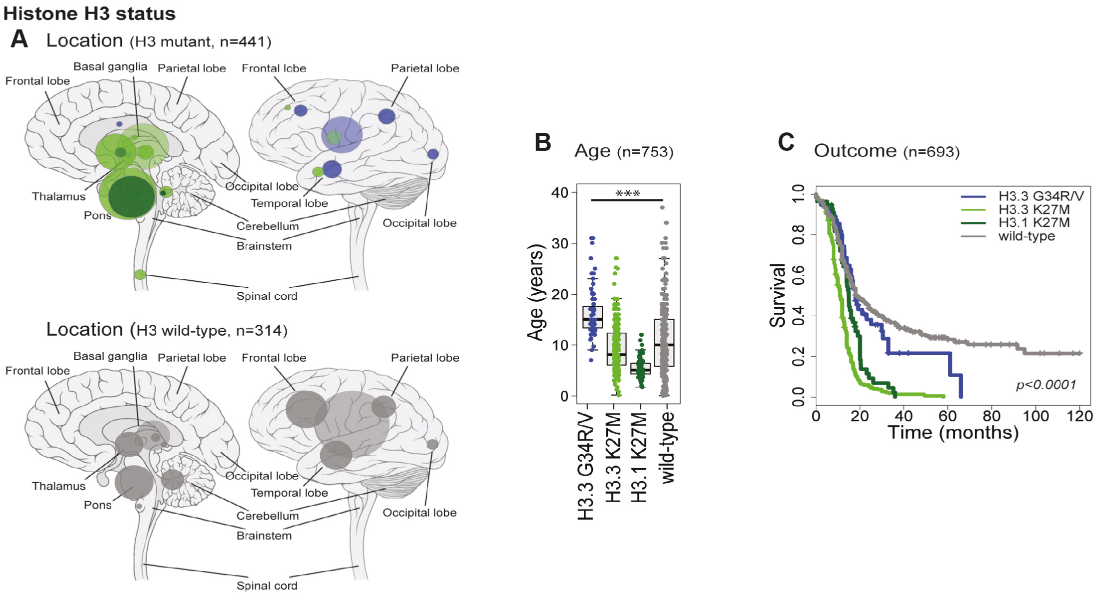

Figure 1-8. Clinicopathological and molecular subgroups of pHGG; the histone subgroups. **A,** Anatomical location of all cases separated by histone mutation (top, n=441) and histone WT (bottom, n=314). Left, sagittal section showing internal structures; right, external view highlighting cerebral lobes. Blue, H3.3G34R/V; green, H3.3K27M; dark green, H3.1K27M. Radius of circle is proportional to the number of cases. Lighter shaded circles represent a non-specific designation of hemispheric, midline, or brainstem. **B,** Boxplot showing age at diagnosis of included cases, separated by histone mutation (n=753). The thick line within the box is the median, the lower and upper limits of the boxes represent the first and third quartiles, and the whiskers 1.53 the interquartile range. ***Adjusted p<0.0001 for all pairwise comparisons, t test. **C,** Kaplan-Meier plot of overall survival of cases separated by histone mutation, p value calculated by the log rank test (n=693) (21).

Histone-mutated tumours show specific pathway moderations; the RTK-PI3K-MAPK pathway is frequently affected. H3.3G34R/V mutated tumours show alterations most frequently at the RTK level opposed to H3.1 K27M mutated tumours which show alterations in PI3K/mTOR. MAPK alterations (including *BRAF*-V600E) are seen in histone wild-type cases (21). Increased BMP signalling is found in H3.1 K27M mutant tumours, largely associated with *ACVR1* mutations (70,71). Others show alterations in the WNT signalling pathway (21) (**figure 1-9**). Genetic alterations seen within pHGG also affect some well-recognised pathways seen within cancer including *TP53* and *PPM1D* mutations which impact on DNA repair (60% of cases), genes responsible for homologous recombination (including *BRCA2, ATM*, and *ATR* amongst others), and genes involved in Fanconi Anaemia (21).

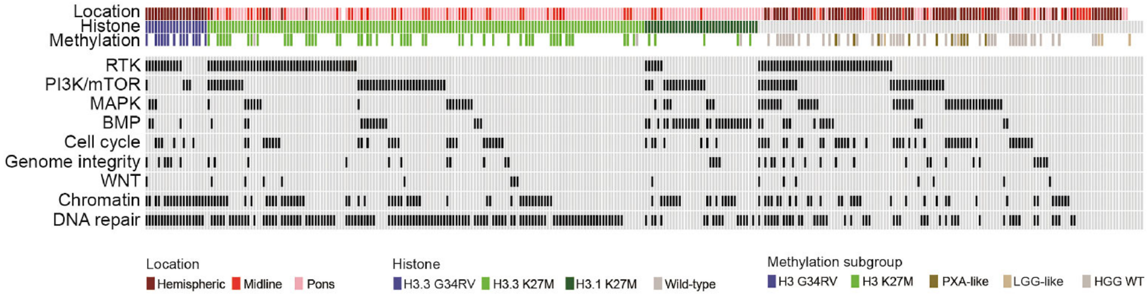

Figure 1-9. Pathway moderations. Oncoprint-style representation of an integrated annotation of somatic mutations and DNA copy-number changes in one or more of nine commonly targeted pathways in 326 pHGG/DIPG. Samples are arranged in columns with pathways labelled along rows. Clinicopathological and molecular annotations are provided as bars according to the included key (21).

Co-segregating mutations include the well-established hemispheric H3.3 G34R/V and *TP53/ATRX* (67), pontine H3.1K27M and *ACVR1* (71,72), midline H3.3K27M and *FGFR1* (73), as well as more novel associations such as H3.3 G34R/V and *ARID1B*, H3.1K27M and *BCOR*, and H3.3 K27M and *ATM/ASXL1* (21). In addition, the H3.3 G34R/V and *IDH1* groups showed significantly enriched

MGMT promoter methylation (63) (around 60% globally hypomethylated and nearly 80% globally hypermethylated respectively) (21), although *MGMT* promoter methylation is largely absent from H3 K27M tumours (21) predicting a poor response to temozolomide. DNA repair pathway mutations are seen frequently (~60%) in association with H3.3 K27M DIPG (21,63,67). Also, analysis of differentially methylated genes identified potential discriminating candidate genes (*OLIG1, OLIG2* and *FOXG1*) in *H3F3A* mutated tumours; lower expression of *OLIG1/2* and higher expression of *FOXG1* was seen in H3.3G34R/V mutated tumours (68).

More generally, alterations in the key biological processes are common across pHGG with over 90% of cases harbouring genetic alterations in one or more; dysregulation of the G1/S cell-cycle checkpoint is common (25%) and also independent of location and subgroup (21). RTK level mutations (in *PDGFRA*) were identified in clusters of HGG enriched for patients with a younger age, (68) and are associated with H3.3 G34R/V, and PI3K/mTOR alterations are enriched in H3.1K27M along with BMP signalling. Nearly 5% of cases harbour alterations affecting the WNT signalling pathway, including *WNT9A, AMER1* and *APC* (21).

Mutations in genes involved in sister chromatid segregation, splicing factors, DNA polymerases, centromere and telomere maintenance are found in pHGG and DIPG. There is also dysregulation of developmental and CNS associated genes, and genes involved in nuclear transport, cell migration and immune response (21). Alterations in *CCND1/2/3* and *CDK4/6* genes of the RB-pathway occur in hemispheric tumours and are absent from the pons (74), whereas amplifications of *CCND2* and deletions of *CDKN2C* show the opposite anatomical association (74). DIPG cases show an almost complete absence of *CDKN2A/B* deletions (74), and a lower frequency of gene mutations including *BCOR, ASXL1*, and *ARID1B* (over 45%) which are involved chromatin modification (21,63).

1.3.5.3 DNA copy number alterations

Differences in copy number alterations are seen between adult and paediatric HGG cases, with gains on chromosome 7 and losses on chromosome 10 diagnostic for most IDH-wildtype glioblastomas of adults, but rarely identified in paediatrics (75). Copy number changes in adult cases can be used for clinical trial design with differences in survival seen when subgrouping by copy number; those that have no copy number changes have a better overall survival (76). Copy number amplifications can also characterise the cellular state of a cell with amplifications in *CDK4, PDGFRA, EGFR* and *NF1* being key features (75). In pHGG, gains of chromosome 1q and losses in 13q and 14q are enriched in paediatric tumours. 17p loss and gains of 9q correlate with a shorter overall survival regardless of the location of the tumour or the subtype (21). Other amplifications at 4q12 (*PDGFRA/KIT/KDR*), 2p24.3 (*MYCN/ID2*), chromosome 7 (*EGFR*), 7q21.2 (*CDK6*) and 7q31.2 (*MET*) are also associated with a shorter overall survival. Deletions in 9p21.3 (*CDKN2A/B*) which correlate with an improved prognosis (21).

However, many pHGG cases show no DNA copy number changes, not specific to location but are associated with a younger age at diagnosis (7.0 versus 10.3 years) (**figure 1-10**). They are also associated with a longer overall survival (21) and this may therefore be worth exploring in infants or younger children with HGG.

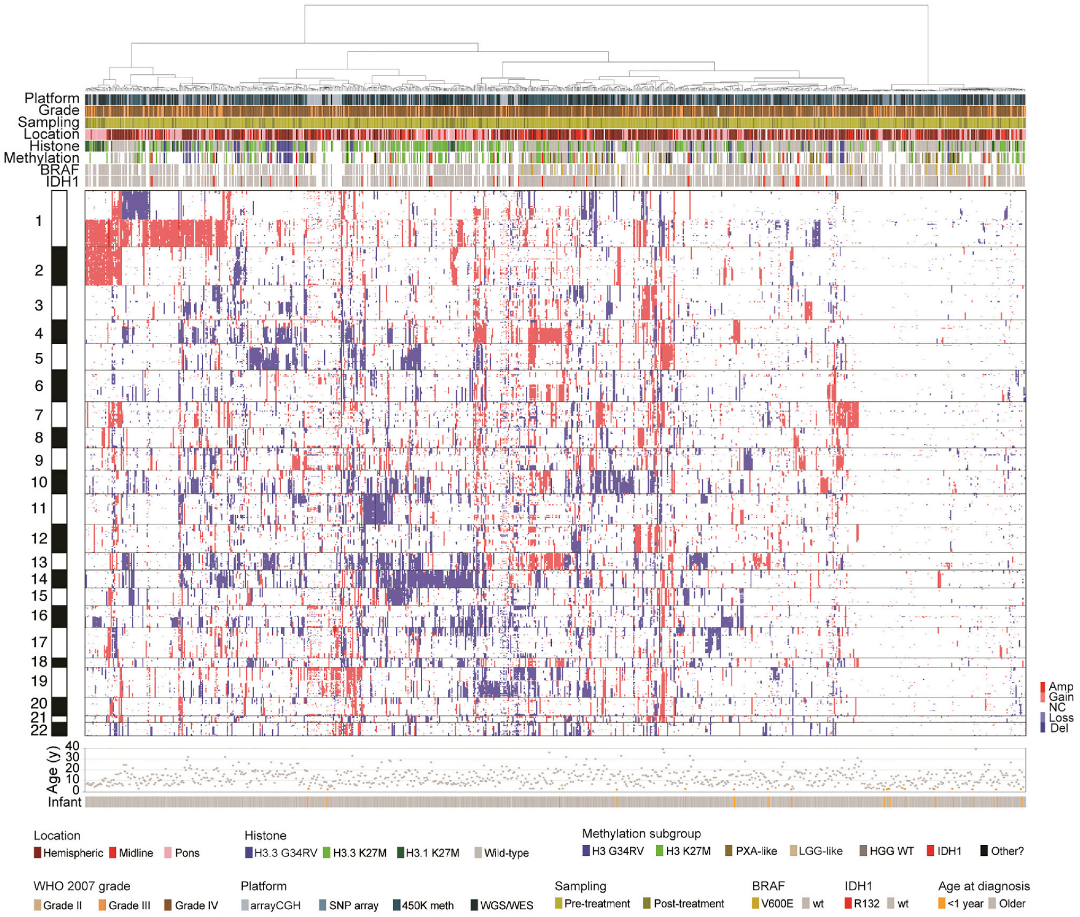

Figure 1-10. Copy number profiling of pHGG/DIPG. Heatmap representation of segmented DNA copy number for 834 pHGG/DIPG (dark red, amplification; red, gain; dark blue, deletion; blue, loss). Samples are arranged in columns clustered by gene-level data across the whole genome. Age at diagnosis is provided below. Clinicopathological and molecular annotations are provided as bars according to the included key (21).

1.3.5.4 Fusions and structural variants

Fusions are known to occur in brain tumours and frequently help to define the classification of subgroups of brain tumours, for example >70% of pilocytic astrocytomas contain a *BRAF* fusion, with *KIAA1549* the most common gene partner (73). *CRAF* gene fusions including *QKI:RAF1* and *SRGAP3:RAF1* are also reported in paediatric LGG (77). The re-classification of the former CNS-PNET tumours identified four new subgroups based on distinct genetic alterations including structural variants involving *FOXR2, CIC, MN1* and *BCOR* genes (78). Structural variants and fusions are known to occur in pHGG cases too; approximately 10% of paediatric glioblastomas are associated with a *MET* fusion including *TFG:MET, CLIP2:MET* and *PTRPRZ1:MET* (79). *ROS1* fusions are reported in paediatric LGG (*GOPC:ROS1* and *CEP85L:ROS1*) (80) and pHGG (81). Novel *DGKB:ETV1, ATG7:RAF1* and *EWSR1:PATZ1* fusions are also reported in pHGG (80), often predicted to be the driving event in the absence of other mutations (80).

Fusions are also reported in adult gliomas with differing effects on outcome; 9% of IDH wild-type astrocytomas (including GBM, AA, diffuse gliomas and pilocytic astrocytomas) contain a targetable fusion with the most frequent involving *FGFR1, MET* and *NTRK* genes (including novel fusions *EGFR:VWC2, FGFR3:NBR1*) (82). 3% of adult glioblastomas harbour rearrangements in *FGFR:TACC*, which are also found in *IDH* wild-type grade II and III gliomas at a similar frequency. They are associated with a poor clinical outcome in these tumours, which may be considered to be a glioblastoma biologically, but sampled in advance of the appearance of high grade features. Alternatively, it could represent an off-target biopsy (83).

1.4 Infant gliomas

Much work has focussed on the molecular pathology of pHGG. However, there remains a lack of data and knowledge to explain the biology of tumours occurring in the infant population. The definition of an infant used in paediatric neuro-oncology varies, but typically refers to children aged <3 - 5 years (5); congenital cases are generally defined as being present at birth (84).

1.4.1 Clinical features of infant gliomas

Infant brain tumours attract clinical attention due to their observed improved outcome. Studies have investigated the outcomes of different treatment modalities in infants. The 'Baby POG I' study included 18 children who were aged less than 3 and diagnosed with an HGG. Four children who were not irradiated after having 24 months of chemotherapy did not develop recurrent disease. Pathological diagnosis (glioblastoma, anaplastic astrocytoma or malignant glioma), the presence/absence of metastases and the degree of surgical resection did not impact on survival of the patients (5). Another study reviewed 'congenital glioblastomas' (occurring in children aged <2 months); five cases of glioblastoma, located in the grey matter adjacent to the ventricles, all showed a survival which was greater than would be expected for older children (30-110 months (median 36 months) with no evidence of disease), and may have been related to the completeness of surgical resection. Conservative surgical approaches have a better outcome due to the highly vascular nature of the tumours which brings increased clinical risk. However, gene expression showed enrichment for receptor tyrosine kinase function, specifically for *RET, ALK, RASGRF2* and *EFNA5* genes (85), indicating a different molecular profile to that reported in pHGG. However, many of the tumours in these early studies were diagnosed based on histology alone and with greater advances in diagnostics that are now accessible, they may not truly represent the tumour groups they have been assigned to. Therefore, a better understanding of these tumours in terms of their molecular characteristics and associated clinical features will lead to a significantly improved treatment and management strategy, improving the survival further.

Well-established HGG entities (including DIPG) occur in the infant population, and although predicted to have a dismal prognosis reported cases also show an improved outcome; two cases are described where MRI scanning identified ponto-medullary lesions consistent with a DIPG. It was decided after clinical discussion not to treat these tumours. However, both cases showed clinical improvement, the achievement of developmental milestones and survival up to the time of writing (aged 10) (86). Another case report describes a brainstem lesion diagnosed in an infant aged 7 weeks, with characteristics favouring a DIPG. Again, no treatment was received and repeated imaging showed regression of the tumour with complete absence by the age of 27 months (87). Another DIPG case (diagnosed in a child aged 2 years) was treated for associated clinical symptoms (shunting for hydrocephalus) but the tumour was not treated directly. Repeated imaging showed regression of the tumour with a complete absence by the age of 6.6 years (88). A further report described a prenatal MRI diagnosis of a diffuse brainstem glioma; the child was born without symptoms, and follow up scans showed a reduction in the size of the lesion (89). This has also been reported in cases of DIGG/DIA; two cases in a 9-month-old and a 6-month-old, who both underwent subtotal resection, did not receive any adjuvant therapy post-operatively and both residual tumours regressed over several months (90).

Usually DIPGs have <10% 2-year survival and are ultimately fatal so these presentations are extremely unusual in this context and brings into question whether these are conclusively DIPG tumours without a histological diagnosis available. These cases also hint at a different molecular biology associated with tumours in the infant population. These findings have significant clinical implications; potentially there is a subgroup of paediatric brain tumours which do not need to be treated as aggressively with potentially harmful adjuvant therapies.

1.4.2 Histological features of infant gliomas

Previous studies have hinted at different histological features within infant gliomas. Haberler *et al* (2007) describe malignant gliomas present in two infants that underwent gross total resection and adjuvant chemotherapy. Follow-up at 18 and 10 months confirmed complete remission of the tumours. The histology showed a high density of 'minigemistocytic shaped' cells with abundant mitoses and absent necrosis, concluding that this may represent a new subtype of glioma (91). Other reported cases all describe tumours that show high grade features; high mitotic activity, cell-rich, palisading necrosis and microvascular proliferation (92), which would lead to a WHO grade of III/IV being assigned. This represents an interesting finding where despite the high-grade histology of these cases, they have an improved survival. Questions are now being raised as to the value of the WHO grading system in pHGG; necrosis and vascular proliferation are two features that help to differentiate WHO grade III and IV tumours, but neither WHO III and IV are reported to be associated with any difference in outcome for pHGG (93). Errors can also be made in diagnosis with reclassification of HGG to LGG reported at 5% in some studies (93), and so other diagnostic tests need to be used in conjunction with histology to maximise accurate diagnosis and this may be very important for infants where there may be variation in histological appearances.

1.4.3 Molecular biology of infant gliomas

The very few infant HGGs studied so far show that they rarely contain histone mutations, although pontine tumours (DIPG) can contain H3K27M mutations (94). Existing studies found tumours which harbour very few mutations and fusions that have not previously been identified in other paediatric brain tumours, including fusions involving the *NTRK* genes (74).

NTRK fusions are not specific to brain tumours. They are found in many other cancer types including colorectal, breast, thyroid, lung and gastrointestinal stromal tumours. The Tropomyosin receptor kinase family is composed of Trk A, Trk B and Trk C which are 3 transmembrane proteins that are encoded by the *NTRK 1, 2* and *3* genes (**figure 1-11**) (95). They are expressed in neuronal tissue, contribute to the normal development and function of the central nervous system and are all activated by neurotrophins. The *NTRK* gene rearrangements represent an opportunity for targetable treatment option for fusion-positive brain tumours (95).

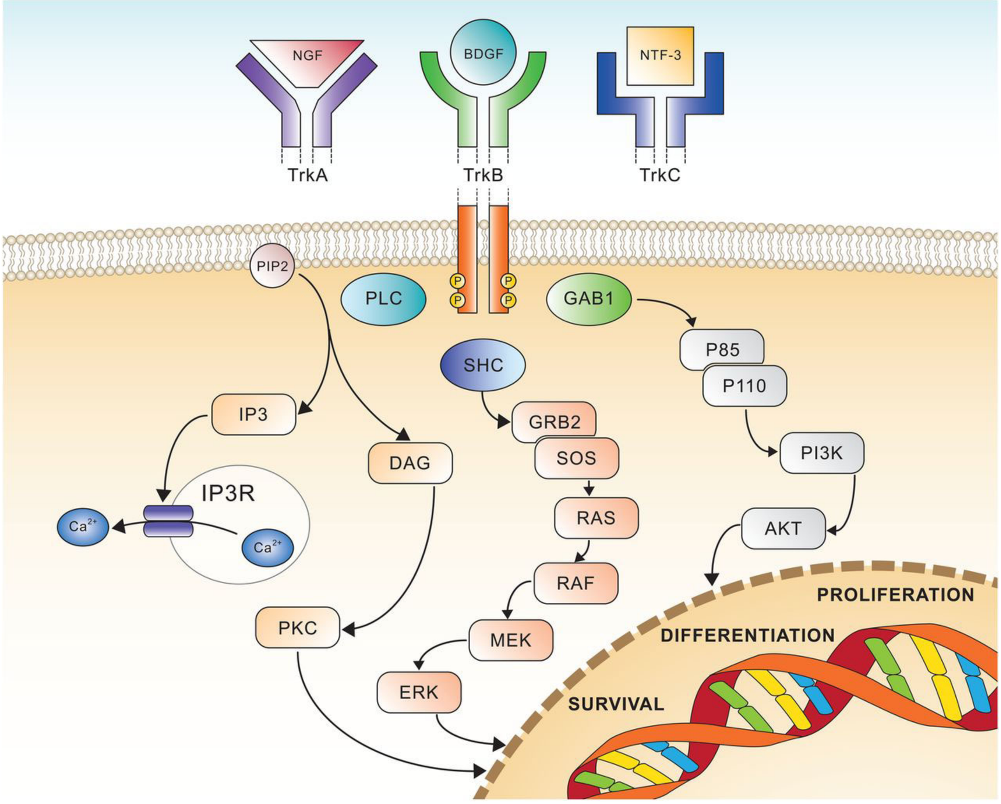

Figure 1-11. Trk receptor signalling. A schematic diagram showing the three major signalling pathways that are involved in survival, differentiation and proliferation in response to the activation of the Trk A, B and C receptors by their respective ligands, nerve growth factor (NGF), brain-derived growth factor (BDNF), and neurotrophin 3 (NTF-3) (95).

NTRK fusions can be found in both HGG and LGGs and studies have identified novel fusions and attempted to understand their function in HGG. A LGG study included 96 pilocytic astrocytomas and using whole genome sequencing, identified novel *QKI:NTRK2* and *NACC2:NTRK2* fusions, and an *RNF130:BRAF* fusion (although the age of the patients was not stated) (**figure 1-12**) (73).

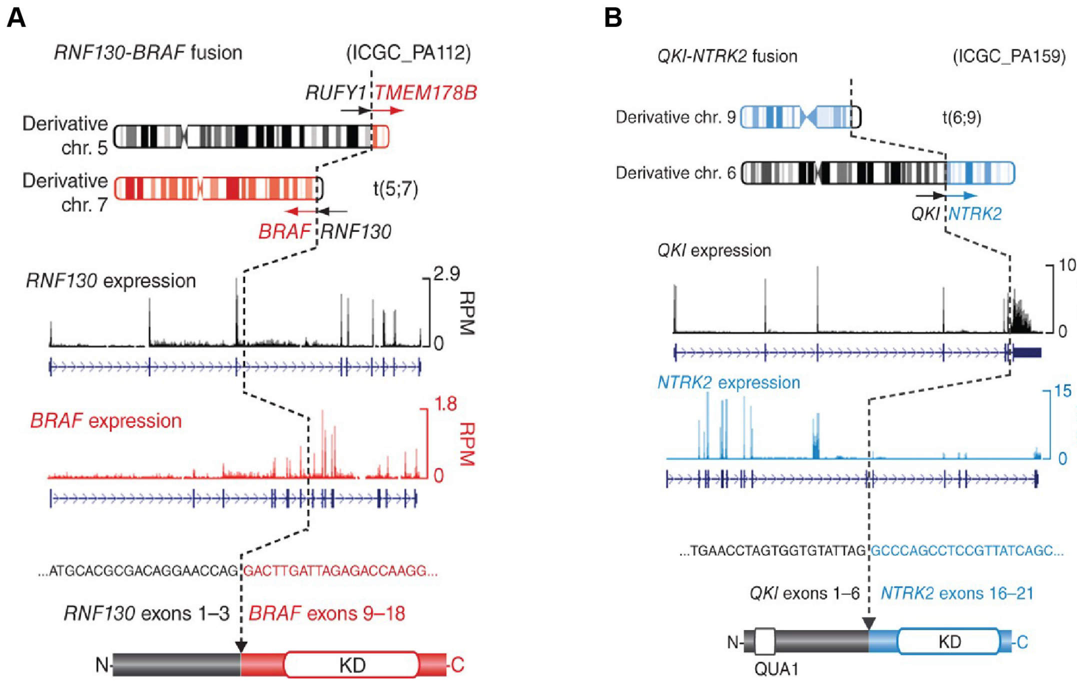

Figure 1-12. Fusions occurring in LGG. **A,** A schematic representation of the *RNF130:BRAF* fusion gene reported in two cases; the translocation is between chromosomes 5 and 7. **B,** A schematic representation of the *QKI:NTRK2* gene found in one case; the translocation is between chromosome 9 and 6 (73).

Also, a *SLMAP:NTRK2* fusion was reported in a single case of parietal ganglioglioma, identified by RNAseq although again, the age of the patient is not stated (96). An HGG study found eight examples of *NTRK* fusion genes in a cohort of HGG cases, specifically *TPM3:NTRK1, BTBD1:NTRK3, ETV6:NTRK3, VCL:NTRK2* and *AGBL4:NTRK2* with three cases of HGG (non-brainstem) present in children aged less than 3 years old (**figure 1-13**). Transduction of TP53-null primary mouse astrocytes with retrovirus expressing Flag-tagged human *TPM3:NTRK1* or *BTBD1:NTRK3* generated HGGs with a very short latency period, and complete penetrance when implanted into mouse brains indicating their role in tumour formation. Elevated phosphorylated AKT and p42/44 MAPK levels compared to normal brain tissue, and features of PI3K and MAPK pathway activation were also found (74). Having confirmed that the *NTRK* fusion proteins induce HGGs, the hematoxylin and eosin (H&E) sections showed abundant pleomorphic nuclei with associated high mitotic activity consistent with HGG. Specifically, tumours from *BTBD1-NTRK3* transduced cells contained giant cells, drawing comparisons with the GBM variant of giant cell glioblastoma (74).

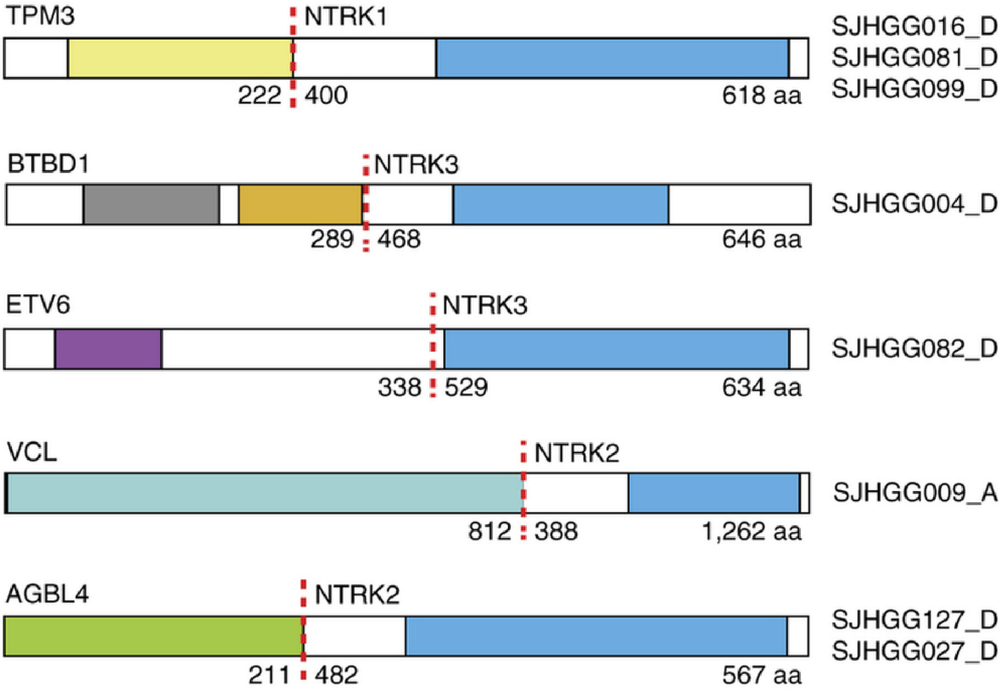

Figure 1-13. *NTRK* fusions occurring in pHGG/DIPG. Examples of *NTRK1/2/3* fusions identified in a cohort of pHGG/DIPG. For each fusion, the dotted red line shows the fusion breakpoints of each gene (74).

Other studies have investigated the functionality of the other *NTRK* genes in fusions; *BCAN:NTRK1* fusions occur in gliomas and generated both *in vitro* and *in vivo* models in adult neural stem cells from p53 -/- mice using CRISPR-Cas9 gene editing. The cells were tumourigenic, formed tumours histologically consistent with HGGs and were sensitive to targeted inhibition (97).

The existing infant glioma studies have shown a very different molecular landscape to that of older pHGG cases, with improved outcome and potential novel genetic drivers with evidence of target inhibition. This represents an opportunity to develop a classification for this group to help refine diagnosis and improve the outcome still further for these very young patients.

CHAPTER 2 – Materials and methods

2.1 Genomic analysis

2.1.1 Patients and samples

All patient samples included were classified as gliomas (WHO grade II, III or IV) age ≤4 years old (including congenital cases) from all CNS locations (including spinal tumours, but excluding optic pathway gliomas). Cases were excluded if they had been diagnosed as a pilocytic astrocytoma with a known *BRAF* fusion or mutation. Ependymal, embryonal, mesenchymal, and germ cell tumours were also excluded. All cases in the infant cohort had undergone either a biopsy and/or a resection of the tumour. Where possible, a hematoxylin and eosin (H&E) slide, 10 unstained sections, formalin-fixed paraffin-embedded (FFPE) tissue rolls, or frozen tissue was provided for each case. In some cases, data alone were provided. A total of 241 cases were entered into the study. Eight cases from King's College and St George's Hospital London (21) and ten cases from St. Jude Children's Hospital in Memphis (74) have been previously published. All patient samples were collected under full Research Ethics Committee approval at each participating center.

2.1.2 Nucleic acid extraction

DNA was extracted from frozen tissue by homogenisation prior to following the DNeasy Blood & Tissue Kit protocol (QIAGEN). DNA was extracted from FFPE pathology blocks after manual microdissection using the QIAamp DNA FFPE Tissue Kit protocol (QIAGEN). Concentrations were measured using a Qubit fluorometer (Life Technologies). RNA was extracted by following the RNeasy Mini

Kit protocol (QIAGEN), and quantified using a Nanodrop 2000 Spectrophotomer (Thermo Scientific).

2.1.3 Cell-Free DNA (cfDNA) extraction from plasma

5-10mL of peripheral blood sample were collected into Cell-Free DNA Collection Tubes (Streck). Blood samples were centrifuged twice for 10 minutes, a first centrifugation at 1,600 g and a second centrifugation at 1,600 g or 16,000 g to remove cellular contents and/or debris. Samples were stored at -80°C until cfDNA extraction. cfDNA isolation from plasma was performed using the QIAamp circulating nucleic acid kit (Qiagen, 55114) following quantification using the Qubit fluorometer (ThermoFisher Scientific, dsDNA HS Assay kit, Q32854) and fragment analysis by 4200-TapeStation (Agilent, Genomic DNA ScreenTape 5067-5366).

2.1.4 Methylation profiling

150 ng of DNA underwent bisulfite conversion and was sent to DKFZ (Heidelberg, Germany), University College London (UCL) Great Ormond Street Institute of Child Health, Ospedale Bambino Gesù (Rome, Italy) or St Jude Children’s Research Hospital genomics centres for methylation array analysis. Either Illumina 450k or EPIC BeadArrays were performed. The data derived was pre-processed using the minifi package in R (v11b4). The Heidelberg brain tumour classifier (molecularneuropatholog.org, v11b4) was used to classify each individual case by assigning a calibrated score to each case, which would inform as to which of the 91 tumour entities featuring in the current classifier (v4) the case most closely resembled. The beta values from the methylation arrays were

clustered based on correlation distance using a Ward algorithm. DNA copy number data was derived from the methylation arrays using combined $\log_2$ intensity data based upon an internal median processed with the R packages minfi and conumee (v11b4) to call copy number in 15,431 bins across the genome.

Differential methylation analysis was carried out using minifi. The results were analysed for gene set enrichment using methylGSA (1.6.1) (rdrr.io/bioc/methylGSA/). The number of CpG islands for each gene was adjusted by both weighted resampling and Wallenius noncentral hypergeometric approximation in methylgeometh. The ontology networks were constructed using ShinyGo (0.61) (bioinformatics.sdstate.edu/go/).

2.1.5 Fusion panel sequencing

A custom fusion panel consisting of 22 genes associated with fusions in paediatric brain tumours (*ALK, BCOR, BRAF, c11orf95, C19MC, CIC, ETV6, FGFR1/3, FOXR2, KIAA1549, MET, MN1, MYB, MYBL1, NTRK1/2/3, RAF1, RELA, TPM3,* and *YAP1*) was designed with a library of probes to ensure adequate coverage of the specified regions (Roche Sequencing Solutions). Where available, 100 to 200 ng of DNA was used for library preparation using KAPA Hyper and HyperPlus Kit (Kapa Biosystems) and SeqCap EZ adaptors (Roche). Following fragmentation, DNA was end-repaired, A-tailed, and indexed adaptors ligated. DNA was amplified, multiplexed, and hybridised using 1 µg of the total precapture library DNA. After hybridisation, capture libraries were amplified and sequencing was performed on a MiSeq and NextSeq (Illumina) (**appendix figure 1**). Quality control, variant annotation, deduplication, and metrics were generated for each sample. The raw list of candidates provided by Manta (https:// github.com/Illumina/manta) was filtered for more than 2 reads covering both genes, common false positive base pairs (bp) positions / fusions outside of the capture set at both ends, common breakpoint/ false positives within 10bp, common false positive gene pairs, fusions within the same gene and homologous sequences greater than 10bp. Breakdancer was used to confirm all the breakpoints in all samples. Sequences either side of the break points were annotated to look for repetitive elements. A BLAT score was obtained to remove loci which were not uniquely mapped. Integrative Genomics Viewer was used to view the fusions.

2.1.6 PCR/Sanger sequencing validation

PCR to validate fusion breakpoints was carried out using primers obtained from Integrated DNA Technologies. The PCR reagents (Invitrogen) were added to a 96 well reaction plate (Life Technologies) in a final volume of 25μl containing 2.5μl 10x Buffer, 0.5μl 10mM dNTP mix, 0.75μl 50mM Mg^{2+}, 2μl of each primer (10μM each), 5μl of DNA (10ng/μl), 0.4μl Taq Polymerase (5U/μl), and 13.85μl of ddH_20. The PCR was performed in a thermocycler with initial denaturation at 94°C for 3 minutes, followed by 38 cycles of denaturation at 94°C for 3 minutes, annealing at 55°C for 30 seconds, and extension at 72°C for 30 seconds, followed by a final extension at 72°C for 5 minutes.

PCR products were cleaned using the ExoProStar S 20 (Sigma-Aldrich) and were sent for Sanger sequencing (DNA Sequencing and Services, University of

Dundee, United Kingdom). Sequences were analysed manually with 4Peaks (Nucleobytes). (**appendix table 1**).

2.1.7 NanoString gene expression analysis

The top 30 genes with the most differentially methylated regions between *ALK*-fusion, *NTRK*-fusion, and fusion-negative cases were selected for an mRNA expression analysis using a custom nCounter platform and nDesign (NanoString). Specimen RNA was mixed in hybridisation buffer with CodeSets and hybridised overnight at 65°C. Samples wash reagents and imaging cartridge were processed on the nCounter Prep Station and imaged on the nCounter Digital Analyser according to the manufacturer’s instructions. Data were normalised with NanoStringNorm v1.2.1 using variance stabilising normalisation. Heat maps were made by clustering the median centered expression values or a correlation matrix based on Euclidean distance using a Ward D2 algorithm.

2.1.8 DNA and RNA sequencing

DNA was sequenced either as whole genome or captured using Agilent SureSelect whole exome v6. Library preparation was performed using 50 to 200 ng of genomic DNA. Following fragmentation, DNA was end-repaired and A-tailed, and indexed adapters ligated. DNA was amplified, multiplexed, and hybridised using 1 µg of total precapture library. After hybridisation, capture libraries were amplified and sequencing was performed on a NextSeq500 (Illumina) with 2 x 150 bp, paired-end reads following the manufacturer’s instructions.

Ribosomal RNA was depleted from 500 to 2,000 ng of total RNA from FF and FFPE using NEBNext rRNA Depletion Kit. Following first-strand synthesis and directional second-strand synthesis, resulting cDNAs were used for library preparation using NEBNext Ultra II Directional RNA Library Prep Kit from Illumina performed as per the manufacturer's recommendations. Exome capture reads were aligned to the hg19 build of the human genome using bwa v0.7.12 (bio-bwa.sourceforge.net), and PCR duplicates removed with PicardTools 1.94 (pcard.sourceforge.net). Single-nucleotide variants were called using the Genome Analysis Tool Kit v3.4-46 based upon current best practices using local realignment around InDels, downsampling, and base recalibration with variants called by the Unified Genotyper (broadinstitute.org/gatk/). Variants were annotated using the Ensembl Variant Effect Predictor v74 (ensembl.org/info/docs/variation/vep) incorporating SIFT (sift.jcvi.org) and PolyPhen (genetics.bwh.harvard.edu/pph2) predictions, COSMIC v64 (sanger.ac.uk/genetics/CGP/cosmic/), dbSNP build 137 (ncbi.nlm.nih.gov/sites/SNP), ExAc, and ANNOVAR annotations. RNA sequences were aligned to hg19 and organised into de novo spliced alignments using bowtie2 and TopHat version 2.1.0 (ccb.jhu.edu/software/tophat). Fusion transcripts were detected using chimerascan version 0.4.5a filtered to remove common false positives.

2.1.9 Paediatric High-Grade Glioma panel

A custom panel of 330 genes derived from our 2017 Cancer Cell paper (21) was designed (**appendix table 2**). Libraries were prepared from 50-200 ng of DNA using the Kapa HyperPlus kit and DNA was indexed utilising 8bp-TruSeq-Custom

Unique Dual Index Adapters (Integrated DNA Technologies). Following fragmentation, DNA was end-repaired, A-tailed and indexed adapters ligated. DNA was then amplified, multiplexed and hybridised using 1 µg of total pre-capture library. After hybridisation, capture libraries were amplified and sequencing was performed on either a MiSeq, NextSeq500 or NovaSeq6000 system (Illumina) with 2 x 150bp, paired-end reads following manufacturer's instructions.

2.1.10 Single-cell RNA sequencing

Disaggregated single cells from fresh frozen biopsies of infant high grade gliomas were subjected to single cell RNA sequencing using SMART-Seq2 methodology in collaboration with Mariella Filbin's team at DFCI in Boston. Following library preparation and sequencing, fastq files, were aligned to the reference genome (hg19) using bowtie, followed by transcript quantification as Transcripts per Million using the rsem pipeline. These data were then combined with publicly available SMARTSeq2 datasets of GBM (75) and DIPG (98) pre- processed in the same way recovered from GEO (GSE131928 and GSE102130) and the single cell portal at the Broad Institute. Log transformed counts were combined as single cell experiments using the R packages scater (1.16.2) and scran (1.16.0) and annotated with combined metadata. Combined data was then clustered using PCA and TSNE. Cell type assignments were made using the R packages singleR (1.2.4) and GSVA (1.36.3) with reference to human neurodevelopmental cell types (99) and those defined as components of bulk tumour profiling.

2.2 Histology

2.2.1 Histology review

Histological review was performed for all cases in the project where an H&E slide had been obtained. Each case was reviewed using the WHO Classification of Tumours of the Central Nervous System (2016). The review was undertaken with the assistance of Professor Thomas Jacques, Consultant Paediatric Neuropathologist (Great Ormond Street Institute of Child Health), whilst blinded to the molecular features of each case. A set of criteria to assess the histological features that are characteristic of gliomas was predetermined and included astrocytic and stromal morphology, and the presence of mitotic figures and necrosis. A second review of these cases was then conducted with consideration of the molecular features that had been identified. This enabled either the confirmation of the original pathology diagnosis of the case (particularly for the well-established tumour subtypes), but also allowed both architectural and cytological features to be derived to characterise the novel infant subgroups of the study.

2.2.2 Immunohistochemistry

Immunohistochemistry for Ki-67 (M7240, DAKO, 1:100) was performed to determine the proliferative index of some of the cases. Pressure-mediated antigen retrieval and the Envision detection system (DAKO K5007) was used, and the slides mounted with Leica CV Ultra mounting medium. The slides were then imaged using a high throughput scanning microscope AxioScan Z1 and quantified using Definiens software.

2.3 *In vitro* culture

2.3.1 Primary culture establishment

Three novel primary cultures formed part of this study: QCTB_INF_R077, QCTB_INF_R102 and ICR_CXJ-020 (corresponding to patient KING_INF_018). Using a sterile scalpel, tissue collected from surgery was minced into as small pieces as possible, and LiberaseTL was added for 10 minutes at 37°C to enzymatically dissociate the tissue. These, as well as non-infant pHGG cultures QCTB-R006 and QCTB-R059, were grown under stem cell conditions as two-dimensional adherent cultures on laminin and/or laminin-fibronectin substrates in serum-free media composed of 1:1 Neurobasal(-A) and DMEM:F12 which was supplemented with NEAA, sodium pyruvate, HEPES, and Glutamaxx. To this, B27(-A), human PDGF-AA (10ng/mL), human PDGF-BB (10ng/mL), human bFGF (20ng/mL), human EGF (20ng/mL) and heparin (2ng/mL) were also added.

2.3.2 Primary culture passaging and storage

Cells were grown as adherent cultures until 80-90% confluency was reached. The cells were then dissociated enzymatically using accutase and counted using a Beckman-Coulter ViCell cell viability analyser. They were then re-seeded into fresh flasks. The infant lines grew best using a 1:2 or 1:3 split, whereas the control lines could be grown comfortably up to a 1:5 split. Each time the cells were passaged, if sufficient cells were available, a vial was stored in the cell bank; cells were mixed with Stem Cell Banker (1 mL) and stored in the freezer at -80°C before being transferred to liquid nitrogen storage when appropriate.

2.4 *In vitro* techniques

2.4.1 Drug assays

The cells were seeded (3,000–5,000 cells per well) into laminin or laminin–fibronectin-coated 96-well plates and treated with TRK inhibitors entrectinib (RXDX-101, Selleckchem), crizotinib (PF-02341066, Selleckchem), milciclib (PHA-848125, Selleckchem) and larotrectinib (LOXO-101, Selleckchem) at concentrations ranging from 0 to 20 µmol/L for 8 days. Each assay was performed in three independent biological replicates of three technical replicates each. The cell viability was assessed with Cell Titer-Glo using a FLUOstar Omega plate reader (BMG, LABTECH). GraphPad Prism software was used to analyse the data and calculate the GI50 values.

2.4.2 Western blotting

The cells were incubated in complete media with the vehicle or increasing concentrations of entrectinib (0.1, 1, 10 µmol/L). The protein was collected 4 hours post-treatment. Samples were lysed using lysis buffer (Cell Signaling Technology) containing phosphatase inhibitor cocktail (Sigma) and protease inhibitor cocktail (Roche Diagnostics). Following quantification using Pierce BCA Protein Assay Kit (Thermo Fisher Scientific), cell extracts were loaded for Western blot analysis. The membranes were incubated with primary antibody (1:1,000) overnight at 4°C, and horseradish peroxidase secondary antibody (Amersham Biosciences) for 1 hour at room temperature. Signal was detected with ECL Prime Western blotting detection agent (Amersham Biosciences), visualised using Hyperfilm ECL (Amersham Biosciences) and analysed using an X-ray film processor in accordance with standard protocols. The primary antibodies used were phospho-AKT (Ser473; Cell Signaling Technology; #4060), phosphop44/ 42 (Thr202/Tyr204; Cell Signaling Technology; #4370), AKT (Cell Signaling Technology, #9272), p44/42 (Cell Signaling Technology; #9102), GAPDH (Cell Signaling Technology; #2118).

2.5 Immunofluorescent staining

Paraffin-embedded tissue section of infant gliomas were deparaffinised using three changes of xylene and ethanol. Heat-mediated antigen retrieval was performed (Dako S1699, pH 6.0) and tissue slides were permeabilised with 0.5% Triton X-100 solution at room temperature for 10 minutes. They were then blocked with the appropriate serum according to the species of secondary antibody at room temperature for 1 hour. For STAT1 staining (AHO0832, Invitrogen, 1:800), Alexa Fluor 488 Tyramide Super Boost Kit was used (B40941, Invitrogen) and the antibody was incubated for 30 minutes at 37 °C. For WNT5A (MA5-15502, Invitrogen, 1:800) and P63 (39692, Cell signalling, 1:900) staining, samples were also incubated at 37 °C for 30 minutes. The sample slides were then washed in PBS three times and incubated with DyLight 649 (DI-2649, Vector, 1:100) and Alexa Fluor 555 (A31572, Invitrogen, 1:300) -conjugated secondary antibodies at room temperature for 1 hour. The nuclei were next counterstained with DAPI and the samples were mounted with Vectashield (H1000, Vector Laboratories). Finally, the slides were examined using the Zeiss Axio Scan.Z1 automated Fluorescence slide scanner.

2.6 *In vivo* techniques

2.6.1 Intracranial injections

All experiments were performed in accordance with the local ethical review panel, the UK Home Office Animals (Scientific Procedures) Act 1986, the United Kingdom National Cancer Research Institute guidelines for the welfare of animals in cancer research and the ARRIVE (Animal Research: Reporting *In Vivo* Experiments) guidelines (100,101). Single-cell suspensions were obtained immediately prior to implantation. NOD.Cg-$\textit{Prkdc}^{\mathrm{scid}}$ $\textit{Il2rg}^{\mathrm{tm1Wjl}}$/SzJ (NSG) mice (Charles River) were anaesthetised with intraperitoneal ketamine (100mg/kg)/xylazine (16mg/kg) and maintained under 1% isoflurane (0.5L/minute). The animals were depilated at the incision site on the head and Emla cream 5% (lidocaine/prilocaine) was applied on the skin. A subcutaneous injection of buprenorphine (0.03mg/kg) was given for general analgesia. The cranium was exposed via a midline incision under aseptic conditions with a scalpel, and a 31-gauge burr hole drilled above the specific injection site. Mice were then placed on a stereotactic apparatus for orthotopic implantation. The site of injection was the cerebral cortex in order to mimic the clinical scenario as closely as possible. The coordinates used for the cortex were $x = -2.0$, $z = +1.0$, $y = -2.5$ mm from the bregma. 300,000 cells in 5µL were stereotactically implanted using a 25-gauge SGE standard fixed needle syringe (SGE 005000) at a rate of 2 µL/minute using a digital pump (HA1100, Pico Plus Elite, Harvard Apparatus). At the completion of infusion, the syringe needle was allowed to remain in place for at least 3 minutes, and then manually withdrawn slowly to minimise any backflow of the injected cell suspension and possible growth of tumours around the meningeal surface of the brain. An intraperitoneal injection of the reversing agent atipamezole (1mg/kg) diluted in Hartmann solution for rehydration was administered. The mice were monitored until fully recovered from surgery and given Carprofen (analgesia) in a gel diet for 48 hours post-surgery. The mice were weighed twice a week and observed for any signs of neurological deficit (seizures, weakness, problems with balance etc) or general loss of condition (hunched back, reduced activity and interaction, unkempt coat) at which point they would be culled and the brains fixed in formalin for 24 hours. The brain was then cut transversely from anterior to posterior, with one half cryopreserved and the remainder embedded for histological review.

2.6.2 Magnetic resonance imaging

Mice were weighed twice a week and imaged by ^{1}H MRI performed on a horizontal bore Bruker Biospec 70/20 (Ettlingen, Germany) equipped with physiological monitoring equipment (SA Instruments, Stony Brook, NY, USA) using a 2cm x 2cm mouse brain array coil, with a field strength of 7T. Anaesthesia was induced using 3% isoflurane delivered in oxygen (1l/min) and maintained at 1-2%. Core body temperature was maintained using a thermo-regulated water-heated blanket. Following optimisation of the magnetic field homogeneity using a localised map shim over the whole brain, a rapid acquisition with relaxation enhancement (RARE) T_2-weighted sequence (repetition time (T_R) = 4500ms, effective echo time (T_{Eeff}) = 36ms, 2 averages, RARE factor = 8, in-plane resolution 98µm x 98µm, 1mm thick contiguous axial, coronal and sagittal slices) was used for the identification of any tumours. All imaging was performed by Dr Jessica Boult, Division of Radiology and Imaging, ICR.

2.7 Novel *NTRK* fusion models

2.7.1 Sequencing of constructs

The novel *KCTD16:NTRK2* fusion and *ETV6:NTRK3* were chosen*.* After reviewing the structure of the fusions, three different breakpoints would be modelled (two for *NTRK3*) (**appendix 2**).

Fusion sequences were designed with a v5 sequence tag at the 5' end. These were manufactured by Life Technologies in 19ABHESP_pMA-T plasmids (3952 – 4373 bp) (**appendix figure 2**). A PCR confirmed the expected sizes for each fusion construct. Bacteria were grown from glycerol stocks provided by Life Technologies and DNA was extracted. Restriction digestion of the AAVS1_Puro_PGK1_3xFLAG_Twin_Strep donor plasmid (**appendix figure 3**) was performed (using EcoRI at restriction sites NotI and SbfI). Finally, the donor plasmid and fusion construct were ligated, NEB 5-alpha competent *E. coli* C2987 bacteria transformed and DNA was extracted.

The PCR reagents (New England BioLabs) were added to a 96 well reaction plate (Life Technologies) in a final volume of 25μl containing 12.5μl NEB-next high fidelity 2x PCR mastermix, 1.25μl of each forward and reverse primer (10μM 1:10 dilution of stock), 5μl DNA template (1ng/μl) and 5μl water per reaction. The PCR was performed in a thermocycler with initial denaturation at 98°C for 2 minutes, followed by 25 cycles of denaturation at 98°C for 10 seconds, annealing at 55°C for 20 seconds, and extension at 72°C for 2 minutes, followed by a final extension at 72°C for 7 minutes.

PCR products were cleaned using the ExoProStar S 20 (Sigma-Aldrich) and were sent for Sanger sequencing (DNA Sequencing and Services, University of Dundee, United Kingdom). Sequences were analysed manually with 4Peaks (Nucleobytes). The fusion and v5 tag were in the correct sequence. A repeat experiment was also performed using the genes *ETV6, NTRK3, KCTD16,* and *NTRK2* acting as a control; sequencing confirmed the expected sequences (**appendix table 3**).

The methods used for the development of the *ALK* fusion model can be found in **appendix 3**.

2.7.2 Electroporation of human neural stem cells

The electroporation protocol was optimised using pmaxGFP plasmids. Cells were pre-treated with ROCK inhibitor for 2 hours prior to electroporation. 1-2 x 10^6 human neural stem cells (E3462, adherent culture on laminin, passage 15) were electroporated using programme A-023 and Solution 2 (two attempts for each fusion/gene). Post-electroporation, all cells were transferred to a T25 flask; media was replaced 24 hours post-procedure to remove dead/dying cells, and expanded into T175 flasks.

2.7.3 Puromycin selection

Successfully electroporated neural stem cells were selected using the puromycin resistance gene within the AAVS1_Puro_PGK1_3xFLAG_Twin_Strep plasmid. A puromycin sensitivity assay showed the lowest concentration at which all the E3462 cells died was 1.25μg/ml. Fresh media containing this concentration of puromycin was added to the T175 flasks with the prediction that electroporated cells would survive. Viable cells were expanded and re-challenged with puromycin; no viable cells for the *KCTD16:NTRK2* fusion remained.

2.7.4 Mouse neural stem cells

Mouse neural stem cells (mNSCs) were substituted for E3462, and the donor plasmid was changed to PBCAG-eGFP (**appendix figure 4**). Restriction, ligation and transformation were performed, and sequencing confirmed that the fusion, v5 tag and GFP marker were retained and within the correct sequence. The electroporation protocol was optimised using the mNSCs. 1-2 x 10^6 mNSCs were electroporated with 1μg of plasmid DNA and transposase, protocol A-023 and Solution 2. A control experiment using PBCAG-eGFP with no fusion was also performed. GFP expression was reviewed 24- and 48-hours post-electroporation using a JuLI Smart Fluorescent Cell Analyser. Post-electroporation, the electroporated cells were expanded into T75 flasks. The cells underwent sorting for GFP positivity using the BeckmanCoulter MoFlo Astrios. Cells were sorted into 6 well plates and expanded. GFP positivity was observed using a fluorescence microscope.

2.7.5 Immunofluorescence for GFP and v5 tag detection

Cells were grown in 8 well chamber slides (Cole-Parmer Instrument Company, WU-01838-03) for 24-72 hours. They were fixed with 4% PFA (ChemCruz, sc-281692) and incubated with 0.7% triton-x100 (Sigma, 058K0073) in PBS for 30 minutes. Cells were then washed with PBS and blocked for 1 hour with blocking solution (10% horse serum (Vector, S-2000) and 10% goat serum (Dako, X0907) in 5% BSA (Sigma, A3059). Slides were incubated at 4°C overnight with primary antibody, washed with PBS next day and incubated with secondary antibody. Slides were then stained with DAPI, washed with PBS and mounted using Vectashield (H1000) mounting medium. Imaging was done using confocal microscopy (Zeiss LSM700). The primary antibodies used were V5 tag (Invitrogen/Life Technologies R960-25) and GFP (goat-FITC conjugated Abcam ab6662). The secondary antibodies used were goat anti mouse 555 (Invitrogen, Catalog # A-21422).

2.7.6 *In utero* electroporation (IUE)

With expertise, practical assistance and training from Dr Ketty Kessler in the Jones Laboratory, embryos of CD1 mice were injected with plasmids into the lateral ventricle and electroporated *in utero* at E13.5. The fusion plasmids were used alone or in combination with CRISPR guide RNAs against *Trp53* (PB-*KCTD16:NTRK2*+PX+/-*Trp53* and PB-*ETV6:NTRK3*+PX+/-*Trp53*). Any live pups were closely monitored for neurological symptoms, and were scanned at regular intervals post procedure (all imaging was performed by Dr Jessica Boult). A mouse from each condition was sacrificed at day 148 to look for evidence of tumour generation. H&E staining was performed according to standard protocols on 3μm sections

2.8 Statistical analysis

Statistical analysis was carried out using R 3.5.0 (www.r-project.org) and GraphPad Prism 7. Categorical comparisons of counts were carried out using Fisher exact test; comparisons between groups of continuous variables employed Student t test or ANOVA. Univariate differences in survival were analysed by the Kaplan–Meier method and significance was determined by the log-rank test. All tests were two-sided and a P value of less than 0.05 was considered significant.

2.9 Data availability

All newly generated data have been deposited in the European Genome–phenome Archive (www.ebi.ac.uk/ega) with accession number EGAS00001003532 (sequencing) or ArrayExpress (www.ebi.ac.uk/arrayexpress/) with accession numbers E-MTAB-7802 and E-MTAB-7804 (methylation arrays). Curated gene-level copy number, mutation data, and RNA-sequencing data are provided as part of the pediatric-specific implementation of the cBioPortal genomic data visualisation portal (pedcbioportal.org).

CHAPTER 3 – Clinical, radiological and pathological profiling of infant gliomas

3.1 Introduction

The definition of an infant used in paediatric neuro-oncology typically refers to children younger than 3 to 5 years (5). Infant tumours reported as HGG appear to be associated with significant differences in clinical outcome, with infant HGG (even with incomplete resection and without irradiation) showing a significantly improved survival compared with those in older children (9,21,102–104). Infant LGG also show differences in clinical outcome, but the reverse; they have a worse outcome compared to older children (30). This may indicate the presence of a distinct group of tumours at the current intersect of LGG and HGG, where histopathologic grading may not be representative of clinical behavior. Treatment outcomes also reflect these differences.

Previous studies have hinted at different histologic features within infant HGG. High densities of “minigemistocytic-shaped” cells with abundant mitoses, absent necrosis and vascular proliferation are described in two cases (one a congenital case, the other diagnosed at 30 months) (91). Interestingly, both these cases were in complete remission at 18- and 10-months follow-up respectively (91). Other examples show moderately hypercellular, mitotic, and necrotic tumours with cellular monotony and a lack of significant pleomorphism, giving a mixed picture of both high- and low-grade features (81). Cytological differences are reported with some cases displaying a more spindled appearance, a relative monotony of cell size, and glial fibrillary acidic protein (GFAP) positivity by IHC, alongside the high-grade features of necrosis and mitotic activity (85). However, all cases have a better outcome than expected for an older child (85). This variation in appearance, and histological high-grade features conflicting with clinical outcome makes diagnosis challenging and argues for the use of molecular investigations, such as methylation profiling, to provide a clearer diagnosis.

Since its publication, the Heidelberg brain tumour classifier has contributed significantly to our understanding of brain tumours including new classifications of both ependymomas (105) and CNS-PNETs (78). DNA methylation profiling has helped to reclassify ependymal tumours into nine molecular subgroups incorporating histological, genetic, demographic and survival data to provide an updated classification (105). CNS-PNETs have been reclassified into four new distinct brain tumour entities, again associated with recurrent genetic alterations, and characteristic histology and clinical outcome data (78). These studies demonstrate two major functions of the classifier; classification of tumours into the existing well-established tumour entities and class discovery. Methylation profiling is also being developed to classify soft tissue sarcomas (106) and to risk stratify prostate cancer cases (107,108). It has also indicated that infant HGG may display a more LGG-like methylation pattern; these tumours have a wide age variation (but include younger patients), are largely hemispheric, driven by *BRAF* V600E*, NF1* or *FGFR2* mutations or RTK fusions, and have a 2-year survival of 74% (21).

Infant HGG are very rare tumours accounting for an annual average of 39 cases in the US (8) and 3.4 per million children in the UK (109). I have collected the largest series of infant HGG assembled to date and have used methylation profiling and histologic review integrated with clinical data to classify and characterise these rare tumours.

3.2 Results

3.2.1 Case numbers and epidemiology

All patient samples included were classified as gliomas (WHO grade II, III or IV) age ≤4 years old (including congenital cases) from all CNS locations (excluding optic pathway gliomas, but including spinal tumours). The age cut-off was decided based on the current definitions of the infant age group. Cases were excluded if they had been diagnosed as a pilocytic astrocytoma with a known *BRAF* fusion or mutation. Ependymal, embryonal, mesenchymal, and germ cell tumours were also excluded (**figure 3-1**).

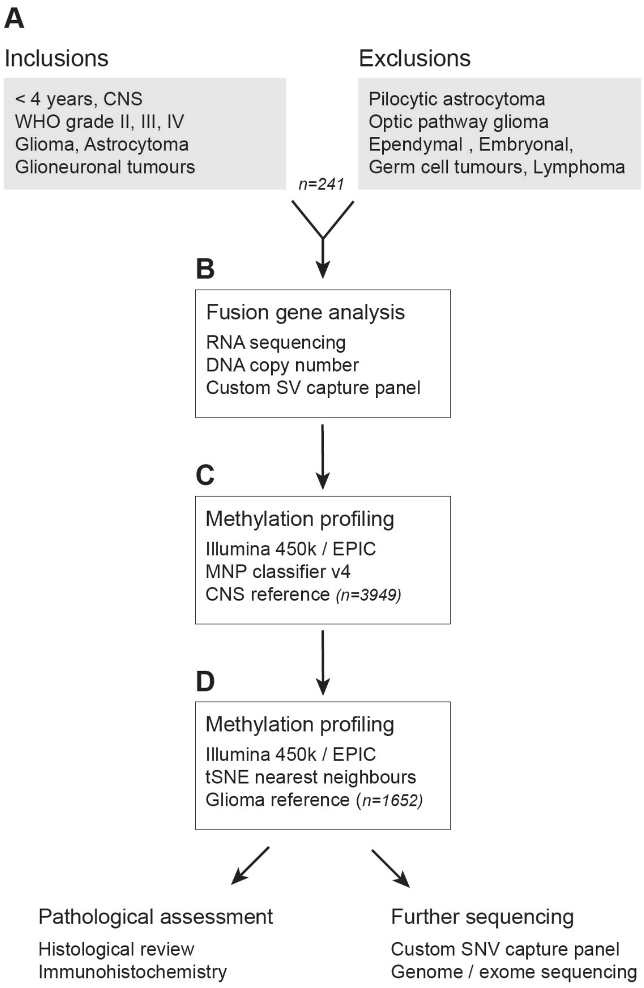

Figure 3-1. Defining the infant glioma study cohort. **A,** Flow diagram providing an overview of the inclusion and exclusion criteria for the assembled cohort of 241 samples from patients younger than 4 years. **B,** Samples underwent fusion gene analysis using a variety of methods, to exclude cases with pathognomic fusions. **C,** Samples then underwent methylation array profiling and analysis by the Heidelberg classifier using a CNS reference cohort (n=3949) to exclude non-glioma tumour entities. **D,** Cases which classified as previously reported high- or low-grade glioma subtypes were excluded by comparing methylation profiles with a glioma reference set (n=1652). The remaining cases underwent further characterisation using histopathological assessment and in-depth sequencing.

Samples were obtained from the following national collaborators (**figure 3-2B**): Great Ormond Street Hospital, London (n=33), King’s College Hospital, London, (n=21), University Hospitals Bristol, (n=9), Newcastle Royal Infirmary, (n=6), St George’s Hospital, London, (n=4). Contributions from international collaborators (**figure 3-2C**) included referrals to the German Cancer Research Center (DKFZ) (n=86), and from Ospedale Pediatrico Bambino Gesù, (n=37), St Jude Children’s

Research Hospital, Memphis, (n=17), Memorial Sloan Kettering Cancer Center, New York, (n=6), Queensland Children's Tumour Bank, Brisbane, (n=5), Universitätsklinikum Hamburg-Eppendorf, (n=5), Children's Cancer Institute, Sydney, (n=2), Children's Hospital of Wisconsin, (n=2), Emory University Hospital, Atlanta, (n=1), St. Petersburg Hospital No. 6, (n=1), Wake Forest School of Medicine, Winston-Salem, (n=1), The Chinese University of Hong Kong, (n=1), Children's National Medical Centre, Washington DC, (n=1), Chaim Sheba Medical Center, Tel Aviv, (n=1), Oregon Health & Science University, Portland, (n=1), and University of Ljubljana, (n=1).

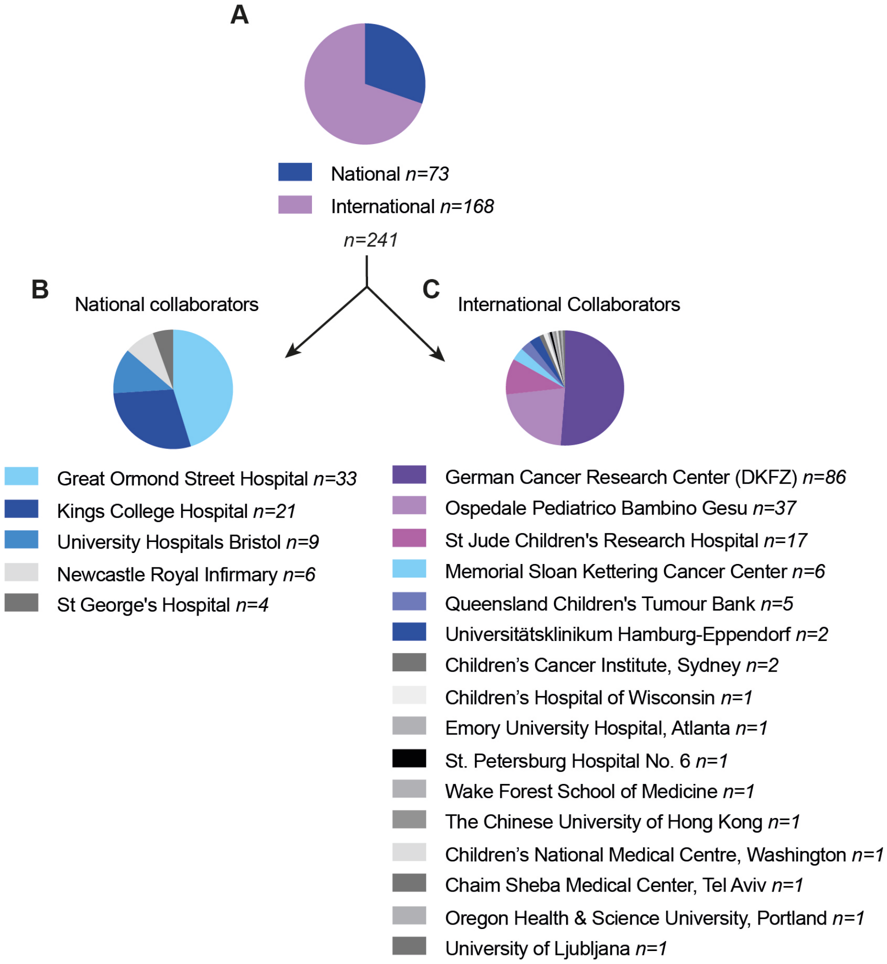

Figure 3-2. International and national collaborators. **A,** Pie chart showing of the overall contribution of cases to the cohort from national and international collaborators. **B,** Pie chart showing the specific national collaborator centres and **C,** international collaborator centres with their case contributions to the total cohort of 241.

Of the total 241 cases, 45.2% (109/241) were female and 54.8% (132/241) were male (**figure 3-3B**). Although all cases in the cohort were reported as aged ≤4 years, not all (n=33) had an available date of birth and/or date of diagnosis to enable a precise age calculation to be deduced. Of those that did have this information available (n=208) 55.3% of cases (115/208) were aged >1 year, and 44.7% (93/208) were aged ≤1 year (**figure 3-3A**). 9.9% (15/158) of the tumours were located in the brainstem, 65.8% (104/158) were located in the cerebral hemispheres, 24.1% (38/158) were located in the midline and 1 case was metastatic (a hemispheric cystic mass, metastatic to the spine) (**figure 3-3C**).

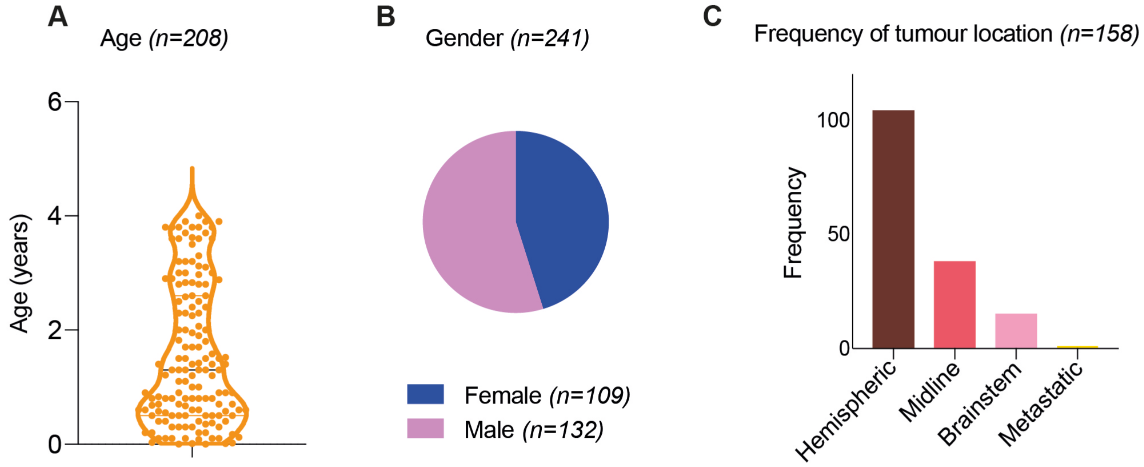

Figure 3-3. Demographics of the infant cohort. **A,** Violin plot showing the age distribution of the infant cohort (n=208, all aged ≤4 years). The line within the plot represents the median. **B,** Pie chart showing the proportion of male and female patients in the cohort (n=241). **C,** Histogram displaying location of the tumours within the CNS (n=158).

3.2.2 Symptoms and signs at presentation

One of the most frequently reported signs was an increasing head circumference and bulging fontanelles (n=13/48) (**figure 3-4**). Other signs resulted from pressure effects at the location of the tumour; hemiparesis (including upper or lower limb weakness, n=8), hemi-hypesthesia (n=1), and sometimes gait disturbances and ataxia (n=5). Several infants also experienced seizure activity (n=10) which varied from generalised seizures, to complex partial and absence seizures. For others, there was significant developmental delay or even regression in their milestones (n=5).

Other more general signs and symptoms included vomiting, poor feeding, irritability, poor weight gain and lethargy (n=12). Some cases presented acutely with signs of intracranial haemorrhage or decreased consciousness (n=3). Eye signs were frequently encountered including strabismus, nystagmus, dilated pupil, diplopia and squint (n=10). Rarer presentations included facial weakness (n=2), torticollis (n=1), stridor (n=1) and an unfortunate case of stillbirth (n=1). Many infants experienced more than one of these clinical features at presentation.

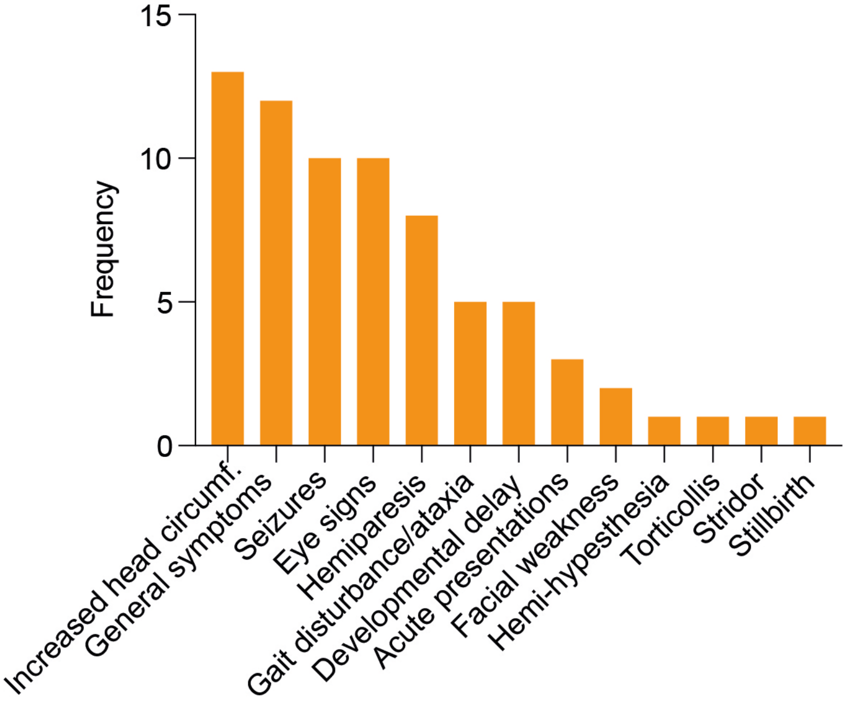

Figure 3-4. Clinical features at presentation. Histogram showing the frequencies of the different signs and symptoms identified in infants at the time of diagnosis (some patients may have more than one clinical feature at presentation).

3.2.3 Radiological appearances

The radiological appearances (available for n=39 cases) were variable and dependent on the type of tumour and location. Several cases of diffuse intrinsic pontine glioma (DIPG, later confirmed to be H3K27M-mutant) were present in the cohort and available MRI imaging showed expected features of expansile, asymmetrical brainstem masses occupying the pons, associated with haemorrhage, extension into the cerebellar peduncles and contrast enhancement (n=4).

The hemispheric tumours were T1 hypointense and T2 hyperintense (n=3), occasionally associated with significant mass effect and in one case bifrontal destruction of the bone (n=1). They comprised a heterogenous mass (occasionally described as ‘giant’ or ‘massive’ lesions (n=3)) with both solid and cystic components (n=12) and some even showed evidence of calcification (n=1). Some cases were also associated with prominent haemorrhage (n=4) and for some this was the cause of the initial presentation (n=2). Perilesional oedema could be observed (n=4), and evidence of necrosis was a rare finding (n=1). When contrast was used, they were either non-enhancing (n=6) or showed little or patchy contrast enhancement (n=7) (**figure 3-5**).

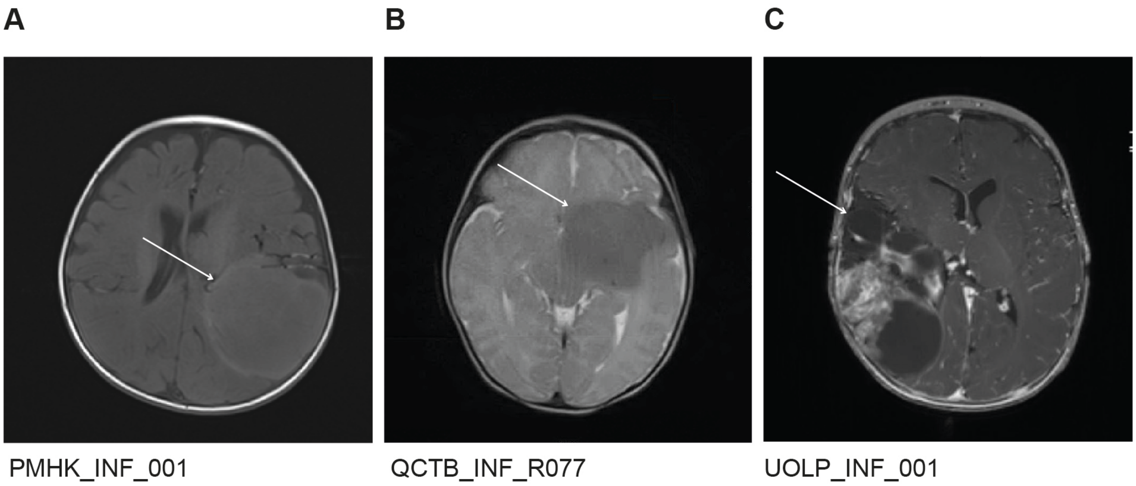

Figure 3-5. Representative MRI images of infantile tumours diagnosed as HGG in the cohort. **A,** PMHK_INF_001, T1 axial scan showing a large left-hemispheric lesion. **B,** QCTB_INF_R077, T2 axial scan showing a relatively well-defined mass in the left frontal lobe. **C,** UOLP_INF_001, T2 axial scan showing a large lesion in the right hemisphere showing solid and cystic components. White arrows indicate tumour.

3.2.4 Refining the infant cohort using the fusion panel

I firstly applied a custom NGS-based fusion panel in order to identify cases with pathognomic structural variants indicative of specific LGG or other entities, which may have been missed or not reported from the original diagnoses. Of the 241 cases in the cohort, 22 cases (9.1%) were found to harbour a *KIAA1549:BRAF* fusion, specific to pilocytic astrocytomas. These cases were initially included as several were annotated as being an ‘unspecified cerebellar astrocytoma’, and others were reported as ‘astrocytoma’ or the diagnosis was ambiguous, and all were excluded from further study. Additional fusions identified included *FGFR1* tandem duplications (n=3) (**figure 3-6B**), characteristic of certain glioneuronal tumours; *MYB/MYBL1* fusions (n=2) (**figure 3-6A**), characteristic of a novel LGG subtype; and a single case of *MN1:BEND2* fusion, characteristic of the novel entity HGNET-MN1 (**figure 3-8A**) (78). These were also excluded, leaving a new total of 213 cases.

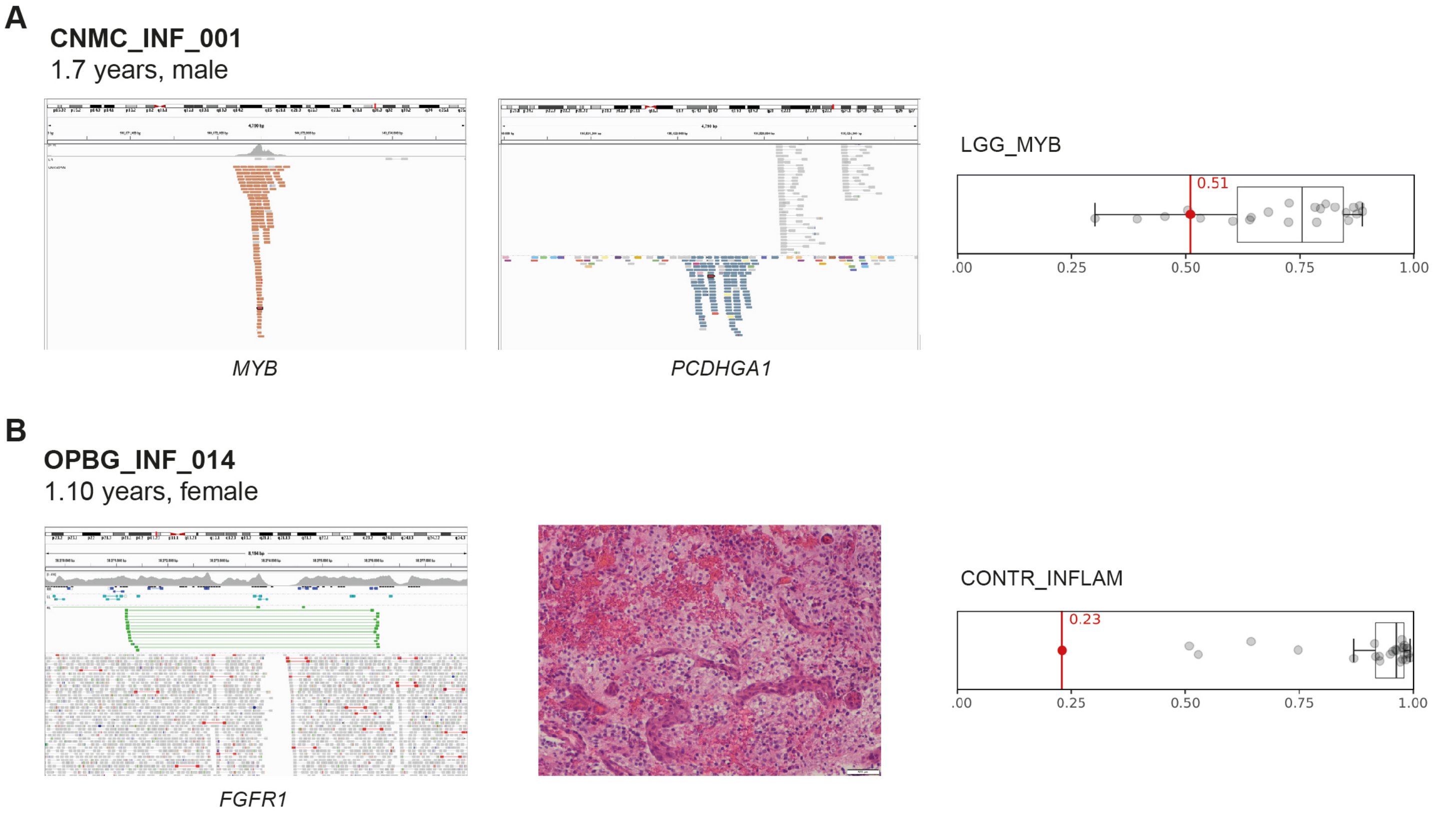

Figure 3-6. Refining the infant cohort using fusion panel sequencing. **A,** CNMC_INF_001 was a 1.7 year old male patient with a hemispheric tumour originally diagnosed as an anaplastic astrocytoma. The fusion panel identified a *PCDHGA1:MYB* fusion. Snapshots from Integrative Genomics Viewer (IGV); orange reads correspond to sequences of *MYB* and paired blue reads correspond to sequences of *PCDHGA1* demonstrating the fusion. This is supported by methylation profiling. Box plot of highest raw score indicated by the red dot, with references cases shown as grey dots; the line within the box is the median, the lower and upper limits of the box represent the first and third quartiles, and the whiskers the interquartile range. **B,** OPBG_INF_014 was a 1.1 year old female patient with a tumour diagnosed as a glioneuronal tumour. The fusion panel identified an *FGFR1* tandem duplication (shown by an IGV snapshot with paired reads in green demonstrating the tandem duplication). Methylation profiling classified this case as CONTR_INFLAM but poor scoring. Box plot of highest raw score indicated by red dot, with references cases shown as grey dots; the line within the box is the median, the lower and upper limits of the box represent the first and third quartiles, and the whiskers the interquartile range.

3.2.5 Methylation profiling of the infant cohort

With the assistance of the Senior Bioinformatician in the Jones Lab, Alan Mackay, publicly available methylation array data was collated from the reference and validation cohorts provided with the initial description of the Heidelberg brain tumour classifier (v11b4) (59), and combined these with our own additional paediatric high grade glioma datasets (21,63) and those from a recent CNS-PNET reclassification study (78). This resulted in a bespoke ‘combined brain tumour reference set’ consisting of 3,949 cases from across the CNS, and spanning all age groups and histologies (**figure 3-7**). This reference set was then used as a comparator for our infant glioma cohort.

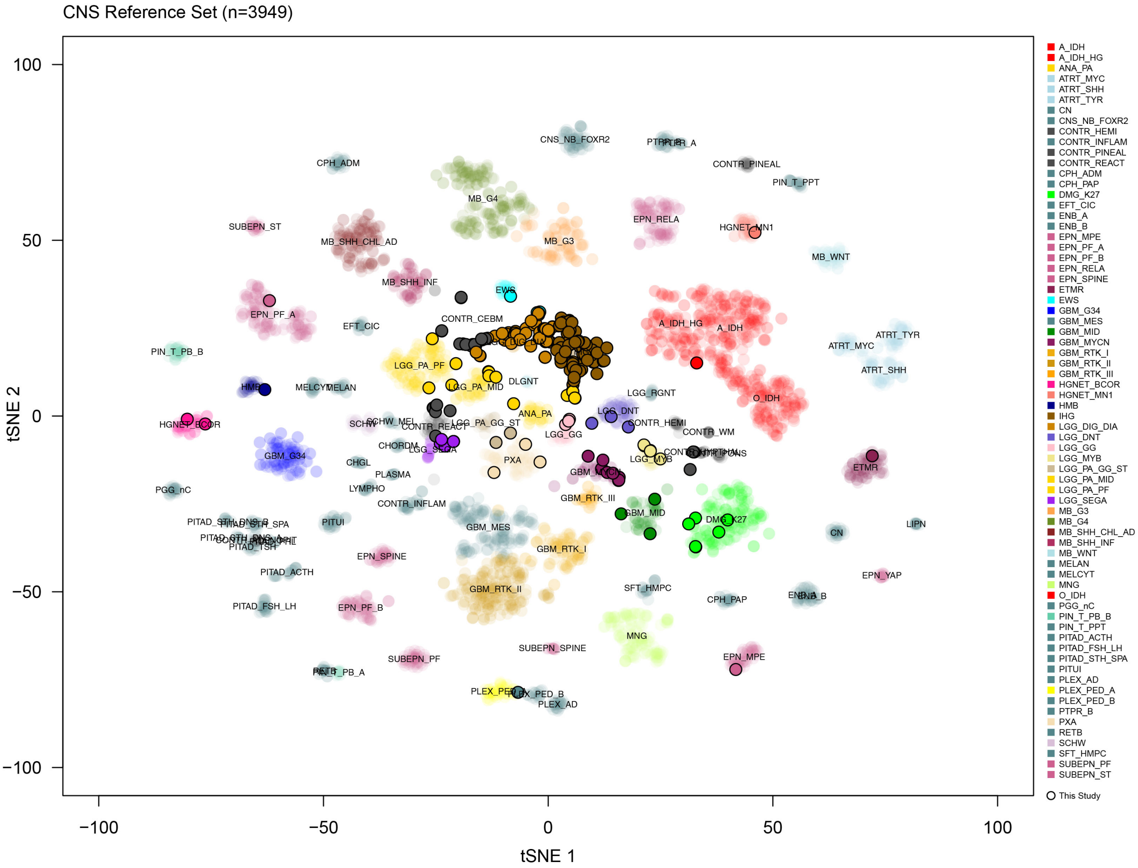

Figure 3-7. Methylation profiling of the infant cohort. t-statistic based stochastic neighbor embedding (t-SNE) projection of a combined methylation dataset comprising the initial, pathognomic fusion-excluded set of the present study (n=198, circled) plus a reference set of entities and subtypes from across the spectrum of CNS malignancies (n=3949). The first two projections are plotted on the x and y axes, with samples represented by dots colored by subtype according to the key provided.

When the remaining samples were compared to the CNS tumour reference set by t-SNE projection, a further 13 cases could be excluded as they clearly clustered with other non-glioma entities, including ependymomas (n=2), embryonal tumour with multiple rosettes (ETMR) (n=1), high-grade neuroepithelial tumour with *BCOR* alteration (HGNET-BCOR) (n=2), haemangioblastoma (HMB) (n=2), Ewing sarcoma (EWS) (n=1), as well as cases that classified as normal control brain tissue (n=3) (**figure 3-8B**).

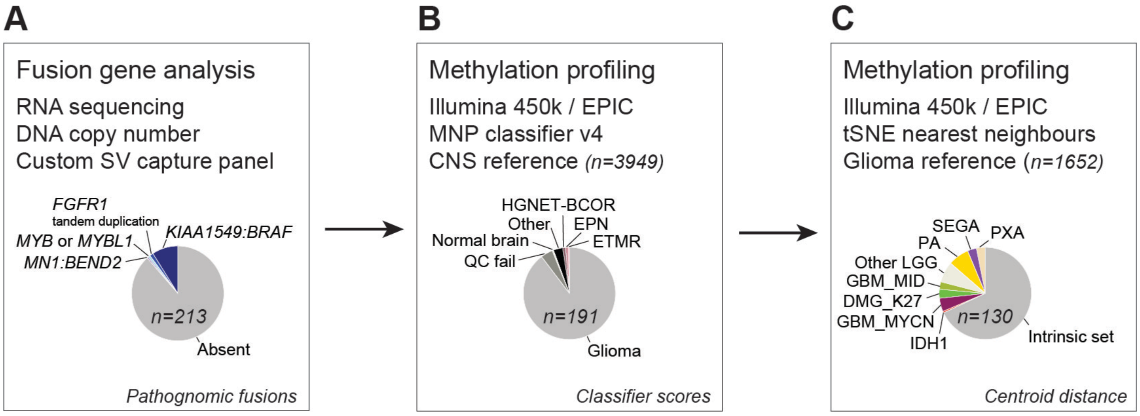

Figure 3-8. Defining an intrinsic set of infant gliomas. **A,** Fusion gene analysis by a variety of means allowed for the identification of 28 fusions marking clearly defined entities that were subsequently excluded from further analysis. **B,** Methylation array profiling and analysis by the Heidelberg classifier excluded a further 12 cases closely resembling non-glioma entities or failing quality control (n=9). **C,** t-distributed stochastic neighbor embedding (t-SNE) projection of the remaining cases highlighted 61 samples which clustered with previously reported high- or low-grade glioma subtypes leaving an intrinsic set of 130 infant gliomas for further characterization by more histopathological assessment and in-depth sequencing.

A further 9 cases failed array quality control; the quantity of DNA submitted was reviewed (referring back to the representative H&E slide to check the percentage tumour and cellularity), the quality of the bisulfite conversion (remaining unmethylated CpGs can alter the classification), and the calibrated score from the classifier (cases that classify very poorly (<0.3) or classify as PLEX_PED_B required careful review). These cases were excluded leaving a series of 191 cases.

Next, these samples were projected onto a glioma-focused subset of the reference cohort, comprised of 1,652 samples of all ages, anatomical locations, and grades. Sixty-one of these infant samples clustered with a known high or low-grade subtype, and were found to have arisen in anatomic areas of the CNS appropriate for their relative subgroup assignment, such as diffuse midline glioma K27M-mutant cases in the pons, pilocytic astrocytoma-like cases in the cerebellum, and PXA-like cases in the cerebral hemispheres (**figures 3-8C, 3-9A**).

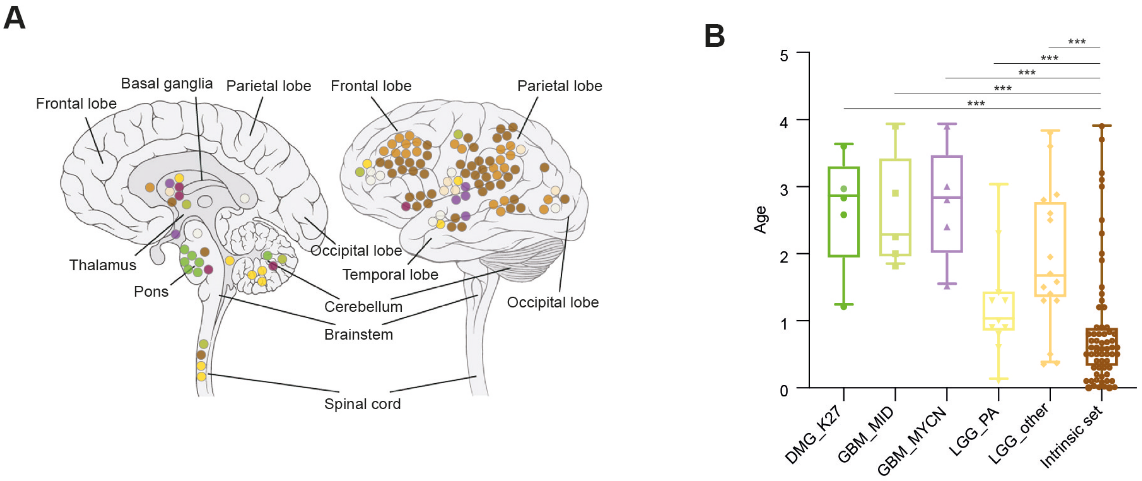

Figure 3-9. Defining the infant cohort by glioma subtype. **A,** Anatomic location of infant gliomas after exclusion of pathognomonic fusions and non-glioma entities by methylation profiling (n=130). Left, sagittal section showing internal structures; right, external view highlighting cerebral lobes. Each circle represents a single case and is colored by the glioma subgroup it most closely clusters with, defined by the key below. **B,** Box and whisker plot showing the age distribution of infant gliomas based on the methylation classification output from the Heidelberg classifier (n=106). The line within the box is the median, the lower and upper limits of the boxes represent the first and third quartiles, and the whiskers the interquartile range. *** <0.0001.

They were also predominantly >1-year-old (**figure 3-9B**). Survival data of these cases showed a worse outcome (*P*=0.0567, log-rank test) compared to the infant LGG cases which had a better outcome.

3.2.6 Novel infant subgroups by methylation profiling

This left a final series of 130 infant gliomas for further analysis, defined as the “intrinsic set” as they appeared to comprise a novel grouping (**figure 3-10**).

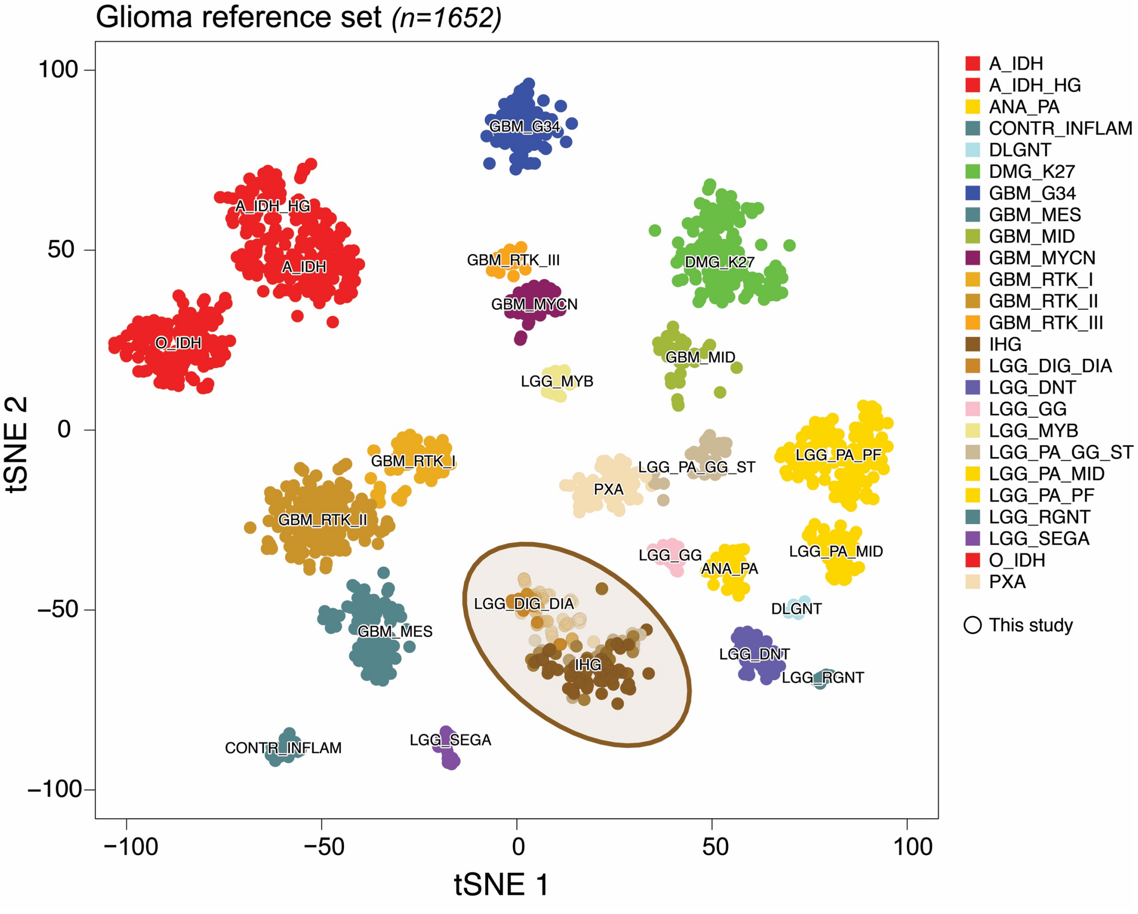

Figure 3-10. Defining the intrinsic set of infant gliomas. t-statistic based t-SNE projection of a combined methylation dataset comprising the intrinsic set of the current study (n=130, circled) plus a reference set of glioma subtypes (n=1,652). The first two projections are plotted on the x and y axes, with samples represented by dots colored by subtype according to the key provided.

These samples included the vast majority of those patients younger than the age of 1 year (49/63, 78%; overall median of the intrinsic set = 7.2 months). The vast majority of these cases were found in the cerebral hemispheres (75/83, 90.4%) (**figure 3-9A**).

This group of tumours formed a continuum that clustered clearly apart from other glioma subgroups in the glioma reference set on the t-SNE projection. They scored most highly as two named subgroups of the methylation classifier - DIGG/DIA (11/130 cases, 8.5%) and the poorly defined infantile hemispheric glioma (IHG) (95/130 cases, 73.1%). Many of these cases, however, did not unequivocally classify as either IHG or DIGG/DIA (24/130 cases, 18.5%) despite their tight clustering, suggesting that the reference classes for these tumours likely need expanding and updating.

There was a male gender predominance in the intrinsic group as a whole (75/130 cases, 57.7%), and particularly within the unequivocal DIGG/DIA cases (8/9) cases, 88.9%), consistent with the current WHO classification (13). Intrinsic set cases were frequently aged $\leq$1 year (specifically, 53/61 IHG cases (86.9%), median = 0.5 years, and all DIGG/DIA cases, median = 0.7 years). Those tumours which clustered more closely along the continuum with DIGG/DIA, but with poor classifier scores (“DIGG/DIA-like”), were predominantly female (14/22 cases, 63.6%) and the majority were aged 1 or more (7/13 cases, 53.8%, median = 1.0 years) (**figure 3-11**).

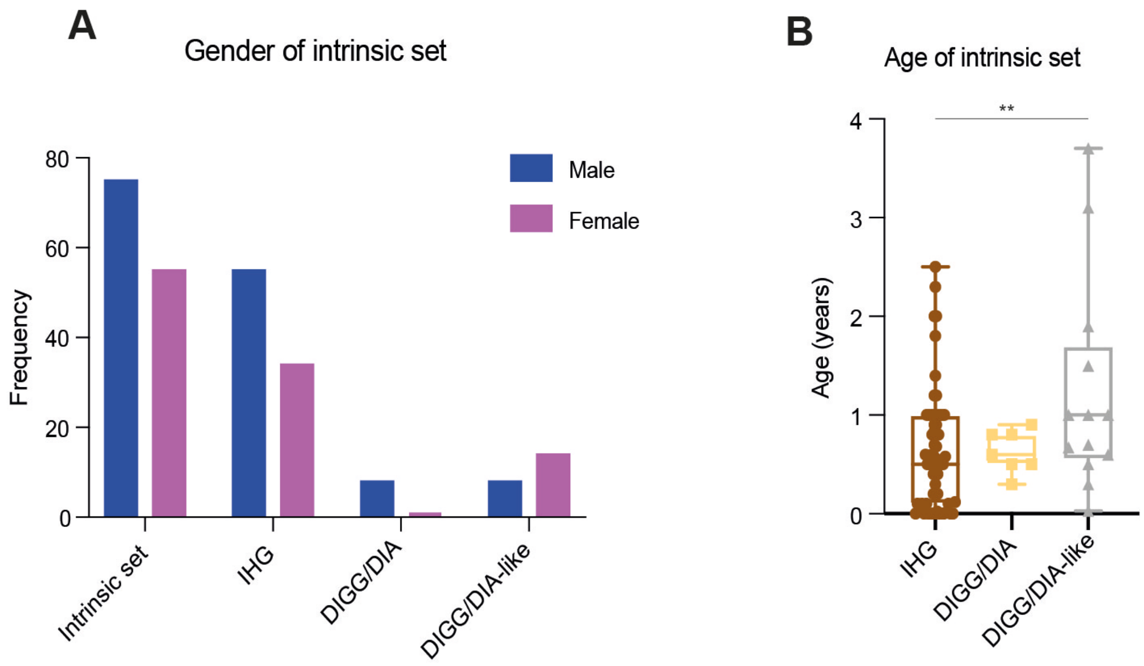

Figure 3-11. Demographics of the intrinsic set. **A,** Histogram showing the gender distribution for the intrinsic set overall, and for the subgroups that are found within the intrinsic set (n=130). **B,** Boxplot showing the age distribution for the intrinsic set (n=83). The line within the box is the median, the lower and upper limits of the box represent the first and third quartiles, and the whiskers the interquartile range. ** 0.0062

3.2.7 Histological features

Histologic examination of those tumours classified as IHG revealed highly cellular astrocytic tumours with cells arranged in uniform sheets throughout the section (10/20, 50%) (**figure 3-12A-C**), although in rare instances some showed less cellularity (**figure 3-12G**). Tumours frequently showed a superficial hemispheric location, often involving the meninges, and had a well-defined border with adjacent normal brain with very little evidence of infiltration. Pseudo palisading necrosis (15/20, 75%) (**figure 3-12D**) and microvascular proliferation (9/20, 45%) were frequently seen, both classic features of high grade tumours. Rarely, focal areas of mineralisation and calcification were present and occasionally the cells displayed a more nodular appearance (**figure 3-12E-F**).

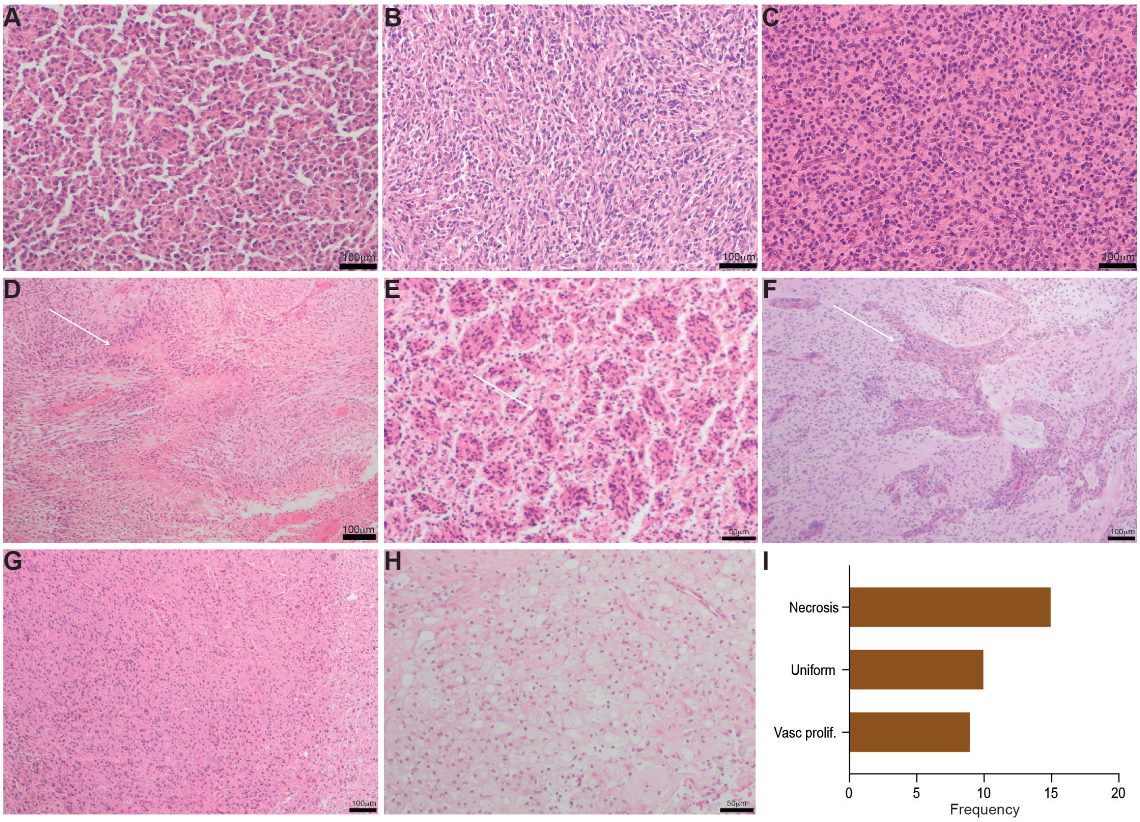

Figure 3-12. Histopathological assessment of IHG cases (architecture). **A – C,** H&E images displaying examples of the high cellularity and uniform architecture of the IHG group. **D,** High grade features including palisading necrosis are frequently seen (white arrow). **E,** H&E image showing a nodular architecture in an IHG case (white arrow). **F,** An IHG case displaying prominent nodularity and some microvascular proliferation (white arrow). **G,** An example of an IHG case which is less cellular and has a less uniform architecture. **H,** Focal xanthomatous change in an IHG case. Scale bars are provided. **I,** Histogram showing the frequency of architectural features within the IHG group cases.

Cytological review of those tumours classified as IHG showed mild to moderate nuclear pleomorphism (8/20, 40%). Spindled nuclei (8/20, 40%) (**figure 3-13A**), often associated with a swirling architectural pattern, an occasional ganglion cell component (1/20, 2%) (**figure 3-13B**), or gemistocyte-like cells (9/20, 45%) (**figure 3-13C**), could be seen either focally or throughout the tumour. However, these cytological features were not present within the same case. Rarely, xanthomatous change could be observed.

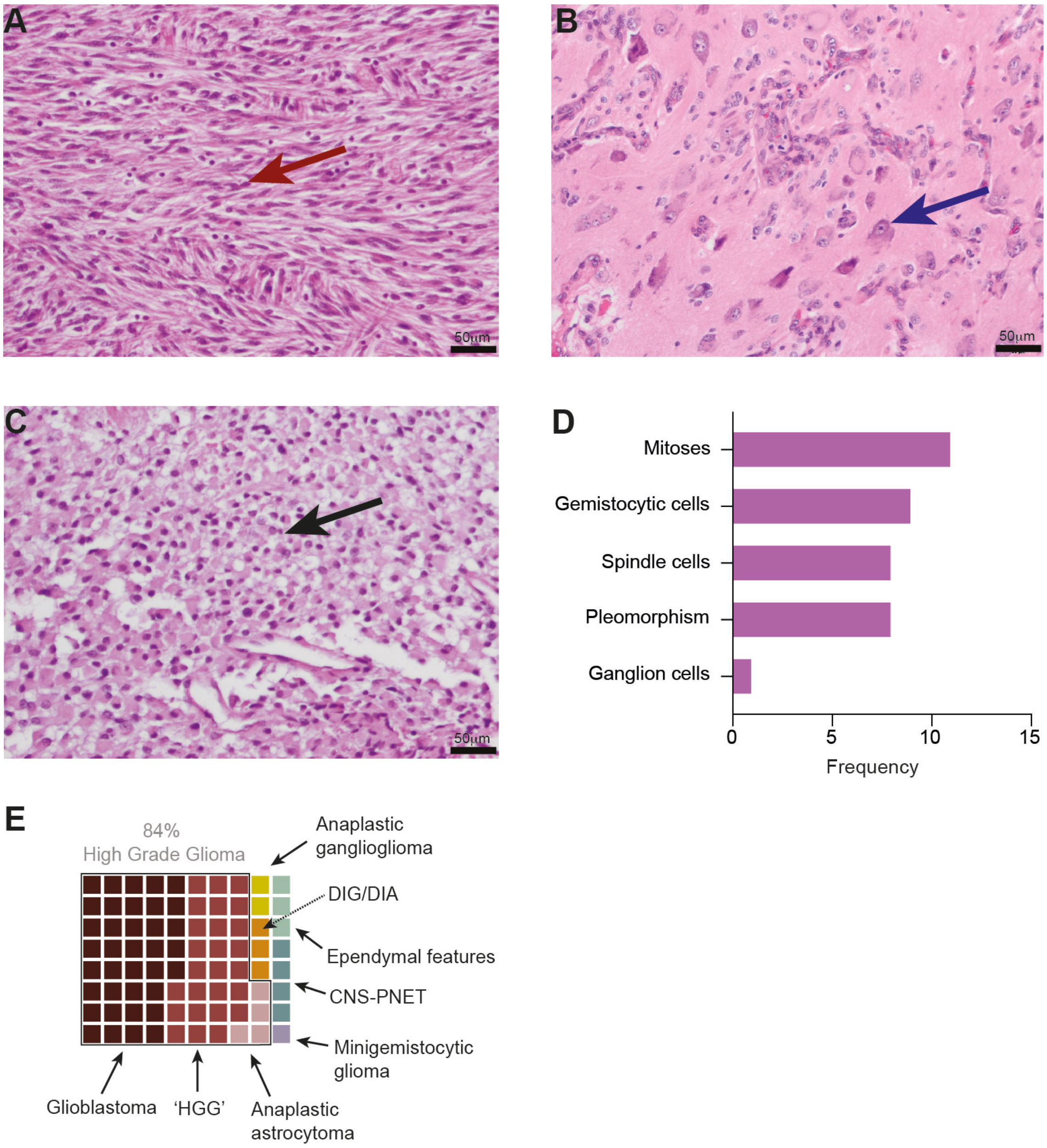

Figure 3-13. Histopathological assessment of IHG cases (cytology). **A,** The cytological appearances show variation with some cases containing focal spindle shaped nuclei (red arrow). **B,** Very occasionally ganglion cell differentiation is seen (blue arrow). **C,** Some cases can show a gemistocyte-like cytological appearance (black arrow). **E,** Tile plot representing the original diagnoses of IHG cases, coloured and ordered according the labels provided.

Consistent with the histological features described, 67 of 80 (84%) IHG cases were originally diagnosed as a high-grade glioma (most frequently anaplastic astrocytoma WHO grade III, and glioblastoma WHO grade IV), although a variety of other diagnoses were included in the original pathology reports. Other diagnoses included anaplastic ganglioglioma (n=2), DIGG/DIA (n=3), CNS-PNET (n=4), ependymoma (or containing ependymal features) (n=3), and a minigemistocytic glioma (n=1) (**figure 3-13E**).

3.2.8 Treatment and survival

All cases which classified as IHG underwent either a biopsy and/or attempted surgical resection. One patient received 6 months of neoadjuvant chemotherapy (POG 8633) before undergoing a resection. Three infants underwent a biopsy only; one baby died at birth and underwent a post-mortem, one was commenced on palliative treatment as a result of a diagnosis of GBM, and one suffered a large intra-tumoural haemorrhage and died 24 hours post-biopsy. Of those infants who underwent surgery, 8 of 12 (67%) underwent a gross total resection and four had a sub- or near total resection (one of these underwent 2nd look surgery).

Detailed treatment information was only available for 18 IHG patients within the cohort. 11 of 18 (61%) of infants received adjuvant therapy post-surgery (HIT-SKK protocol, n=7; Baby POG, n=2; SYJC07, St Jude n=1; vincristine, n=1). Three cases experienced local progression (one underwent a re-resection for the original disease and another was treated with irinotecan and bevacixumab). Radiotherapy was not given in any reported cases. One infant experienced a severe neurological insult post-surgery and because a complete resection had been achieved, chemotherapy was not used.

Survival data was available for 105 patients in the infant cohort. The overall survival of the IHG group showed a significantly improved outcome compared with cases classified as HGG, with a median overall survival similar to those considered LGG and DIGG/DIA, with the important caveat that detailed treatment information was not available across the entire cohort. The HGG subtype exclusions were predominantly >1-year-old and showed a tendency toward a worse outcome than the other infant tumours (P = 0.0567, log-rank test) (**figure 3-14**).

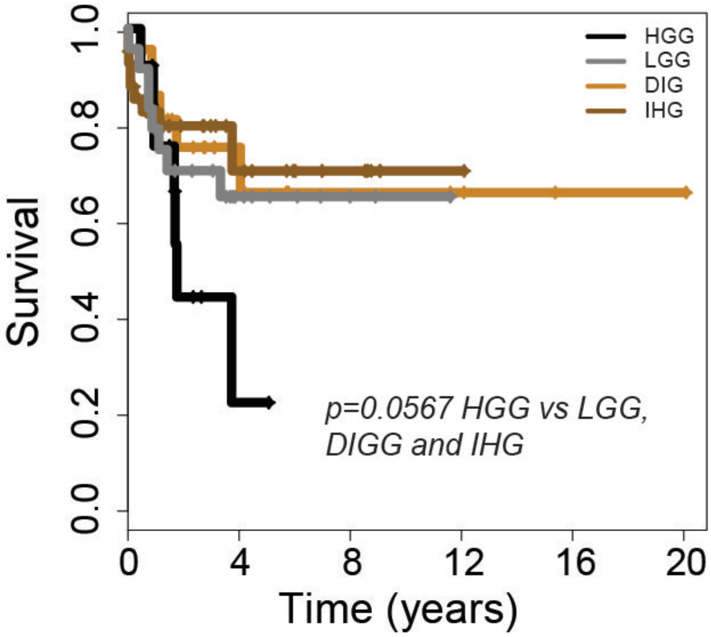

Figure 3-14. Overall survival of the infant cohort. Kaplan–Meier plot of overall survival of cases separated by methylation subgroups DIGG (desmoplastic infantile ganglioglioma/astrocytoma) (n=21), IHG (infant hemispheric glioma) (n=43), LGG (other low-grade glioma subgroups) (n=28), and HGG (other high-grade glioma subgroups) (n=13). P value is calculated by the log-rank test (P=0.0566 for HGG vs. rest).

3.3 Discussion

The signs and symptoms at presentation in the infant cohort are very variable, and particularly challenging to identify given their young age. Data from paediatric neuro-oncology centres shows that from 2004-2006 the total diagnostic interval (TDI) ranged from 1 day to 6.9 years (median 3.3 months) (110). The launch of campaigns such as ‘HeadSmart: Be Brain Tumour Aware’ with the aim of increasing both professional and public awareness has helped to reduce the TDI to a median of 6.7 weeks, with the aim of reaching 5 weeks (110). Other studies have shown that the age and type of the tumour can impact on the TDI; craniopharyngiomas, optic pathway gliomas and LGG have the longest TDI ranging from 10.4 – 15.1 weeks. The 12-18-year age group had a median TDI of 12.1 weeks, for 5-11 years it was 8 weeks, and for 0-5 years it was 6 weeks (111). Although the TDI was not available for our infant cohort, lower TDIs associated with infants is an interesting finding possibly related to close observation of infants by parents or other care givers, making signs more noticeable if they appear. In adults studies have shown associations between the molecular subgroup of the tumour and clinical presentation with *IDH1* mutant tumours more likely to present with seizures (59-74% of cases) compared to *IDH1* wildtype (18-34% of cases) (112).

A first key finding from the infant cohort relates to the difficulty of differential diagnoses in these very young children, with approximately 10% of cases unequivocally classifying as other tumour entities on the basis of methylation profiling (59) or the presence of pathognomonic gene fusions (78) even after discounting misdiagnosed or mis-assigned pilocytic astrocytomas. Often this uncertainty is reflected in the original pathology report, with atypical features highlighted. However, the highly heterogeneous nature of high-grade glial tumours provides for a broadly inclusive category in the current WHO classification, which in many cases may result in what is considered to be a relatively uncontroversial histologic diagnosis despite widely varying morphologies. Similarly, combined genetic and epigenetic analyses reveal a third of remaining cases to be biologically identical to known high- or low-grade glioma subtypes, with substantially different prognoses reflective of the known clinical course of the relevant tumour categories. Together, these data make the important points that histopathologic evaluation alone is insufficient to predict outcome, and that high-grade gliomas predominantly occurring in older childhood may also present in the infant population with little survival benefit from standard treatment protocols.

After these exclusions, there remains what we define as an intrinsic set of infant gliomas, which are largely restricted to the cerebral hemispheres and occur in the youngest patients, usually younger than 12 months old. These patients, despite more than three quarters unequivocally reported as WHO grade III or IV astrocytoma, have an overall survival more akin to lower-grade tumours. They appear to form a biological continuum of disease between the recognized MAPK-driven desmoplastic lesions (DIGG/DIA), which may respond clinically to targeted *BRAF* V600E inhibitors even after previous chemotherapy (113), and a novel assignation of infantile hemispheric glioma (IHG). This ‘biological continuum’ is further hinted at from the histological review with DIGG/DIA tumours characterised by a spindle-shaped cell morphology or gemistocytic-shaped astrocytes (13). Both of these cytological features were also found in the IHG and DIGG/DIA-like cases. Some IHG cases also contained focal areas of ganglion cell differentiation (some cases even being reported as anaplastic gangliogliomas), hinting at a possible change in histological appearance with age. Although IHGs were mostly reported as HGGs, diagnostic features of these tumours were absent in the DIGG/DIA group. Although radiologically they are typically large (sometimes described as massive) hemispheric solid-cystic lesions, and occur in predominantly male children ≤1 year, the potential for misdiagnosis in these cases is considerable, with 16% of our series originally having differential diagnoses including CNS-PNET and ependymomas. Methylation profiling is a tool to ensure an accurate diagnosis particularly as grading of these tumours also remains ambiguous.

The WHO histological grading system is used to predict the response to treatment and the overall outcome for a patient (13). Pilocytic astrocytomas were excluded but DIGG/DIA cases remained as they typically occur in infants (42). The IHG group do not have an assigned WHO grade (at the time of writing) due to the paucity of available survival data.

However, not all the infants diagnosed as IHG cases have a good outcome. Treatment decisions used in the very early cases impacted on their survival; infants who were diagnosed as an HGG by biopsy were palliated due to the poor prognosis. Others progressed and died of their disease. Therefore, when grading these tumours, some reflection of this variation is required in the assignation, and further work is needed to help identify a way of assessing which cases are going to behave more aggressively.

CHAPTER 4 – Molecular landscape of novel infant subgroups

4.1 Introduction

Paediatric high-grade gliomas (HGG) are strongly associated with unique location-dependent mutations in histone H3 variants H3.3 (*H3F3A*) and H3.1 (*HIST1H3B/C*) including two recurrent amino acid substitutions (K27M and G34R/V) (48,67), which together account for nearly half of all paediatric HGG and identify robust biological subgroups (68,114). Histone wild-type cases are comprised of a highly diverse set of tumours, ranging from those with some of the highest somatic mutational burdens in human cancer (patients with bi-allelic mismatch repair deficiency syndrome; (115,116) to others with few if any nucleotide variants which fall into a 'LGG-like' methylation class, occur in younger children and have a better overall survival than other HGG cases (21).

Current molecular data for infant HGG is limited, but EGF receptor (*EGFR*) and platelet-derived growth factor receptor A (*PDGFRA)* expression is reported as uniformly low in congenital glioblastomas (GBM), with a low level or absence of copy number alterations in these genes (85,94). *TP53* and *PTEN* mutations, *CDKN2A/B* deletions, and other copy-number alterations often seen in older children are also not typically found in infant HGG (117). Occasional *BRAFV600E* mutations are found, particularly in DIGG/DIA (118), whereas histone and *IDH1* mutations are rare.

The most common somatic alterations seen in infants appear to be gene fusion events, particularly *NTRK1/2/3*. Although not specific to brain tumours (95), these were found to span both LGG and HGG in large-scale studies in children, with novel *QKI:NTRK2* and *NACC2:NTRK2* fusions found in pilocytic astrocytomas (73), and *AGBL4:NTRK2*, *TPM3:NTRK1*, and *ETV6:NTRK3* fusions found in patients with HGG who were less than 3 years of age (74). More recently, several case reports have identified additional receptor tyrosine kinase (RTK) gene fusions in infant gliomas of differing histologies (9,81,119–126). Some fusions are also pathognomic of certain LGG and HGG entities in infants including pilocytic astrocytomas with *KIAA1549:BRAF* fusions (73), and the recently classified CNS HGNET_MN1 and CNS EFS-CIC with *BEND2:MN1* and *CIC:NUTM1* fusions (which occur in infants but are not infant-specific tumour entities) respectively (78).

There are many different *NTRK* fusions which occur in cancer, with COSMIC listing 11 types (including *TPR:NTRK1, TFG:NTRK1, ETV6:NTRK3*) occurring in tumours of the skin, large intestine, thyroid, soft tissue and salivary glands (127). RTK fusions are known to occur in other infantile cancer types, specifically infantile fibrosarcoma (IF) and congenital mesoblastic nephroma (CMN), with approximately 70 - 90% of IF containing an *ETV6:NTRK3* fusion, but also *EML4:NTRK3* and *LMNA:NTRK1* fusions reported (128). Importantly, they represent a targetable treatment option for tumours that are found to have these fusions (95).

Having refined the infant cohort to an intrinsic set of 130 cases by excluding known LGG and HGG entities through methylation profiling, and having shown that the IHG group have characteristic histological appearances, it was necessary to further explore the molecular profile of this new group of tumours.

4.2 Results

4.2.1 Mutation landscape of infant gliomas

Gene sequencing (panel, exome, or genome) was available for 65 cases of the infant cohort, including 41 of the intrinsic set. Samples excluded as representing other glioma subtypes were found to harbour mutations consistent with such tumours, including *IDH1 R132H* (found in cases of A_IDH and A_IDH_HG), *H3F3A K27M* and *HIST1H3B K27M* (both found in cases of DMG_K27M), as well as common co-segregating variants in *TP53, NF1, PTEN, PIK3CA*, and *ACVR1*. We also observed deletions of *CDKN2A/B* and amplification of *PDGFRA,* frequently associated with paediatric HGG subtypes (**figure 4-1A**).

These mutations were almost entirely absent from the intrinsic set. High-scoring DIGG/DIAs and “DIGG/DIA-like” tumors were found with *BRAF V600E* (n = 3) or *PIK3R1* mutations and isolated mutations in bromodomain-containing genes (*BRD8, BRD4, BRD2*), as well as a single *CD109* deletion and an *NF1* mutation. One DIGG/DIA-like case harboured amplifications in both *MYC* and *MYCN*, in addition to *TP53* and *PIK3CA* mutations. Interestingly, the tumours which classified as part of the IHG group contained very few mutations (isolated bromodomain-containing gene mutations (*BRD2* n=1)), with a distinct absence of *H3F3A, HIST1H3B, TP53, ACVR1, PTEN* and *PIK3CA* mutations (**figure 4-1B**).

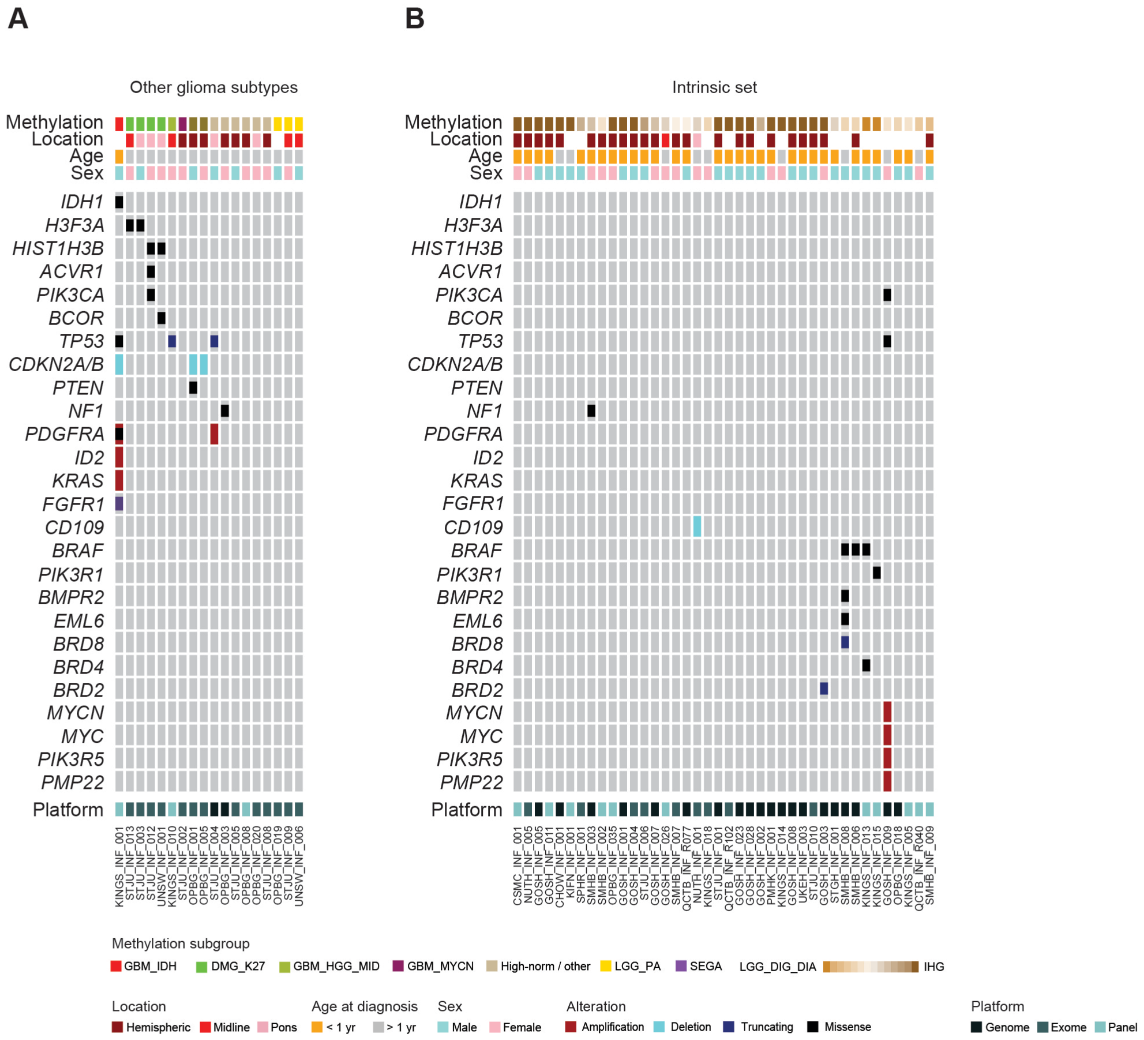

Figure 4-1. Mutations in infant gliomas. **A,** Oncoprint representation of an integrated annotation of single-nucleotide variants and DNA copy-number changes for infant gliomas excluded as other subgroups (n=24). **B,** Oncoprint representation of an integrated annotation of single-nucleotide variants and DNA copy number changes for infant gliomas in the intrinsic set (n=41). Samples are arranged in columns with genes labeled along rows. Clinicopathologic and molecular annotations are provided as bars according to the included key.

4.2.2 Copy number analysis

A proportion of the intrinsic set (36/130, 28%) were found to have whole-arm DNA copy number changes including 2p gain (n=5), 6q loss (n=7), 8p gain (n=3), 12p gain (n=6), 16p gain (n=3), 17p loss (n=3), 21q gain (n=3) and loss (n=3), and 22q loss (n=8) (**figure 4-2**).

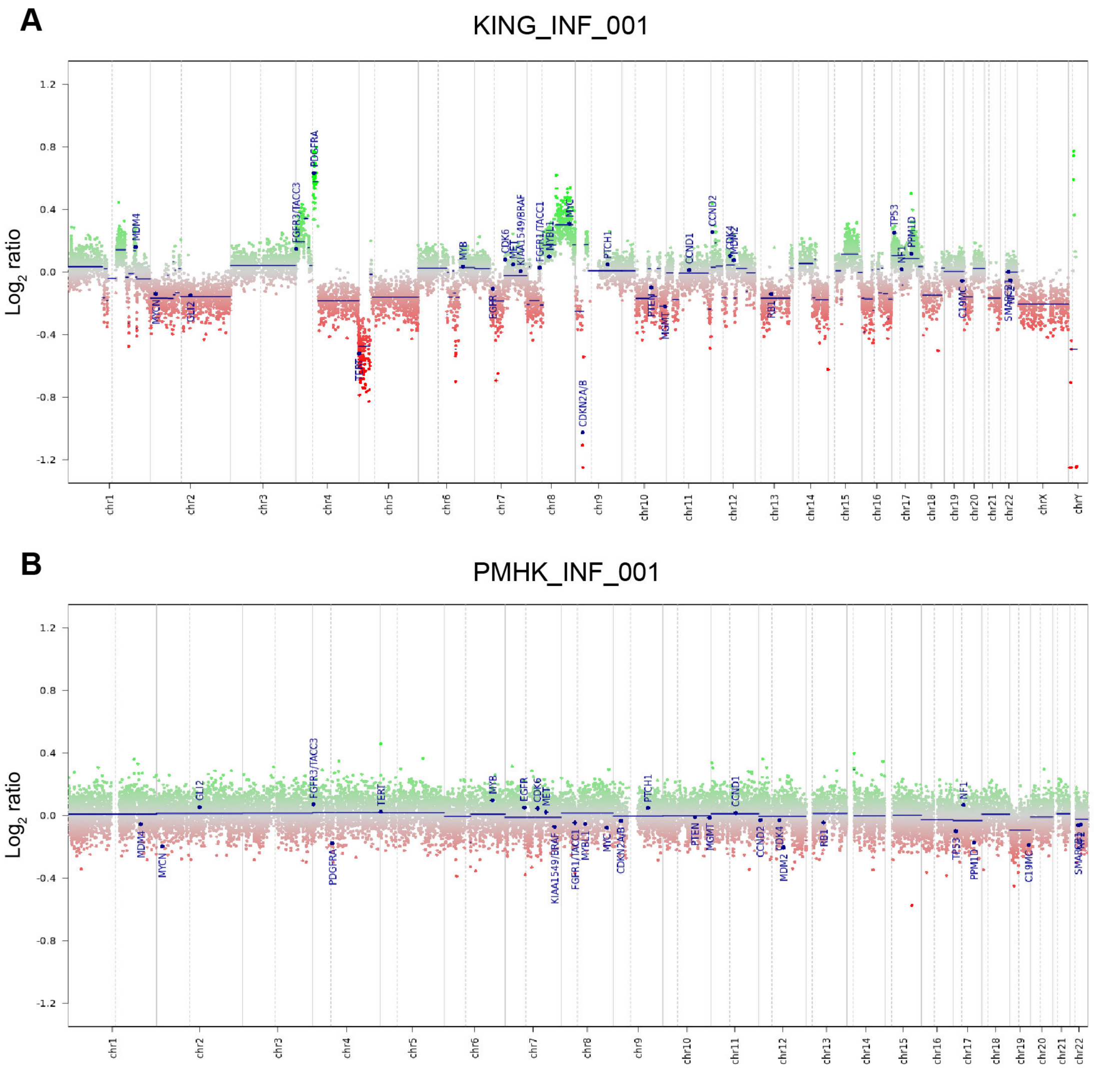

Figure 4-2. Variation between infant DNA copy number profiles. **A,** Copy number profile of KING_INF_001 demonstrating a highly rearranged profile including an amplification in *PDGFRA* and deletion of *CDKN2A/B.* **B,** The copy number profile of PMHK_INF_001 shows no identifiable copy number alterations from the profile. Profiled on the Illumina 450k (KING_INF_001) and EPIC (PMHK_INF_001) BeadArray platform (green, amplification or gain; red, deletion or loss).

However, the majority of intrinsic cases harboured few if any large-scale copy-number alterations, with many demonstrating a very flat or copy neutral profile (94/130, 72%) (**figures 4-2B, 4-3**), which is significantly more frequent than those reported in the meta-analysis of pHGG/DIPG cases, with only 28% showing no changes (21). DIGG/DIA tumours were not associated with any large-scale copy number alterations (7/94, 7.4%), again significantly less than those seen in pHGG/DIPG (*P*=<0.00001 Fishers Exact Test).

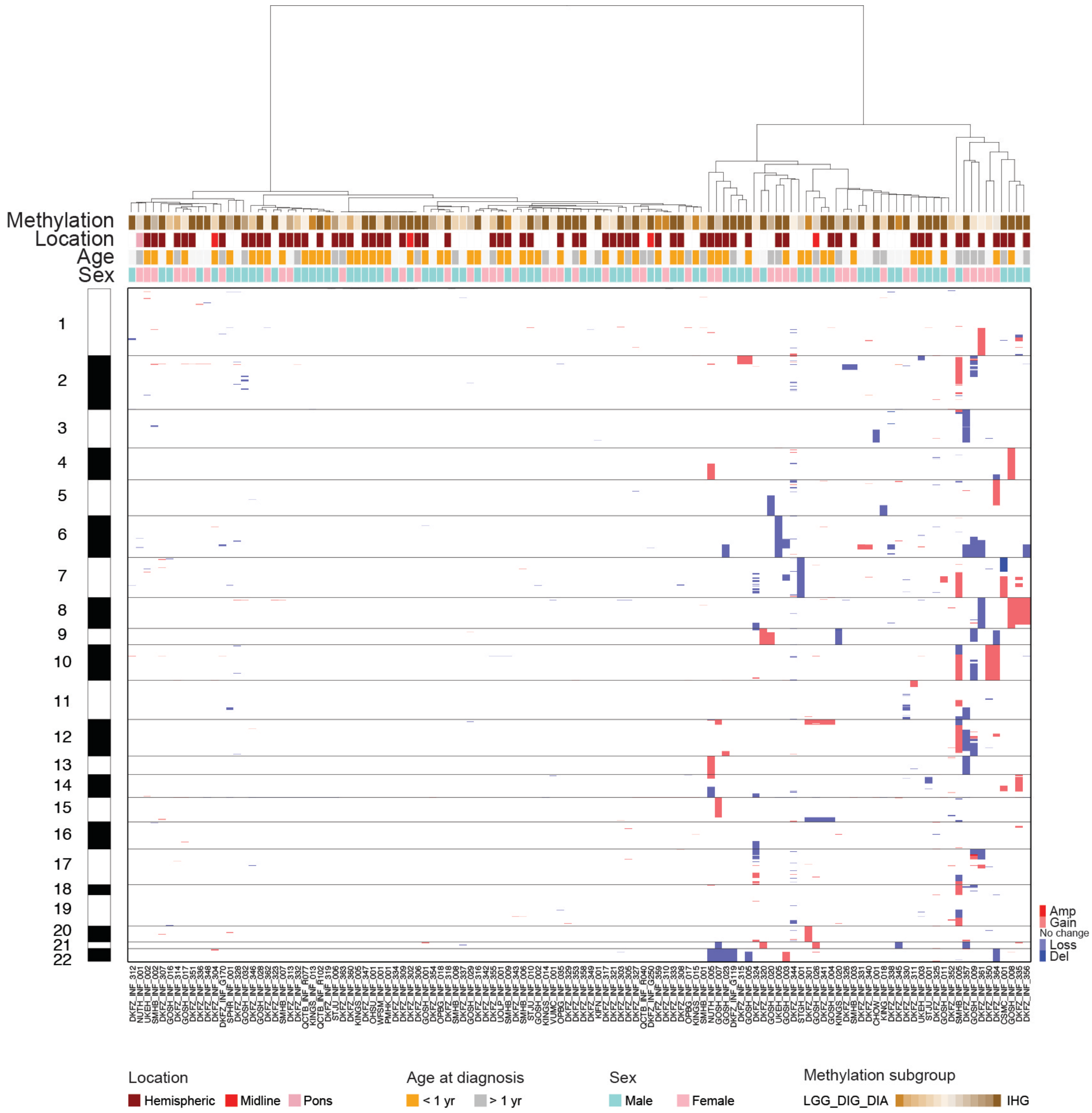

Figure 4-3. DNA copy number profiling of the intrinsic set. Heatmap representation of segmented DNA copy number for 130 intrinsic samples of infant glioma profiled on the Illumina 450k or EPIC BeadArray platform (dark red, amplification; red, gain; dark blue, deletion; blue, loss). Samples are arranged in columns clustered by contiguous categorical copy number states based upon log ratio thresholds of ±0.1 for gain/loss and ±0.5 for amplification and deletion. Clustering used Euclidean distance and a ward algorithm. Clinicopathological and molecular annotations are provided as bars according to the included key.

As fusion genes have been reported in infant HGG cases in the published literature, and in the absence of any other driving events identified in the cases of the intrinsic set so far, copy-number data derived from methylation arrays was analysed; this identified intragenic breakpoints in RTK genes associated with an equivalent breakpoint in another gene indicative of a partner. These RTK fusion intragenic breakpoints were found in 53/71 (75%) cases across the whole cohort. There were no differences in the number of large-scale copy-number changes between fusion-positive and fusion-negative cases ($P = 0.567$, t test) (**figure 4-4A**). Notably, the only significant focal differences were those marking common gene fusions at the *ALK* and *NTRK3* loci (**figure 4-4B**).

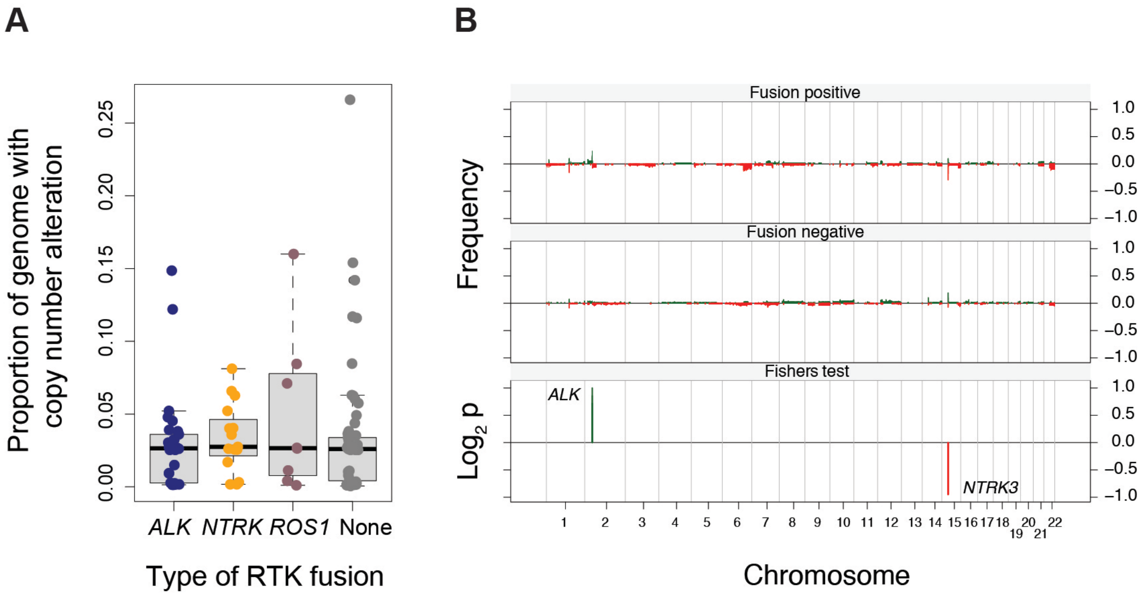

Figure 4-4. Fusion-associated DNA copy number alterations in the intrinsic set. **A,** Boxplot of copy number changes separated by RTK fusion type. The thick line within the box is the median, the lower and upper limits of the boxes represent the first and third quartiles, and the whiskers 1.5x the interquartile range. **B,** Frequency histogram (y axes) of copy number changes plotted according to chromosomal location (x axes) for fusion-positive (top) and fusion-negative (middle) cases. Bottom - $\log_2$ p values derived from a Fishers test comparison between fusion-positive and -negative cases are plotted against chromosomal location (x axis). Copy number gains are plotted in green, losses in red.

32/39 *ALK* fusion cases (82.1%) were associated with an intragenic copy number breakpoint. For the intra-chromosomal alterations, these included focal gains (*PPP1CB:ALK*) or losses (*CCDC88A:ALK*) spanning the two genes brought together by the structural variant. Inter-chromosomal fusions often showed copy number imbalances within the respective partner genes (*ZC3H7A:ALK,* *SPECC1L:ALK, MSI2:ALK* and *MAD1L1:ALK).* The breakpoints in *ALK* were always found in the intronic region between exon 19 and 20 with the resultant portion predicted to include the tyrosine kinase domain of *ALK* (**figure 4-5**).

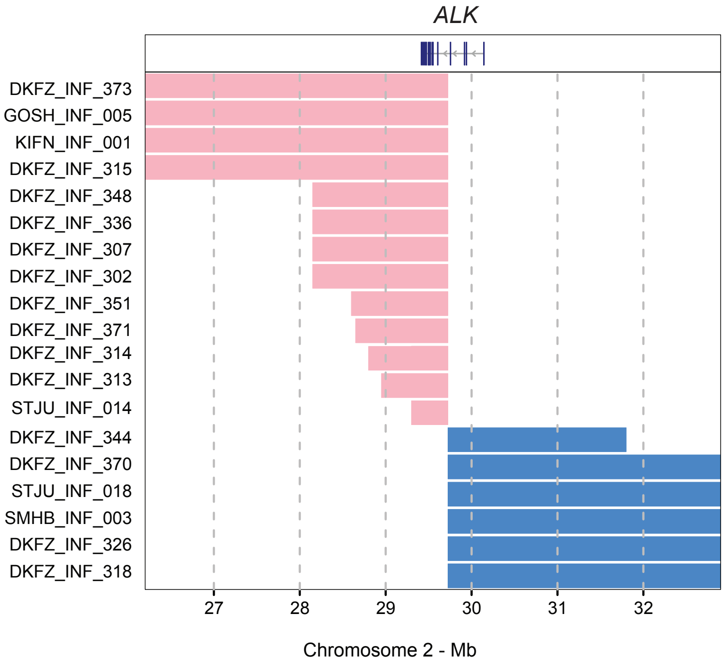

Figure 4-5. Copy-number–associated fusion genes in infant gliomas. Segmented DNA copy-number heat map for *ALK* breakpoint cases, plotted according to chromosomal location. Pink, gain; blue, loss.

However, 7 of 39 *ALK* fusions appeared to be copy neutral. By contrast, only 13 of 24 (54.2%, *P*=0.0234) *NTRK* fusion cases showed identifiable intragenic copy number breakpoints, including 8/12 *ETV6:NTRK3* fusions, but all *NTRK1* fusions (n=3) were copy neutral.

A novel brain tumour NGS fusion panel was developed and validated, applicable to both FFPE and FF samples (with the assistance of Elisa Izquierdo and Alan Mackay in the Jones lab (63). All cases with available DNA of sufficient quality were sequenced using the panel (n=116). Where possible, these were validated through a combination of genome, RNA, and/or Sanger sequencing, as exemplified for *ETV6:NTRK3* and the novel *ZC3H7A:ALK* fusions (**figure 4-6**).

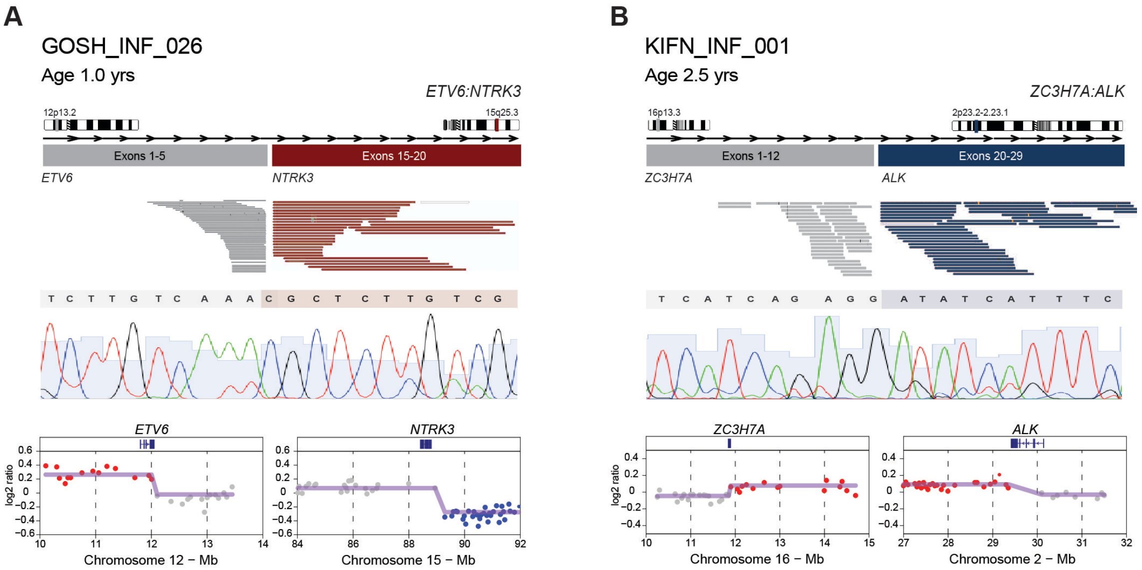

Figure 4-6. Copy-number–associated fusion genes in infant gliomas. **A,** *ETV6:NTRK3.* Cartoon representation of the fusion structure, with reads on either side of the breakpoint coloured by gene partner and taken from an Integrated Genome Viewer snapshot. Below this is a Sanger sequencing trace spanning the breakpoint. Underneath are copy-number plots ($\log_2$ ratio, y-axis) for chromosomal regions spanning the breakpoints (x-axis). Points are coloured red for copy-number gain, blue for loss, and grey for no change. The smoothed values are overlaid by the purple line. **B,** *ZC3H7A:ALK*. Cartoon representation of the fusion structure, with reads on either side of the breakpoint coloured by gene partner and taken from an Integrated Genome Viewer snapshot. Below this is a Sanger sequencing trace spanning the breakpoint. Underneath are copy-number plots (log2 ratio, y-axis) for chromosomal regions spanning the breakpoints (x-axis). Points are coloured red for copy-number gain, blue for loss, and gray for no change. The smoothed values are overlaid by the purple line.

The fusion was detected in three or more methods for 11 cases, two methods for 28 cases and was only detected using copy number analysis for 32 cases; four fusions were detected by copy number but not the fusion panel, and DNA was not available for the other cases (**appendix table 4**).

ALK fusions were the most frequent type of fusion identified (n=39), the vast majority of which were in the intrinsic set (35/39, 90%), specifically within the IHG group (32/95 cases, 33.7%). No examples were found in the DIGG/DIA group, and only 3 cases occurred in the DIGG/DIA-like group (3/24 cases, 12.5%) (**figure 4-7**).

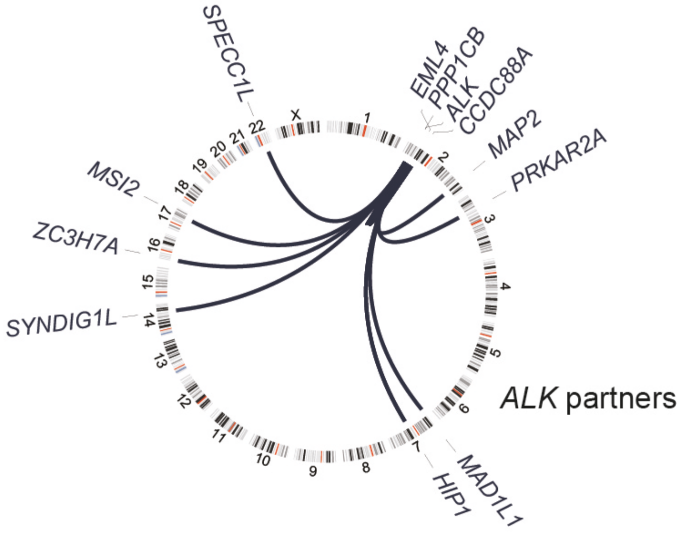

Figure 4-7. *ALK*-associated fusion genes in infant gliomas. Circos plot of gene fusions targeting *ALK* (dark blue). Lines link fusion gene partners according to chromosomal location, represented by ideograms arranged around the circle.

Although rare outside the intrinsic set, an *SPTBN1:ALK* fusion was confirmed in a LGG_SEGA case (calibrated score 0.92), and an *ALK* fusion (partner unknown) and an *EML4:ALK* fusion were present in poor scoring CONTR_INFLAM and PLEX_PED_B cases that were excluded from the intrinsic set based on their t-SNE projection (as a LGG and non-glioma respectively). However, given the high frequency of *ALK* fusions in the IHG group, it is possible that they are IHG cases with other factors influencing the output of the array such as DNA quality or tumour cellularity. *ALK* fusions were both intra-chromosomal (*PPP1CB:ALK* (n=8), *EML4:ALK* (n=5), *SPTBN1:ALK* (n=1), and *CCDC88A:ALK* (n=8)) inter-chromosomal (*MAP2:ALK* (n=1), *HIP1:ALK* (n=1), *PRKAR2A:ALK* (n=1), *MAD1L1:ALK* (n=1), *MSI2:ALK* (n=1), *SPECC1L1:ALK* (n=2), *SYNDIG1L:ALK* (n=1), *ZC3H7A:ALK* (n=1), and *CLIP2:ALK* (n=1)) (**figure 4-8**).

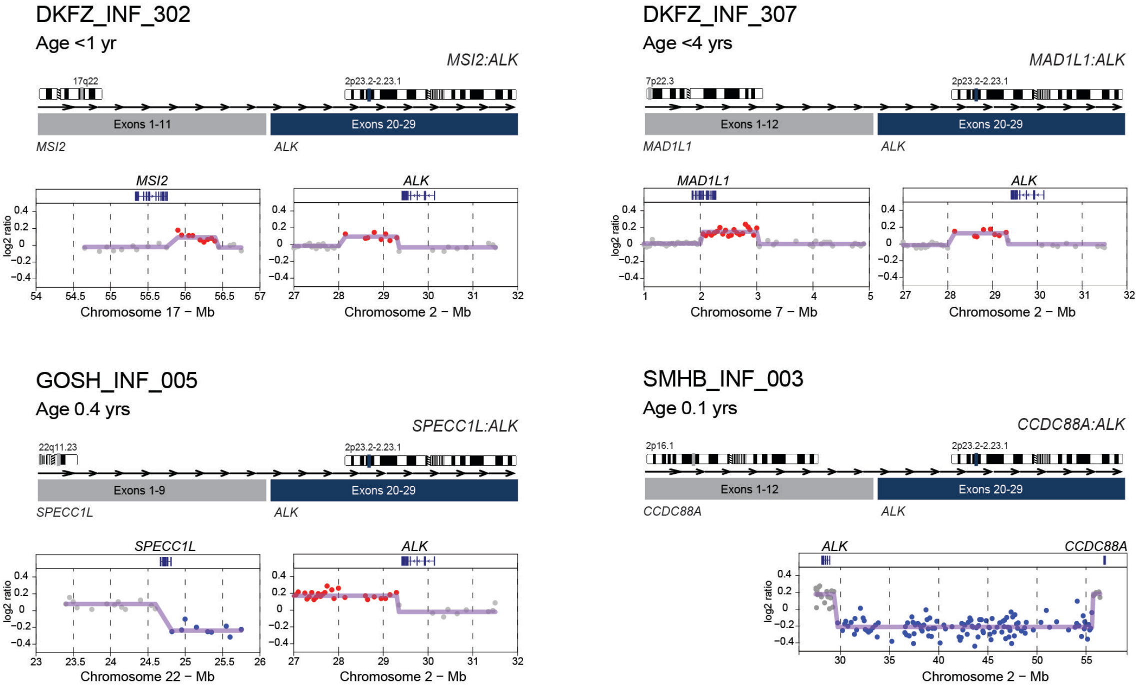

Figure 4-8. Copy number-associated fusion genes in infant gliomas. Cartoon representation of the *ALK* fusion structure, with copy number plots (log_2 ratio, y axis) for chromosomal regions spanning the breakpoints (x axis) underneath. Points are coloured red for copy number gain, blue for loss, and grey for no change. The smoothed values are overlaid by the purple line.

NTRK fusions were identified in all 3 genes (*NTRK1* (n=3), *NTRK2* (n=7) and *NTRK3* (n=14), predominantly *ETV6:NTRK3* (n=9) but also recurrent *EML4:NTRK3* (n=2) and *TPM3:NTRK1* (n=3) fusions (**figure 4-9**). 15 *NTRK* fusions occurred within the intrinsic set (15/130 cases, 11.5%) with 12 occurring in the IHG group (12/95, 12.6%), 3 cases in the DIGG/DIA-like group (3/24 cases, 12.5%) and an absence of *NTRK* fusions in the DIGG/DIA group. *NTRK2* rearrangements targeted numerous novel partners (e.g. *KCTD16:NTRK2* (n=1) and *AGBL4:NTRK2* (n=2)), but were largely found in other glioma subtypes occurring in the appropriate anatomic locations (e.g., DMG_K27M in midline regions), suggesting an important difference in *NTRK2* compared with *NTRK1/3* fusion–positive cases. Three fusions (*ETV6:NTRK3*, *KCTD8:NTRK2*, and *NTRK2* fusion (partner unknown)) were also identified in three PXA tumours which were excluded based on their methylation class (calibrated scores PXA 0.54, 0.51 and 0.83 respectively) and t-SNE projection. The non-diagnostic calibrated scores, histological diagnosis ranging from low-grade neuroepithelial tumour to GBM, and the fact that cases are reported of *NTRK*-fused infant HGG with histological features of a PXA (129) may indicate a small group of the previously described PXA-like cases (21) in the cohort.

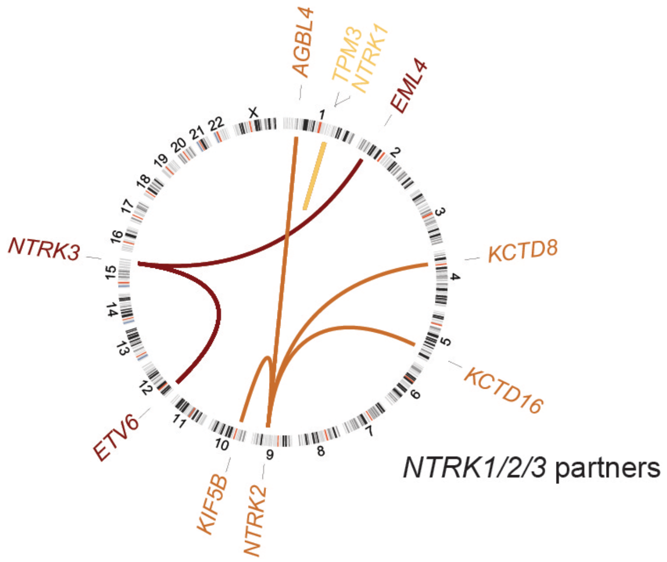

Figure 4-9. *NTRK*-associated fusion genes in infant gliomas. Circos plot of gene fusions targeting *NTRK1* (light orange), *NTRK2* (orange), and *NTRK3* (dark orange). Lines link fusion gene partners according to chromosomal location, represented by ideograms arranged around the circle.

ROS1 fusions on the other hand were almost all detected by copy number analysis (11/12, 92%), and strongly associated with the intrinsic set, specifically the IHG group (10/95, 10.5%.) 11/12 were associated with short intra-chromosomal losses with a breakpoint within the *ROS1* gene (**figure 4-10**).

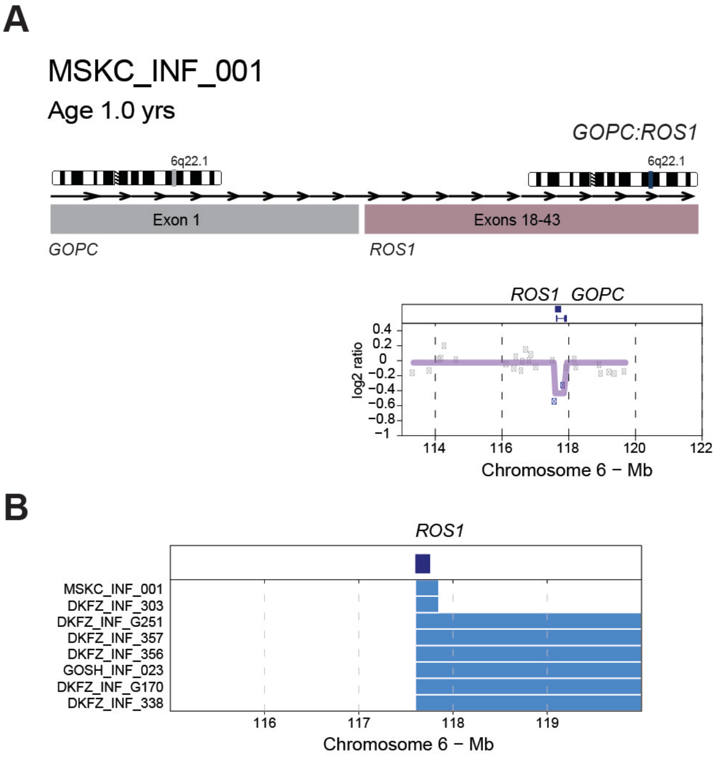

Figure 4-10. Copy number-associated fusion genes in infant gliomas. **A,** Cartoon representation of the *ROS1* fusion structure. **B,** Segmented DNA copy-number heat map for *ROS1* breakpoint cases, plotted according to chromosomal location. Pink, gain; blue, loss.

MET fusions were the least frequent RTK fusion (n=5), all identified via copy number changes. 4 of 5 were in the IHG group (4/95, 4.2%), the other in a high scoring GBM_MYCN case. The copy number profiles showed a short intra-chromosomal loss involving the *MET* gene (**figure 4-11**).

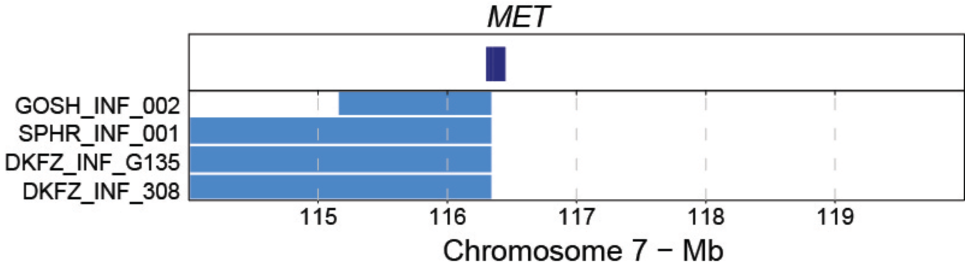

Figure 4-11. Copy number-associated fusion genes in infant gliomas. Segmented DNA copy-number heat map for *MET* breakpoint cases, plotted according to chromosomal location. Pink, gain; blue, loss.

Of the intrinsic set cases that had previously undergone panel, exome or genome sequencing (and no mutations had been identified), 25 of 41 (61%) harboured fusions in either *ALK* (n=10), *NTRK1/2/3* (n=2, 2, and 8, respectively) *ROS1* (n=2), or *MET* (n=1). The fusion-positive cases were mostly classified as IHGs (n=21) or DIGG/DIA-like tumours (n=4). Within the wider glioma cohort we identified *FGFR1:TACC1* (n=2) and *FGFR3:TACC3* (n=1) fusions, which were found in an *IDH1* mutant, a DMG_K27, and an ETMR respectively.

4.2.3 Fusion frequency in paediatric HGG

We also examined the likely frequency of RTK fusions across the full spectrum of pHGG subtypes by looking for intragenic breakpoints in a series of publicly available methylation datasets for a total of 5466 CNS tumours with 1543 HGG and DIPG cases (age was known for 1143, with 424 aged 3 - 20 years, 203/424 (47.9%) female and 221/424 (52.1%) male) (**figure 4-12A**). Of the HGG/DIPG cases aged 3 - 20, only 2 nominated *ALK* fusions were identified, showing these fusions appear to be specific to the infant cohort. In common with our anecdotal observations in our infant cohort, we observed three *ROS1* fusions in cases classifying as LGG_SEGA (3/28), and intragenic breakpoints were found in *MET* in *IDH1* mutated cases aged >20 years (4/103 3.9%) and in 6/424 (1.4%) cases in the cohort (**figure 4-12B**). Candidate *NTRK2* fusions were found in 1/48 (2.1%) of GBM_MID cases (and 5/424 (1.2%) of the entire cohort) and *NTRK3* fusion candidates found in 11/190 (5.8%) of DMG_K27 cases (aged <20), and in 13/424 (3.1%) HGG cases as a whole, much lower frequencies than those seen in the intrinsic set. *ROS1* fusions were also seen in 3/424 (0.7%) of the cohort. *NTRK1* fusions were identified in 17/424 (4.0%).

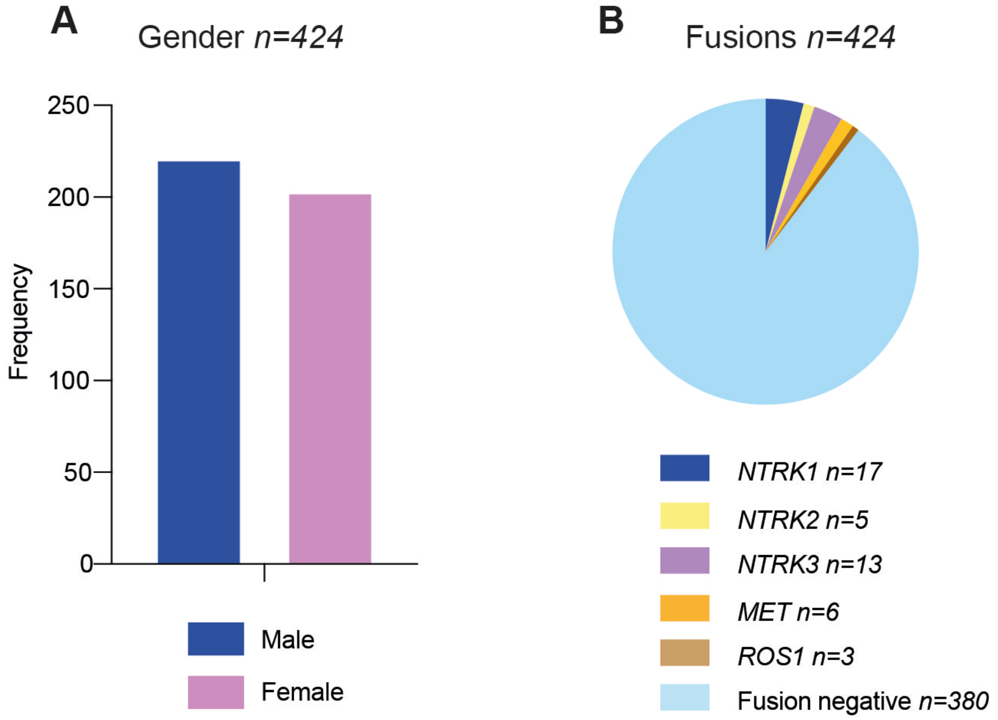

Figure 4-12. Fusion frequency (identified by copy number alteration (CNA)) in older children. **A,** Histogram showing the gender frequency in a cohort of n=424 cases of HGG aged <20 years old. **B,** Pie chart showing the number of RTK fusions identified by CNA within the cohort (n=457).

4.2.4 Fusion-negative cases

With 61.1% of the IHG group and 50% (65/130) of intrinsic set containing an RTK fusion, those that were considered fusion-negative underwent whole genome sequencing (n=6) to look for novel fusions or another driving event. This identified several inter-chromosomal translocations including *BCAT:NMD3, UFD1L:HR, GPHN:LOH12CR1, OPHN1:MRPL22 and BCL2L13:PLCL2.* Some large-scale copy number alterations were found (loss of chromosome 19 and 7, and gain of 8) and somatic SNVs and InDels involving *AMER1, NPHP3, MYH7B, BRD2* and *DRD4* genes. All of these finding require further validation. However, no consistent genetic drivers or RTK fusions were found in these cases (**figure 4-13**).

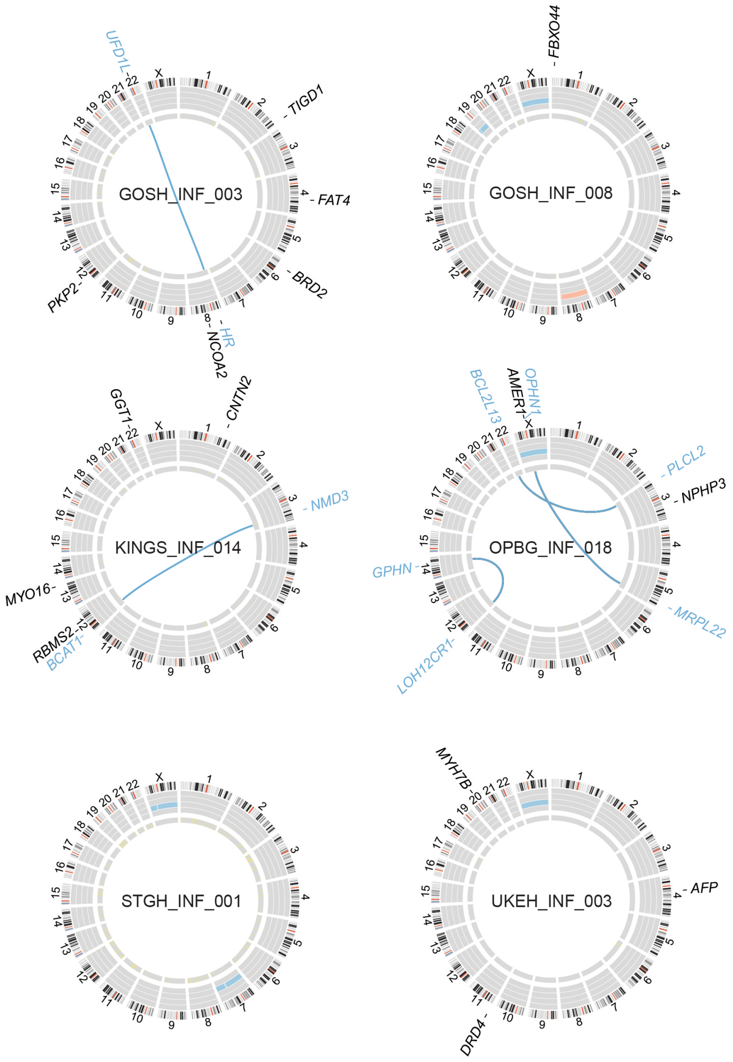

Figure 4-13. Whole genome sequencing of fusion-negative infant glioma cases. In each case, Circos plots provide somatic SNVs and InDels on the outer ring, DNA copy number changes (dark red, amplification; red, gain; dark blue, deletion; blue, loss) and loss of heterozygosity (yellow) on the inner rings, and inter-chromosomal translocations (blue) inside the circle.

4.2.5 Clinico-pathological correlation

With the caveat that limited survival data was available for intrinsic set cases (n=63), we nonetheless observed that the presence of any fusion resulted in a trend towards a longer overall survival compared with those which were fusion-negative (*P* = 0.0687, log-rank test). Although very small numbers, the *ROS1* fusion cases in the intrinsic set showed a slightly better outcome than the *ALK* and *NTRK* fusions which both followed a similar clinical course (**figure 4-14**).

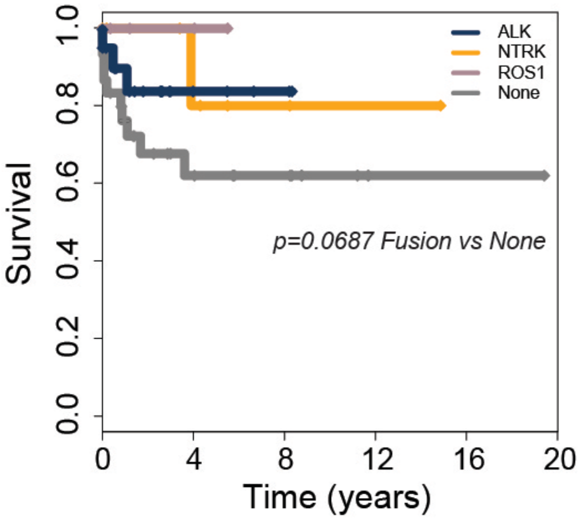

Figure 4-14. Infant glioma survival. Kaplan–Meier plot of overall survival of cases separated by fusion event (*ALK* n=22, *NTRK* n=13, *ROS1* n=7, none n=21, total n=63). P value is calculated by the log-rank test (P = 0.085 for any fusion vs. none).

Having identified characteristic histological and cytological features associated with the IHG group, including spindle-shaped and gemistocytic-like cells (see chapter 3), a subsequent review with reference to the molecular characteristics of each case showed no association between the microscopic features and the fusion type. However, only 1/6 of the fusion-negative cases contained pleomorphic nuclei, visible mitoses and a uniform architecture hinting that a fusion may influence the presence of some of these histological and cytological features (**appendix table 5**).

The proliferation index as assessed by Ki-67 staining highlighted cases presenting with both frequent and sparsely positive nuclei. There was a significantly elevated Ki-67 index in *NTRK* fusion–positive compared with fusion-negative IHG cases (*P*= 0.0479, t test), although not for *ALK* (*P*=0.3622, t test) (**figure 4-15**). Notably, the *NTRK* (median = 22.5) and *ALK* (median = 15.6) fusion–positive indices are at the upper end of values reported (130) for older patients with grade IV (median = 15.8) and grade III (median = 11.8) glioblastomas and anaplastic astrocytomas, with fusion-negative cases (median = 5.6) closer to grade II astrocytomas (median = 3.0) (130).

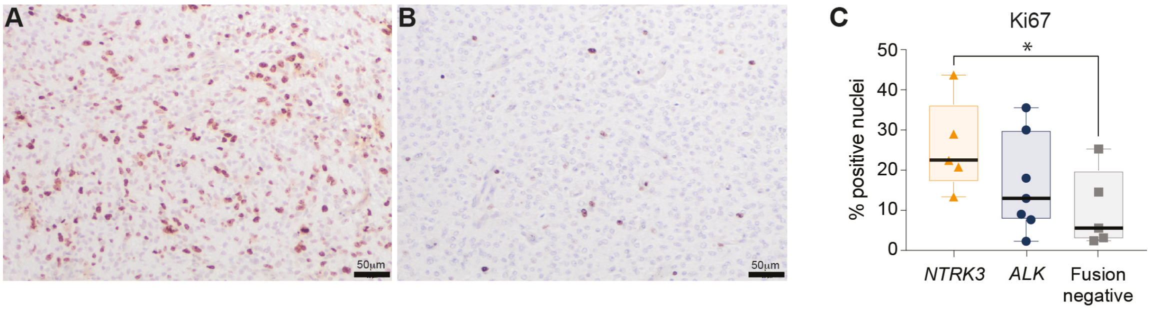

Figure 4-15. Proliferation index in fusion-positive vs. negative cases. **A,** Immunohistochemistry for Ki67 showing strong, frequent nuclear positivity. **B,** Immunohistochemistry for Ki67 showing only isolated positive nuclei. Scale bars are provided. **C,** Boxplot of Ki67 nuclear positivity in IHG cases by immunohistochemistry, separated by cases containing *NTRK3* fusions (orange), *ALK* fusions (dark blue) or fusion-negative (grey). The thick line within the box is the median, the lower and upper limits of the boxes represent the first and third quartiles, and the whiskers 1.5x the interquartile range. * p<0.05, t-test.

In order to determine whether fusion-positive infant glioma cases shared similar methylation profiles with other fusion-positive infantile tumours, the intrinsic set were compared with publicly available data from 10 IF and 20 CMN cases by means of t-SNE projection. The infant gliomas clustered apart from the mesenchymal tumours, despite the overlap of driving *ETV6:NTRK3* fusions (**figure 4-16**).

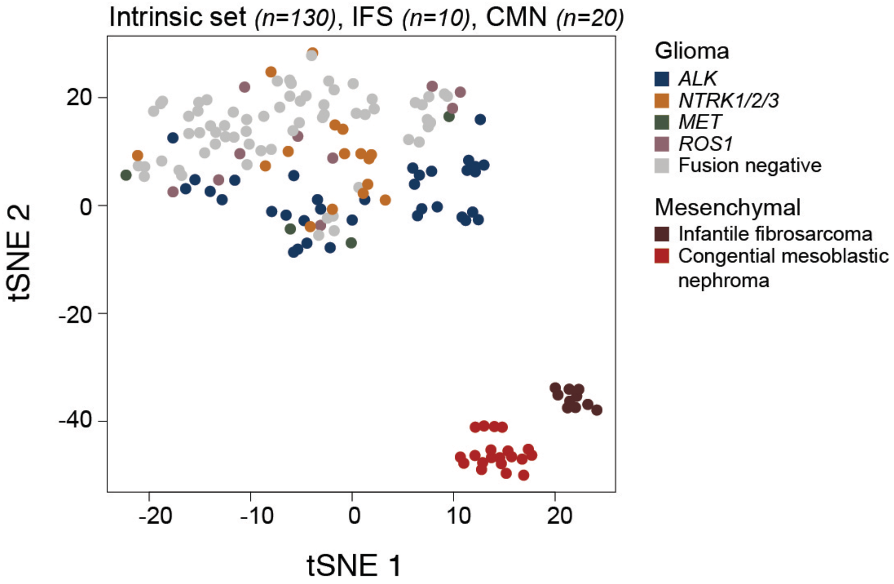

Figure 4-16. Comparison with other fusion-positive infantile tumours. t-statistic based stochastic neighbor embedding (t-SNE) projection of a combined methylation dataset comprising the intrinsic infant glioma set (n=130) as well as two *ETV6:NTRK3*-driven mesenchymal tumours, infantile fibrosarcoma (n=10) and congenital mesoblastic nephroma (n=20). The first two projections are plotted on the x and y axes, with samples represented by dots coloured by subtype according to the key provided.

4.2.6 Differentially methylated regions

In order to explore epigenetic differences between the fusion-positive and negative cases, we performed a methylation-based gene ontology analysis which highlighted little overlap between differentially methylated regions of *ALK* fusion, *NTRK* fusion, and fusion-negative cases with only 1-4% pairwise concordance between different subgroups, and no features common to all three groups (**figure 4-17**).

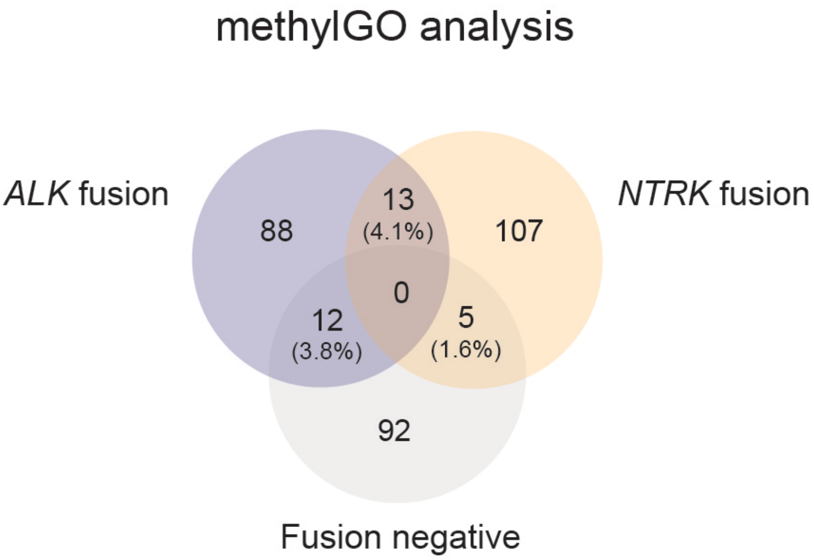

Figure 4-17. Methylation-based gene ontology analysis. Pie chart showing overlap of significant gene ontology annotations of differentially methylated regions between *ALK*-fusion, *NTRK*-fusion and fusion-negative infant glioma cases.

ALK fusion cases were significantly associated with dysregulation of genes associated with glutamate receptors, synapses, signal transduction, and morphogenic stages of development, whereas *NTRK* fusion cases were linked with genes controlling neuronal differentiation and the earliest stages of embryogenesis, as well as signaling via the JNK cascade. In contrast, fusion-negative cases were predominantly associated with the response to multiple endogenous stimuli, particularly the TGFβ pathway, and the regulation of stem cell pluripotency and cell fate (**figure 4-18**).

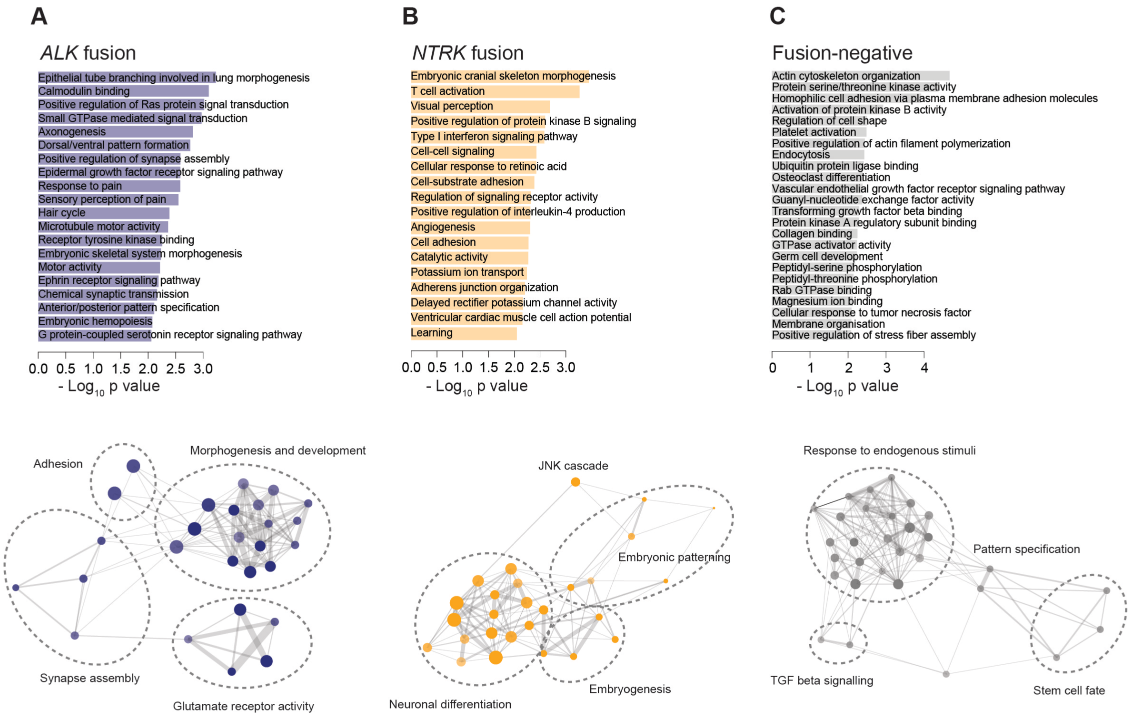

Figure 4-18. Epigenetic alterations in fusion-positive and fusion-negative infant gliomas. **A,** Differential methylation-based gene ontology analysis for *ALK* fusion cases, represented in bar plots of $-\log_{10}$ P value for labeled highest-scoring categories (top) and aggregated ontology networks (bottom). **B,** Differential methylation-based gene ontology analysis for *NTRK*-fusion cases, represented in bar plots of $-\log_{10}$ P value for labeled highest-scoring categories (top) and aggregated ontology networks (bottom). **C,** Differential methylation-based gene ontology analysis for fusion-negative cases, represented in bar plots of $-\log_{10}$ P value for labeled highest scoring categories (top) and aggregated ontology networks (bottom). Node size is proportional to the number of genes, shading represents $-\log_{10}$ P value (darker is higher). Thickness of connecting lines reflects the percentage of overlapping genes

Although only exploratory due to the small sample sizes, and needing independent validation in an independent cohort, as exemplars of the differential epigenetic regulation of key genes controlling these processes in the distinct subgroups, consistent reduction in methylation at CpG sites governing expression of *WNT5A* in *ALK* fusion cases, *STAT1* in *NTRK* fusion cases, and *TP63* in fusion-negative samples was observed. This resulted in differential protein expression as assessed by multi-labelled immunofluorescence with antibodies directed against these targets, with representative examples shown for WNT5A and STAT1 in *ALK*-fusion and *NTRK*-fusion cases, respectively.

STAT1 varied in expression level across cases with both focal and generalised expression seen. WNT5A expression was very focal in *ALK* positive cases. TP63 expression was not detected across any groups (**figure 4-19**).

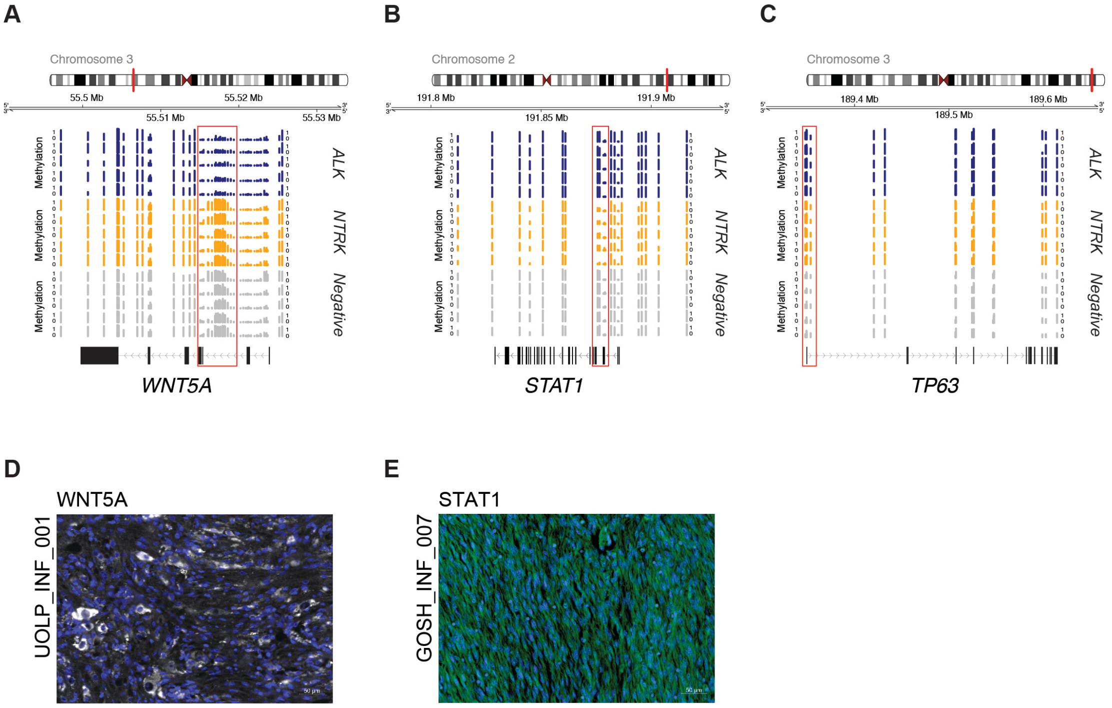

Figure 4-19. Epigenetic alterations in fusion-positive and fusion-negative infant gliomas. **A,** Genome browser view of the *WNT5A* locus, with lower methylation, provided as bar plots, in selected *ALK*-fusion (blue) cases compared to *NTRK*-fusion (orange) and fusion-negative (grey) cases. **B,** Genome browser view of the *STAT1* locus, with lower methylation, provided as bar plots, in selected *NTRK*-fusion (orange) cases compared with *ALK*-fusion (blue) and fusion-negative (grey) cases. **C,** Genome browser view of the *TP63* locus, with lower methylation provided as bar plots, in selected fusion-negative (grey) cases compared with *ALK*-fusion (blue) and *NTRK*-fusion (orange) cases. Chromosomal ideograms are provided, with the red bar indicating the cytoband in which the locus is found. Differentially methylated probes are highlighted by the red box. **D,** Immunofluorescence staining of an antibody directed against WNT5A (white) in an *EML4:ALK* fusion infant glioma case, UOLP_INF_001. DAPI is used as a counterstain. Scale bar, 200µm. **E,** Immunofluorescence staining of an antibody directed against WNT5A (green) in an *ETV6:NTRK3* fusion infant glioma case, GOSH_INF_007. DAPI is used as a counterstain. Scale bar, 200µm.

Using a NanoString assay for the 30 most differentially methylated genes between subgroups, some differences in expression were noted between *ALK/NTRK* fusion-positive and negative subgroups in a series of 21 infant HGG for which there was sufficient material (10 *ALK*, 6 *NTRK*, and 5 fusion-negative cases). Notably, although TP63 protein expression was not observed in any of the samples, differential overexpression of the transcript was observed for fusion-negative cases (**figure 4-20**).

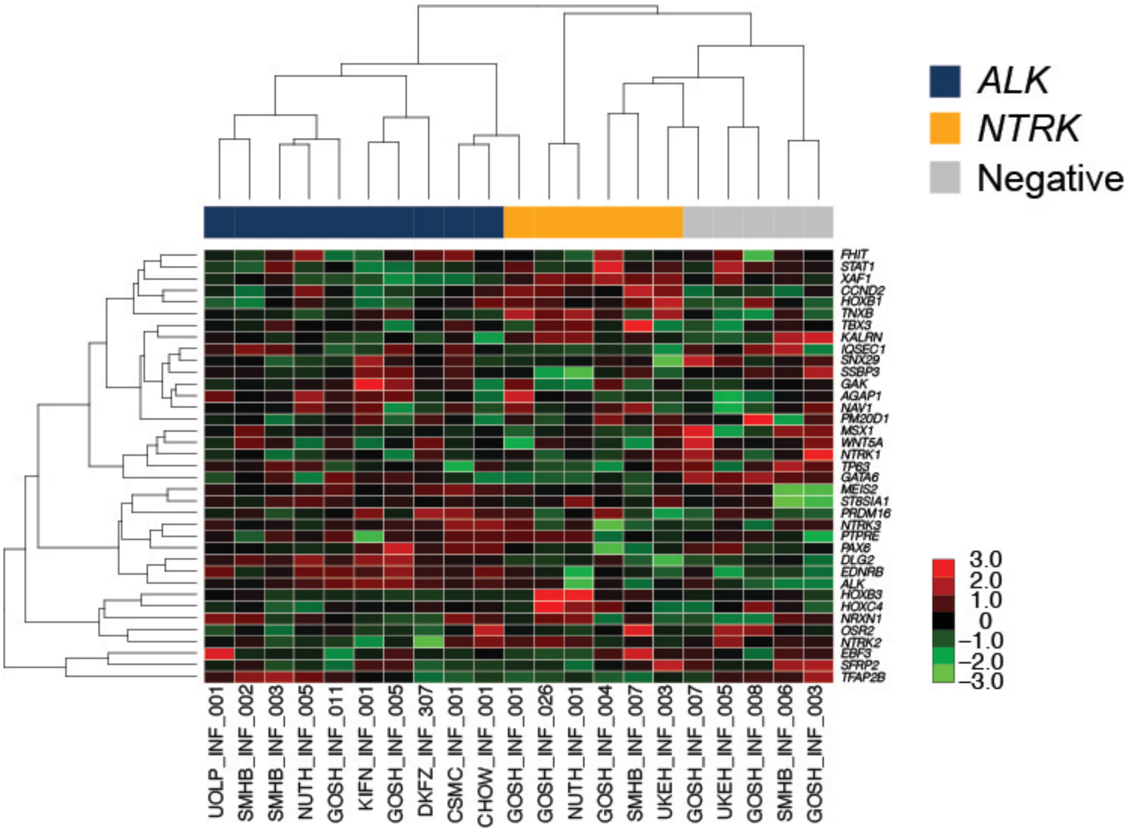

Figure 4-20. NanoString expression analysis. Heat map representing gene expression values from a NanoString assay of 30 most differentially methylated genes between *ALK*-fusion (blue), *NTRK*-fusion (orange), and fusion-negative (grey) cases. Expression values are coloured according to the scale provided.

4.2.7 Single-cell RNA sequencing analysis

With the assistance of Dr Mariella Filbin at the Dana-Farber Cancer Institute in Boston, we began an exploratory single-cell RNA sequencing analysis of *NTRK1* (QCTB_INF_R102, *TPM3:NTRK1*), *NTRK2* (KING_INF_018, *KCTD16:NTRK2*) and *NTRK3* (OPBG_INF_035, *ETV6:NTRK3)* fusion-positive tumours to investigate cellular subpopulations in these subtypes.

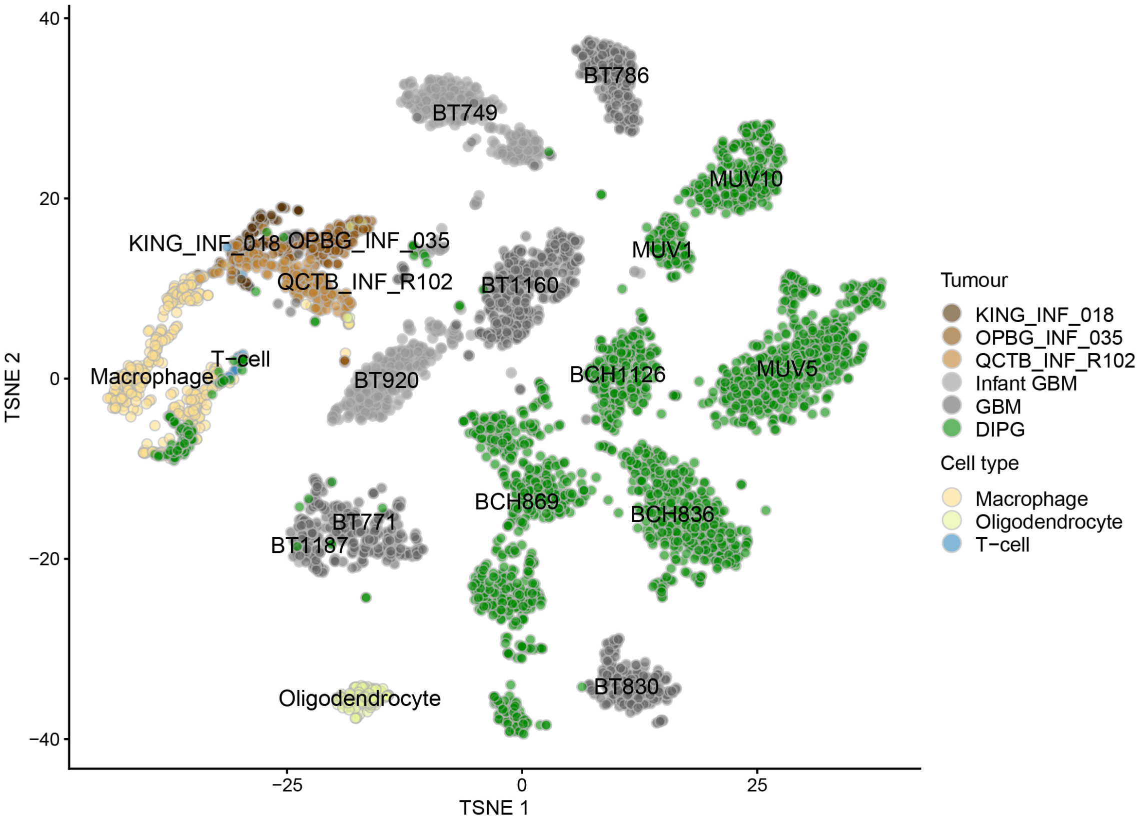

Figure 4-21. Single-cell RNA sequencing of *NTRK*-fusion-positive infant gliomas. t-SNE projection of the *NTRK*-fusion-positive infant gliomas QCTB_INF_R102 (*TPM3:NTRK1*), KING_INF_018 (*KCTD16:NTRK2)* and OPBG_INF_035 (*ETV6:NTRK3*) plotted again other infant GBMs, GBMs in older children and DIPGs. The composition and association of the tumours in terms of cell type (macrophages, oligodendrocytes, and T-cells) is indicated by the coloured key.

Unfortunately these experiments were halted during the Covid-19-enforced lab shutdown, and only preliminary analysis has very recently been able to be undertaken. When projected onto a t-SNE with publicly available data from other infant GBMs, GBMs from older children and DIPGs (75,98,99), the cells from the *NTRK*-fusion-positive cases clustered separately to these other tumour types (**figure 4-21**). Also, they clustered in close proximity to a macrophage/microglia cluster, and there was a notable macrophage/microglia and T cell population present in KING_INF_018 (approximately 40% macrophages/microglia) and also in QCTB_INF_R102 (approximately 15% macrophages/microglia), similar to another sample reported as infant GBM (BT1187) (75) which appeared to be predominantly macrophages/microglia (>90%) and a large proportion of T cells (**figure 4-22**). These levels of immune cell infiltrate were largely absent from other tumour types (save for one DIPG with a particularly high T cell component), with DIPGs instead showing a higher degree of oligodendrocyte-like differentiation. This was completely lacking in the three *NTRK*-fusion-positive tumours. Additional informatic analysis of these data are continuing.

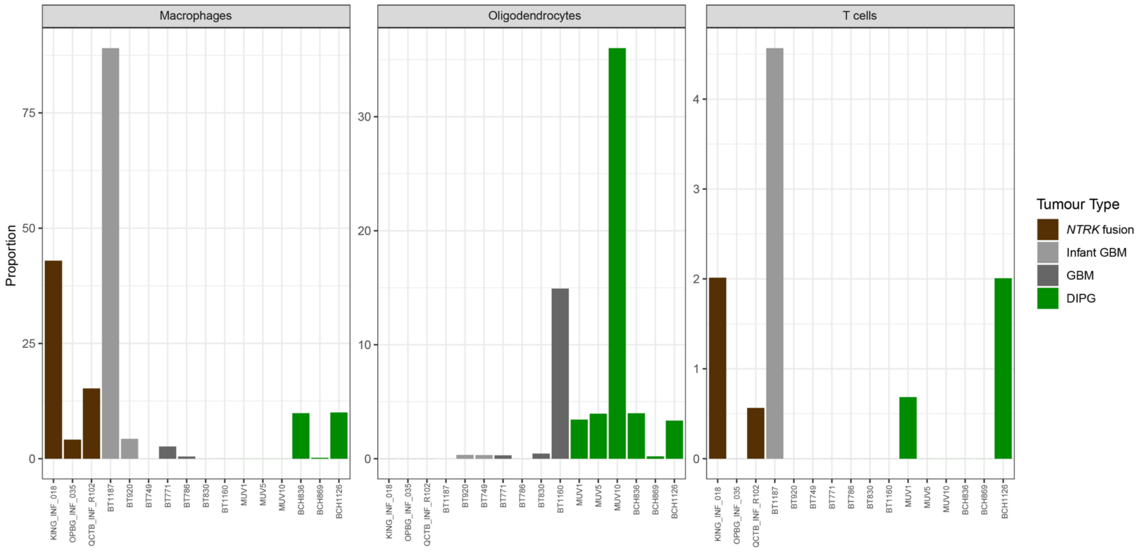

Figure 4-22. Bar plots of cell proportions. Bar plots showing the proportions of the labelled tumours (including the *NTRK*-fusion-positive infant gliomas QCTB_INF_R102 (*TPM3:NTRK1*), KING_INF_018 (*KCTD16:NTRK2)* and OPBG_INF_035 (*ETV6:NTRK3*)) that are composed of macrophages, oligodendrocytes or T cells.

4.3 Discussion

After excluding gliomas occurring in the infant population which resembled other established entities and subtypes, there remained what we termed the ‘intrinsic’ set of cases, which are largely restricted to the cerebral hemispheres, occur in the youngest patients (usually younger than 12 months old) and lack the key molecular features of both HGG and LGG. Tumours representing what was termed ‘IHG’ in the Heidelberg classifier made up the largest proportion of these cases, and were strikingly defined by nearly two thirds of tumours harbouring fusions in genes encoding the RTKs *ALK, NRTK1/2/3, ROS1*, and *MET.* Individual fusions did not predict for specific histological features. Although structural variants involving these genes within the age group have been described in case reports (81,119–126) and a recent larger study (n = 29) (9); the current report represents a uniquely powerful study of these rare tumors by accumulating a series of 82 infant cases with RTK fusions with full methylation profiles.

Molecularly, these variants included interstitial microdeletions such as those at chromosome 2p23 resulting in the fusion of *CCDC88A* or *PPP1CB* and *ALK* (9,125) and at 6q21 fusing *ROS1* and *GOPC* (previously known as *FIG*, and originally described in an adult GBM cell line (131); additional focal DNA copy-number losses targeted *MET* at 7q31 (79). There were multiple instances of inter-chromosomal copy-number gains fusing *ALK* to a series of novel partners, including *MAD1L1* (7p22), *ZC3H7A* (16p13), *MSI2* (17q22), *SYNDIG1* (20p11), and *SPECC1L* (22q11), as well as the intra-chromosomal *EML4:ALK* fusion that is well characterised in non–small cell lung cancer and others (132). As well as lung cancer, *ALK* fusions have been identified in other cancer types such *WDCP:ALK* fusions occurring in colonic tumours (133), and *CARS:ALK* fusions in soft tissue tumours (134), however they were very rarely seen in a series of 424 HGG cases in older children (aged <20 years) highlighting the infant-specific nature of these fusions in glioma. Therefore, copy number profiling should be considered as a screening method and the presence or absence of a copy number alteration for any infant glioma case should be validated ideally with panel or RNA sequencing to prevent a false positive or negative result. However, where a fusion associated copy number change was found, this was frequently the only copy number alteration identified. Notably, 51/457 (13%) tumours in patients up to the age of 20 years were found to harbour copy number alterations suggestive of others possible RTK fusions, particularly *NTRK2* and *NTRK3*; this is a significant percentage of cases, but very likely to be an overestimate. Validation of these candidates is needed to be certain.

An example of where these older cases may be important comes from the HERBY trial, which evaluated the use of bevacizumab in addition to temozolomide or radiotherapy as a phase II, randomised, multi-centre trial in patients aged between 3 -18 years who were newly diagnosed with non-brainstem HGG. I contributed to the molecular profiling of this cohort carried out by the Glioma Team, through the application of the custom fusion panel described in this chapter (63). Here we identified an *NTRK2* fusion in a non-infant hemispheric WHO grade IV GBM (with additional somatic mutations), which was included in the group of MAPK pathway-driven ‘PXA-like’ tumours (63). This group (predominantly *BRAF* V600E or *NF1* mutant) were found to contain significantly more CD8+ tumour infiltrating lymphocytes in contrast to other HGG/DMG, which had a distinct absence of immune cell infiltrates. Strikingly, the tumours with CD8+ tumour infiltrating lymphocytes also had an improved survival when bevacizumab was used in their treatment (63). Considering the ‘immune responsive’ tumour cell population and the high frequency of microglia identified by single-cell RNA sequencing in the *NTRK2*-fusion-positive KING_INF_018 case, this may merit further exploration of the immune cell infiltrate in infant HGG to see if this correlates with outcome, can be used to predict outcome, or be enhanced through treatment.

ALK fusion gene breakpoints always occurred in the intronic region between exon 19 and 20 in every case, also reported in non-small cell lung cancer (NSCLC) (135). In very rare instances, this can occur in the intronic region between exon 18 and 19 (136). Multiple *ALK* partners are associated with synapse formation and activity (*CCDC88A, HIP1, SYNDIG1*), neuronal cytoskeletal reorganization (*CCDC88A, SPECC1L*), and microtubule assembly (*MAP2, PRKAR2A, EML4*), as well as PI3K/MAPK signaling (*PPP1CB, CCDC88A, SPECC1L*) and cell-cycle progression (*MAD1L1*; (137–145). Thus, in addition to the activated kinase activity of the ALK receptor itself, these fusions likely disrupt key regulatory processes in neurodevelopment, as exemplified by the differential methylation of genes controlling these processes that were observed. *ALK* itself is known to be expressed in foetal brain with a role in neurodevelopment (146,147). Interestingly, the fusion partner is important for treatment in NSCLC with tumours harbouring *EML4:ALK* responding better to ALK inhibitors and showing improved overall survival compared to fusion-negative cases and those with different fusion partners (148).

The *NTRK* genes had a variety of inter-chromosomal partners, with around half of cases marked by a DNA copy imbalance at either locus. Notably, *NTRK2* fusions (also described in LGG; (73)) were largely found in tumours classifying as other glioma subtypes, as were the previously described *FGFR:TACC* fusions (149). *NTRK* fusions, although found at a higher frequency than in older paediatric HGG, were less frequently marked by copy number alterations with all *TPM3:NTRK1* fusions being copy neutral.

Approximately 80 different 5' fusion partners of the *NTRK* genes are reported across different tumour types (150). All three *NTRK* genes are involved in nervous system physiology and development (95). However, coexistent somatic mutations may be important and individual cases hint at this across fusion types; an *NTRK* fusion case in the infant cohort classified as a GBM_RTK_III and contained an *EVT6:NTRK3* fusion, a *PTEN* mutation and *CDKN2A/B* deletion. The fusion did not confer any survival advantage for this child likely as a result of the other mutations. Another case diagnosed as a GBM histologically (PXA 0.54 by methylation profiling) with a *KCTD8:NTRK2* fusion and a coexistent *CDK2NA/B* deletion is alive and in remission at last follow-up. A further infantile midline tumour (diagnosed as AA by histology, DMG K27 0.99 by methylation profiling) containing an *AGBL4:NTRK2* fusion in addition to a *H3F3A K27M* mutation had a survival of 2.51 years. This shows that the background mutations have a significant impact on the outcome of fusion-positive cases.

Despite the frequency of alterations identified, not all of the intrinsic infant gliomas were found to harbor RTK fusions. These fusion-negative cases (at least on the basis of the platforms used in this study) had a lower proliferation index compared with *NTRK*-positive cases, but a worse prognosis under standard treatment. Given the lower proliferation index, the worse survival is surprising. However, a great number of cases are needed for assessment in each group to be more definitive. Certainly, the increased proliferation index in NTRK-fusion positive cases associated with an improved survival could be an indicator of better responsiveness to adjuvant therapy and could support the potential impact of Trk inhibitors useage in these cases. Although we could identify no apparent recurrent genetic driver of the fusion-negative subgroup, even with whole-genome sequencing of a subset of cases, there were clear epigenetic differences compared with fusion-positive cases. These included dysregulated gene networks associated with the regulation of stem cell pluripotency, plausibly suggesting an immature progenitor cell phenotype for these genetically bland lesions. In contrast, *NTRK*-fusion cases were associated with an embryonic, neuronal developmental program, and *ALK*-fusion cases with later AMPA-receptor synaptic plasticity signatures.

The presence of recurrent *ALK/NTRK/ROS1/MET* fusions also represents clearly targetable alterations, in common with subgroups of adult epithelial tumours (151,152), and their identification through screening approaches and routine diagnostic sequencing panels (80,153–155) makes them amenable to selection for clinical trials despite their rarity. The distinct morphologic variants, the restricted spatial and temporal patterns of presentation, and the specificity of oncogenic events largely in the absence of other mutations or large-scale chromosomal rearrangements suggests an exquisite developmental susceptibility for transformation that would account for this rare subgroup of tumours. However, further work is needed to explore all intrinsic infant glioma subgroups, in particular the fusion-negative cases. It is clear that these tumours harbour unique biology with associated clinicopathologic differences and should no longer be diagnosed or treated in the same way as their older counterparts.

CHAPTER 5 – Longitudinal sampling of infant glioma

5.1 Introduction

Paediatric HGG has a very poor prognosis. As a result, re-biopsy or re-resection of these tumours is very rare, and the acquisition of samples is challenging. However, longitudinal sampling represents a tantalising opportunity to observe and identify changes in the molecular profile of these tumours as they evolve, and in response to treatment. They also can help to identify potential resistance mutations and mechanisms that have important implications for future drug development.

Published longitudinal studies featuring paediatric HGG are very limited. Our recent study which used a hybrid-capture NGS panel to molecularly profile 233 paediatric patients with solid tumours featured some paediatric HGG cases. 90% of the patients in this study had an episode of progression or relapse before they were enrolled but only the initial tumour sample was requested. At least one genetic alteration was detected in 70% of cases, 51% of which were clinically actionable (156). Interestingly, 8 patients had paired samples sequenced at different stages of treatment; six of these showed different variants at different time points; *PTEN, NF1* and *TP53* mutations were found in the second sample of a paediatric *BRAF* V600E positive HGG case treated with the MEK inhibitors dabrafenib and trametinib. In a second case of *H3F3A* and *TP53* mutant glioma (mutations present in both samples), a *PTEN* mutation was detected at diagnosis and a *PIK3CA* mutation at progression (156). These examples show that these tumours have a changing molecular profile; re-biopsy is necessary to detect these changes so that treatment can be adapted where necessary and appropriate.

Other studies further support the value of re-biopsy at relapse in paediatric cancer; the 'Individualized Therapy for Relapsed Malignancies in Childhood' (INFORM) study molecularly profiled (using WES, WGS, methylation profiling, RNA sequencing, and expression microarray analysis) primary tumours (featuring both sarcomas and brain tumours amongst others) with identification of druggable targets (157). Re-biopsy samples were also profiled in the same way again demonstrating that the tumours were evolving and even helped to identify the onset of secondary malignancies rather than relapse (157).

Longitudinal studies in adult glioma have demonstrated the influence of treatment on the evolving molecular profiles of HGG. A study featuring 222 patients with gliomas were profiled into three groups; *IDH* mutant and 1p/19q co-deleted, *IDH* mutant without 1p/19q co-deletion and *IDH* wild-type tumours (47). Driver mutations were retained at recurrence (as seen in paediatric cases) but there was very little evidence of recurrence-specific gene alterations within the cohort. However, the type of treatment did influence the molecular profile; alkylating agents were associated with a hypermutator phenotype across the three groups, although this did not impact on survival (47). It is important to detect these treatment-induced mutations which could have important implications for the use of alkylating agents in paediatric cases, particularly in infants. Allelic-depth (the number of reads which align to a particular variant) can be compared between two samples to see if there has been an increase, decrease or no change (47).

Studies have also hinted at differences in immune infiltration profiles in glioma related to their mutational spectrum; increased infiltration of CD4+ T cells, neutrophils and macrophages are reported in in *EGFR* mutated LGG, and are also correlated with a worse survival (158). Also, it is reported that *IDH* wild-type status in WHO grade II-IV gliomas is associated with increased levels of tumour infiltrating lymphocytes and *PD-L1* expression with *IDH* mutant tumours having higher levels of *PD-L1* promotor methylation thereby influencing expression (159).

This longitudinal study aims to look for changes in the molecular profile of a small series of infant HGG which could be potentially correlated with treatment and clinical outcome.

5.2 Results

5.2.1 The sample cohort

The longitudinal cohort was composed of 10 cases with a total of 22 samples. Nine cases featured within the initial infant glioma study (and were all part of the intrinsic set); these were either the first biopsy or resection sample for each case and were therefore designated ‘A’. Nine cases were composed of paired samples (therefore annotated ‘A’ and ‘B’), and a single case had four samples available (A-D). A new case was added to the cohort which didn’t feature in the initial study, designated HMCI_INF_001; only samples from the second and third resections were available and these were designated ‘B’ and ‘C’ respectively.

Of the 10 cases, 4/10 (40%) were female and 6/10 (60%) were male. 9/10 cases were aged <1 year at diagnosis (median 0.45 years). The location of the tumour was known for 9/10 cases; all had a hemispheric location. 7/10 (70%) of cases were diagnosed as a HGG/glioblastoma based on histology, and 3/10 (30%) were diagnosed as a DIGG/DIA (**figure 5-1**).

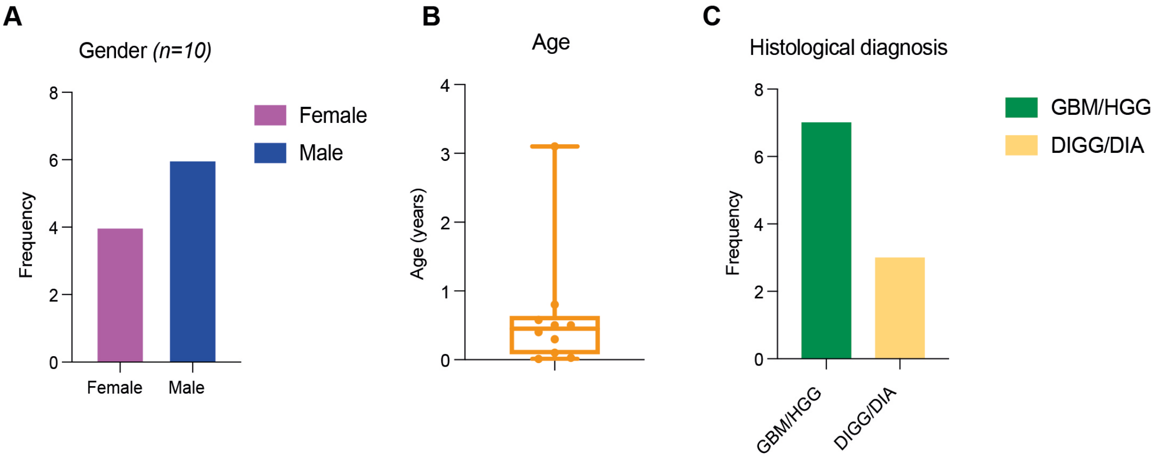

Figure 5-1. Demographics of the longitudinal cohort. **A,** Bar chart showing the gender distribution of the longitudinal cohort (n=10, key provided). **B,** Box plot showing the age distribution of the longitudinal cohort. **C,** Bar chart showing the proportion of different histological diagnoses within the longitudinal cohort (key provided).

Two cases (GOSH_INF_005, a 5 month old male infant, and OPBG_INF_035 a 6 month old female infant (see chapter 7)) underwent an initial biopsy of hemispheric tumours (sample A). GOSH_INF_005 was diagnosed with a GBM and commenced on POG 8633 chemotherapy, undergoing a resection 6 months after the initial diagnosis (sample B) **(table 5-1)**. The child remains alive with a complete response to treatment. OPBG_INF_035 was also diagnosed with a GBM, and was commenced on chemotherapy undergoing a resection 3 months later (sample B). An *ETV6:NTRK3* fusion was identified in both samples by myself and the child was then treated with crizotinib monotherapy and then larotrectinib, and remains alive with significantly reduced tumour burden **(figure 5-2)**.

GOSH_INF_028 (6 month old male infant) underwent a partial resection of a hemispheric tumour (sample A), diagnosed as a GBM. After starting HIT-SKK chemotherapy he underwent second surgery 3 months after the first (sample B) due to local progression. The child was alive with a complete response at last follow up. GOSH_INF_003 (3.7 month old female) had a subtotal resection of a hemispheric tumour (sample A) but underwent ‘second look surgery’ 1 week later (sample B) with a near gross total resection. Diagnosed with a GBM, POG 8633 chemotherapy was commenced. There was no progression or relapse and the child remains alive and well. HMCI_INF_001 (10 month old male) underwent a subtotal resection of a hemispheric tumour diagnosed as a GBM (sample A, although not available for this study). He was treated with Baby POG chemotherapy but progressed and underwent another resection (sample B) and a further resection 3 months later (sample C). The child died of neurological complications secondary to the tumour. DKFZ_INF_307 (1 month old male) who underwent a gross total resection of a hemispheric GBM (sample A), and was treated with HIT-SKK chemotherapy for 6 months. He progressed 5 months after the completion of chemotherapy, partial resection was performed (sample B), and he started temozolomide for 6 months. An *ALK* fusion was identified and he was treated with ceritinib. The child is alive with stable disease **(figure 5-2)**.

SMHB_INF_008 (3.2 year old male) underwent a gross total resection of a hemispheric lesion (sample A) diagnosed as a DIGG/DIA. No adjuvant therapy was given, but he developed a lesion in the left temporal lobe (considered metastatic) 2 years later which was resected (sample B). He was commenced on chemotherapy for 1 year, and remains alive at last follow up. PMHK_INF_001 (5 day-old female) underwent a gross total resection (sample A) after acute presentation with haemorrhage in a left parietal lesion. Diagnosed as a GBM, she started vincristine chemotherapy, at 18 months she underwent a further resection (sample B) due to recurrence and was commenced on trametinib. A *ROS1* fusion was identified in this tumour and she was commenced on entrectinib with a partial response. A further resection was performed at 21 months (sample not in study); sequencing at the referring institution identified *PTCH1* and *KMT2D* mutations. The child is alive and continues on treatment. Unfortunately, clinical data was not available for SMHB_INF_007 or SMHB_INF_009 (**figure 5-2**).

Sample ID	Age (years)	Gender	Location	Sample A type	Diagnosis	Adjuvant treatment	Sample B type	Further treatment	Outcome
GOSH_INF_005	0.40	Male	Hemispheric	Biopsy	GBM	Chemo	Resection	N/A	Alive (CR)
OPBG_INF_035	0.50	Female	Hemispheric	Biopsy	GBM	Chemo	Resection	Trk inhibitors	Alive (PR)
GOSH_INF_028	0.50	Male	Hemispheric	STR	GBM	Chemo	Resection	N/A	Alive (CR)
GOSH_INF_007	0.30	Female	Hemispheric	STR	GBM	N/A	2nd look surgery	Chemo	Alive
HMCI_INF_001	0.80	Male	Hemispheric	STR	GBM	Chemo	Resection (x2)	N/A	Died (NC)
DKFZ_INF_307	0.10	Male	Hemispheric	GTR	GBM	Chemo	Subtotal resection	ALK inhibitor	Alive (SD)
SMHB_INF_008	3.20	Male	Hemispheric	GTR	DIGG/DIA	N/A	Resection	Chemo	Alive
PMHK_INF_001	0.01	Female	Hemispheric	GTR	GBM	Chemo	Resection	MEK/Trk inhibitors	Alive

Table 5-1. Clinical data of longitudinal cohort. A table summarising the available clinical data of patients in the longitudinal cohort including age, gender, location, type of sample and treatment. GTR = Gross Total Resection. STR = Subtotal Resection. GBM = glioblastoma. CR = complete response. PR = partial response. NC = neurological complications.

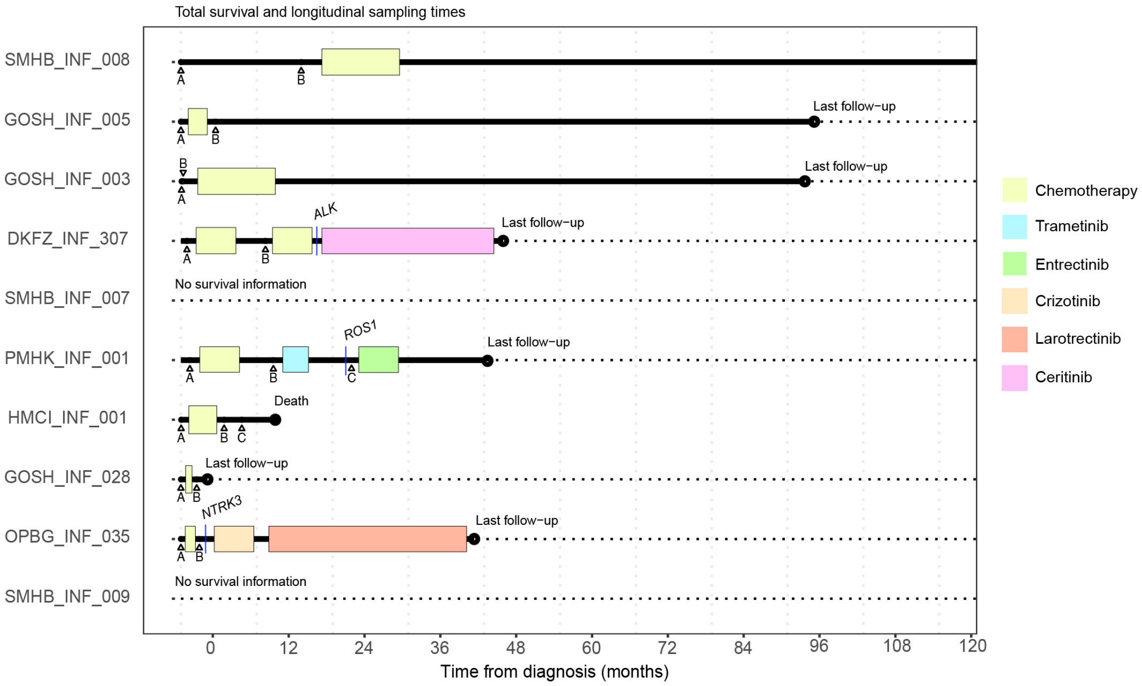

Figure 5-2. Longitudinal cohort sample timelines. Swimmers plots showing the timeline of when the different samples were taken for cases within the longitudinal cohort. The primary sample is labelled A, and subsequent samples are labelled B, C, and D where applicable. The last known follow-up is also labelled. Clinical information was not available for SMHB_INF_009.

5.2.2 Histological review

3/7 of longitudinal cases which classified as an IHG by the methylation classifier had an H&E slide available for histological review (GOSH_INF_003, GOSH_INF_005, HMCI_INF_001) (**figures 5-3, 5-4 & 5-5**). Architecturally, the paired samples showed consistent features of high cellularity and uniformity (**figure 5-3, 5-4A, 5-5A**).

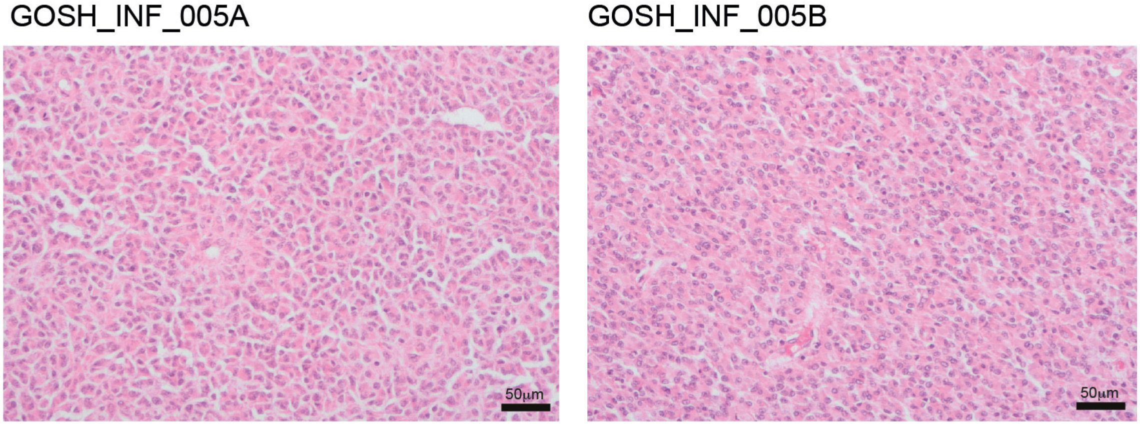

Figure 5-3. Representative H&E images of GOSH_INF_005A and B. Calibration bar in bottom right corner of image. Each image labelled with name of case.

However, cytologically differences were seen; GOSH_INF_003B showed an area where the stroma became loose with prominent spindled cells identified (**figure 5-4D**) which were very striking compared to the gemistocytic cells of the primary sample (**figure 5-4A**). Also, within this area, possible ganglion cell differentiation was observed (**figure 5-4C**) with focal areas of possible lymphocytic infiltration (**figure 5-4E**). Necrosis was present in both GOSH_INF_003A and B.

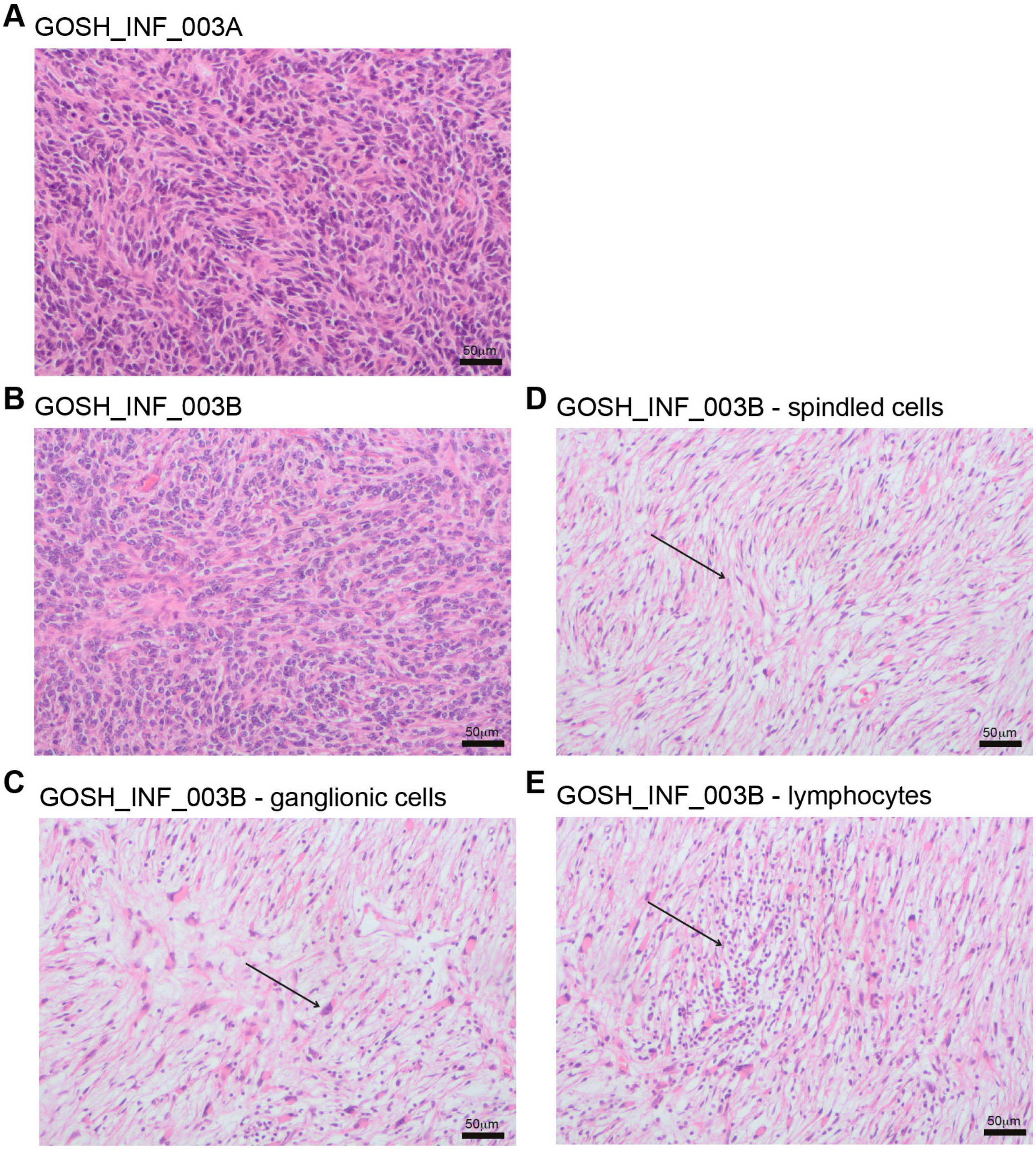

Figure 5-4. Histological review of IHG longitudinal cases. **A,** Representative H&E image of GOSH_INF_003A (primary resection). **B,** Representative image of GOSH_INF_003B (second resection). **C,** H&E image showing possible ganglionic cells in GOSH_INF_003B (black arrow). **D,** H&E image showing spindled cells (black arrow) in GOSH_INF_003B. **E,** H&E image showing possible lymphocytes (black arrow) in GOSH_INF_003B. Calibration bar in bottom right corner of image. Each image labelled with name of case and respective histological feature identified (where appropriate).

As mentioned above, the HMCI_INF_001A sample was not available for analysis. However, HMCI_INF_001B showed high cellularity, spindled cells, mitoses and mild-moderate pleomorphism, features consistent with an IHG, and also showed focal areas of xanthomatous change (also identified in one case in the first infant study) (**figure 5-4B**), and multinucleated giant cells (**figure 5-4C**). These giant cells appeared to be immune in origin, consistent with an inflammatory process rather than tumour giant cells. HMCI_INF_001C showed focal areas of haemosiderin consistent with previous bleeding (possibly as a result of previous surgery) (**figure 5-4D**), and focal areas of possible lymphocytic infiltration and calcification. Also, some of the cells appeared to be much larger than others (**figure 5-4E**).

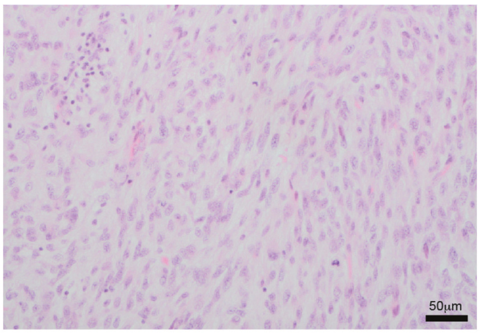
A HMCI_INF_001B

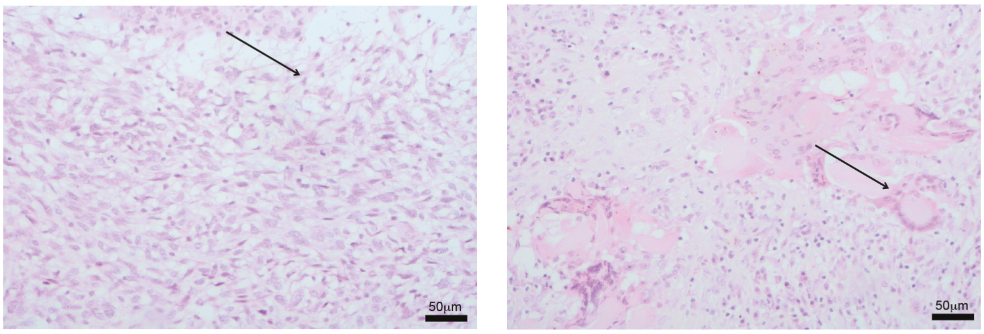
B HMCI_INF_001B - xanthomatous areas
C HMCI_INF_001B - giant cells

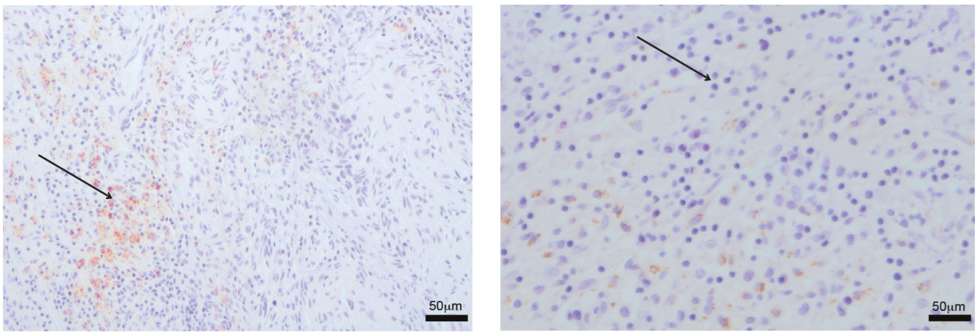
D HMCI_INF_001C
E HMCI_INF_001C - lymphocytes

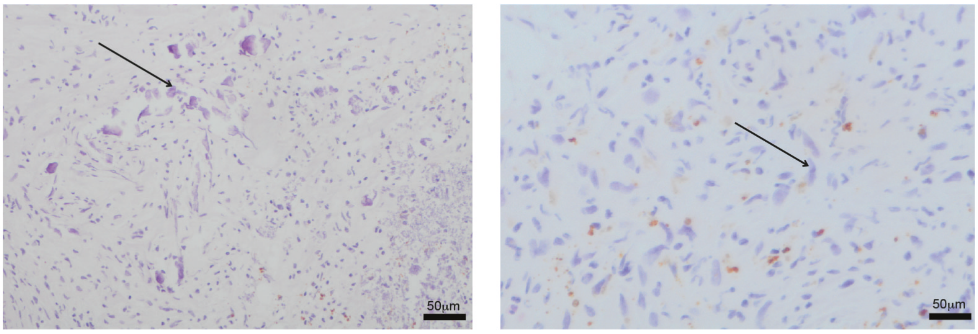
F HMCI_INF_001C - calcification
G HMCI_INF_001C - larger cells

Figure 5-5. Histological review of IHG longitudinal cases. **A,** Representative H&E image of HMCI_INF_001B (second sample). **B,** H&E image showing xanthomatous areas (black arrow) in HMCI_INF_001B. C, H&E image showing giant cells (black arrow) in HMCI_INF_001B. **D,** Representative H&E image of HMCI_INF_001C (third sample), black arrow indicating haemosiderin. **E,** H&E images showing possible lymphocytes (black arrow). **F,** H&E image showing calcification (black arrow). **G,** H&E image showing and larger cells (black arrow) identified in HMCI_INF_001C. Calibration bar in bottom right corner of image. Each image labelled with name of case and respective histological feature identified (where appropriate).

Histological review of the DIGG/DIA-like cases (SMHB_INF_007, SMHB_INF_008 and SMHB_INF_009) also showed some subtle differences (**figure 5-6**). SMHB_INF_009A showed a cellular tumour with cells containing a round to oval nucleus and prominent smalls vessels. SMHB_INF_009B, although only a very small sample, showed a much less cellular infiltrate with nuclei which were more spindled in shape (**figure 5-6C**). SMHB_INF_008A showed a cellular tumour with round to oval shaped nuclei infiltrated with small vessels. SMHB_INF_008B showed a very similar appearance with the addition of occasional multi-nucleated cells (**figure 5-6B**). The four samples of SMHB_INF_007 consistently showed a cellular tumour with focal areas of spindled cells and other areas where the nuclei were more rounded. Palisading necrosis was seen prominently in samples A and B, and mitoses were identified in samples A and C but otherwise there were no differences between them.

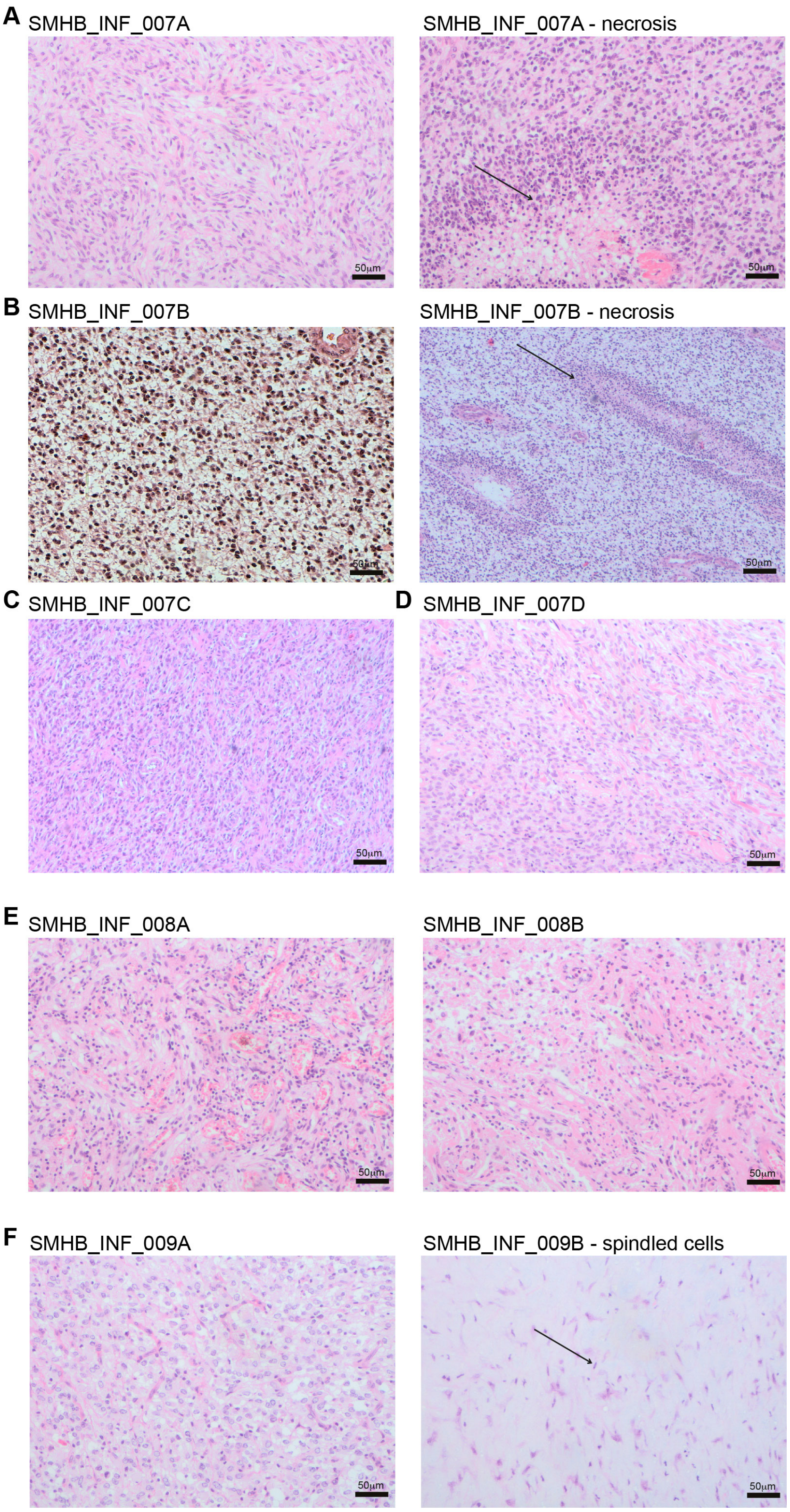

Figure 5-6. Histological review of non-IHG cases. **A,** Representative H&E images of SMHB_INF_007A, and necrosis is indicated by the black arrows). **B,** Representative H&E images of SMHB_INF_008A and B. **C,** Representative H&E image of SMHB_INF_007C. **D,** Representative H&E image of SMHB_INF_007D. **E,** Representative H&E images of SMHB_INF_008A. **F,** Representative SMHB_INF_009A and B. Spindled cells are indicated by the black arrow. Calibration bar present in the bottom right corner of each image.

5.2.3 Methylation profiling

The longitudinal samples were profiled using the methylation array to compare the profiles within each case, and between cases. To confirm that the samples from each case belonged to the same patient, we looked at 65 (450k) and 59 (EPIC) high-frequency, explicitly built in (labelled in the manifest and targeted) SNPs included in the array design by Illumina. These have been used in studies to cluster samples based on ethnicity (160). We clustered the longitudinal cases according to the beta values corresponding to these SNPs (**figure 5-7**). The paired tumour samples annotated as having been collected from the same patient were found to have concordant SNP profiles for all 10 cases within the cohort.

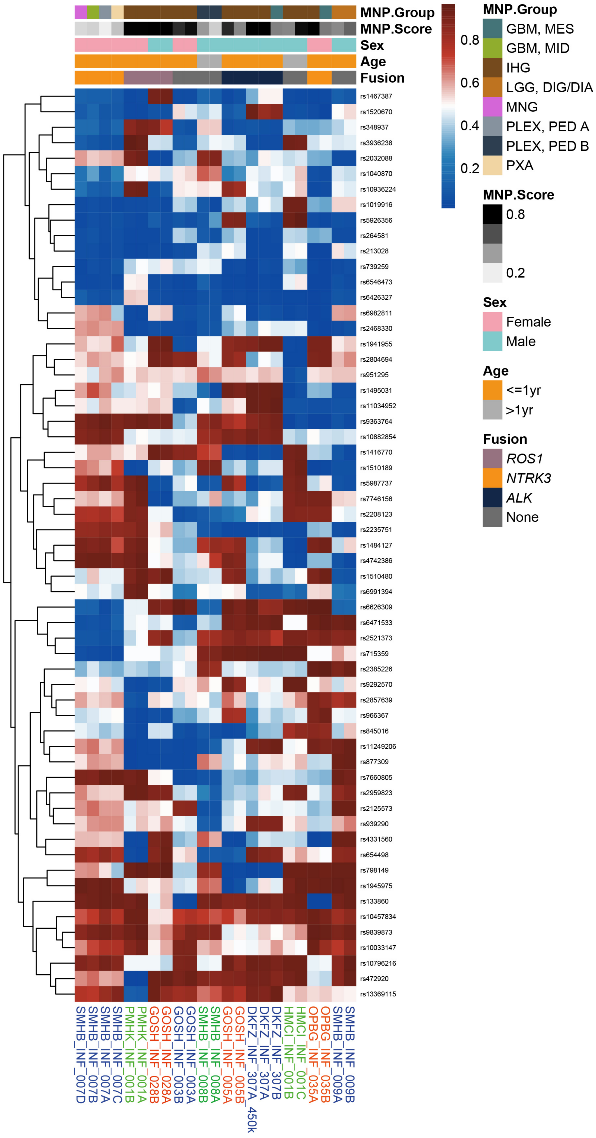

Figure 5-7. SNP heatmap. A heatmap showing the methylation profiles of the 22 cases within the cohort looking at 60 CpG sites (listed on the right hand side). A scale reflecting the beta values is provided (red; hypermethylated, blue hypomethylated). The methylation class, methylation score, sex, age and fusion positivity are labelled in bars at the top with keys to these shown.

The samples were then quality control checked by reviewing the level of bisulfite conversion for each sample. The SMHB_INF_007C sample showed a particularly high number of unconverted probes compared to all other samples in the cohort and was therefore excluded from further methylation analysis. Methylation profiling showed that 7/10 of the primary samples classified as IHG tumours (**figure 5-8**).

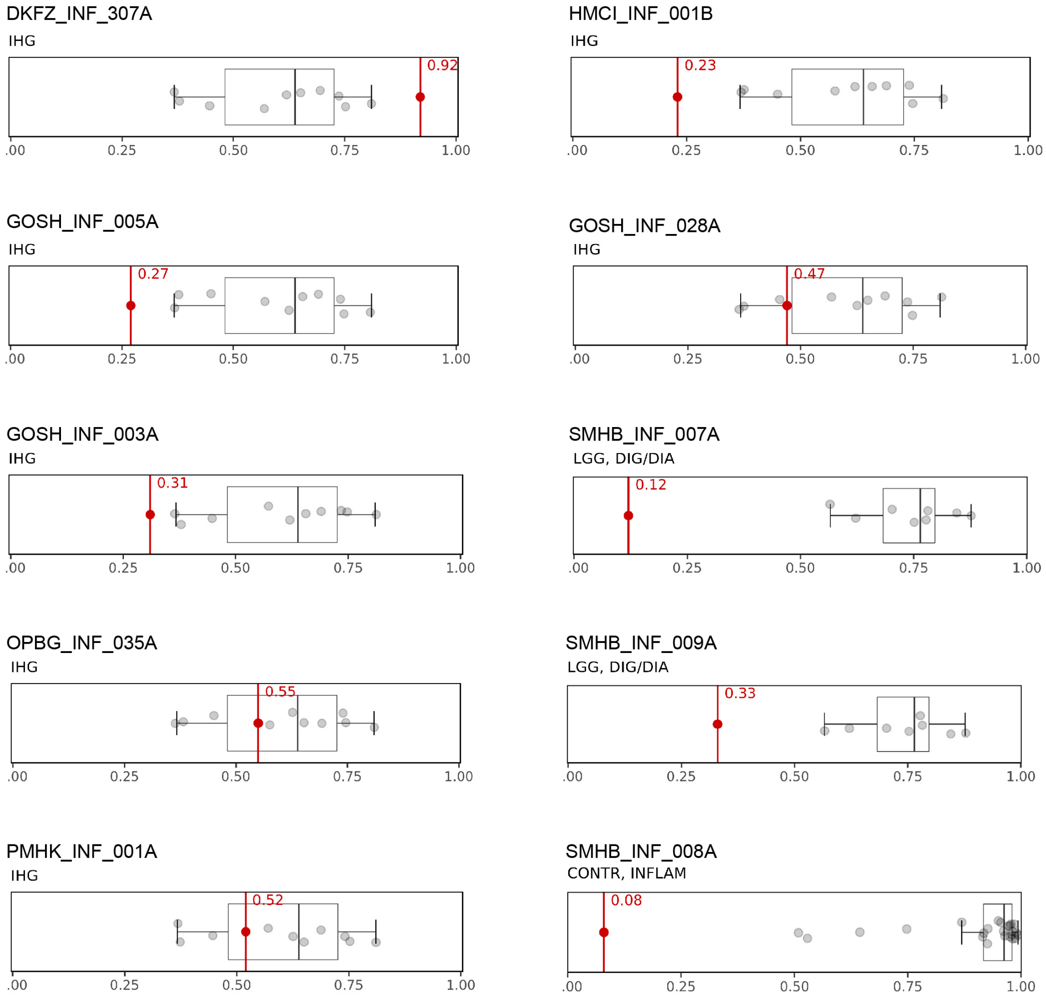

Figure 5-8. Boxplots of methylation classifier raw scores. Boxplots showing the methylation classifier raw scores for the initial samples for all cases in the longitudinal cohort. The raw score of each case is coloured red and labelled. The grey circles refer to the references cases shown as grey dots; the line within the box is the median, the lower and upper limits of the box represent the first and third quartiles, and the whiskers the interquartile range.

The remaining 3/10 cases could not be classified into any established entities; when projected onto the pan-glioma set t-SNE (including the infant intrinsic set cohort), they plotted either within the DIGG/DIA cluster or as a continuum between the IHG and DIGG/DIA groups; they were annotated as ‘DIGG/DIA-like’ tumours (**figure 5-9**).

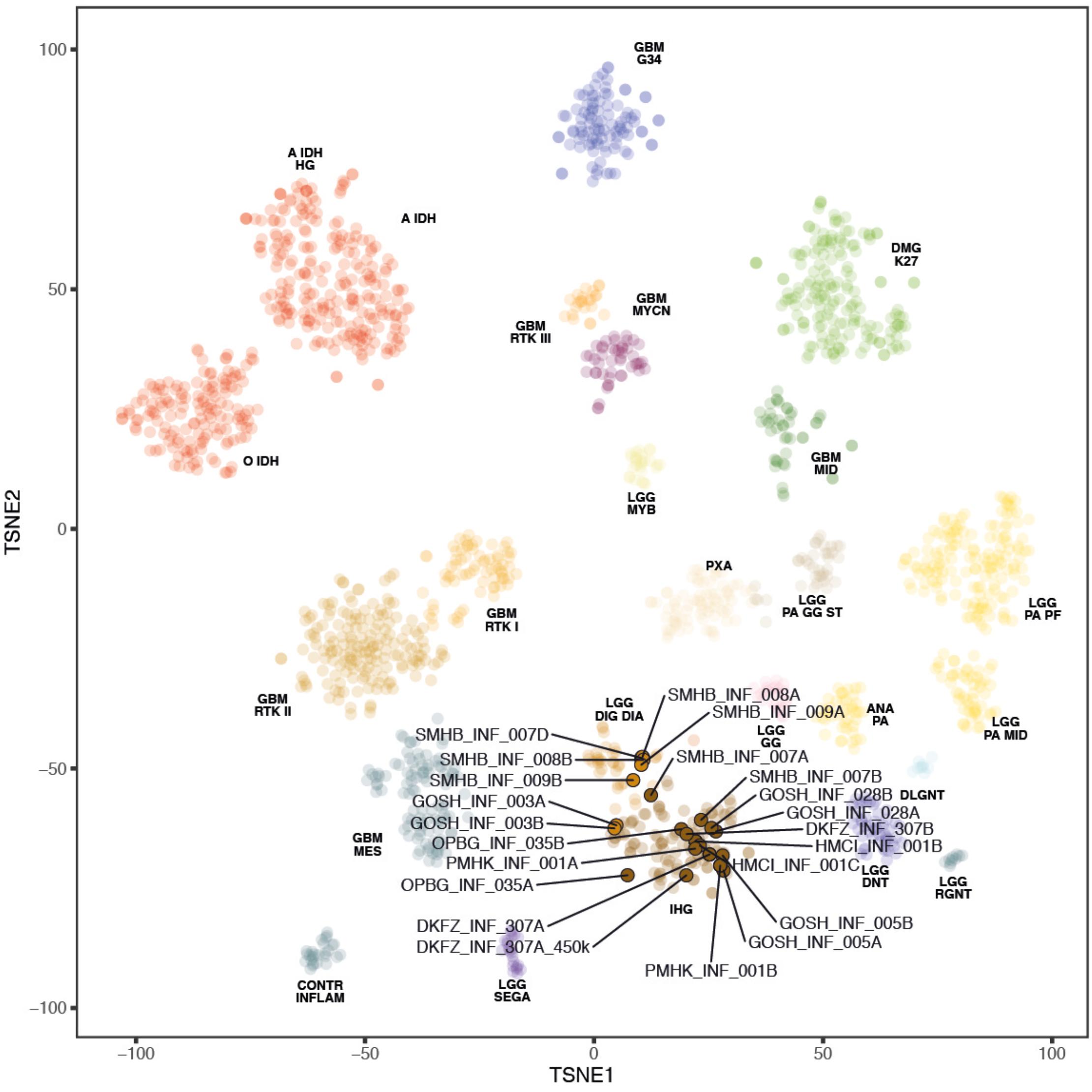

Figure 5-9. t-SNE projection of the longitudinal cohort. Longitudinal cases projected onto the pan-glioma reference set and infant intrinsic set. Longitudinal cases are in full colour, outlined with a black circle, and are labelled with the infant ID. The second t-SNE shows a magnified view of the longitudinal cohort projection, with each paired case joined by a line (grey).

When adding the paired samples, the IHG cases projected adjacent to each other within the same cluster. The longitudinal samples for 2/3 ‘DIGG/DIA-like’ showed similar findings with the samples projecting adjacent to each other on the t-SNE. However, SMHB_INF_007 showed some variation; all three samples were not in close proximity to each other with ‘A’ and ‘B’ positioned within the IHG cluster, and ‘D’ plotting in the DIGG/DIA cluster (**figure 5-10**).

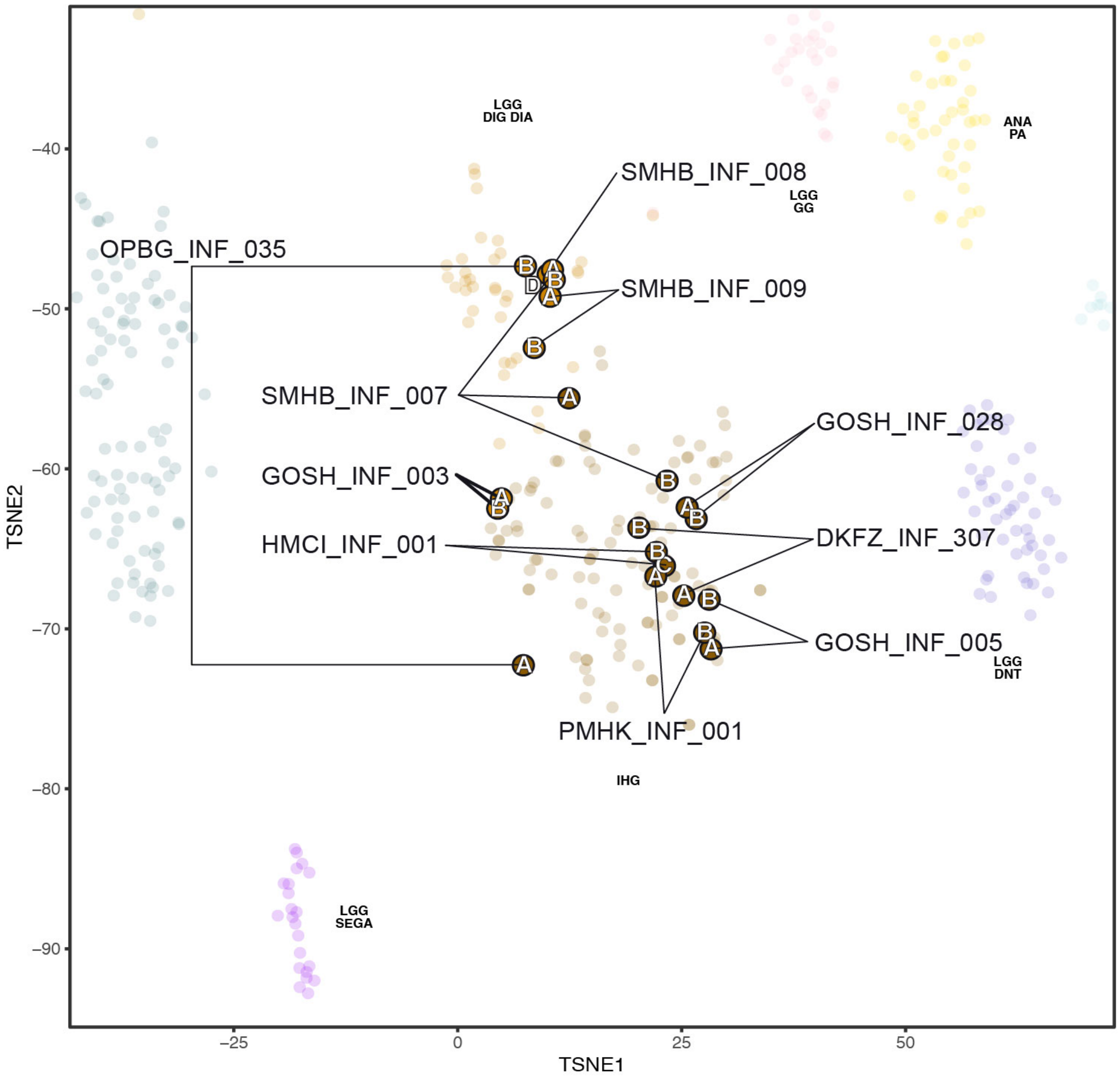

Figure 5-10. t-SNE projection of the longitudinal cohort. A magnified view of the longitudinal cohort projection is shown, with each paired case labelled A & B, or A-D, and linked to the case ID label with a solid black line.

5.2.4 Copy number analysis

Using the same methodology for the original infant cohort, copy number data was derived from the methylation data and processed using the R package conumee (**figure 5-11**). The copy number profiles for OPBG_INF_035A and B were excluded from this analysis as they did not pass QC due to considerable variation across the copy number profiles so changes within and between the samples could not be identified. However, despite SMHB_INF_007C being excluded from the methylation analysis by QC, it was included in the copy number analysis as it passed QC on this aspect.

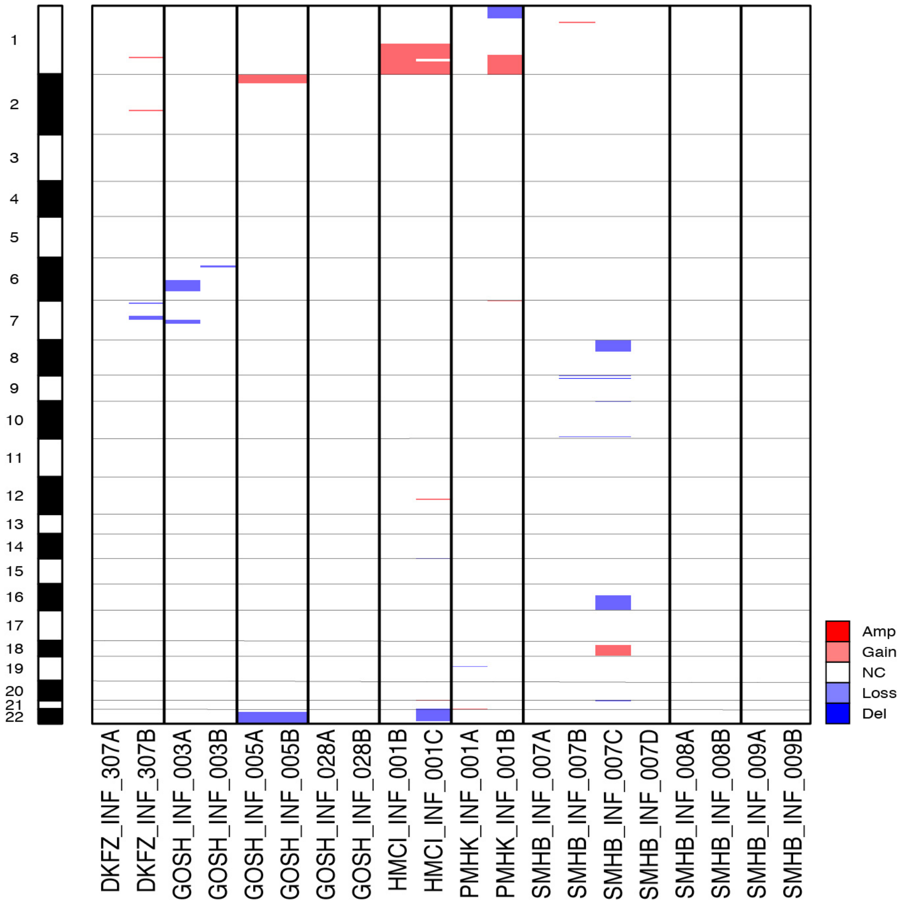

Figure 5-11. DNA copy number profiling of the longitudinal set. Heatmap representation of segmented DNA copy number for 20 longitudinal samples of infant glioma profiled on the Illumina 450kor EPIC BeadArray platform (dark red, amplification; red, gain; dark blue, deletion; blue, loss).

The analysis showed large scale copy number alterations in HMCI_INF_001, consistent across paired samples (1q gains) (**figure 5-12B**). A small gain (1q) and loss (1p) were seen in PMHK_INF_001B, changes which were not seen in the primary sample. HMCI_INF_001C acquired a loss on chromosome 22 which was not seen in HMCI_INF_001B, and DKFZ_INF_307B showed small gains on chromosome 1 and 2, and losses on chromosome 7 which were not observed in the primary sample. SMHB_INF_007 showed that the primary sample had a very flat profile but B and C showed very small losses on chromosomes 9 and 10. In addition, sample C also showed losses on chromosomes 8 and 16, and a gain on chromosome 18. However, sample D showed a flat profile similar to the primary sample (**figure 5-12C**). GOSH_INF_003A showed small gains on chromosome 6 and 7 which were not present in GOSH_INF_003B. GOSH_INF_028A and B, SMHB_INF_008A and B and SMHB_INF_009A and B showed consistently flat profiles.

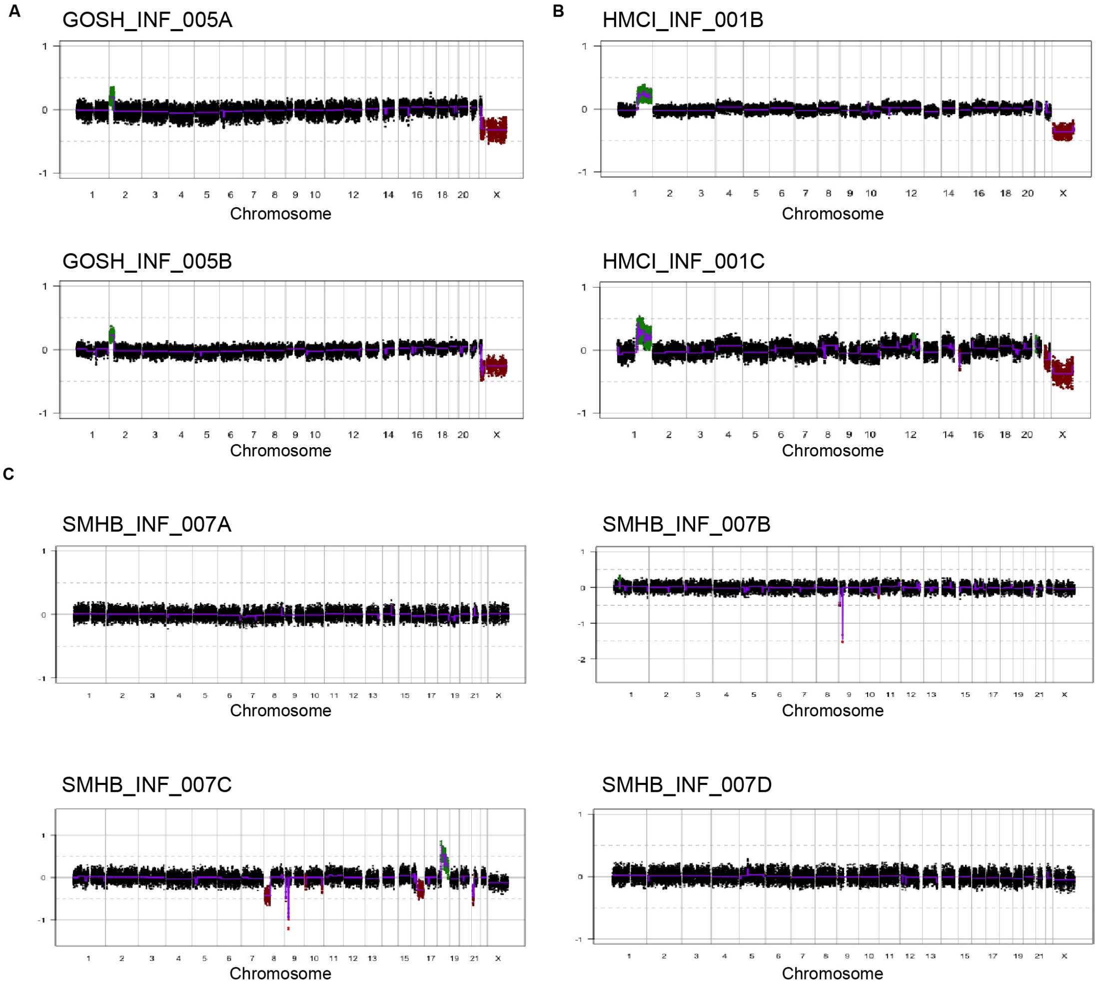

Figure 5-12. DNA copy number profiles. **A,** Copy number profiles of GOSH_INF_005A and B profiled on the Illumina 450kor EPIC BeadArray platform (red, amplification or gain; blue, deletion or loss). **B,** Copy number profiles of HMCI_INF_001B and C profiled on the Illumina 450kor EPIC BeadArray platform (red, amplification or gain; blue, deletion or loss). **C,** Copy number profiles of SMHB_INF_007A, B, C and D profiled on the Illumina 450kor EPIC BeadArray platform (red, amplification or gain; blue, deletion or loss).

Copy number profiles of GOSH_INF_005A and B showed changes consistent with the *SPECC1L:ALK* fusion (small gains on chromosome 2 associated with *ALK*, and losses on chromosome 22, associated with *SPECC1L* (**figure 5-12A**), as did DKFZ_INF_307 (consistent with the *MAD1L1:ALK* fusion (**figure 5-13**). PMHK_INF_001 (*ROS1*), GOSH_INF_028 (*ROS1*), and SMHB_INF_007 (*EML4:NTRK3*) (**figure 5-14**) were all copy neutral fusion-positive cases from the initial analysis of the primary samples, and this was further supported when comparing the profiles of the paired samples.

5.2.5 Sequencing

The longitudinal cohort cases (n=20) were sequenced with the DNA fusion panel (except DKFZ_INF_307A and B as material was not available). Fusions had already been identified in the primary samples of the following cases; DKFZ_INF_307 (*MAD1L1:ALK*) (**figure 5-13**), GOSH_INF_005 (*SPECC1L1:ALK*), SMHB_INF_007 (*EML4:NTRK3*), and OPBG_INF_035 (*ETV6:NTRK3*).

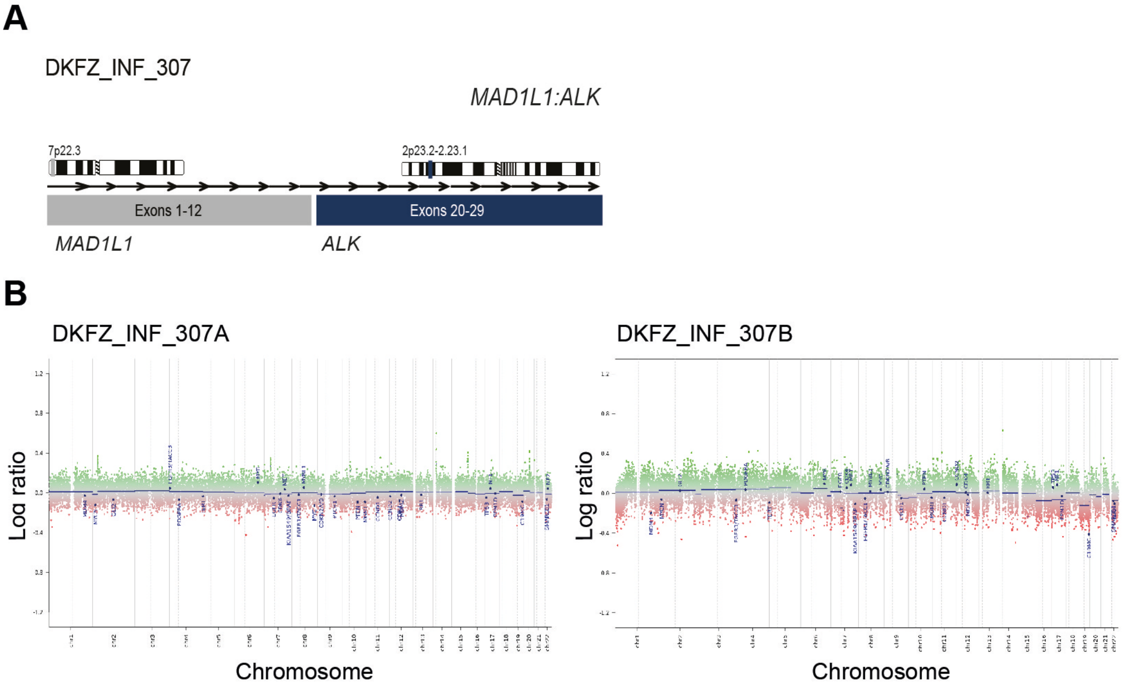

Figure 5-13. RTK fusions in longitudinal samples; DKFZ_INF_307. **A,** Schematic cartoon representation of *MADL1L:ALK* fusion identified in DKFZ_INF_307A and B. **B,** Copy number profiles of DKFZ_INF_307A and B derived from methylation array data. Red, loss or deletion; green, gain or amplification.

The fusion panel and FISH (performed by Anna Burford) confirmed that the *EML4:NTRK3* fusion was present in all four SMHB_INF_007 samples (**figure 5-14**).

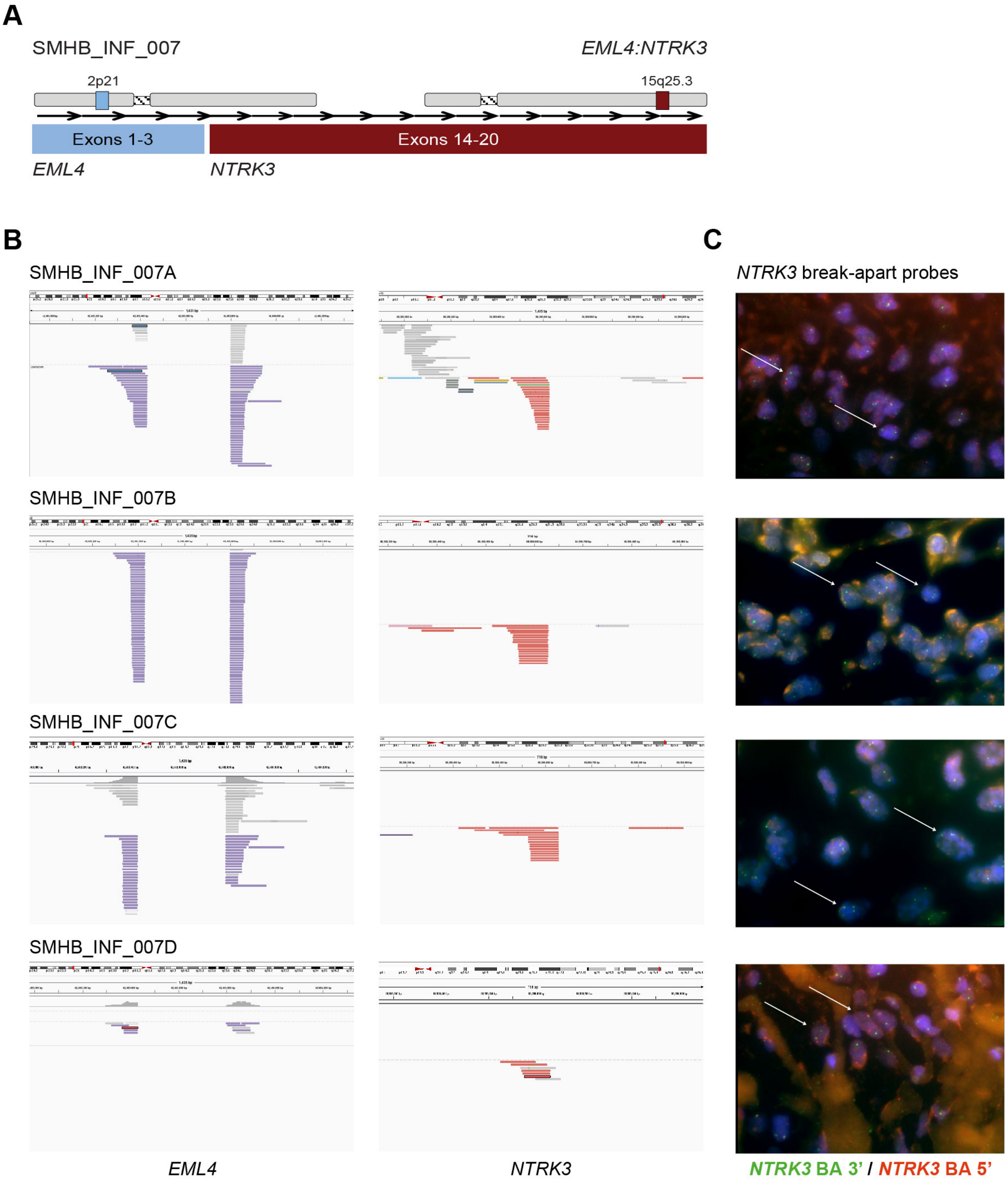

Figure 5-14. SMHB_INF_007 longitudinal case. **A,** Schematic cartoon representation of the *EML4:NTRK3* fusion identified across all four longitudinal samples of SMHB_INF_007. **B,** Images from Integrative Genomics Viewer (IGV) of the *EML4:NTRK3* fusion identified in each case via the DNA fusion panel (purple reads, *EML4*; red reads, *NTRK3*). **C,** Fluorescence in situ hybridisation (FISH) using an *NTRK3* break-apart probe for FFPE sections across the longitudinal samples. The white arrows are pointing to cells which are fusion-positive. *NTRK3* BA 3' (green), *NTRK3* BA 5' (red).

In addition, the fusion panel confirmed the *SPECC1L:ALK* fusion in GOSH_INF_005B B (**figure 5-15A-D**), and the *ETV6:NTRK3* in OPBG_INF_035 (**figure 5-16**).

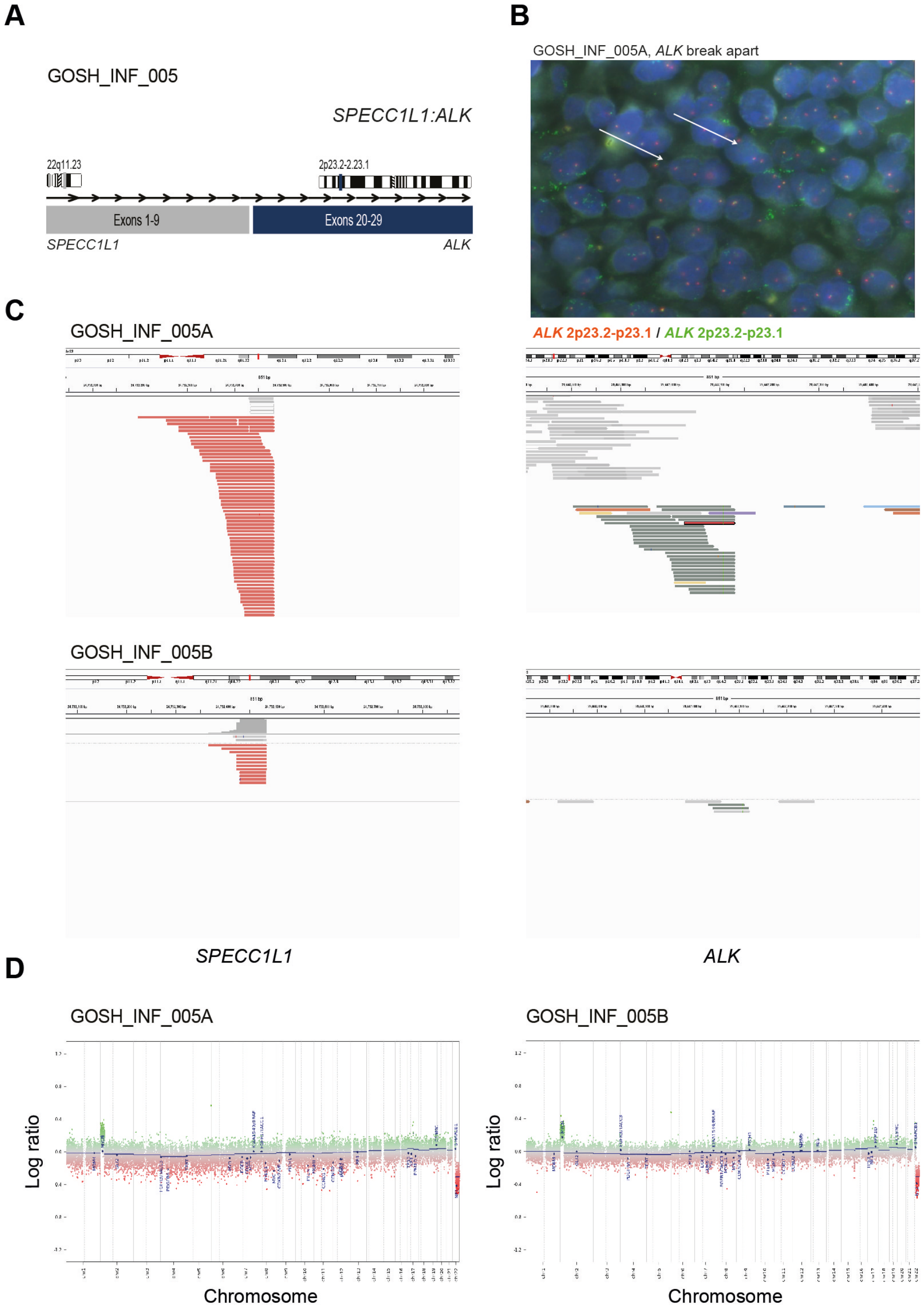

Figure 5-15. RTK fusions in longitudinal samples. **A,** Schematic cartoon representation of the *SPECC1L1:ALK* fusion identified in GOSH_INF_005A and B. **B,** Fluorescence in situ hybridisation (FISH) using an *ALK* break apart probe performed on an FFPE section of GOSH_INF_005A. The white arrows indicate fusion-positive cells. *ALK* BA 2p23.2-p23.1 (red), *ALK* 2p23.2-p23.1 (green). **C,** Integrative Genomics Viewer (IGV) snapshots showing the *SPECC1L1:ALK* fusion identified in GOSH_INF_005A and B via the DNA fusion panel. Red, SPECC1L1; grey, *ALK*. **D,** Copy number profiles of GOSH_INF_005A and B derived from methylation array data. Red, loss or deletion; green, gain or amplification.

SMHB_INF_008A and B, SMHB_INF_009A and B, GOSH_INF_003A and B, HMCI_INF_001B and C and GOSH_INF_028A and B were also sequenced via the fusion panel but they were fusion-negative.

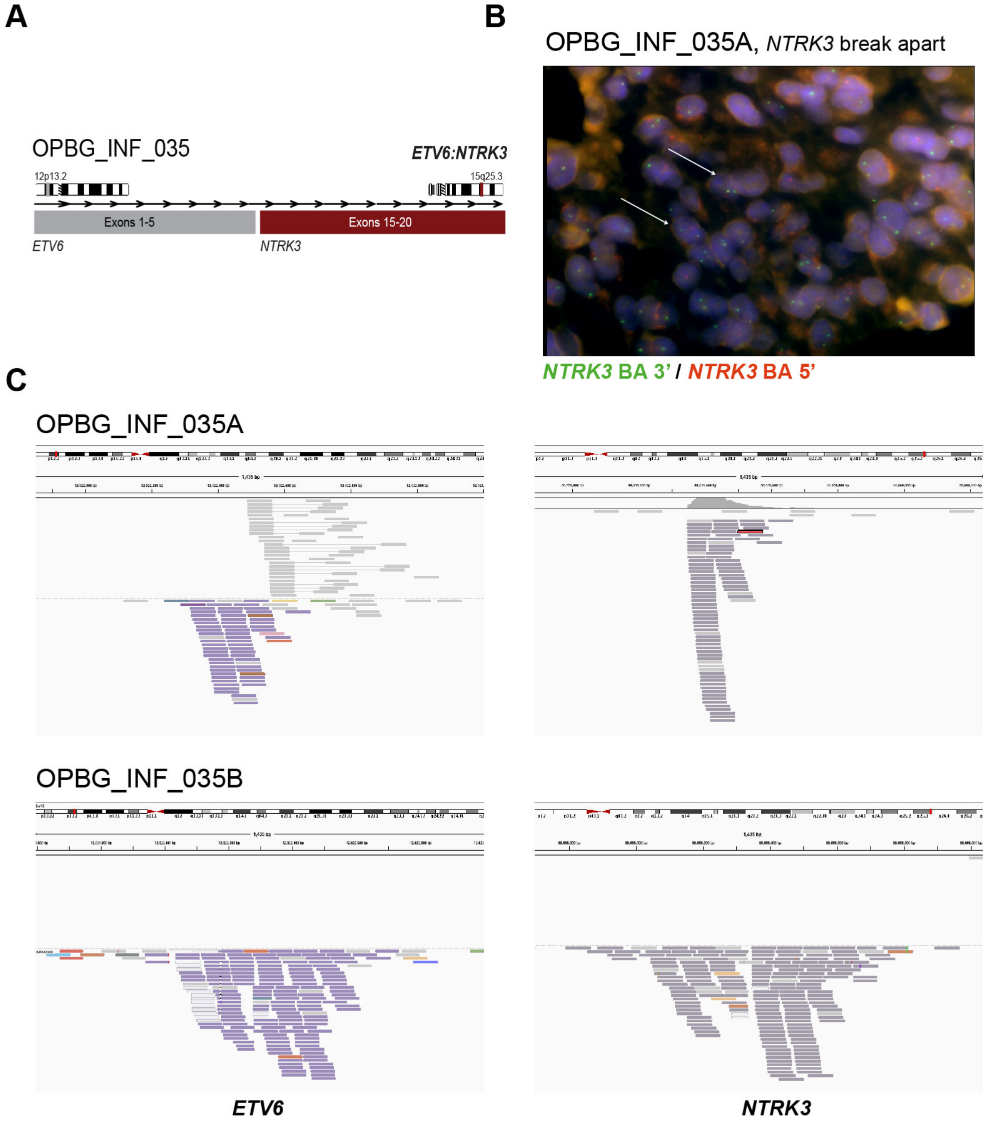

Figure 5-16. OPBG_INF_035 longitudinal case. **A,** Schematic cartoon representation of the *ETV6:NTRK3* fusion identified in this case. **B,** Fluorescence in situ hybridisation (FISH) using an *NTRK3* break apart probe on a FFPE slide of OBPG_INF_035A. The white arrow indicates fusion-positive cells. **C,** Integrative Genomics Viewer (IGV) snapshots for the DNA fusion panel sequencing for OPBG_INF_035A and B. (Purple reads, *ETV6*; grey reads, *NTRK3*).

However, the GOSH_INF_028 samples underwent WGS and a *HNRNPD:ROS1* fusion (*ROS1* was not included in the fusion panel design) was identified in both samples, and also a *ROS1* fusion in PMHK_INF_001A; RNA sequencing performed by the referring institution confirmed the *ROS1* fusion in PMHK_INF_001B. Only the *SPECC1L:ALK* and *MAD1L1:ALK* fusions were associated with small copy number changes.

All 22 samples underwent either WGS (n=6) or WES (n=16) to determine whether acquired mutations could be identified over time – a major caveat is the lack of germline DNA for somatic subtraction in all cases.

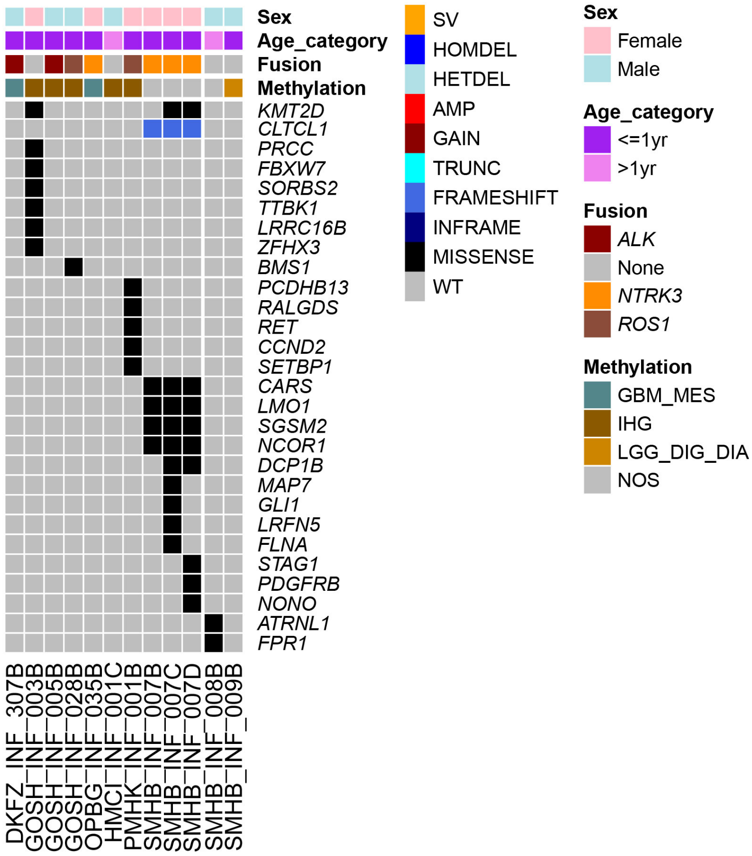

Figure 5-17. Oncoprint of somatic mutations. An oncoprint of the somatic mutations identified through WES, WGS and HGG panel sequencing of the longitudinal cohort (the type of mutation is indicated by the key provided. The gender, age, methylation group and fusion type are labelled in bars at the top, with reference to the keys provided.

The cases were filtered for known pHGG, COSMIC and census coding variants (although it cannot be ruled out that these may be germline SNPs). 62% of variants were consistently identified across sample pairs including *KMT2D* in DKFZ_INF_307, *TTF1* in GOSH_INF_005, *FGFR4* in HMCI_INF_001 and *ARID1A* in SMHB_INF_008. A subtraction was then performed whereby the diagnostic sample was used as the reference (**figure 5-17**). Variants identified in the secondary sample(s) which were not detected in the primary included *KMT2D* in SMHB_INF_007C and D, *ZFHX3, LRRC16B, TTBK1, SORBS2, FBXW7,* and *PRCC* in GOSH_INF_003B, *CLTCL1, CARS, LMO1, SGSM2*, and *NCOR1* in SMHB_INF_007B, C and D, *MAP7, GLI1, LRFN5,* and *FLNA* in SMHB_INF_007C and D, with *STAG1, PDGFRB* and *NONO* present in SMHB_INF_007D only. Three cases contained variants in *KMT2D* (DKFZ_INF_307, GOSH_INF_003 and SMHB_INF_007) but there were no variants identified which were common to all longitudinal samples. Also, there was a distinct absence of the mutations frequently associated with pHGG including *H3F3A, HIST1H3B, ACVR1, TP53, NF1, PDGFRA, PIK3CA* and *IDH1* mutations.

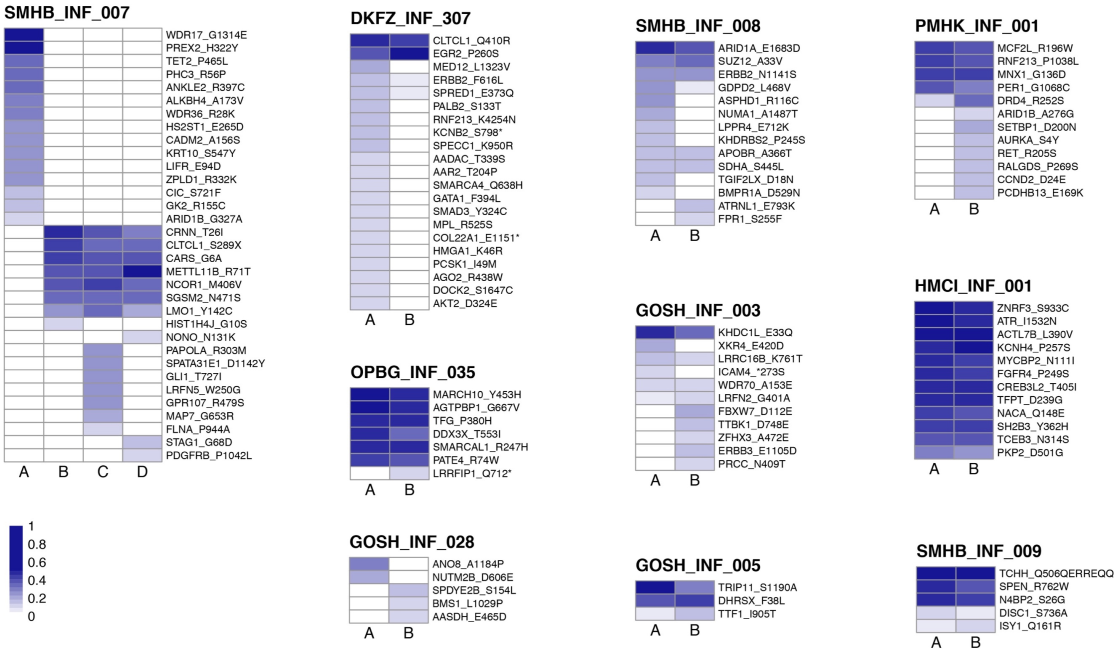

Figure 5-18. Allelic depth of somatic mutations. Oncoprints for cases where differences in the allelic depth of SNPs and known mutations between the initial and secondary samples were identified across the longitudinal cohort. Scale for levels of shading provided.

In the absence of a germline subtraction, I wanted to determine whether certain variants identified in both samples may be selected for, or against, over time and in response to treatment, suggestive that they may indeed be somatic. To see if these variants were expanding in secondary samples, the allelic depth of all coding variants identified was then compared between paired samples (**figure 5-18 & 5-19**). 9/10 cases showed an increased allelic depth of variants in the secondary sample(s) including *EGR2* in DKFZ_INF_307, *METTL11B, NONO, STAG1* and *PDGFRB* in SMHB_INF_007, *ARID1B, SETBP1, AURKA, RET, CCCND2* and *PCDH1B* in PMHK_INF_001 (**figure 5-19B**), *AASDH, BMS1* and *SPDYE2B* in GOSH_INF_028B and *SUZ12, ERBB2, ATRNL1, SDHAA* and *FPRN* in SMHB_INF_008. Whilst 71 variants across all 10 cases showed a decreased allelic depth across the paired samples including *ERBB2* and *GDPG2* in SMHB_INF_008, *TRIP11* in GOSH_INF_005 and *MCF2L, RNF213,* and *PER1* in PMHK_INF_001 (**figure 5-19B**).

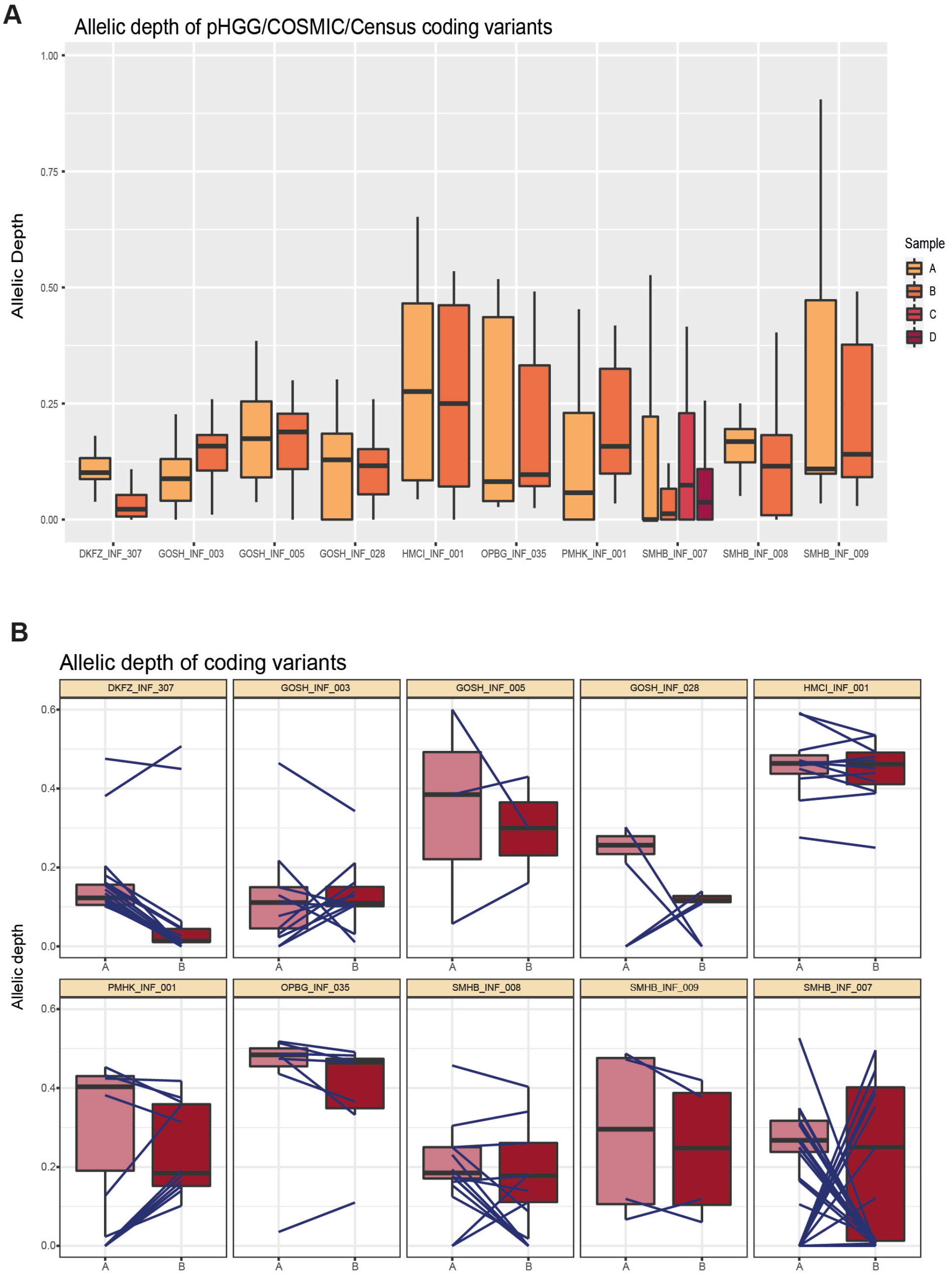

Figure 5-19. Allelic depth. **A,** Box plots of allelic depth of pHGG/COSMIC/Census coding variants shown for each of the samples in the longitudinal cohort. The different samples are coloured according to the key provided. The line within the box is the median, the lower and upper limits of the box represent the first and third quartiles, and the whiskers the interquartile range. **B,** Pair-plots for showing the differences in allelic depth between paired samples for particular coding variants identified. The line within the box is the median, the lower and upper limits of the box represent the first and third quartiles, and the whiskers the interquartile range. The first sample is labelled 'A' and the second 'B'. The lines connecting the two samples represent the allelic depths of particular genes highlighting the difference between the two samples.

5.3 Discussion

Infant HGG cases are very rare; longitudinal samples of these tumours are therefore scarce but potentially provide a valuable insight into their evolution. Although only 10 cases with paired samples were gathered within our cohort, they showed some important results. The histological review of the recurrent IHG cases revealed some subtle cytological differences compared to the primary samples with a change in cell morphology to spindle shaped, a loose stroma and ganglion cell differentiation observed; in this particular case, the child remains alive 8 years post diagnosis. Case reports and studies show similar features in recurrences of infant HGG with evidence of differentiation and reduced proliferative activity seen in published longitudinal samples (9,161). The presence of multinucleated giant cells in one case is consistent with chronic inflammation; given the previous surgery this may be linked, but also may show an important accessibility of the immune system in these cases particularly given the prominence of possible lymphocytes seen focally. Further panels of immunohistochemistry may be useful.

When analysing the neoantigen ratios in adult cases, the observed-to-expected ratio strongly correlates with the initial and recurrent tumours of each patient; the neoantigen depletion level in the recurrence sample is reflective of the initial tumour with no consistent evidence of immunoediting deduced (47). Higher levels of CD4+ T cells are seen in primary tumours with observed-to-expected neoantigen levels >1, whereas higher levels of macrophages and neutrophils were seen in the recurrent tumours with a ratio of <1 (47). Mutation status, treatment, and neoantigen ratios of glioma influence the immunological tumour microenvironment, and monitoring changes in this microenvironment using re-biopsy may therefore be useful to predict prognosis going forward.

The use of methyl CIBERSORT in glioma research has utilised a more robust approach to analysing the immune profile of a tumour; the more traditional methods of using panels of IHC and flow cytometry have significant limitations in that they can miss immune populations and do not identify functional phenotypes such as resting or active lymphocytes (162). CIBERSORT can analyse both expression data and methylation data derived from bulk tumour samples against a validated signature matrix; this is then used to define different immune cell fractions within a tumour (162). It has been recently used to develop a reference signature that defines different non-cancer cell types which then can be used to estimate the infiltrations of these cells in CNS tumour cohorts (163). Using CIBERSORT to analyse the methylation array data of both the primary and longitudinal cohort would be useful to further explore the levels and differences in immune cell infiltration and the role of the immune system in these tumours.

In general, the methylation profiles remained stable with longitudinal samples clustering adjacent to the primary sample. The longitudinal samples of one case (SMHB_INF_007) did not cluster as well; however they also showed reduced levels of bisulfite conversion (seen across all samples from the SMHB referral centre, possibly related to storage) compared to the other samples which may account for this observed difference.

Longitudinal studies of methylation profiles have shown differences which can be used to predict behaviours and outcome; a comparison of the DNA methylation profiles of 77 patients (200 samples) diagnosed with diffuse glioma found that *IDH* wildtype and *IDH* mutant 1p-19q co-deleted glioma cases retained their epigenetic profiles across longitudinal sampling. However, *IDH* mutant non-co-deleted gliomas showed epigenetic shifts across recurrence; the *IDH* mutant tumours more frequently display the CpG island methylator phenotype (G-CIMP), which can be further divided into G-CIMP-high and G-CIMP low (164). A subset of *IDH* mutant LGG G-CIMP-high tumours retain their DNA methylation phenotype when they relapsed. However, a small proportion of *IDH* mutant LGG G-CIMP-high tumours undergo disease progression but showed G-CIMP-low epimethyl phenotypes in the recurrent samples. By profiling the hypomethylated CpG sites associated with recurrence for each case, this data could be used to predict which tumours are likely to recur (164).

The initial phase of this study highlighted the presence of RTK fusions *(ALK/ROS1/MET/NTRK)* characterising the tumours within the intrinsic set, with evidence supporting these as the driving alteration in the absence of other background mutations. 6/10 cases in the longitudinal cohort were positive for RTK fusions (*ROS1* (n=2), *ALK* (n=2), *NTRK3* (n=2)); these fusions were retained across the paired longitudinal samples. This has also been shown in longitudinal liquid biopsy sampling in *NTRK* fusion-positive colorectal carcinoma; longitudinal sampling of ctDNA in a patient with *LMNA:NTRK1* positive tumour confirmed the fusion via ddPCR in each of the samples, tracked the number of copies of the fusion (correlated with treatment), as well as identifying potential resistance mutations in *NTRK1* (165). *NTRK* fusions are also reported in longitudinal studies of metastatic cutaneous malignant melanoma; a small study identified *NTRK1* and *NTRK2* fusions in the metastatic lesions by sequencing, and confirmed that the cutaneous primaries were also positive for the fusion via immunohistochemistry (166). In our previous study of a recurrent astroblastoma in a 6 year old girl, the characteristic *MN1:BEND2* fusion was detected in all 11 samples indicating that this was an early clonal event driving the pathogenesis of the tumour (167). A doubling of the genome was found in later samples, as well as variants in genes involved in NF-KB signalling and evidence of pathway activation suggesting a possible role in progression (167), also suggesting that re-biopsy has an important role in tumour monitoring.

Re-biopsy of progressive lesions is important to check for the presence of fusions and for monitoring the molecular profile of a tumour; a *GCC2:ALK* fusion was identified in a primary lung adenocarcinoma which was subsequently treated with crizotinib achieving 18 months of progression free survival (the fusion was not detected in liquid biopsies during this time). However, a new lung lesion was biopsied and the fusion was confirmed which lead to treatment with ceritinib achieving a partial response at last follow up (168). A study of 16 patients with primary and recurrent pHGG showed that the methylation subgroup is maintained at recurrence, and that histone mutant tumours retain their histone mutation in longitudinal sampling, with *ACVR1* and *TP53* mutations also conserved throughout tumour progression (169). However, mutations in *PDGFRA, PIK3R3, ERBB2*, and *EGFR* are often found in recurrence samples of pHGG but not in the primary sample, particularly associated with histone and *IDH1* wild type tumours, with a trend towards an increased mutational burden at recurrence (169).

Our cohort also showed some examples of evolving copy number changes within samples; new changes identified in SMHB_INF_007B and C were absent in D. This may reflect heterogeneity of the tumour and illustrate the variation seen as a result of tumour sampling. Some recurrent pHGG tumour samples show an increased number of allelic imbalance regions, and others show genome wide loss of heterozygosity events resulting in a copy neutral genome, a finding compatible with radiotherapy induced changes (169). Copy number changes can be associated with progression, and can vary according to the location of sampling; the astroblastoma case featured some samples with a flat profile and others (from a different phylogenetic branch) showing whole arm copy number gains (167).

Sequencing did identify differences in the presence and allelic depth of coding variants between paired samples. However, we did not identify any recurrent variants (excluding RTK fusions) or any of the well-recognised mutations known to occur in pHGG including *H3F3A, HIST1H3B, ACVR1, TP53* and *PIK3CA*. Studies have shown that mutational burden tends to increase at recurrence in 70% of cases of adult gliomas. Shared fractions of mutations are also comparable between different subtypes of glioma, and also associated with the age at diagnosis (47). Our own study showed the acquisition of *PTEN, NF1, TP53* and *PIK3CA* mutations in two cases of non-infantile paediatric HGG cases (156). Driving alterations were also maintained and not acquired across sample pairs, particularly in *IDH1* mutant co-deleted 1p/19q cases (47), but differences in the number of cells containing particular events may change, particularly if an event is linked to clonal expansion, although significant consistent differences are not seen when comparing the initial and recurrent tumours (47). However, consideration should be given to the time frame when secondary surgery was undertaken in the infant cases; two cases were biopsied and then underwent resections following chemotherapy 3 – 6 months later; the resection was therefore likely of the residual original tumour, albeit post-treatment. Three had gross total resections, and two of these were treated with chemotherapy before a second resection 11 – 24 months later and therefore can be considered to be genuine recurrences. Two cases underwent a subtotal resection followed by adjuvant chemotherapy before the second resection, so again are not strictly recurrences but regarded as progressive tumours. However one case underwent a subtotal resection and then 1 week later underwent second-look surgery (without chemotherapy) where sample B was taken (GOSH_INF_003). Therefore, the re-resection was of the original tumour over a very short time period and not a relapse; new mutations would not be expected, other than possible differences related to tumour heterogeneity. However, when looking at new coding variants, 6 were identified in sample B that were not present in sample A, and the allelic depth of the variants identified in this case also show increasing levels. The histology of sample B also showed some striking changes not identified in sample A. This hints that changes can happen very quickly in these tumours, not influenced by chemotherapy, or are related to sampling and heterogeneity of the tumour.

CHAPTER 6 – Infant glioma modelling

6.1 Introduction

Models of paediatric HGG are required to help understand many of the features of these tumours including their growth, invasion and their response to treatment in the context of their phenotypic and molecular features. Patient-derived models (*in vitro* and *in vivo*) are potentially useful tools for preclinical studies of paediatric HGG due to their retention of the molecular characteristics of the original tumour (170). The models require careful classification and characterisation to better understand the underlying biology and provide a resource for the development of novel therapeutic approaches (171). Treating clinicians can also derive valuable information to help shape patient management plans in real-time (170,172). However, given the poor prognosis of paediatric HGG, the time taken to establish these models and properly characterise them, this can be a very challenging aim to achieve for individual cases, although the data derived can be used to shape drug development programmes and develop clinical trials thereby improving the knowledge and outcome for the disease in general (171).

Despite these clear benefits, sufficient progress has been hindered by several factors including a lack of available material from which to derive these models (171). Acquiring patient-derived samples requires excellent engagement with clinical colleagues through multi-disciplinary team (MDT) meetings where new and existing patients are discussed and treatment strategies planned. Research teams can attend theatre to collect a sample of tumour and blood at the time of surgery. Viable tumour cells can be grown as either 2D (adherent culture) or 3D (neurospheres, non-adherent), with the aim of mimicking the *in vivo* tumour features (173). The ability to establish a cell culture is dependent on the characteristics of the tumour; they grow at different rates, not always in both conditions, and can require culture-specific modifications to the media to optimise their growth (170,173).

Formerly, cell line models were grown as monolayer cultures in serum-containing media. The first molecular characterisation of paediatric HGG cell line models (KNS42, SF188, and UW479) was published in 2009; the high turnover, and ability to proliferate indefinitely (through dysregulation of the RB1, p53 and RTK/AKT/PI3K pathways) provided useful models upon which to experiment, with KNS42 representing the first H3.3 G34V histone mutant *in vitro* model (171). Subsequently, the use of short-term cultures was developed using serum-free media (to avoid the media containing undefined components which may impact on growth etc) allowing the generation of many models across different HGG types; these models more closely mimic the clinical disease as they retain the genetic characteristics and can be obtained from biopsy or resection specimens (170). Tissue derived from post-treatment biopsies/resections or at progression, and the use of rapid autopsy, have created models which provide data about the evolutionary trajectory of tumours from diagnosis, through treatment to end-stage across different tumour types (47).

Different methods exist to engineer both *in vitro* and *in vivo* models with the purpose of exploring functional aspects of driver events and their therapeutic potential. Existing studies have successfully modelled gene fusions using combined approaches, including using CRISPR-Cas9 and homology-directed repair to model *EWSR1:WT1* fusions (characteristic of the rare paediatric sarcoma, desmoplastic small round cell tumour) in human mesenchymal cells (174). The approach uses a donor template which contains a selectable marker (puromycin resistance gene driven by a PGK marker), flanked by short segments representing homology arms derived from the translocating loci of *EWSR1* and *WT1* (174). Viral mediated delivery of the CRISPR-Cas9 system has also been successfully used to model fusions; guide RNAs that target the *EML4* and *ALK* loci and Cas9 are transferred into an adenoviral vector which efficiently infect the lung epithelium of adult mice by intratracheal instillation. One month after infection, the lungs showed small lesions and by 6-8 weeks larger tumours were visible, histologically consistent with NSCLC. Complete or partial regression was also demonstrated in response to treatment with crizotinib for two weeks (175). Designing and engineering models of fusions seen in infant HGG, and increasing the number of patient-derived infant HGG cultures are therefore priorities to better understand the biology of the novel subgroups, and both therapeutic and resistance mechanisms.

6.2 Results

6.2.1 Establishment of primary-patient derived *in vitro* cultures

For several cases included in my molecular study, we were able to establish patient-derived models. The clinical details of these cases will be discussed in chapter 7. QCTB_INF_R077 was acquired from collaborators at Queensland Children’s Tumour Bank contained an *ETV6:NTRK3* fusion (identified by RNA sequencing and FISH). In my hands, the cells grew as an adherent culture on laminin but did not grow in 3D as neurospheres. Phenotypically, they were elongated with processes extending from the cell body towards neighbouring cells but there was insufficient cell density to reach confluency in a T25 flask over several months. The addition of ROCK inhibitor to the media had no noticeable effect, and changing the growth substrate to fibronectin resulted in good initial cell adherence but detachment after two days (n=2). A mix of both laminin and fibronectin (1:1) resulted in an adherent culture; cells were passaged into T25 flasks and were dependent on high densities of cells for continued growth. Neurotrophin 3 (NT3, the ligand for the TRK C receptor) was added to the media and the concentration of all other growth factors were doubled allowing the growth of sufficient cells to allow limited assays (**figure 6-1A**).

QCTB_INF_R102 was a cryopreserved sample also provided by Queensland Children’s Tumour Bank; a *TPM3:NTRK1* fusion was identified via the fusion panel using DNA extracted from frozen tissue. The cells were grown in 2D (they did not grow in 3D) using the laminin-fibronectin substrate, with the addition of nerve growth factor (NGF, ligand for TRK A receptor) to the media; with these modifications the cell density was sufficient to allow limited assays (**figure 6-1B**).

A

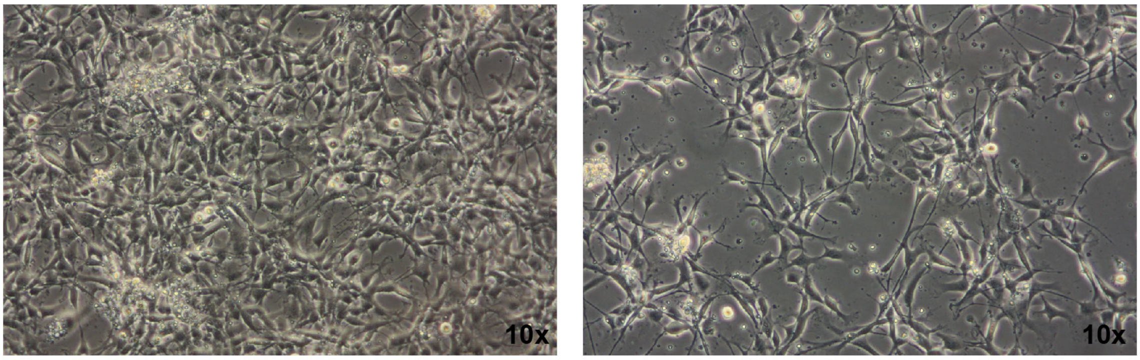

QCTB_INF_R077 (adherent, passage 5)

B

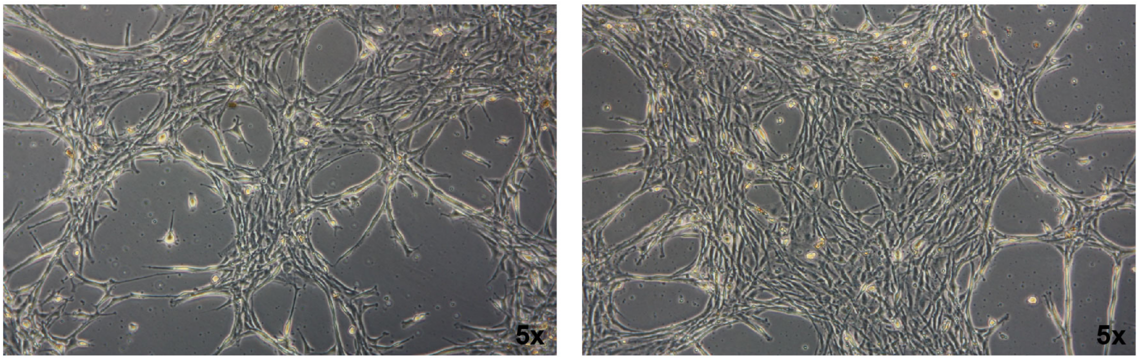

QCTB_INF_R102 (adherent, passage 4)

Figure 6-1. Infant glioma cell cultures. **A,** Light microscopy images of QCTB_INF_R077 in 2D adherent culture at passage 5. **B,** Light microscopy images of QCTB_INF_R102 in 2D adherent culture at passage 4. The magnification is provided in the bottom right hand corner of the image.

A common feature of both QCTB_INF_R077 and QCTB_INF_R102 infant lines was the limited number of passages that were possible before the cells ceased proliferating (passage 11). In later passages, the cells appeared larger, differentiated and remained static with no obvious further growth (**figure 6-2**).

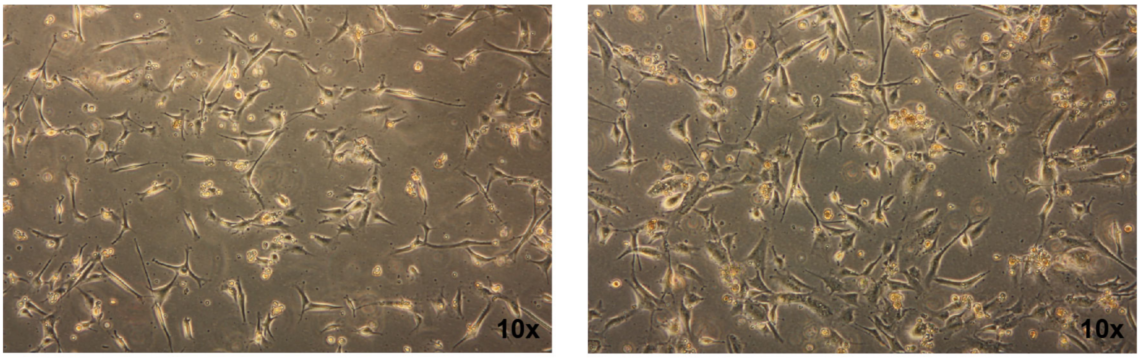

QCTB_INF_R077 (adherent, passage 7) QCTB_INF_R077 (adherent, passage 11)

Figure 6-2. Morphological changes of QCTB_INF_R077. Light microscopy images showing QCTB_INF_R077 cells in 2D adherent culture at passage 7 and 11. The magnification is provided in the bottom right hand corner of the image.

OPBG_INF_035 contained an *ETV6:NTRK3* fusion and no other background mutations. The cell culture was initially successful with cells adherent on laminin-fibronectin; however when approaching confluency the cells detached (n=3). The cells were therefore cryopreserved.

GOSH_INF_028 was derived from a 7-month-old male infant with a right frontal lobe tumour. WGS of DNA extracted from the frozen tumour sample identified an *HNRNPD:ROS1* fusion. However, in culture (2D on laminin-fibronectin) the cells did not grow and remained static. With the ligand for the *ROS1* receptor currently unknown (176), the culture was cryopreserved. Unfortunately, no patient-derived cell cultures containing *ALK* fusions were available or collected during the course of this study.

QCTB_R006 and QCTB_R059 were obtained from older paediatric HGG cases and were therefore used as controls; QCTB_R006 was from a frontal lobe tumour of a 9.5 year old male child, diagnosed as a GBM (histone wild-type by sequencing). QCTB_R059 was derived from a thalamic tumour of a 10.4-year-old female child. The tumour contained an *H3F3A* K27M mutation identified by sequencing. They were grown as 2D adherent cultures (laminin and laminin-fibronectin) with normal and double concentrations of growth factors +/- neurotrophins (**figure 6-3**).

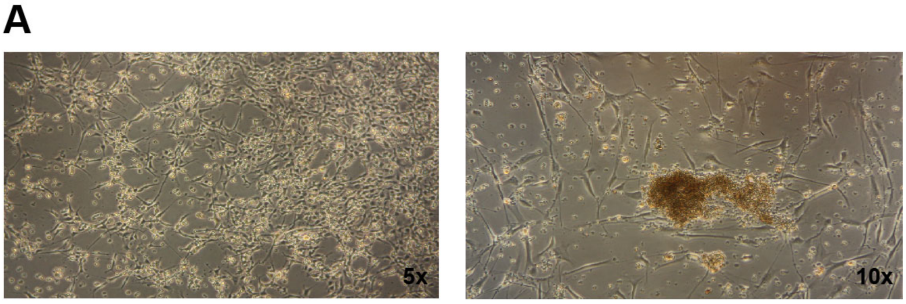

OPBG_INF_035 (adherent, passage 3)

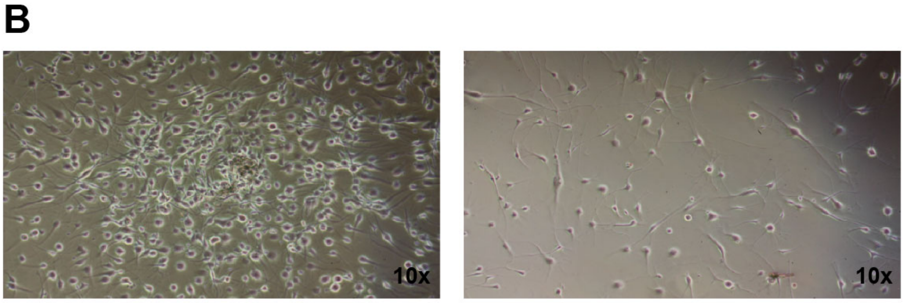

GOSH_INF_028 (adherent, passage 1)

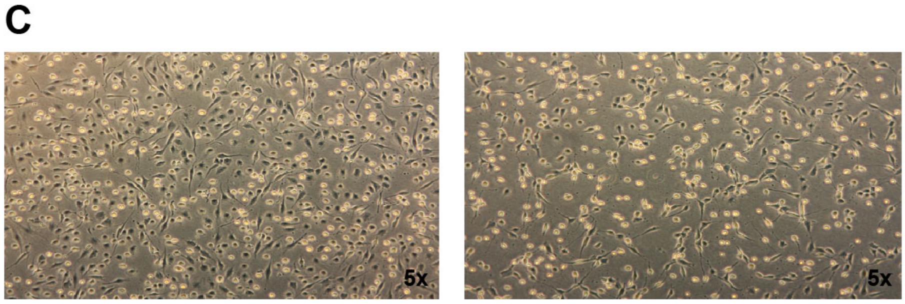

QCTB_R006 (adherent, passage 20)

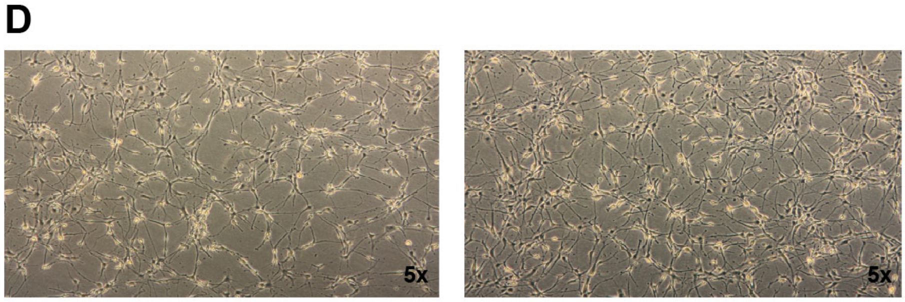

QCTB_R059 (adherent, passage 22)

Figure 6-3. Patient derived infant glioma cultures. **A,** Light microscopy images of OPBG_INF_035 in 2D adherent culture at passage 3. **B,** GOSH_INF_028 in 2D adherent culture at passage 1. **C,** Control line QCTB_R006 in 2D adherent culture at passage 20. **D,** Control line QCTB_R059 in 2D adherent culture at passage 22. The magnification is provided in the bottom right hand corner of the image.

6.2.2 Characterisation of established infant cultures

Methylation profiling was undertaken for tumour samples and cultured cells of QCTB_INF_R077 and QCTB_INF_R102. QCTB_INF_R077 tumour classified as a poor scoring IHG (calibrated score 0.08) and the cells also classified poorly (meningioma (MNG), calibrated score 0.15). QCTB_INF_R102 tumour classified as an IHG (calibrated score 0.99) and the cells scored poorly (PLEX, PED B, calibrated score 0.13). OPBG_INF_035 tumour classified as an IHG (calibrated score 0.99) and the cells classified as a GBM_MES (calibrated score 0.53), with IHG scoring second (calibrated score 0.13). When projected onto the pan-glioma t-SNE the methylation profile from the cells associated with the IHG and DIGG/DIAA tumours; the OPBG_INF_035A tumour and cells remained in close proximity (in the IHG cluster), but OPBG_INF_035B tumour projected to the DIGG/DIA group. The QCTB_INF_R077 cells and QCTB_INF_R102 cells also projected to the DIGG/DIA cluster, distant to their parent tumours which were located in the IHG cluster (**figure 6-4**) (59). Short tandem repeat (STR) analysis performed for QCTB_INF_R077 cells confirmed that there was no contamination or evidence of infection .

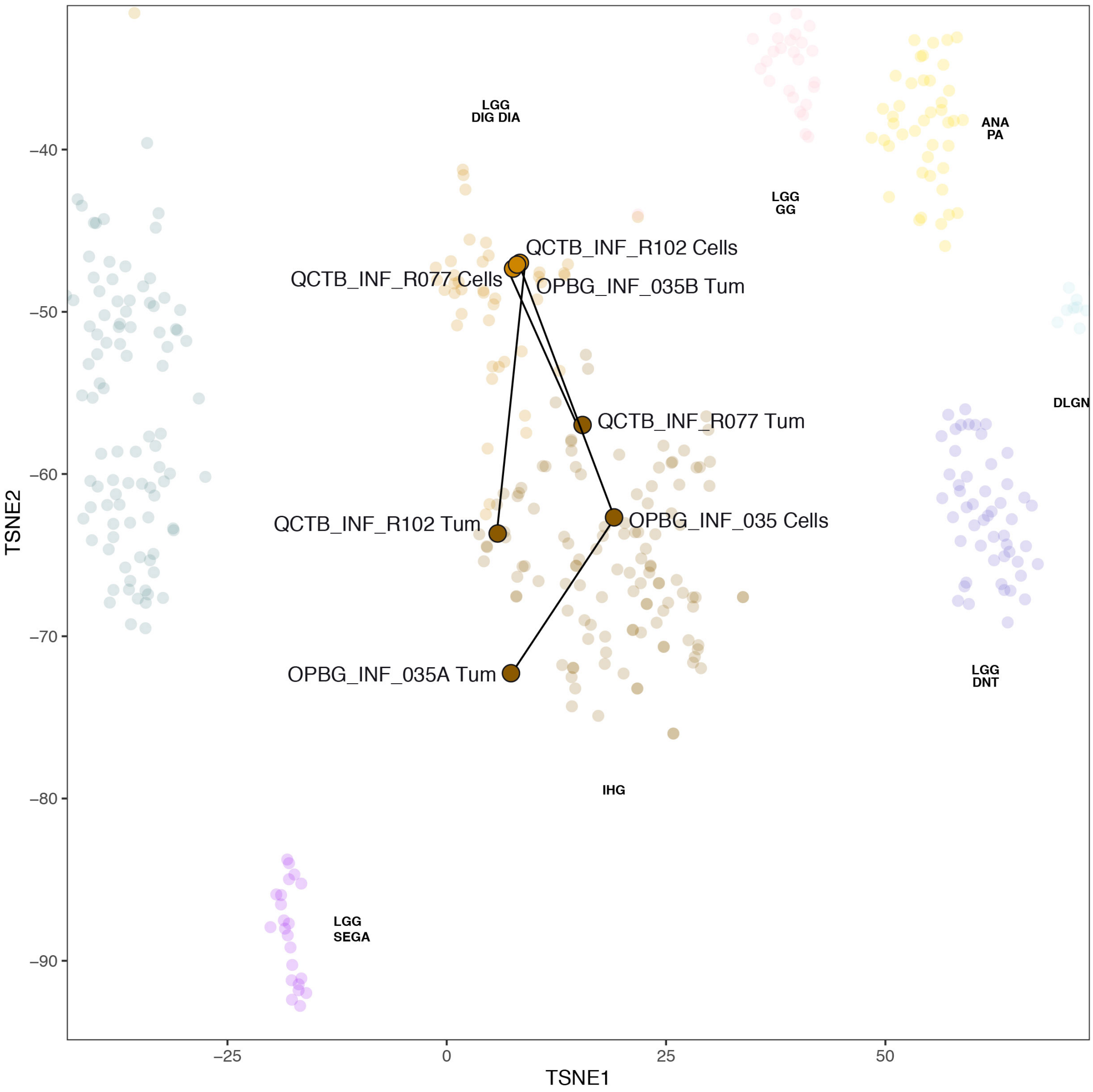

Figure 6-4. Methylation profiling of tumour and cells. t-SNE projection of the methylation profiles of the infant glioma cell culture models and the respective tumours from which they have been derived. Each culture and tumour are labelled and is represented by an enlarged circle in full colour.

Immunofluorescence studies (performed by Valeria Molinari) comparing QCTB_INF_R077 with QCTB_R006 and QCTB_R059 based on the expression of glioneuronal and mesenchymal markers showed that QCTB_INF_R077 expressed the stem/differentiation markers (Nestin/GFAP, Sox2, Olig-2, CNPase, Musashi-1, TUJ-1) and the mesenchymal markers (Vimentin, Desmin and aSMA). In contrast, QCTB_R006 and QCTB_R059 showed some

Nestin/GFAP, Musashi-1, TUJ-1 and Olig-2 expression, but very little Vimentin and Desmin expression. FISH studies (performed by Anna Burford) confirmed the presence of the fusion, but also showed that cells at passage 7 had become tetraploid (**figure 6-5**).

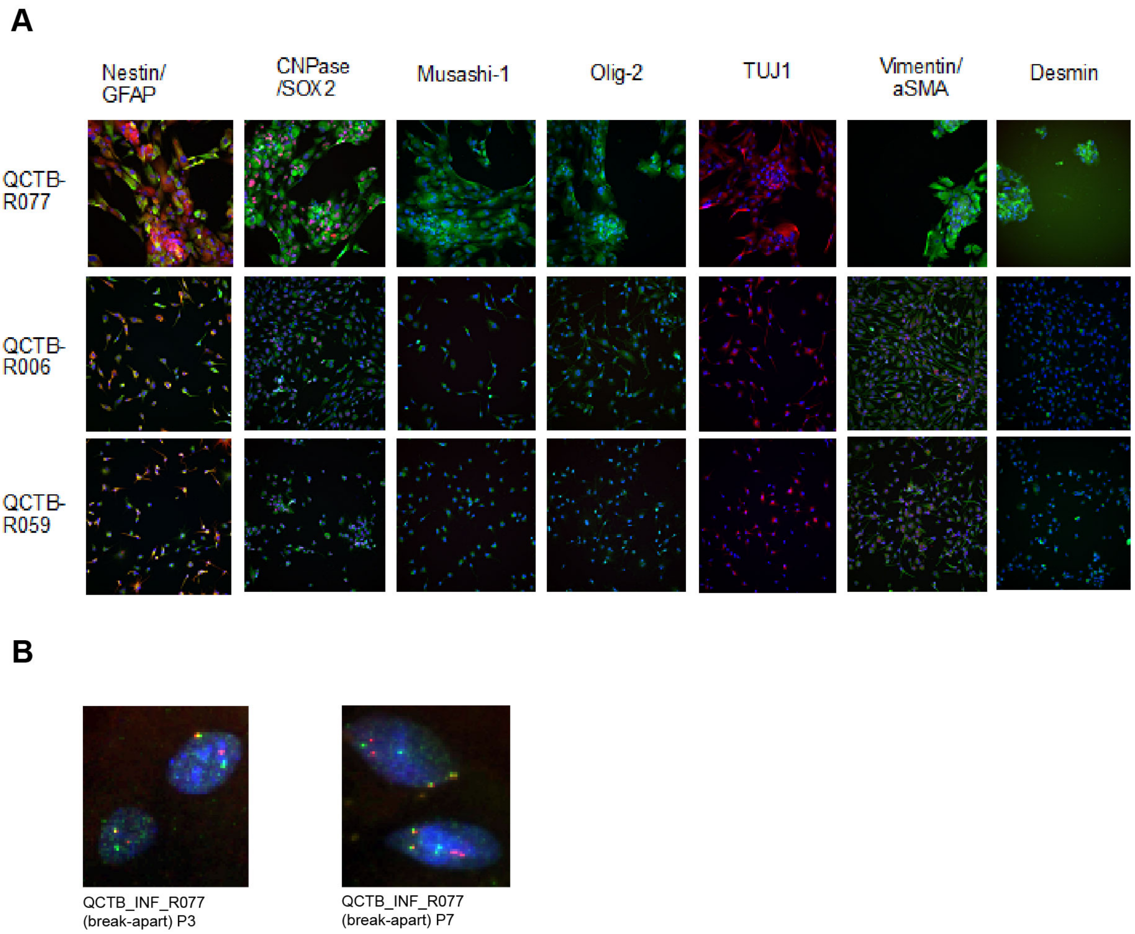

QCTB_INF_R077 (break-apart) P3

QCTB_INF_R077 (break-apart) P7

Figure 6-5. Characterising the QCTB_INF_R077 infant cell culture. **A,** Immunofluorescence panel comparing the profiles of QCTB_INF_R077, QCTB-R059 and QCTB-R006. GFAP (green), Nestin (red), CNPase (green), SOX2 (red), Musashi-1 (green), Olig-2 (green), TUJ1 (red), Vimentin (green), aSMA (red) and Desmin (green). **B,** Fluorescence in situ hybridisation (FISH) to detect the *ETV6:NTRK3* fusion using break-apart probes in cells from two different passages of QCTB_INF_R077. *ETV6*; green, *NTRK3*; red.

6.2.3 Trk inhibitor screening in infant high-grade glioma primary cultures

Focusing on the models which grew best, their *in vitro* sensitivities to four small-molecule inhibitors of TrkA/B/C were compared with the two fusion-negative pediatric glioma cultures (QCTB_R006 and QCTB_R059). *NTRK* fusion–positive cells were more sensitive to entrectinib, crizotinib, and milciclib, with differential sensitivities ranging from 2- to 9-fold over fusion-negative cells (P = 0.0253, crizotinib; P = 0.0786, entrectinib; P = 0.0141, milciclib) (**figure 6-6**).

A

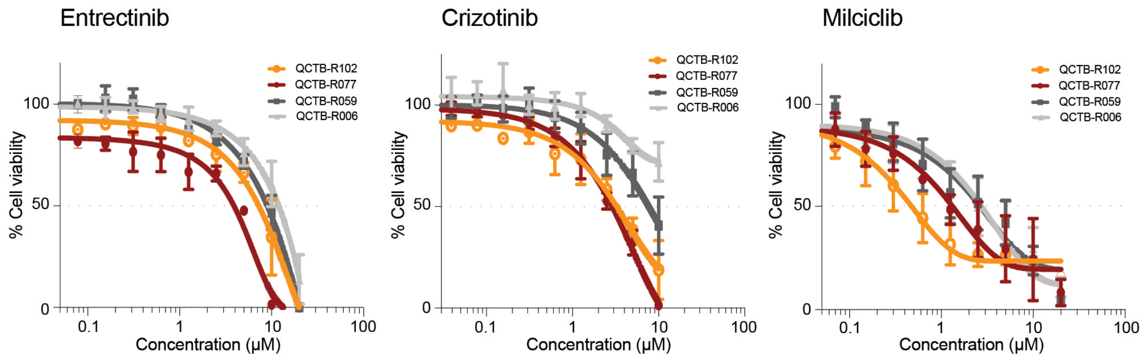

B

	Crizotinib	Entrectinib	Milciclib
QCTB-R077	2.8μM	4.6μM	1.8μM
QCTB-R102	3.5μM	7.6μM	0.3μM
QCTB-R059	8.2μM	9.3μM	8.9μM
QCTB-R006	10.0μM	12.3μM	10.3μM

Figure 6-6. Preclinical experience with Trk inhibitors in fusion-positive infant glioma. **A,** Concentration–response curves for three Trk inhibitors tested against two *NTRK* fusion-positive infant glioma cell cultures (QCTB-R102, *TPM3:NTRK1*, light orange; QCTB-R077, *ETV6:NTRK3*, dark red) and two fusion-negative glioma cultures (QCTB-R006, light grey; QCTB-R059, dark grey). Concentration of compound is plotted on a log scale (x-axis) against cell viability (y-axis). Mean plus SE are plotted from at least n=3 experiments. **B,** Table of the GI50 values for each of the cell cultures tested.

In vitro sensitivity to larotrectinib was also tested; three different formulations of the drug were tried (including pre-solubilised) however no sensitivity was observed across all cultures. Anecdotally, we received similar reports from multiple other labs and chose not to pursue this compound further.

In order to look for evidence of pathway modulation in response to treatment, QCTB_INF_R102 cells were treated with increasing concentrations of entrectinib (0, 0.1, 1, 10μM), and phospho-ERK and phospho-AKT levels assessed by Western blot analysis. There was a clear reduction in downstream signaling via both phospho-AKT and phospho-ERK, demonstrating MAPK/PI3K pathway modulation in response to increasing concentrations of entrectinib (particularly 0.1 and 10μM). Despite the loading control not being equal, a trend is still seen indicating the downregulation of pAKT and pERK (**figure 6-7**).

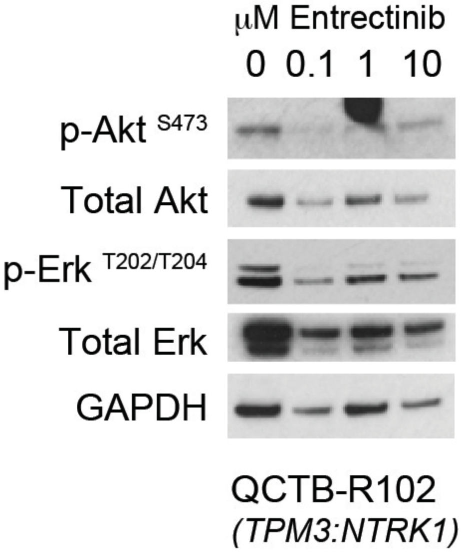

Figure 6-7. Pathway modulation in response to Trk inhibitors. Western blot analysis of phosphorylated and total Akt and Erk for QCTB-R102 cells (*TPM3:NTRK1*) treated with increasing concentrations of entrectinib.

6.2.4 Establishment of orthotopic xenografts in mice

Having established cultures *in vitro*, tumourigenicity was assessed via attempted *in vivo* modelling. Prior to my arrival in the team, two experiments (performed by Dr Maria Vinci and Dr Katy Taylor in 2014) involved intracranial injection (hemispheric) of QCTB_INF_R077 cells into NOD.Cg-*Prkdc*^{scid} *Il2rg*^{tm1Wjl}/SzJ (NSG) mice (n=3 and 5), however no tumours were visible by MRI (last scanned at day 351 post-injection and terminated at 1 year). Subsequent experiments (performed by myself and supervised by Dr Diana Carvalho) used mice at a younger age (6-7 weeks) to determine whether this influenced the tumourigenicity of the cells. MRI scans confirmed the correct site of injection but again showed no evidence of tumour formation confirmed by histology (n=3, terminated at 1 year). A fourth experiment used younger mice still (3-4-weeks); MRI scans at day 71 and 142 post-injection confirmed the correct site of injection but once more showed no evidence of tumour formation, confirmed by histology (n=6) (**figure 6-8**). Sufficient cell densities were not available to attempt *in vivo* studies with QCTB_INF_R102.

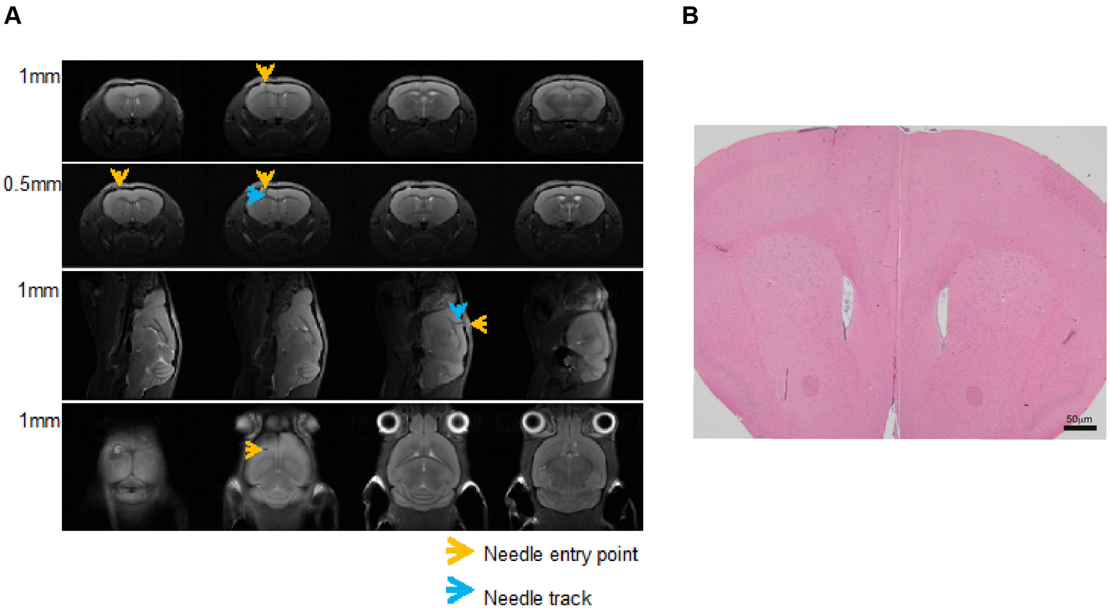

Figure 6-8. Intracranial injections of QCTB_INF_R077. **A,** T2-weighted MRI images of one mouse from the cohort on day 142 post intra-cranial injection. **B,** H&E coronal image of a mouse brain at the conclusion of the experiment (day 365).

6.2.5 *ALK* modelling (DKFZ)

To assess the tumourigenic potential of the most commonly detected *ALK* gene fusion variant (*PPP1CB:ALK*) in a model system, our collaborators at DKFZ (David Jones and Britta Ismer) attempted to generate an *in vivo* model using two complementary somatic gene transfer-based methods (RCAS/Ntv-a viral gene transfer and *in utero* electroporation (IUE)). Although not generated by myself, this was included in our published study (177), and is analogous to my own attempts to generate novel models of *NTRK* fusions using the same IUE techniques (below). When using the RCAS approach with injection of cells producing *PPP1CB:ALK* containing virus at p0 on a Cdkn2a-null background, tumour formation was rare (2/19 mice), and only after 300 days. In contrast, IUE at E14.5 with *PPP1CB:ALK* alone was able to generate consistent tumour formation with 100% penetrance, albeit with a relatively long latency of more than 250 days. Although not commonly found in the human disease, when combined with CRISPR/Cas9-mediated knockout (KO) of either *Trp53* or *Cdkn2a* for practical purposes, highly efficient tumour formation was observed with a median survival of 32 and 52 days, respectively (**figure 6-9A & 6-9B**).

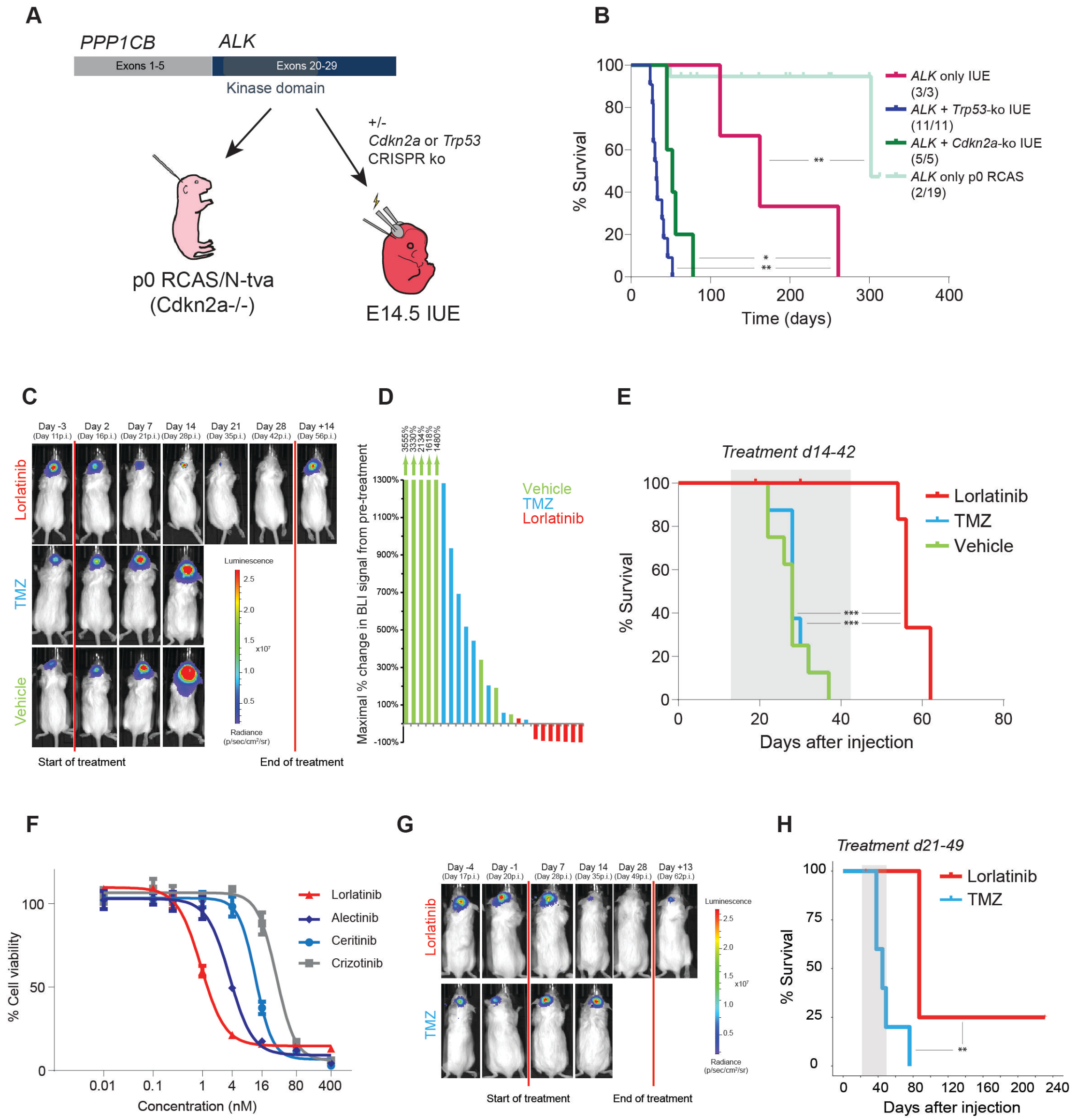

Figure 6-9. Preclinical modelling of *ALK*-fused glioma. **A,** Schematic representation of the *in vivo* modeling workflow. IUE, *in utero* electroporation; KD, kinase domain. **B,** Kaplan–Meier curve of injected animals using IUE and p0-RCAS method: *PPP1CB:ALK* only IUE, *PPP1CB:ALK Trp53*-KO IUE, *PPP1CB:ALK* + *Cdkn2a*-KO IUE and *PPP1CB:ALK* p0-RCAS only. *, $P < 0.05$; **, $P < 0.01$. **C,** and **D,** Effect of targeted *ALK* inhibition on growth of allografted *PPP1CB:ALK* + *Cdkn2a*-KO mouse tumour cells *in vivo*. p.i., post injection. **E,** Targeted inhibition significantly prolonged the survival of *PPP1CB:ALK* + *Cdkn2a*-KO allografted mice compared with temozolomide or vehicle controls. Two mice in the lorlatinib group were sacrificed due to technical complications with drug delivery, with no tumour being evident upon dissection of the brain. ***, $P < 0.001$. **F,** Primary cells derived from a *PPP1CB:ALK* fusion+ *Cdkn2a*-ko mouse tumor display sensitivity to various targeted ALK inhibitors. **G,** Effect of targeted *ALK* inhibition on growth of allografted *PPP1CB:ALK* only mouse tumour cells *in vivo*. p.i., post injection. **H,** Targeted inhibition significantly prolonged the survival of *PPP1CB:ALK* only allografted mice compared with temozolomide. **, $p<0.01$. Work performed by David Jones and Britta Ismer (DKFZ).

PPP1CB:ALK mice +/- *Cdkn2a*-KO gave rise to tumours which reflected the human disease. Histological review of the human tumour by myself showed the typical foci of palisading necrosis and mitotic activity indicative of a high grade tumour. It was highly cellular and composed of cells which were glial in origin, with clear astrocytic differentiation. The cytology of the tumour showed moderately pleomorphic nuclei with some cells displaying a gemistocytic-like appearance. Small vessels were scattered throughout the tumour. The mouse tumour also reflected these appearances, with a highly cellular tumour showing prominent high-grade features of mitotic activity and palisading necrosis. Cytologically, the cells also showed a gemistocytic-like appearance. All tumours would be classified as high-grade astrocytomas or glioblastomas. Staining for the HA epitope tag included at the C-terminus of the *ALK* fusion protein in the IUE/*Cdkn2a*-KO setting indicated widespread expression of the fusion protein, with invasion of individual tumour cells into the brain parenchyma (**figure 6-10**).

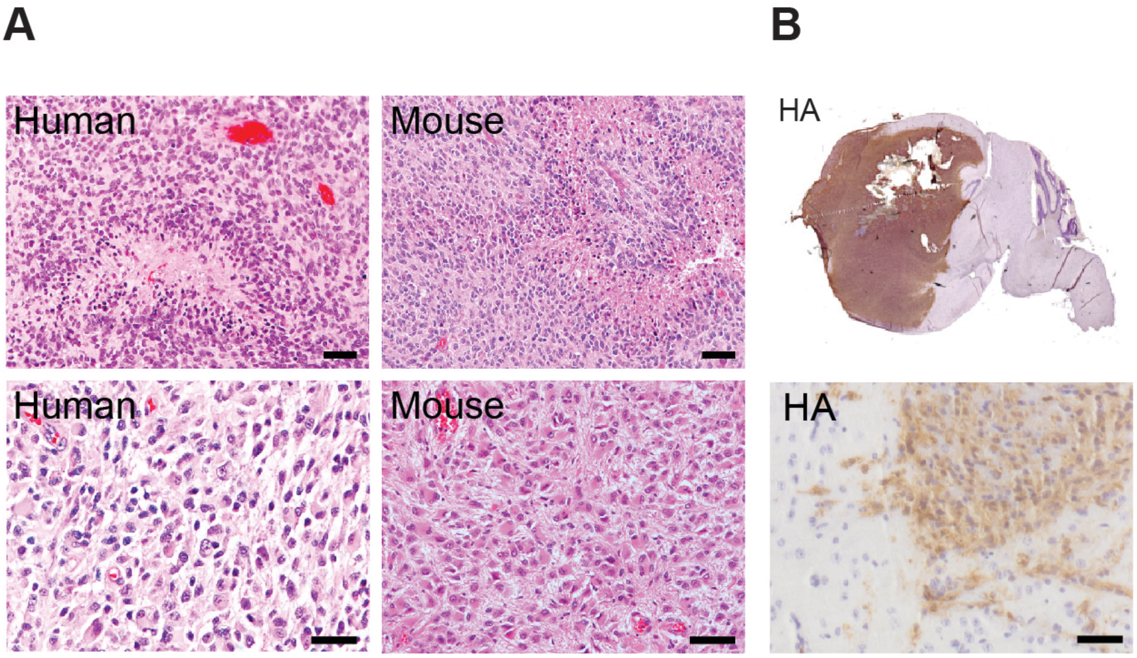

Figure 6-10. Preclinical modelling of *ALK*-fused glioma – histology. **A,** H&E staining of representative human *ALK* fusion-positive tumours and *PPP1CB:ALK* +/- *Cdkn2a*-ko IUE mice showing evidence of palisading necrosis (top) and clear astrocytic differentiation (bottom). **B,** Whole-brain HA-tag staining of a representative *PPP1CB:ALK* + *Cdkn2a*-ko IUE mouse indicating expression of the *ALK* fusion transgene (top) and single tumour cells infiltrating into the normal brain parenchyma (bottom). Sample processing performed by David Jones and Britta Ismer.

Further work carried out at DKFZ identified *in vitro* efficacy of four targeted *ALK* inhibitors in neurospheres derived from this model. (**figure 6-9F**) (**appendix 12**). Furthermore, lortatinib was tested in vivo due to its reportedly good blood–brain barrier penetration, and compared with temozolomide. Although temozolomide was found to slow tumour growth in comparison with vehicle control, all tumours in these two treatment arms continued to grow. In contrast, all but one lorlatinib-treated animal displayed a significant reduction in BLI signal compared with the pretreatment baseline. This imaging response corresponded with a significant increase in survival in the lorlatinib-treated group compared with the two control arms (P < 0.0001; although all tumours regrew after stopping treatment after 28 days, with all mice ultimately needing to be sacrificed due to onset of tumour symptoms). (**figure 6-9C, D & E**). A similar experiment was performed in mice transplanted with cells from an *ALK* fusion–only mouse tumour (**figure 6-9G & H**), with a similar tumour regression and survival increase with lorlatinib (P = 0.004, log-rank test). Overall, these findings provide a strong preclinical rationale for the potential use of targeted ALK inhibition in a clinical setting.

6.2.6 *NTRK* modelling

We sought to implement the IUE techniques used by DKFZ in our own lab to model the fusions *KCTD16:NTRK2* and *ETV6:NTRK3*. In parallel, I wanted to explore the effect of these fusions *in vitro* in the neural stem cell context.

After designing the sequences for the *KCTD16:NTRK2* fusion and two versions of the *ETV6:NTRK3* fusion (with a v5 sequence tag at the C-terminus), they were manufactured in 19ABHESP_pMA-T plasmids (3952 – 4373 bp). PCR confirmed the expected sizes for each fusion construct. After restriction digestion and ligation of the donor plasmid (AAVS1_Puro_PGK1_3xFLAG_Twin_Strep), followed by transformation of NEB 5-alpha competent *E. coli* C2987 bacteria, the constructs were sequenced confirming that the fusion and v5 tag were in correct sequence. Control constructs using the genes *ETV6, NTRK3, KCTD16,* and *NTRK2* with v5 tags were also created (**figure 6-13**).

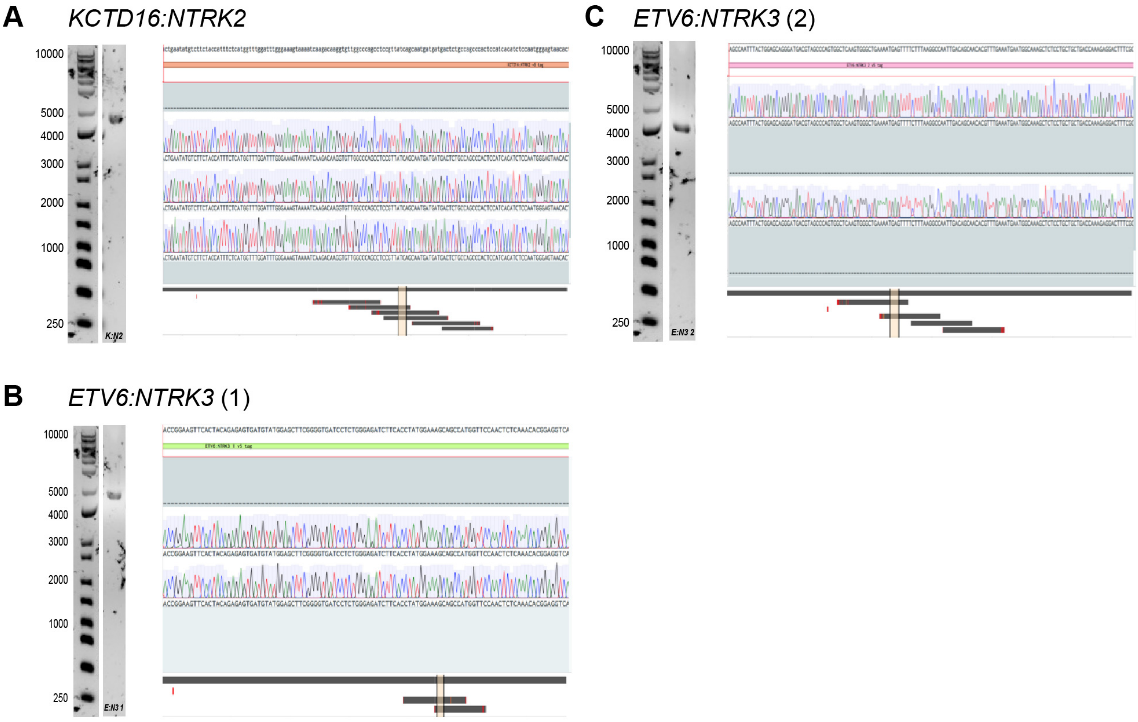

Figure 6-13. *NTRK* fusion constructs. **A,** PCR gel showing the 1kb DNA ladder and the band for the *KCTD16:NTRK2* fusion + v5 tag, and the Sanger sequencing output. **B,** PCR gel showing the 1kb DNA ladder and the band for the *ETV6:NTRK3* (1) fusion + v5 tag, and the Sanger sequencing output. **C,** PCR gel showing the 1kb DNA ladder and the band for the *ETV6:NTRK3* (2) fusion + v5 tag, and the Sanger sequencing output.

After optimising the electroporation protocol using pmaxGFP plasmids, 1-2 x 10^6 human neural stem cells (E3462) were electroporated and expanded into T175 flasks. Immunofluorescence was performed on the cells to identify the v5 tag and therefore confirm successful integration of the fusion; the results did not show any positivity for either the fusions or control genes (**figure 6-14**).

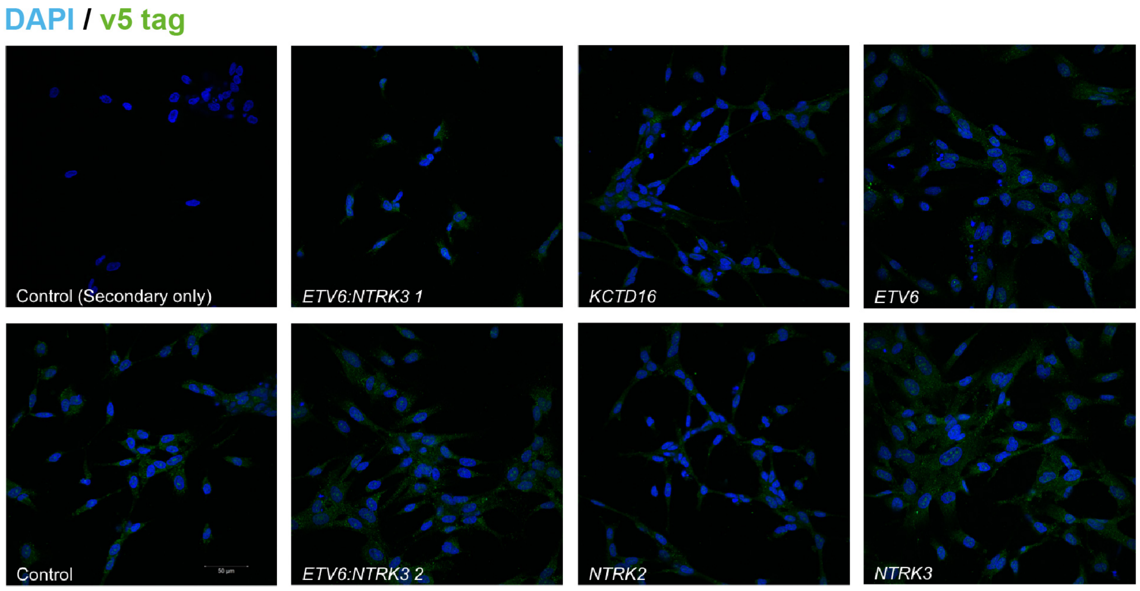

Figure 6-14. Immunofluorescence for v5 tag. A panel of immunofluorescence images for E3462 human neural stem cells electroporated with DNA containing the respective fusions and genes (labels in white in bottom left hand corner of image.) DAPI; blue, v5 tag; green.

However, the puromycin resistance gene of the donor plasmid was used to select for successfully electroporated neural stem cells. A puromycin sensitivity assay showed the lowest concentration at which all the E3462 cells died was 1.25μg/ml (**figure 6-15A**). After 48 hours, most cells had died/were dying and the remaining viable cells were re-seeded. Colonies of cells were sustained for both *KCTD16:NTRK2* and *ETV6:NTRK3* fusions (**figure 6-15B & 6-15C**). However, no viable cells remained for the control constructs.

After expansion and puromycin re-challenge no viable cells remained for the *KCTD16:NTRK2* fusion. Two viable colonies of *EVT6:NTRK3* electroporated cells remained after four challenges of puromycin. Phenotypically, they were more spindle shaped compared to their non-electroporated counterparts (**figure 6-15D**). A repeat experiment was performed with *KCTD16:NTRK2* but again no viable cells were achieved. Due to low cell density, the remaining *ETV6:NTRK3* electroporated cells did not proliferate to achieve sufficient numbers for further assays, and without *KCTD16:NTRK2* electroporated cells for comparison, the experiment was concluded and the remaining cells were cryopreserved.

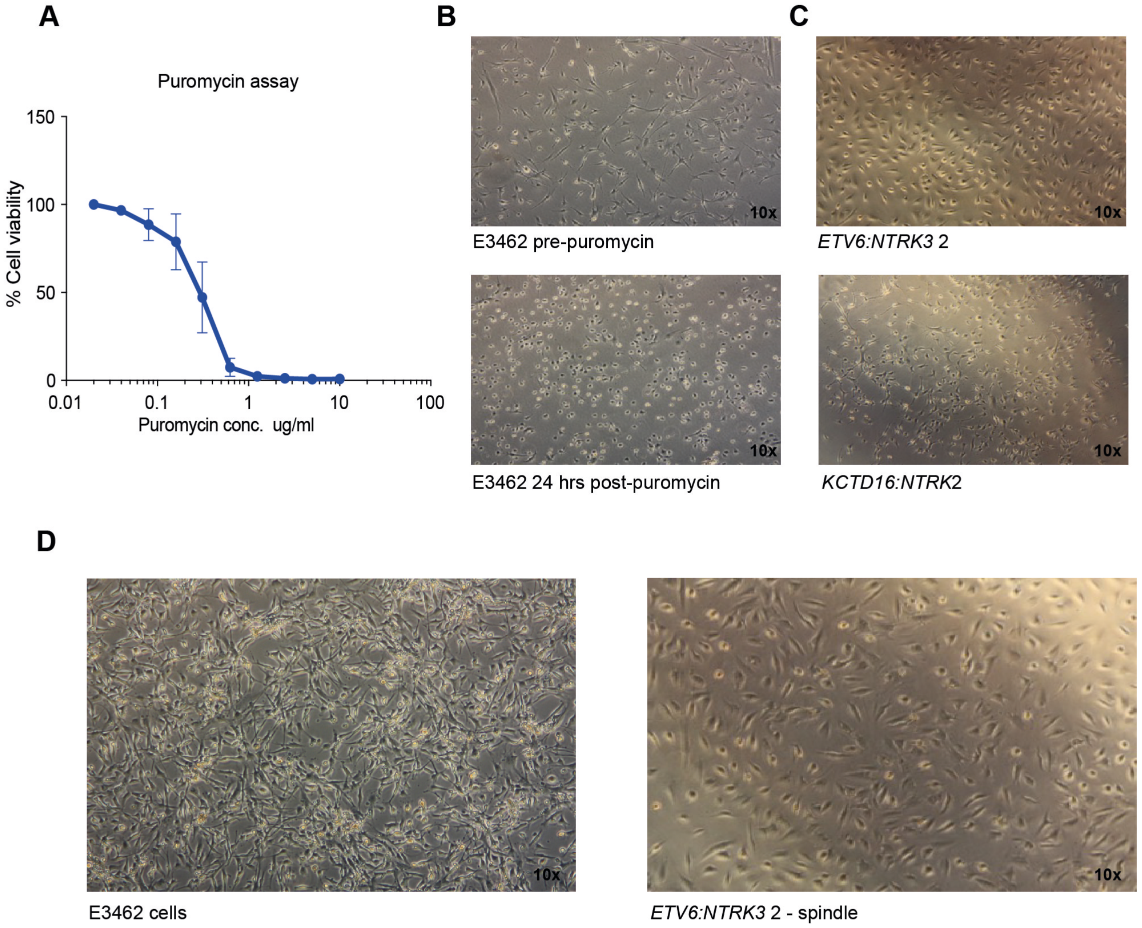

E3462 pre-puromycin

ETV6:NTRK3 2

E3462 24 hrs post-puromycin

KCTD16:NTRK2

E3462 cells

ETV6:NTRK3 2 - spindle

Figure 6-15. Cell selection using puromycin resistance. **A,** A concentration-response curve for E3462 human neural stem cells using puromycin. **B,** Light microscopy images of E3462 human neural stem cells pre-puromycin and 24 hours post-puromycin. **C,** Light microscopy images showing viable cells for both *ETV6:NTRK3* and *KCTD16:NTRK2* electroporated E3462 human neural stem cells. **D,** Light microscopy images showing control E3462 human neural stems cells and *ETV6:NTRK3* electroporated E3462 human neural stem cells, showing a spindled morphology. The magnification is provided in the bottom right hand corner of the image.

6.2.7 Mouse neural stem cells

Mouse neural stem cells (mNSCs) were substituted for E3462, and the donor plasmid was substituted for PBCAG-eGFP. After restriction, ligation and transformation sequencing confirmed that the fusion, v5 tag and GFP marker were retained and in the correct sequence, 1-2 x 10^6 mNSCs were electroporated per fusion. GFP expression was reviewed 24- and 48-hours post-electroporation using a fluorescent cell analyser; <5% of cells showed strong positivity.

The cells were sorted for GFP positivity; 6.47% positive cells were sorted for the control (PBCAG-eGFP), 5.03% for *KCTD16:NTRK2* and 1.66-3.0% for *ETV6:NTRK3*. GFP positivity was confirmed using fluorescence microscope imaging (**figure 6-16**).

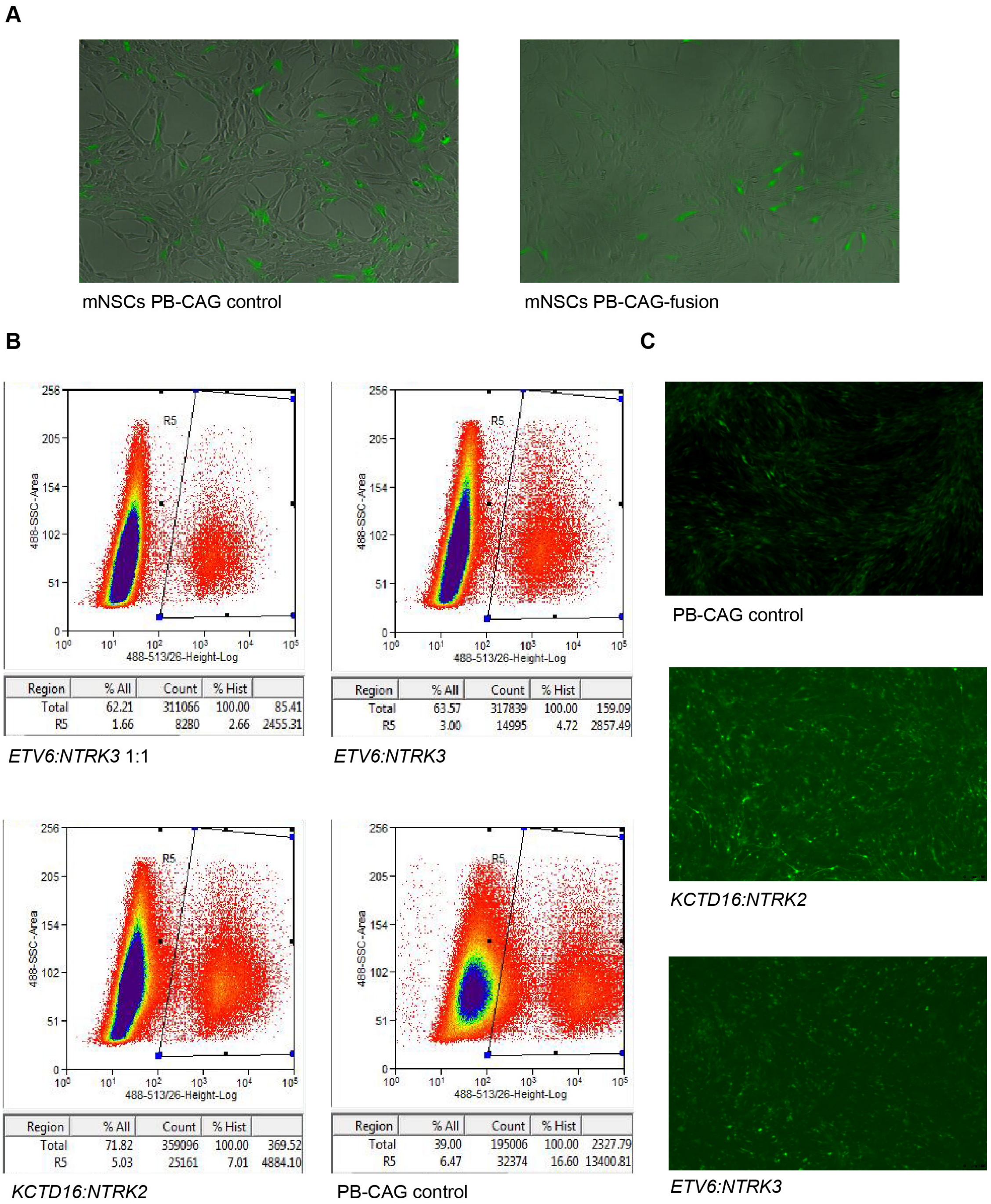

mNSCs PB-CAG control

mNSCs PB-CAG-fusion

Region	% All	Count	% Hist	
Total	62.21	311066	100.00	85.41
R5	1.66	8280	2.66	2455.31

ETV6:NTRK3 1:1

Region	% All	Count	% Hist	
Total	63.57	317839	100.00	159.09
R5	3.00	14995	4.72	2857.49

ETV6:NTRK3

Region	% All	Count	% Hist	
Total	71.82	359096	100.00	369.52
R5	5.03	25161	7.01	4884.10

KCTD16:NTRK2

Region	% All	Count	% Hist	
Total	39.00	195006	100.00	2327.79
R5	6.47	32374	16.60	13400.81

PB-CAG control

PB-CAG control

KCTD16:NTRK2

ETV6:NTRK3

Figure 6-16. Selecting the fusion-positive mouse neural stem cells (mNSCs). **A,** Microscopy images from the JuLI microscope showing fluorescent green GFP-positive cells for the mNSCs electroporated with the PB-CAG control and the PB-CAG-fusion. **B,** Images of the output from the MoFlo after cell sorting for GFP positivity for each of the conditions; the area of the graph selected by the box indicates the GFP positive cells. The overall percentage is provided in the table below. **C,** Fluorescent microscope images of the cells from each condition post-sorting for GFP. Fluorescent green; GFP positive.

Immunofluorescence for the expression of both GFP and the v5 tag showed positivity in both the *ETV6:NTRK3* and *KCTD16:NTRK2* electroporated cells. Only GFP positivity was seen in the PBCAG-eGFP control (**figure 6-17A-D**).

To further support the successful integration of the fusion into the genome of the cells, western blot was used to look for increased PI3K/AKT pathway activation and the presence of the v5 tag; it showed an increased phospho-AKT for both the *KCTD16:NTRK2* and *ETV6:NTRK3* electroporated cells, however the v5 tag was not detected (**figure 6-17E**).

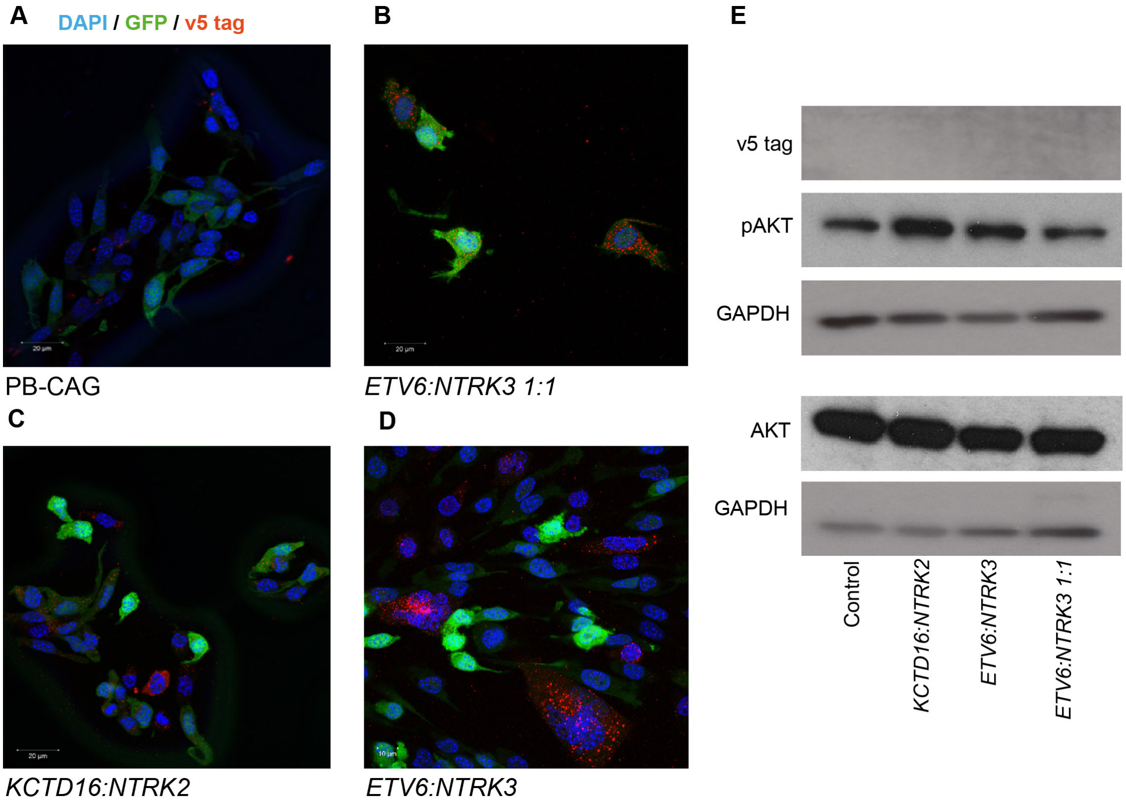

PB-CAG

ETV6:NTRK3 1:1

KCTD16:NTRK2

ETV6:NTRK3

Figure 6-17. Immunofluorescence to detect GFP and v5 tag. **A,** Immunofluorescence of mouse neural stem cells electroporated with the empty PB-CAG vector. Green; GFP, red; v5 tag. **B,** Immunofluorescence of mouse neural stem cells electroporated with *ETV6:NTRK3* (1:1 ratio of transposase to DNA). Green; GFP, red; v5 tag. **C,** Immunofluorescence of mouse neural stem cells electroporated with *KCTD16:NTRK2*. Green; GFP, red; v5 tag. **D,** Immunofluorescence of mouse neural stem cells electroporated with *ETV6:NTRK3* (2:1 ratio of transposase to DNA). Green; GFP, red; v5 tag. E, Western blot analysis of phosphorylated and total Akt and v5 tag for the electroporated mNSCs.

6.2.8 *In utero* electroporation

With the assistance of Dr Ketty Kessler, 47 embryos were electroporated (E13.5, hemispheric location) with *KCTD16:NTRK2* and *ETV6:NTRK3* fusions alone, or with the fusion and *Trp53* knockout. 33 pups (70.2%) were born and survived to adulthood across all conditions. Serial MRI scans (day 57 and 118 post-IUE) of these mice showed no evidence of tumour formation (**figure 6-18**). At day 145, a mouse from each experiment was sacrificed and histological review showed no evidence of tumour for all experiments.

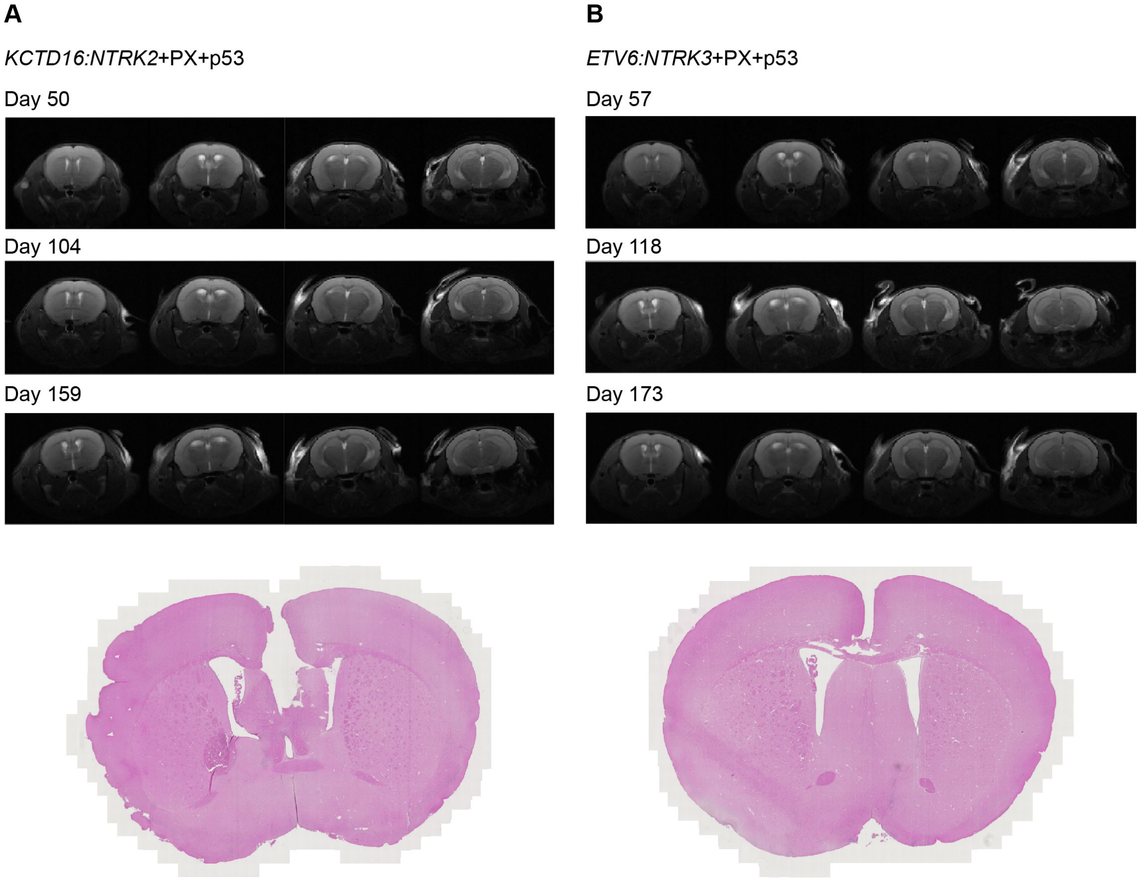

Figure 6-18. *In utero* electroporation (IUE). **A,** T2-weighted MRI images at day 50, 104 and 159 post-IUE, with H&E histology image of brain (below) from a mouse sacrificed on day 145 for the *KCTD16:NTRK2*+PX+p53 experiment. **B,** T2-weighted MRI images at day 57, 118 and 173 post-IUE, with H&E histology image of brain (below) from a mouse sacrificed on day 145 for the *ETV6:NTRK3*+PX+p53 experiment.

Regrettably, further work using these models was not possible due to the onset of the COVID-19 pandemic.

6.3 Discussion

A striking finding of this study is that we found highly recurrent fusions in genes encoding the RTKs *ALK, NTRK1/2/3, MET* or *ROS1,* some of which were well known in other cancers, but many which had not been previously reported and with their tumourigenicity unknown. Further, none of these fusions had been evaluated in the specific context of glioma. The most common *ALK* fusion, *PPP1CB:ALK*, was found to be tumourigenic when introduced in prenatal, although largely not postnatal, mice, demonstrating the importance of developmental context associated with the oncogenicity of these alterations. *ALK* fusion–positive tumours were also found to be sensitive to targeted ALK inhibition *in vitro* and *in vivo*, resulting in tumour shrinkage and extension of survival in the latter in contrast to the standard chemotherapeutic agent temozolomide. Another published study showed similar results; immortalised normal human astrocytes expressing the *CCDC88A:ALK* fusion showed an increased proliferation rate, dose-dependent sensitivity to ALK inhibitors and were tumourigenic *in vivo* (9).

Critically, *NTRK* fusion cases were also found to respond to targeted inhibitors in patient-derived models *in vitro* in common with isolated reported cases (126). However, the infant glioma models were not tumourigenic after multiple orthotopic implantation experiments in immunodeficient mice, precluding *in vivo* assessment. This may be related to the age of the mice used with differences in the brain microenvironment, neuronal development or expression possibly being factors (178). A mouse post-natal day 7-10 is considered to be equivalent to a human full-term (37 – 42 weeks' gestation) infant (179); therefore even the youngest mice we used in our study (3-4 weeks) would be equivalent to a 5-8-year-old child. IUE may offer a better approach for generating infant glioma models; previously it was considered to be limited as conventional plasmids remained episomal and therefore could be lost or inactivated during cell division of glial cells (112). However, the development of the DNA transposon system such as piggyBac has overcome this and allowed successful transgenesis (112), and the use of CRISPR/Cas 9 mediated gene knockouts has allowed the successful generation of different HGG models, including our *ALK* fusion model developed in Heidelberg. Intracranial injection of pups 12-24 hours after birth at the point of optimal neuronal expression may better mimic the clinical setting and the microenvironment that the human tumour cells are derived from and potentially improve the *in vivo* tumourigenicity of these models. The basic procedure can also be performed rapidly using hypothermic induced anaesthesia (180). However, it is limited by potential damage to the brain tissue through the injection of a volume of fluid, and also the impact of subsequent maternal care with a risk of rejection or cannibalism (180). Attempting an experiment with a reduced number of cells (perhaps 50,000 rather than 250,000) to reduce the fluid volume, and careful aftercare would allow us to explore the tumourigenicity of these cultures further. However, with the success of the IUE *ALK*-fusion approach, this would be more worthwhile.

Although at the time of writing our IUE experiment with the engineered *NTRK* fusions (*KCTD16:NTRK2* and *ETV6:NTRK3*) has not generated any tumours, *NTRK* fusions have been successfully engineered to demonstrate tumourigenicity; the *BCAN:NTRK1* fusion, reported to occur in HGG, has been modelled in mouse adult neural stem cells (derived from *p53* -/- mouse brains) using plasmid nucleofection associated with a GFP marker. When orthotopically implanted into immunocompromised mice, 4 of 5 mice generated tumours at the site of injection within 125 days. Histologically they reflected the features of an HGG, and also demonstrated sensitivity to entrectinib both *in vitro* and *in vivo* (97). Promising initial findings from the engineered *in vitro NTRK* fusion models in this study (with immunofluorescence supporting the successful introduction of the fusion) were prohibited from further work due to COVID-19. However, future studies would include sequencing of the *in vitro* models post GFP sorting, cell proliferation assays to compare growth rates between electroporated and non-electroporated cells, *in vitro* drug assays testing the sensitivity of the models to TRK inhibitors, western blot analysis to assess pathway modulation in response to TRK inhibitor treatment, and additional IUE to explore tumourigenicity. These models may also allow us to explore the possible age-related incidence and possible senescence of these tumours.

The established infant cell cultures only reached passage 10 before showing evidence of differentiation and tetraploidy identified in QCTB_INF_R077 cells. This is unusual when compared to other paediatric HGG cultures such as QCTB_R059 and QCTB_R006 which can continue beyond passage 30. However, it also may reflect an intrinsic characteristic of oncogene-induced senescence or maturation of the tumour (9). These changes are also observed in other tumour types including neuroblastoma; maturing and mature neuroblastomas show aberrations in chromosome number with triploidy (most frequent) and occasionally pentaploidy linked to maturation (181). Progressive tumour shrinkage and complete regression is reported in localised neuroblastoma only treated by 'watchful waiting' (182). It is also associated with pilocytic astrocytomas; studies have shown evidence of senescence with increased senescence-associated beta-galactosidase activity, a reduced proliferation index and increased expression of *CDKN2A/P16*^{INK4a} (183). Others have shown the upregulation of IL6 and IL1B (known as senescence-associated secretory phenotype (SASP) factors) in primary pilocytic astrocytoma cell cultures (184). MicroRNA expression levels also correlate with senescence in these tumours with MiR-146a one of the most up-regulated and known to modulate inflammatory mediators associated with senescence (185). *IGFBP7* and *TIMP1* are also upregulated and are known to be transcriptional inducers of SASP (185). This feature of infant HGG cultures may reflect the clinical behaviour of the tumours (see chapter 7) and may have implications for optimal timing of treatment with TRK inhibitors, possibly related to changes in fusion expression.

Although efficacy of TRK inhibitors was seen for entrectinib, milciclib and crizotinib, the lack of sensitivity of all lines to larotrectinib was surprising given the efficacy reported in isolated case reports (126,186) and from the phase 1/2 clinical trial (187). To the best of my knowledge there are no published studies showing sensitivity of glioma cell lines to larotrectinib. However, *in vitro* studies of other tumour types do show sensitivity; a study featuring colorectal carcinoma, lung adenocarcinoma and acute myeloid leukaemia cell lines all harbouring *NTRK* fusions demonstrated dose-dependent inhibition and downstream signalling following treatment with larotrectinib (188). Having explored different formulations to see if this impacted on *in vitro* efficacy of the drug without any noticeable impact on the cells, further assessment of pathway modification by western blot is needed. It is possible that the drug undergoes some form of modification *in vivo* to allow it to function, or the methods used to grow the cells *in vitro* (i.e. growth in 2D rather than 3D, or media components) in some way prevent the drug from entering the cells; this will be important to understand the mechanism of action. However, larotrectinib has already proven to be safe and efficacious clinically to the fusion-positive patients who have been treated with it helping to improve survival.

The rarity of infant HGG cultures is further compounded by the difficulties in establishing them in culture as previously described. Further studies analysing the secretome and proteome may provide useful data; adipocyte-released factors can modulate growth and influence the expression profile, but also pro-inflammatory and angiogenic factors are secreted into the medium to a higher extent in some glioma cultures (189). Also, the expression of Cx43 in glioma cells results in the release of matrix metalloproteinase 3 (MMP3) and osteopontin associated with extracellular matrix remodelling (190). Further work to explore the secretome and proteome in infants may help to identify key dependencies that could be utilised for these cultures.

Modification of the media used to grow the infant cultures was necessary to support their growth. Replacing serum-based media with defined growth factors suitable for neural stem cells has helped to retain the expression profiles and tumourigenicity of glioma cell lines (191). Other studies have also shown that modifying the media dependent on the cell of origin of the tumour can be important (192). There is a lack of consensus of the ideal media components to grow primary tumours with over 20 protocols published (191), and differences seen between 2D and 3D cell cultures of the same tumour adds to the complexity, with some studies arguing that 3D better mimics the *in vivo* setting (191). Heterogeneity within a culture and between cultures of the same line needs to be considered and more growth factor combinations can help to support this heterogeneity (191). Identifying the presence of the fusion within infant cultures, and with data from the *in vitro* and *in vivo* modelling work supporting this as the driver, the addition of neurotrophins to the media were a necessary measure for culture establishment.

The *in vitro* and *in vivo* sensitivity of these fusion-positive cultures, combined with individual case studies from the clinic will provide very useful pre-clinical data for the development of clinical trials using such agents to treat infant HGG. If validated in larger trials, such agents may represent attractive options to spare the long-term sequelae of chemotherapy and radiotherapy, while maintaining the generally good prognosis of these patients (81,119,161).

CHAPTER 7 – RTK inhibitors and the treatment of infant gliomas

7.1 Introduction

Tumours reported as HGG in infants are associated with improved outcomes compared to HGG in older children. Whether this is due to their molecular characteristics or a better response to established treatment modalities needs to be determined. Gross total resection is the primary treatment objective, followed by adjuvant chemotherapy with a general reluctance to implement radiotherapy in children of such a young age (5).

The Baby POG I study included four children <3 years of age diagnosed with a malignant glioma, who underwent 24 months of chemotherapy without radiation treatment and did not develop recurrent disease. They also found that histology, the presence/absence of metastases and the degree of surgical resection did not impact on survival (50% at 5 years) (5). Similar or improved survival rates are seen in other studies with a 5-year overall survival rate of 59% reported in infants with HGG after prolonged chemotherapy treatment alone (103). When radiotherapy is used, studies have shown a survival benefit; 16 patients diagnosed with HGG and treated with focal radiation therapy showed a 5-year overall survival rate of 66.3% (193).

Reported cases of infant HGG treated with surgery alone have also shown remarkably positive outcomes. Five reported cases of patients with congenital glioblastomas who survived surgery (with only one patient receiving a gross total resection) all showed a better outcome than predicted (85), with two infant cases who both underwent subtotal resection of their tumours and not receiving any adjuvant therapy postoperatively showing regression of the residual tumours (90). Similarly, a congenital GBM which underwent a limited debulking procedure alone underwent spontaneous resolution over the following 21 months (194).

The improved outcome both with chemotherapy and with surgery alone is particularly significant in this age group when considering the risk of declining cognition (195) and the development of leukoencephalopathy post–radiation treatment (196). Twenty infants who received radiation therapy before the age of 3 years showed evidence of impaired cognition in 85% of cases, with more than half of these requiring special education (5). Follow up of these children showed that cognition continues to decline over time (5). Chemotherapy appears to be less neurotoxic in infants but also has risks associated with its use; a study showed that 19 of 23 infants had MRI evidence of leukoencephalopathy (without clinically apparent symptoms), and neurocognition was lower in these infants. However, it was at a higher level when compared to children who had undergone radiation therapy (52). Therefore, adjuvant therapy needs to be used with caution in these very young children.

Targeted therapy for RTK fusion-positive cases, of the kind described in earlier chapters, including entrectinib and larotrectinib, has been frequently reported in paediatric solid tumours. A phase 1 multicentre trial looked at 17 fusion-positive primary CNS tumours or locally advanced/metastatic solid tumours in patients aged 1 to 21 years; anti-tumour activity was demonstrated in all fusion-positive cases treated with larotrectinib (197). A male infant born with an infantile fibrosarcoma of the tongue (*ETV6-NTRK3* positive) was treated with surgical resection but within a few months showed progression and lymph node involvement. After commencing larotrectinib the child was in complete remission after 16 months of treatment (198). A study of 5 patients with locally advanced *ETV6-NTRK3* positive infantile fibrosarcoma used larotrectinib as a presurgical treatment; all patients demonstrated a partial response to larotrectinib and underwent surgical resection after a median of 6 cycles, showing that Trk inhibitors could be used for optimising surgical resection (199). Trials have also been conducted with adult tumours harbouring *NTRK* fusions; one such study involved a phase 1 dose-escalation study using larotrectinib. Eight patients with *NTRK* fusion-positive solid tumours were enrolled (including soft tissue sarcoma, salivary gland, lung, thyroid and gastrointestinal stromal tumours (GIST)). All patients demonstrated good tolerability and tumour response with some patients showing an almost 100% reduction in the size of the tumour from baseline (200). A trial with entrectinib featuring 54 adults with advanced or metastatic solid tumours or varying types again demonstrated good tolerability and safety profile, and efficacy with 57% of patients showing an objective response, 7% of which had a complete response (188).

In some cases, targeted treatment may not be necessary. In one report, a 3-month-old girl was diagnosed with a large hemispheric malignant glioma which underwent a gross total resection and 2 further resections. Tumour profiling revealed a *PPP1CB-ALK* fusion but given the age of the child, she was not treated with chemotherapy and remains disease free (119) implying that these tumours can be successfully treated with surgery alone, even those which are fusion-positive.

Here are presented case histories of infant gliomas from the study cohort, describing the treatment modalities used and subsequent outcomes.

7.2 Results

7.2.1 Infant HGG case studies

Three patients in our cohort, two with *ETV6:NTRK3* fusion-positive tumours and one with a *SPECC1L:NTRK2* fusion, were treated with Trk inhibitors. The first case, OPBG_INF_035, was a girl diagnosed with a large frontal mass at 36 weeks' gestation, referred to us by the Ospedale Pediatrico Bambino Gesù Hospital in Rome, Italy. It was a large, heterogenous mass with solid, cystic, and hemorrhagic components. A biopsy was performed after birth and it was diagnosed histologically as a glioblastoma (WHO grade IV). My own histological review confirmed the presence of high-grade features (prominent necrosis and pleomorphism), but also showed a cellular tumour composed of focal areas of gemistocytic-like cells. A Ki67 stain undertaken in our laboratory showed a particularly high score of 43.7.

Methylation profiling confirmed the suspicions from the histological features that the tumour was an IHG (raw score 0.55, calibrated score 0.99), with no large-scale copy number alterations (**figure 7-1**).

OPBG_INF_035 - 0.5 years old

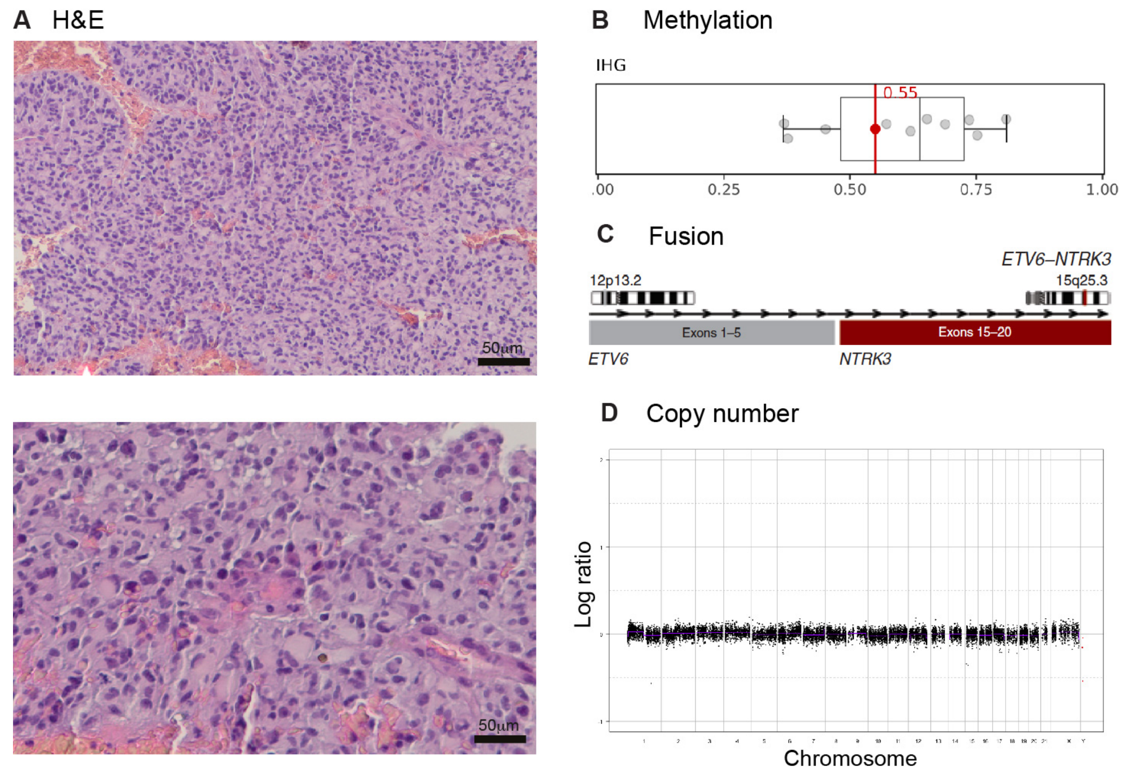

Figure 7-1. Characterisation of OPBG_INF_035. **A,** Low and high power representative histological images of the tumour. **B,** Boxplot of the raw score output from the methylation classifier. **C,** Schematic cartoon of the ETV6:NTRK3 fusion identified in this case. **D,** Copy number profile for OPBG_INF_035 derived from the methylation data.

An *ETV6:NTRK3* fusion was identified by the custom fusion panel from both the biopsy and resection specimens, as well as a sample of CSF provided from the referring hospital (201) (**figure 7-2**).

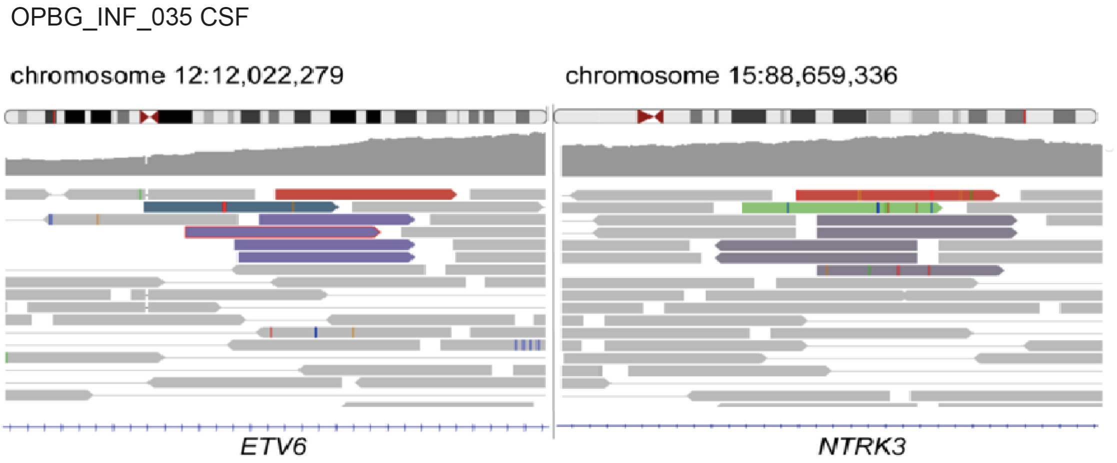

Figure 7-2. Fusion identification from OPBG_INF_035 CSF sample. After sequencing DNA extracted from a CSF sample using the fusion panel, images from IGV demonstrating an *ETV6:NTRK3* fusion present in the sample (201).

Exome sequencing confirmed that the fusion was the only somatic mutation present in this case. The child subsequently received chemotherapy (methotrexate, vincristine, etoposide, cyclophosphamide, thiotepa) before undergoing a subtotal resection 3 months later. 4 months post-surgery the child was commenced on crizotinib. An MRI scan performed after 9 months of treatment with crizotinib showed a 56% reduction in the size of the remaining solid component of the tumour compared with the post-surgery MRI scan (RANO criteria size reduction of >50% and stable). After an additional 3 months of treatment with larotrectinib, the remaining solid component showed a further reduction in size, now reaching 73% (**figure 7-3**). Clinically, the child remains well, is learning to walk with aides and is now starting pre-school.

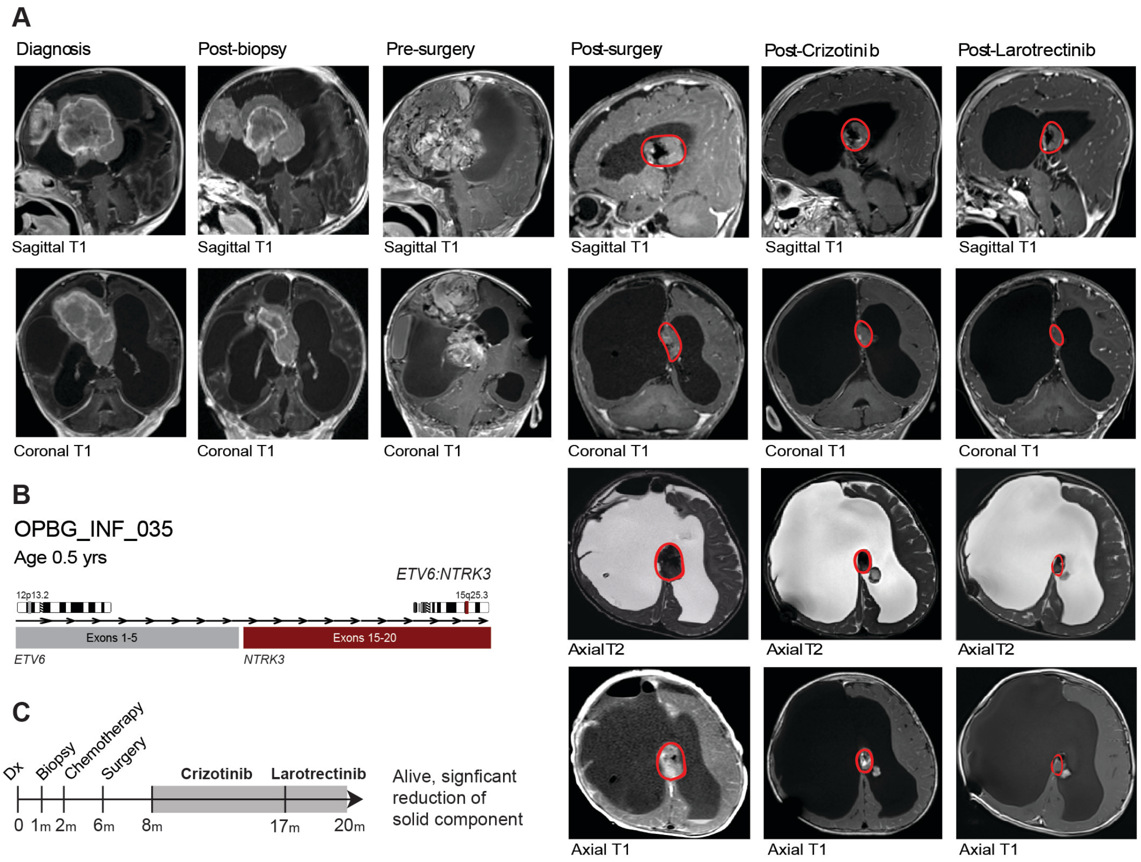

Figure 7-3. Clinical experience with *NTRK*-fusion cases – OPBG_INF_035. A, Clinical history of OPBG_INF_035, with confirmed *ETV6-NTRK3* fusion. MRI images show diagnosis, post-biopsy, pre/post-surgery, post-crizotinib and post-larotrectinib timepoints, with sagittal and coronal T1 for all, and additionally axial T2 and T1 for post-surgery and Trk inhibitors, with tumour circled in red. **B,** Schematic cartoon of the *ETV6:NTRK3* fusion diagnosed in this case. **C,** Timeline of clinical interventions is provided below, with Trk inhibitor treatment shaded in grey.

The second patient, MSKC_INF_006, was referred to us from the Memorial Sloan Kettering Cancer Center in New York, US. The child presented with a generalized seizure at age 11 months (**figure 7-4**). An MRI scan revealed a pontine mass with central hemorrhage; initially there was some uncertainty with the diagnosis with the differential diagnosis between cavernous haemangioma and pontine glioma. The child underwent surgery and a gross total resection was achieved. Histologically the tumour was composed of a compact arrangement of neoplastic cells with both minigemistocytic and epitheliod features. They focally formed perivascular pseudorosettes. Immunohistochemistry showed focal positivity for synaptophysin and NeuN, ATRX and INI1 expression was retained, and there was no loss of H3K27me3. Mitotic activity was not conspicuous but the Ki67 proliferation index was focally 8-10%. The lesion resembled tumours reported as minigemistocytic astrocytomas of infancy, and based on these appearances it was felt it would recur locally. On balance, it was diagnosed as a low-grade neuroepithelial neoplasm. The child developed a recurrence, at which point vincristine and carboplatin were commenced and a complete response was achieved. However, the tumour progressed two years after the original resection; a further gross total resection was achieved; the histological appearances showed a neuroepithelial tumour but with increased proliferative activity compared to the first resection (Ki67 proliferation index of 12.7%). The features now resembled a ganglioglioma, dominated by atypical astroglial components. Methylation profiling classified the original tumour as a low scoring PXA (raw score 0.18, calibrated score 0.51), with a gain of chromosome 7 and a copy-neutral *ETV6:NTRK3* fusion was identified via RNA sequencing conducted at the referring institution. The child was treated with larotrectinib after an *ETV6:NTRK3* fusion was identified, with the aim of preventing further recurrence. To date, the child remains well with no evidence of recurrence after 12 months of treatment.

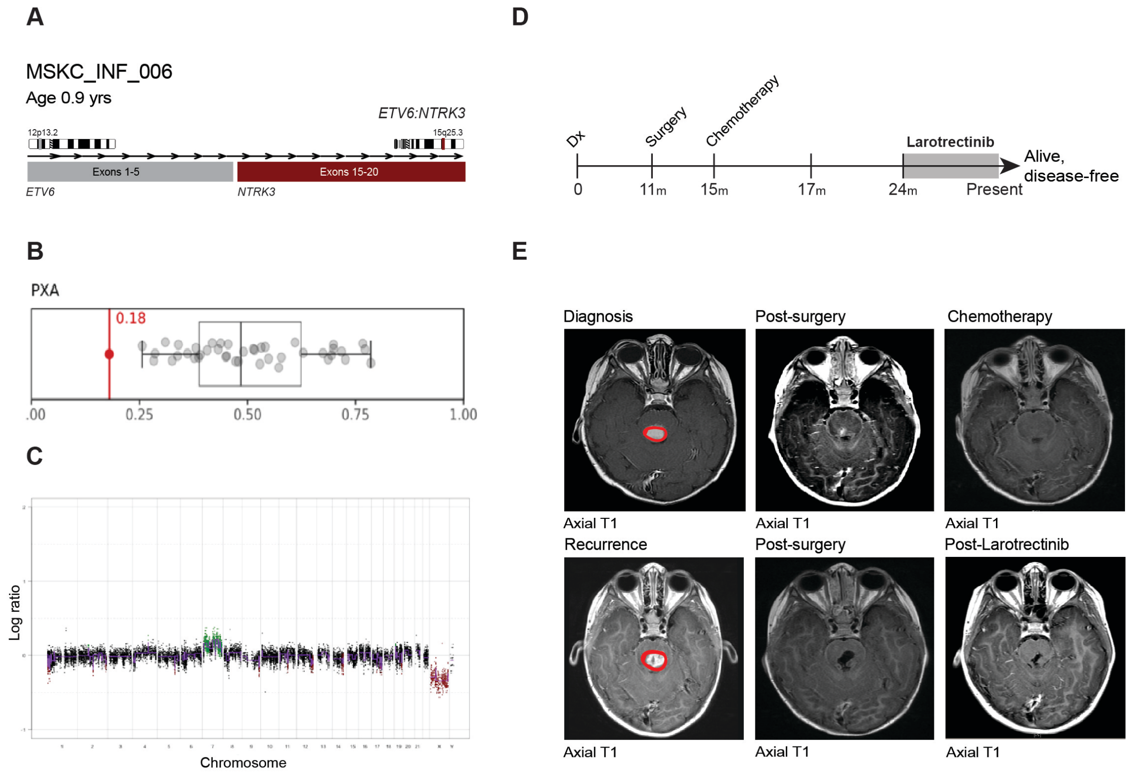

Figure 7-4. Preclinical and clinical experience with Trk inhibitors in fusion-positive infant glioma. **A,** Schematic cartoon of the *ETV6:NTRK3* fusion identified in MSKC_INF_006. **B,** Boxplot showing the raw score from the methylation classifier. **C,** Copy number profile derived from the methylation data (Green; amplification or gain, red; loss or deletion). **D,** Clinical history of MSKC_INF_006. Timeline of clinical interventions is provided, with Trk inhibitor treatment shaded in grey. **E,** Diagnosis and post-larotrectinib post-contrast axial T1 MRI scans are provided, with tumour circled in red.

Notably, the patients from whose tumours two of our primary cell lines were derived have both received surgery only to date, and remain well. QCTB_INF_R077 was referred to us from the Queensland Children's Tumor Bank in Brisbane, Australia. The infant was diagnosed with a tumour in the left frontoparietal lobe *in utero;* an obstetric ultrasound at 22 weeks' gestation identified an echogenic mass measuring 2.4cm in the left cerebral hemisphere, thought to be either haemorrhage or a space-occupying lesion. 4 days after birth, the infant underwent an MRI scan which showed a relatively well-defined lesion in the left frontal lobe, measuring 4.2 x 3.5 x 5.1cm with limited evidence of mass effect; at this stage it was considered to be a developmental lesion such as an epidermoid lesion rather than a neoplasm, and given the limited mass effect it was considered to be slow growing. The infant underwent a further MRI at 37 days which showed that the lesion had increased in size to 6.2 x 4.5 x 6.7cm. It was now causing significant mass effect with evidence of obstructive hydrocephalus, and given the increase in size over a short period of time, it was now considered to be a primary CNS tumour. The infant therefore underwent biopsy and subsequent resection.

Histologically, the tumour showed a relatively circumscribed interface with the adjacent brain and a very narrow zone of infiltration. It was composed of moderately pleomorphic short plump spindle cells with both sheeted and fascicular architectural patterns. A reticulin stain also showed background collagen deposition. IHC showed strong immunoreactivity for vimentin, CD56 and CD99, with focal staining of GFAP, S100, Desmin, NeuN, chromogranin and synaptophysin. Ki67 was moderately high, approaching 20% in some areas (**figure 7-5**). It was very difficult to classify into one of the established WHO entities; the differential diagnosis included a variant of DIGG but the imaging did not support this and the proliferative activity predicted an aggressive course. It was reported as a primary neuroepithelial tumour of uncertain histogenesis and histological features of malignancy (probably WHO grade III). It was referred to another institution for review who confirmed the appearance of a ‘high grade neuroepithelial tumour’; the management decision was that treatment should be surgical resection only followed by palliative care when appropriate.

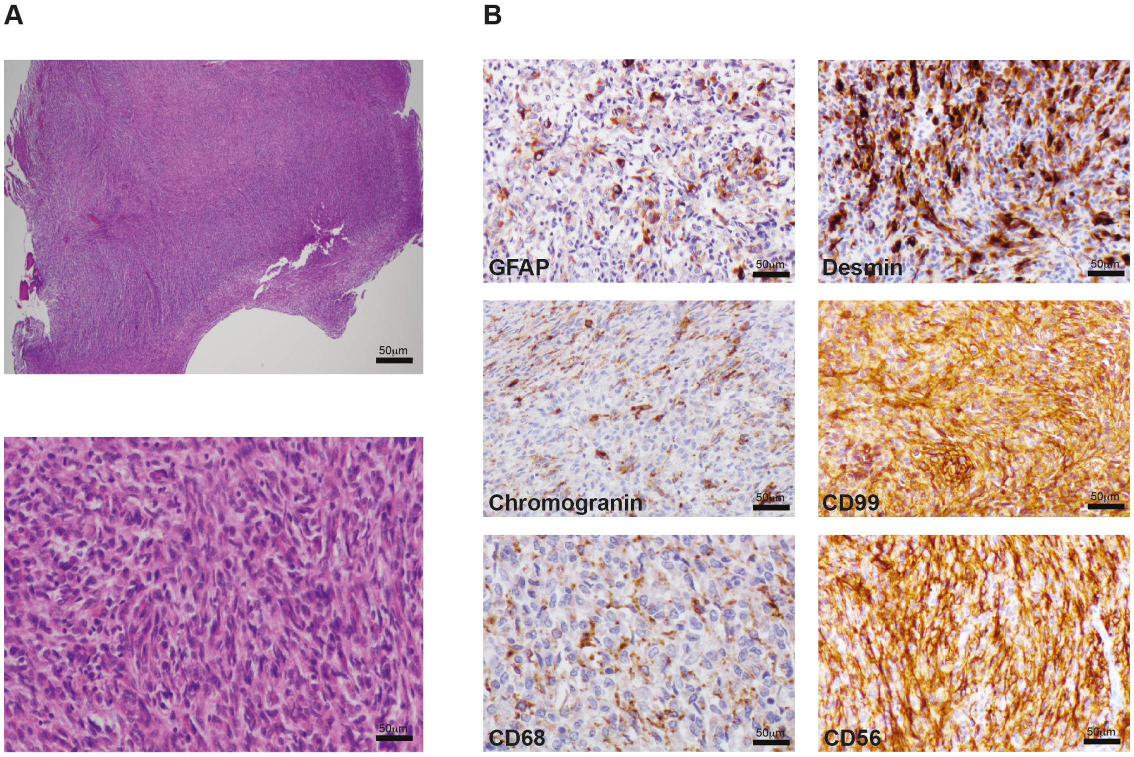

Figure 7-5. Histology review of QCTB_INF_R077. **A,** High and low power H&E images showing the architectural and cytological features. **B,** Panel of immunohistochemistry. The name of each stain is labelled in the bottom left hand corner of the image. Representative areas are shown for each stain. Brown staining indicates positivity.

The tumour was also profiled by the Glioma Team (ICR) and was the first infant case studied, prior to my arrival in the team. The spindle cell appearance in an infant case showed commonalities with infantile fibrosarcoma (characterised by *ETV6:NTRK3* fusions) and so FISH studies were undertaken by Anna Burford; this identified an *ETV6:NTRK3* fusion (validated by PCR and RNA sequencing). Methylation profiling could not classify this case (highest calibrated score 0.1 IHG) and showed no large-scale copy number alterations. However, small DNA copy number alterations (loss on *ETV6* and gain on *NTRK3*) were consistent with the fusion. No other somatic mutations were found in this case from exome sequencing data (**figure 7-6**).

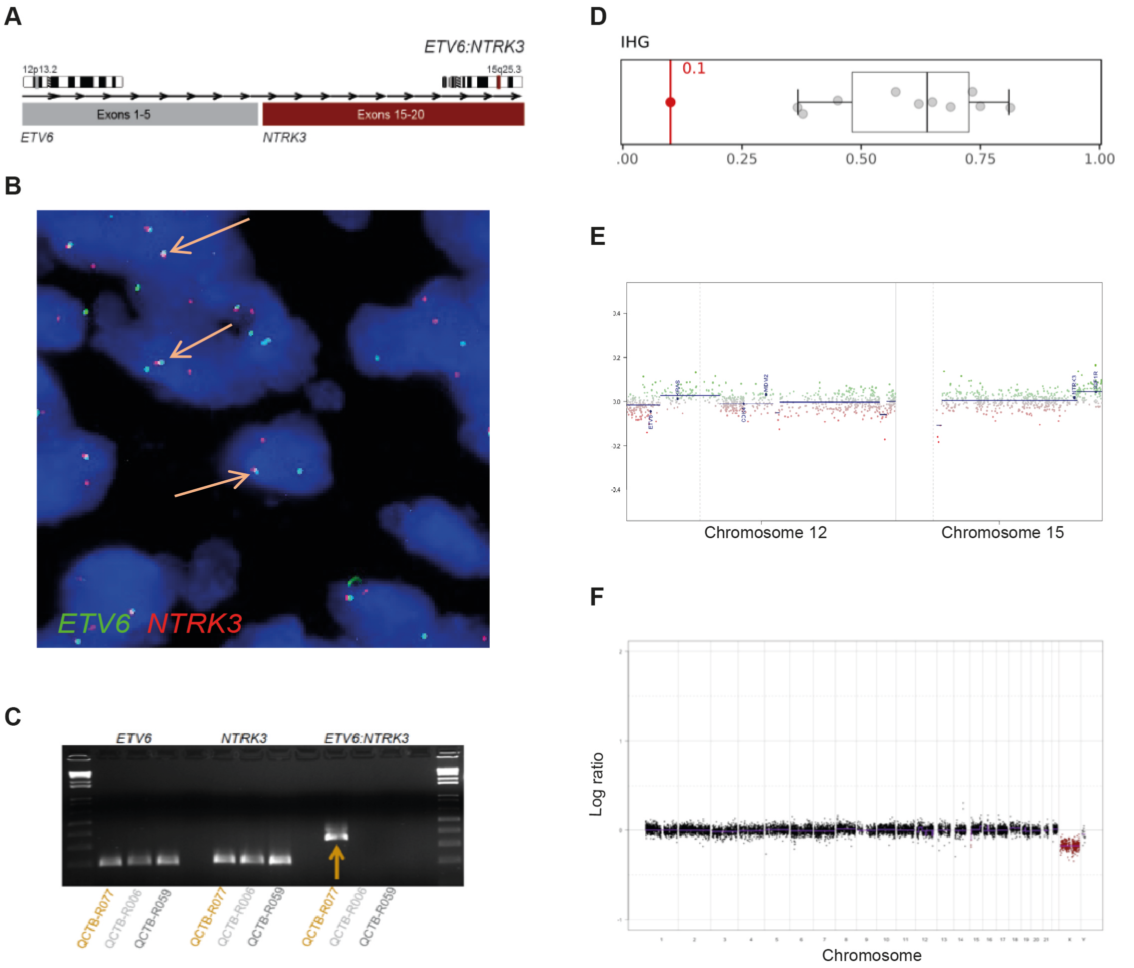

Figure 7-6. Molecular characterisation of QCTB_INF_R077. **A,** Schematic cartoon of the *ETV6:NTRK3* fusion identified. **B,** Fluorescence in situ hybridization (FISH) using fusion probes; the yellow arrows indicate positive fusion signals (green signal; *ETV6*, red signal; *NTRK3*). *C,* PCR confirming the *ETV6:NTRK3* fusion. **D,** Boxplot of the raw score derived from the methylation classifier. **E,** Copy number profiles (derived from methylation data) of chromosomes 12 and 15 with gene names labelled. F, Complete copy number profile. Green; amplification or gain. Red; deletion or loss.

The child was not treated with any adjuvant therapy. At 8.47 years old, there has been no progression or relapse; the most recent MRI scan at 8.47 years has shown no tumour recurrence, no convincing evidence of residual tumour and confirms that the child remains in complete remission (**figure 7-7**).

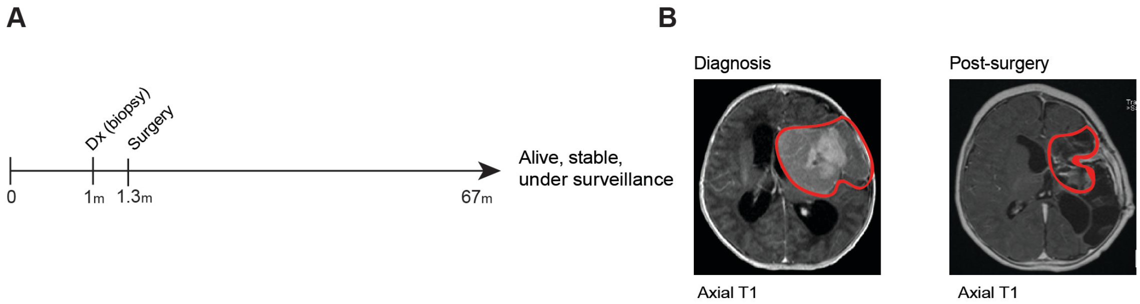

Figure 7-7. Clinical history of QCTB_INF_R077 with confirmed *ETV6:NTRK3* fusion. **A,** Timeline of clinical interventions. **B,** Diagnosis and post-surgery axial T1 MRI scans are provided, with tumor circled in red.

The second patient, QCTB_INF_R102 was also referred from the Queensland Children’s Tumor Bank, was 8 months old and presented with multiple vacant seizures. An MRI scan identified a tumour in the left temporal lobe. He subsequently received a gross total resection. Histologically, the tumour demonstrated two morphologic patterns; the first was low grade with cells forming a microtrabecular architecture, a moderate degree of pleomorphism, some multinucleated cells, numerous eosinophilic granular bodies, sparse perivascular lymphocytes and minimal proliferative activity. The second component was overtly malignant and composed of small, less-differentiated cells, mitotic activity, palisading necrosis and focal vascular proliferation. Some focal rhabdoid morphology is also seen in the malignant areas. It had a tumour-brain interface that was relatively well circumscribed without a diffusely infiltrating component. Immunohistochemistry showed positivity for GFAP, with focal positivity for the neuronal markers NFP, synaptophysin, NeuN and MAP2. There was also focal expression of CD34, desmin, EMA. Expression of INI1 and SMARC-B1 were preserved, and the tumour was negative for cytokeratins, SMA and IDH1 R132H mutation antibody.

Overall, the tumour showed both glial and neuronal differentiation with focal evidence of malignant transformation. It was concluded that it could be either a malignant glioneuronal tumour or a malignant PXA, WHO grade III. However, it was re-reviewed with clinicopathological correlation; the young age, superficial location (with dural attachment at surgery) were most consistent with a desmoplastic infantile ganglioglioma (WHO grade I-II). The atypical features were considered to be of uncertain significance. With reference to the histological diagnosis, the tumour was sequenced to look for a *BRAF V600E* mutation (reported in cases of DIGG/DIA) but this was negative. However, further molecular profiling undertaken was undertaken by the Glioma Team; methylation profiling classified the tumour as an IHG (raw score 0.37, calibrated score 0.99) with no large-scale copy number changes. Fusion panel sequencing identified a *TPM3:NTRK1* fusion which was copy-neutral. No other somatic mutations were found via exome sequencing. The child did not receive any adjuvant therapy post resection and is currently 6.77 years old, and remains stable with no evidence of recurrence or spinal metastasis, and is under regular surveillance (**figure 7-8**).

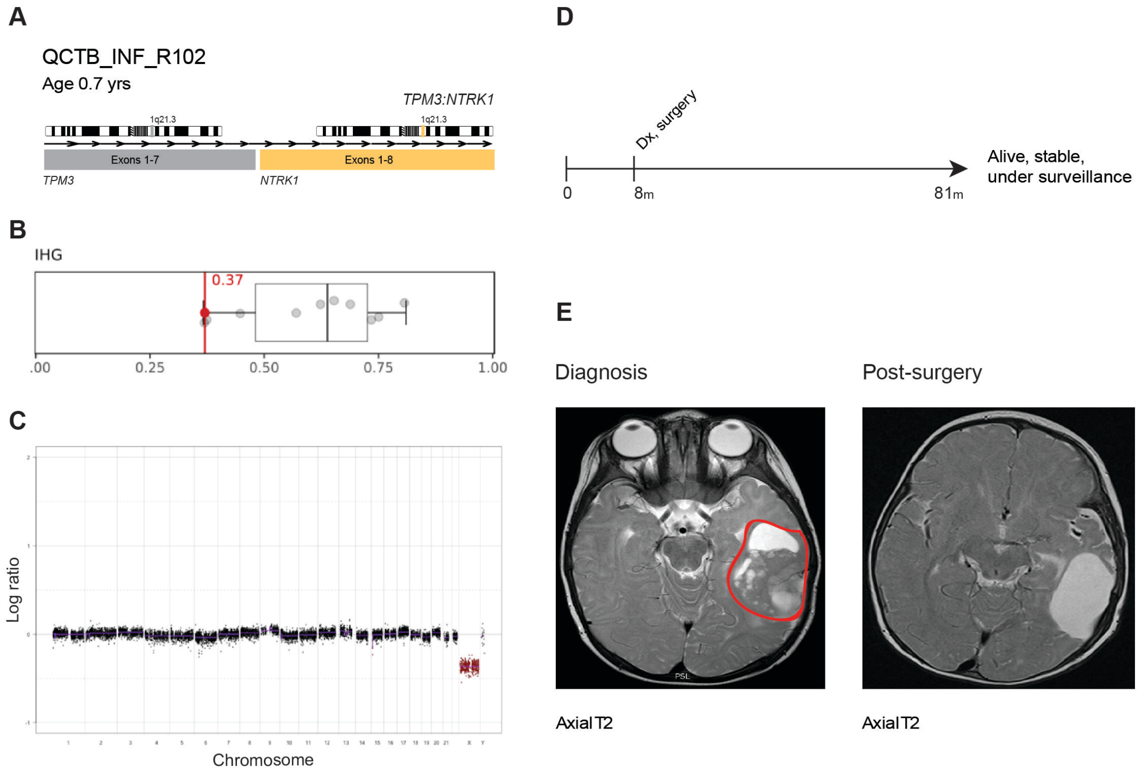

Figure 7-8. Clinical history of QCTB_INF_R102, with confirmed *TPM3:TRK1* fusion. **A,** Schematic cartoon of the *TPM3:NTRK1* fusion. **B,** Boxplot of the raw score derived from the methylation classifier. **C,** Copy number profile derived from the methylation data (green; gain or amplification, red; deletion or loss). **D,** Timeline of clinical interventions. **E,** Diagnosis and post-surgery axial T1 MRI scans are provided, with tumor circled in red.

In addition to these, we also had an example of a case with an *ALK* fusion treated with ceritinib. DKFZ_INF_307 was a 1-month-old male infant referred from the Beaumont Hospital in Dublin, Ireland but came to our attention via our collaborators in Heidelberg. The infant underwent a left craniotomy with gross total resection, and was diagnosed with a glioblastoma (WHO grade IV). Methylation profiling (performed in 2014) showed that the tumour did not classify with any known entities; as more infant cases began to be profiled using the classifier in DKFZ, it became clear that this was in fact an IHG (raw score 0.92, calibrated score 0.99). Copy number analysis showed no large-scale copy number alterations. However, small gains were identified associated with *ALK* (chromosome 2) and *MAD1L1* (chromosome 2) indicating a possible rearrangement; RNA sequencing confirmed a *MAD1L1:ALK* fusion. The patient underwent successive rounds of HIT SKK/ACNS and temozolomide chemotherapy, eventually showing progressive disease after both; he was commenced on ceritinib, resulting in stable residual disease for nearly two years to date (**figure 7-9**).

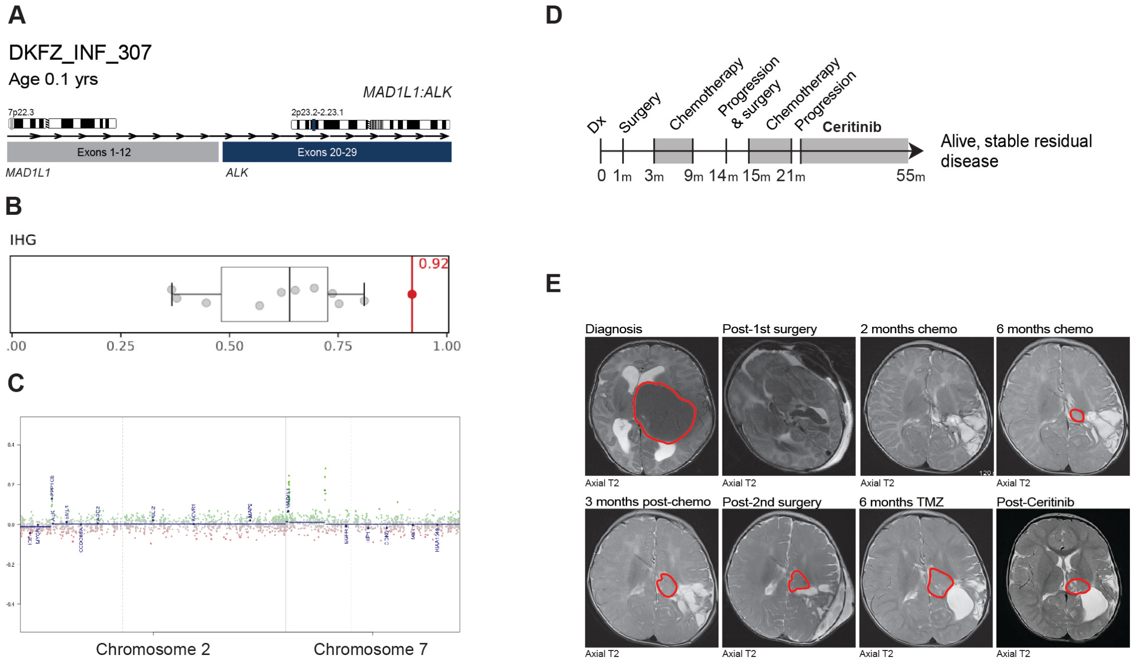

Figure 7-9. Clinical history of DKFZ_INF_307, with confirmed *MAD1L1:ALK* fusion. **A,** Schematic cartoon of the *MAD1L1:ALK* fusion. **B,** Boxplot showing the raw score output from the methylation classifier. **C,** Copy number profiles for chromosomes 2 and 7 derived from the methylation data. Genes are labelled. Green; amplification or gain, red; loss or deletion. **D,** Timeline of clinical interventions is provided with treatment shaded in grey. **E,** Axial T2 MRI scans from diagnosis and successive surgeries and chemotherapeutic regimens are provided, in addition to treatment with the ALK inhibitor ceritinib, with tumour circled in red.

7.2.2 Infant HGG of the spine

KING_INF_018 refers to a patient with an HGG of the spine being treated at the Royal Marsden Hospital NHS Trust under the care of Dr Lynley Marshall and Dr Fernando Carceller (Consultants in Paediatric & Adolescent Neuro-Oncology and Drug Development). I have used tumour samples derived from this case to establish a novel patient-derived cell culture in our laboratory (corresponding to cell culture ICR_CXJ-020), and collected longitudinal plasma for the study of ctDNA of the child on treatment with larotrectinib.

7.2.2.1 Clinical history and imaging

KING_INF_018 is a young girl, 1.5-years-old at the time of diagnosis, an ex-premature infant and an IVF non-identical twin who was born by caesarean section at 33 weeks, with intrauterine growth retardation detected at 29 weeks. She did not meet the expected developmental milestone for walking and was originally thought to have cerebral palsy. However, an MRI scan of her spinal cord revealed a large mass at the level of T8 down to the conus. She underwent a thoraco-lumbar laminoplasty with subtotal debulking of the tumour (**figure 7-12A**). We collected a small sample of tumour at the time of operation.

Histologically, the tumour was composed of cells which varied in appearance. They were predominantly composed of large nuclei with dense chromatin and ill-defined cytoplasm but frequently showed a more piloid appearance. The cells infiltrated the parenchyma and were located adjacent to neurons, some of which showed reactive features. Some of the tumour cells resembled dysplastic neurons. Some vascular hyperplasia was seen, but mitoses were inconspicuous, and Rosenthal fibres, granular eosinophilic bodies and necrosis were all absent. IHC showed positivity for GFAP and preservation of ATRX. CD34, IDH1 and H3K27M were all negative. The Ki67 proliferation was 2-3% and therefore considered to be low. These features are consistent with a complex case; the infiltrative nature and atypical features would suggest a high grade tumour.

However, the lack of mitotic activity does not support this. Differential diagnoses considered were ganglioglioma (given the dysplastic appearing neurons) and a midline glioma both of which were not supported by the IHC profile. After review by several neuropathologists, and discussion at an MDT meeting, it was diagnosed as an infiltrative HGG of the spinal cord, WHO grade III. Sequencing performed by the referring institution showed that the tumour was *BRAF* fusion & mutation negative and confirmed the *H3F3A* wildtype status (**figure 7-10**).

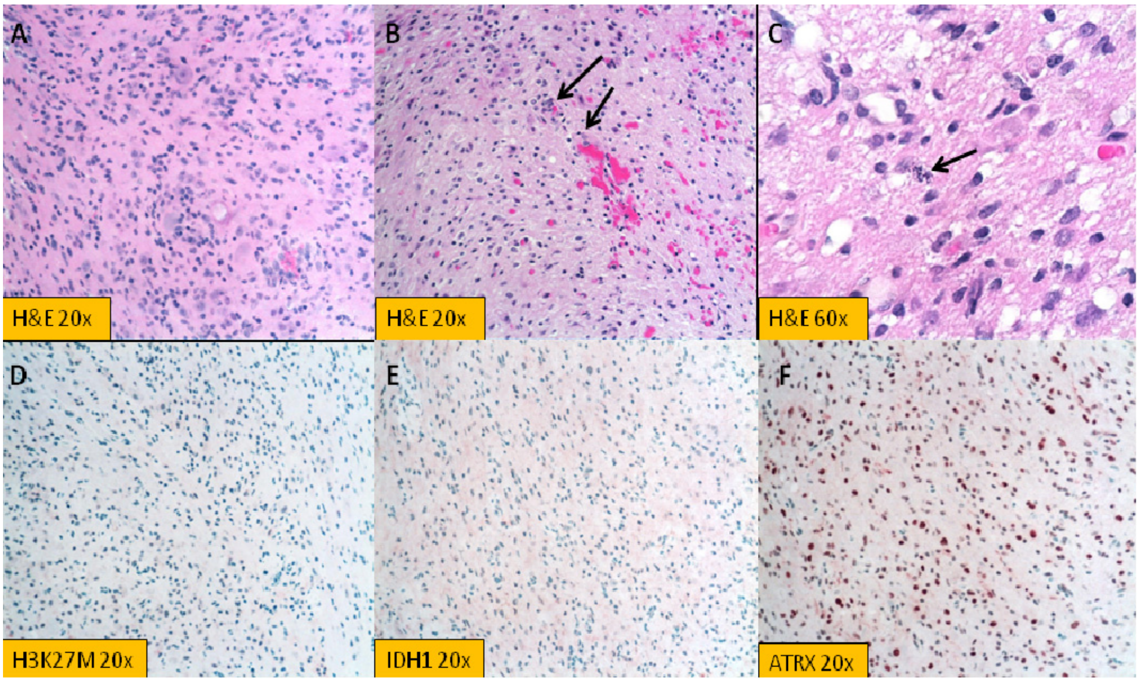

Figure 7-10. Histology review of KING_INF_018. **A,** H&E section of the tumour. **B,** H&E section demonstrating entrapped neurons (black arrows). **C,** H&E section demonstrating mitotic figures (black arrow). **D,** Immunohistochemistry for H3K27M mutation. **E,** Immunohistochemistry for IDH1. F, Immunohistochemistry for ATRX. Brown staining indicates positivity (172). Photographs: Zita Reisz.

Having been diagnosed as an HGG, and due to an incomplete resection, the patient was treated with adjuvant Baby SFOP protocol chemotherapy and completed 4 cycles. Given her age, it was decided not to treat her with radiotherapy. Subsequent MRI scans showed stable disease.

7.2.2.2 Characterisation

Methylation profiling of the tumour classified it as a poor scoring LGG_PA_PF (calibrated score 0.30), located in the continuum between the IHG and DIGG/DIA group on a t-SNE projection. Fusion panel sequencing identified a *KCTD16:NTRK2* fusion which was validated by PCR and Sanger sequencing (**figure 7-11**).

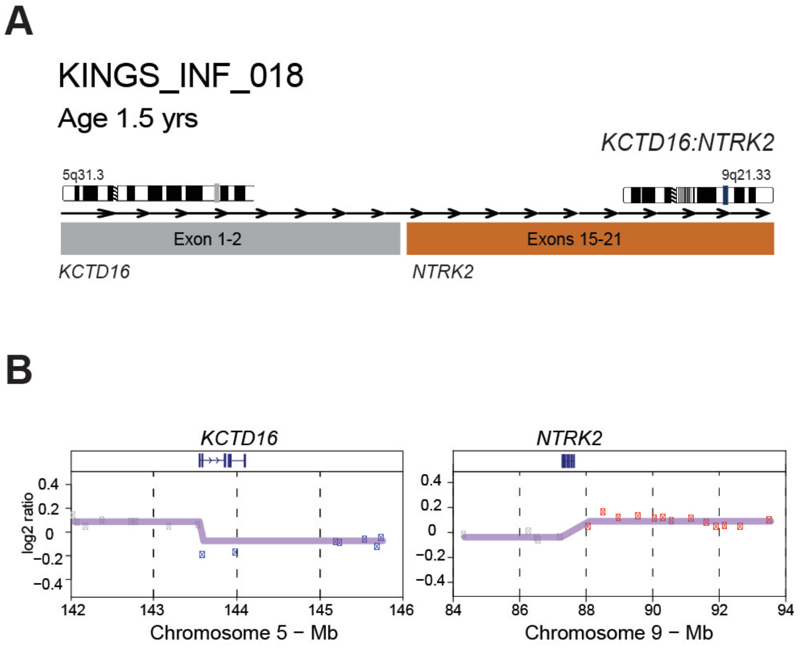

Figure 7-11. *KCTD16:NTRK2.* **A,** Cartoon representation of the fusion structure. **B,** Copy number plots (log2 ratio, y axis) for chromosomal regions spanning the breakpoints (x axis) underneath. Points are colored red for copy number gain, blue for loss, and grey for no change. The smoothed values are overlaid by the purple line.

Copy number review showed no large-scale chromosomal arm changes. However, it did reveal a small loss associated with the *KCTD16* gene and a small gain at *NTRK2* further validating the fusion. Exome sequencing did not identify any background mutations in this case; this was confirmed by routine profiling using the NGS paediatric solid tumour panel developed at the Centre of

Molecular Pathology (Royal Marsden NHS Hospital Trust), followed by discussion at the Molecular Tumour Board (156).

7.2.2.3 Trial with larotrectinib

As a result of the identification of the *KCTD16:NTRK2* fusion in our lab the child was enrolled onto the larotrectinib SCOUT trial which aims to assess the safety and efficacy of the drug in children. To date, she has had 18 cycles of the drug, taken orally at 100mg/m2 twice daily with a 28 day continuous dosing cycle. However, it was necessary to decrease the dose to 75mg/m2 due to prolonged neutropaenia. The MRI scan post cycle 12 showed a 20.6% reduction in the size of the tumour compared to baseline representing stable disease (**figure 7-12**).

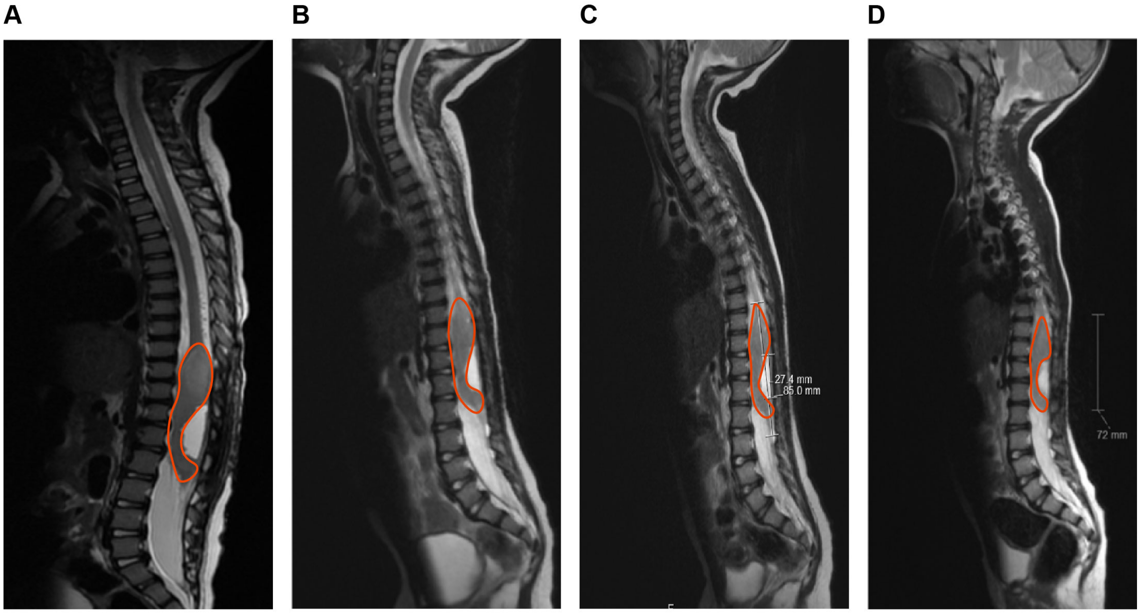

Figure 7-12. MRI scans during treatment. **A,** MRI T2 weighted sagittal image of the spine post-surgery. **B,** MRI T2 weighted sagittal image of spinal tumour at baseline after chemotherapy. **B,** MRI T2 weighted sagittal image post cycle 2 of larotrectinib. **C,** MRI T2 weighted sagittal image post cycle 12 of larotrectinib. Tumour is outlined by a red line in each image.

7.2.2.4 *In vitro* and *in vivo* studies

The KING_INF_018 tumour sample was processed in accordance with the laboratory protocols to establish an *in vitro* culture. The cells grew as a 2D adherent culture on laminin-fibronectin substrate. However, they would not grow in 3D as neurospheres. The growth rate was subjectively very slow taking many months before the cells would reach 80-90% confluency in a T12.5/T25 flask. They would not grow successfully in flasks that were larger than this. The addition of BDNF, NT3 and NT4 growth factors to the media improved the growth rate of the cells.

The phenotypic appearance of the cells was different to that seen in the other two infant cultures; the cells were very spindle-shaped and grew in very close contact with each other, often forming a wave-like architecture. Very rarely separate groups would grow in the same flask but cells of these groups would remain very adherent to each other.

With sufficient cells available, drug assays were performed using entrectinib and larotrectinib (as described in chapter 2). In line with findings from QCTB_INF_R077 and QCTB_INF_R102, ICR_CXJ-020 showed increased sensitivity to entrectinib compared to the fusion-negative lines (*P*=0.1487, IC50 = 4.6μM, 7.6μM 1.9μM respectively), and showed no sensitivity to larotrectinib *in vitro* (**figure 7-13**).

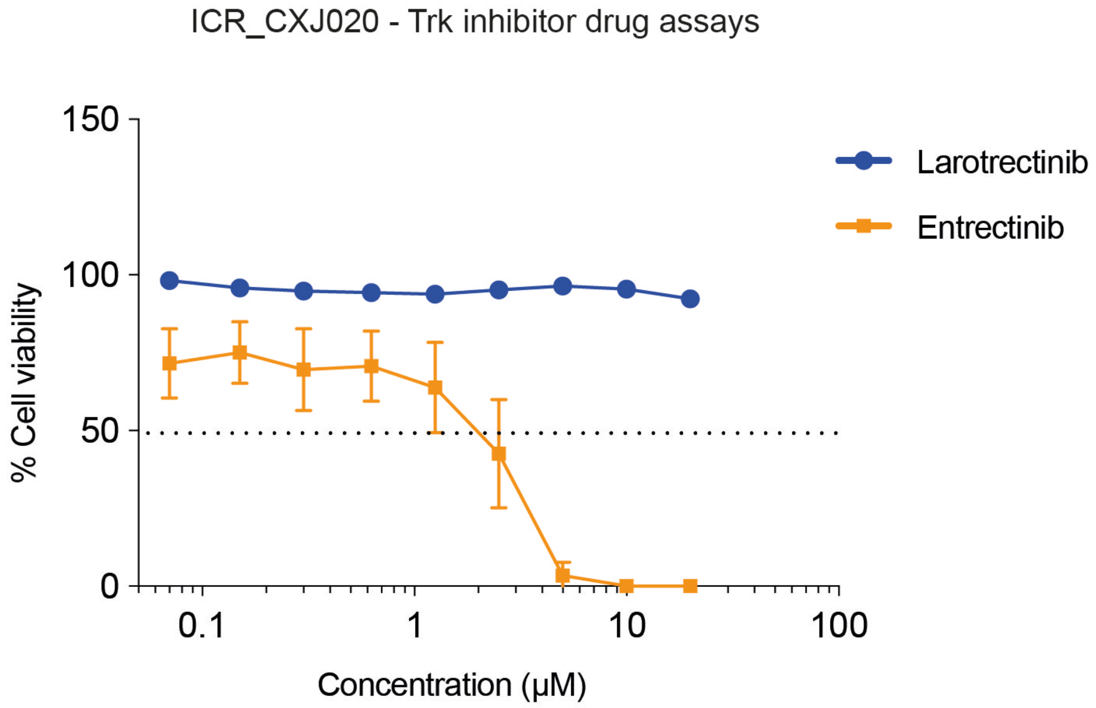

Figure 7-13. ICR_CXJ020 response to Trk inhibitors. Concentration–response curves for entrectinib (Trk inhibitor, orange line) and larotrectinib (Trk inhibitor, blue line) tested against the *NTRK* fusion–positive infant glioma cell cultures ICR_CXJ020 (*KCTD16:NTRK2*). Concentration of compound is plotted on a log scale (x-axis) against cell viability (y-axis). Mean plus SE are plotted from at least n=3 experiments. GI50 marked by dotted line.

In addition, 250,000 cells at passage 6 were injected intracranially (hemispheric location) into four NSG mice (Charles River) aged 3-4 weeks. MRI scanning at day 138 post-injection revealed irregularities to the surface of the brain and a slightly increased size of the right lateral ventricle of one mouse; these changes may be responses to the intracranial-injection. The other three mice showed no evidence of tumour formation (**figure 7-14**).

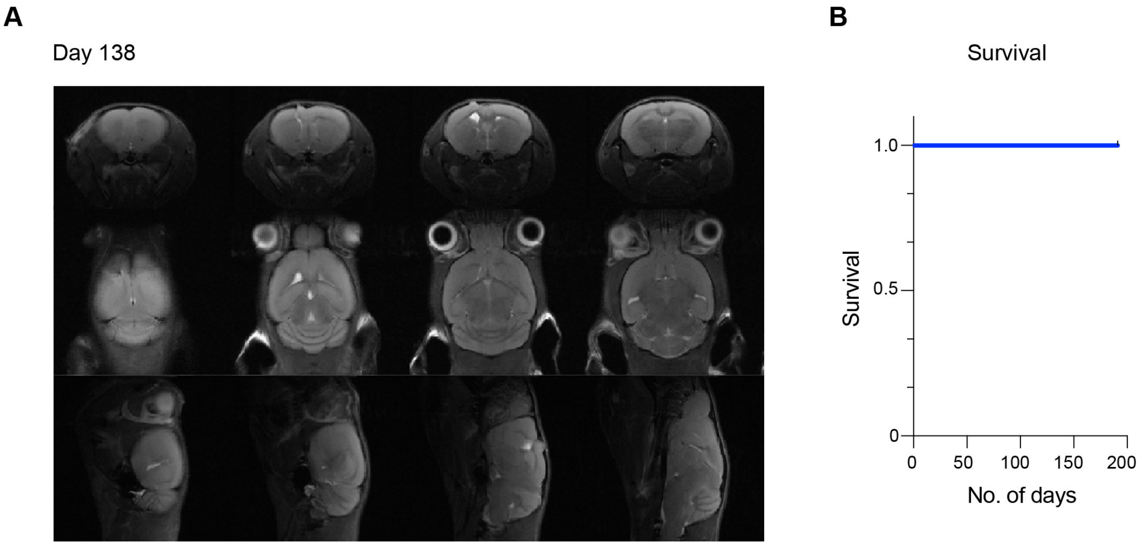

Figure 7-14. MRI imaging post-intracranial injection of ICR_CXJ020. **A,** T2-weighted MRI images of one mouse from the cohort on day 138 post intra-cranial injection. **B,** Kaplan-Meier plot of overall survival of the 4 mice in the *in vivo* study to date.

7.3 Discussion

The presence of recurrent *ALK/NTRK/ROS1/MET* fusions in infant gliomas makes them amenable to selection for targeted treatment and clinical trials. The individual examples described in Chapter 6 show the successful use of targeted Trk inhibitors both *in vitro* and in the clinical setting. Larger trials also show similar results; a phase 1-2 trial of solid fusion-positive tumours with larotrectinib featured 55 patients aged between 1 month and 76 years (11 cases aged <5 years), with 17 different fusion-positive tumour types. They showed a response rate of 75% with only grade 1 adverse events (187). Although no fusion-positive brain tumours featured in the study, the positive response combined with the good side-effect profile of the drug shows promise for similar trials of fusion-positive infant gliomas with larotrectinib; such a trial is currently being developed by the CONNECT Consortium in response to the collaborative work of my study (202). This trial will enroll 15 newly diagnosed children (aged 1 month to 21 years) with *NTRK* fusion-positive HGG, treated with larotectinib monotherapy or combined with chemotherapy or radiotherapy (dependent on age and clinical indication). The primary objectives are to assess the disease control rate after 2 cycles, and to characterise the plasma and tumour pharmacokinetics of larotrectinib by analysing the re-resected tumour samples post-treatment (where clinically indicated). The drug tolerability, safety profile, and progression-free survival compared to conventional chemotherapy regimens will also be monitored. In addition, cfDNA derived from CSF samples will be used to assess fusion detection (202). This trial will potentially provide much-needed data about the efficacy of larotrectinib in infant HGG.

Trials with entrectinib have also shown promising results; three phase 1-2 trials using oral entrectinib for the treatment of locally advanced or metastatic *NTRK*-fusion-positive solid tumours showed that 31 of 54 patients had an objective response with 7% of these being a complete response and 50% a partial response. The drug was well tolerated and had a manageable safety profile (203). Although all patients enlisted in these trials were aged >18 years, the results show clinically meaningful responses can be achieved which may also be seen in the treatment of infant fusion-positive brain tumours.

Although great success is being shown for targeted therapies, we also describe successful outcomes for infants (QCTB_INF_R077 and R102) who have undergone surgery alone with no adjuvant treatment and continue to do well with stable disease. Other cases with a similar treatment approach and outcome are also reported including an infant with a *PPP1CB:ALK* fusion who underwent a gross total resection followed by two subsequent resections (the first for cyst fenestration, and the second to remove a growing nodule from the site of the original resection (124). However, the histological appearances of these stable tumours may provide some indication as to why no chemo- or radiotherapeutic intervention is needed in some of these cases; in the case of the *PPP1CB:ALK* fusion, the histology at the third resection of a growing residual nodule 4 years after the first revealed a tumour that was low cellularity, composed of mature ganglionic cells and very few mitoses and therefore diagnosed as a ganglioglioma (WHO grade I), very different to the high grade glioma features that the tumour showed at initial resection (124).

It is reported that post-radiotherapy or as a result of a tumour predisposition syndrome, tumours can develop at the previous resection or treatment site which are not consistent with the initial diagnosis (204). The histological diagnosis of QCTB_INF_R102 was a desmoplastic infantile ganglioglioma (WHO grade I-II), consistent with prominent glial and neuronal components to the tumour. However, this was not a straight-forward diagnosis; high-grade areas observed, as well as ‘rhabdoid cells’ which show similar features to the gemistocytic-like cells seen in IHG cases. Methylation profiling classified it as an IHG (0.98) rather than a DIGG. Also, on histological review one high-scoring *EML4:ALK* fusion-positive IHG case (UOLP_INF_001) also showed a focal area of ganglion cells; this tumour was diagnosed *in utero* but was not resected until 5 months after birth (gross total resection). The tumour was diagnosed histologically as a high-grade neuroepithelial tumour (with consistent high-grade features of necrosis, vascular proliferation and prominent mitoses) but interestingly ganglioneuroblastoma was also in the differential diagnosis. The child was not treated with adjuvant therapy and has been doing well clinically. The initial resection of MSKC_INF_006 was diagnosed as a low grade neuroepithelial tumour (containing prominent gemistocytic cells, often seen in IHG cases (see chapter 3)) but the later resection was diagnosed as a ganglioglioma. Although illustrated by very small numbers, the excellent outcomes of the cases which show a ganglion cell component to the tumour, combined with the fact that they have received no adjuvant therapy may provide evidence to support the importance of differentiation and decreased proliferation, possibly through oncogene-induced senescence for the improved outcome of IHG cases (9).

This is also hinted at by the *in vitro* growth of these cell cultures; as previously described, both QCTB_INF_R077 and QCTB_INF_R102 successfully grow to passage 11 after which the proliferation rate reduces, their phenotype changes (they appear larger) and then remain static, mimicking the clinical timeline of these patients. Similar changes have been reported in paediatric pilocytic astrocytomas; a pilocytic astrocytoma cell culture model with doxycycline-induced oncogene induced senescence showed up-regulated senescence-associated secretory phenotype factors (IL1B and IL6), also seen in primary pilocytic astrocytoma cell cultures (184). Also, studies have reported that neural stem cells transduced with *BRAF V600E* mutation showed a reduced proliferation rate, and increased nuclear diameter and overall size of the cells, and induced markers of oncogene-induced senescence such as PAI-1, acidic β-galactosidase and p16^{INK4a} (205). This may advocate an approach of ‘watchful waiting’ after initial attempt at gross total resection surgery to monitor how the tumour will behave, before considering whether to use a targeted approach.

However, although many infant cases show improved survival and have good responses to treatment (particularly those which are fusion-positive), there are some that do not do as well, including the fusion-negative cases. At present, with such a small number of cases for which clinical data is available, it is not clear which factors are important in predicting which cases will do worse than others.

Paediatric HGG of the spine usually associated with a very poor prognosis but are also very rare (206). A study of 28 patients (mean age of 11.28 years) with WHO grade III or IV tumours showed a median overall survival of 2.5 years after receiving surgery, chemotherapy and radiotherapy. Interestingly, an age of <5 years was a positive prognostic indicator of overall survival along with complete surgical resection (206). However, being a midline location, histone mutations can also be found in these cases; a 4-year-old boy with a cervical and upper thoracic spinal HGG (WHO grade IV) showed positivity for H3K27M by IHC and was therefore diagnosed as an DMG H3K27M-mutant and died 4 months after diagnosis (207). Radiotherapy post-surgery has been the conventional form of treatment, even in paediatric cases, with children who undergo surgery without adjuvant therapy having the worst prognosis overall (208). KING_INF_018 was treated with chemotherapy but not radiation. A histone mutation was not found to be present by IHC or exome sequencing. The tumour has continued to remain stable on larotrectinib, raising the possibility of senescence and differentiation in this case too. It also hints at an optimal window for treating these tumours with targeted inhibitors, after which they are less likely to respond; although the time point of which is currently challenging to define given the limited evidence, but early after surgery may show clinical benefit particularly if gross total resection has not been achievable. Longitudinal sampling of cases like this, either through tissue or liquid biopsy may help to identify this.

cfDNA has been very useful in identifying biomarkers of HGG in both serum and CSF including *IDH1, ACVR1, ATRX, TP53, PDGFRA, NF1* and *PTEN* mutations, 1p/19q co-deletion and MGMT methylation status (209). Our study (for which I am a co-author) on molecular profiling in paediatric tumours featured 12 cases where cfDNA was derived from plasma; 3 of these patients showed concordance of results with FFPE tumour DNA samples. In 5 samples new variants were identified which were not detected in the FFPE samples, including a new *ALK* hotspot mutation in a neuroblastoma case which already contained an *ALK* F1174L mutation thus showing the potential value of cfDNA sequencing, and further illustrating tumour heterogeneity (156). Our secondary study (for which I am also a co-author) showed this value applicable to paediatric HGG; ctDNA from CSF was at higher concentrations than that derived from plasma or serum (67% versus 26% and 33%), but also cfDNA levels could be correlated with disease progression in DMG_K27 cases (n=2), and improved survival in *BRAF V600E* positive hemispheric cases (n=2). ctDNA could also be used in fusion detection with an *ETV6:NTRK3* fusion identified via fusion panel sequencing in CSF derived from the infant case OPBG_INF_035 (201). Another study also looked at cfDNA from plasma samples from 13 patients with gliomas (10 GBMs) and identified somatic copy number alterations in 5 of 13 patients, comparable to the original tumour and with CSF samples. However, the detection in the CSF was dependent on glioma grade, size and the quantity of cfDNA (210). CSF may be the more optimal method of monitoring due to the reduced sensitivity of biomarkers from serum samples, possibly related to the ability of the blood-brain barrier to obstruct the passage of tumour DNA into the circulation (211). Some studies quote sensitivities of 58% for CSF samples compared to 0% for serum samples in GBM cases (209). CSF-derived cfDNA has also enabled the identification of the H3.3K27M mutation in cases of DIPG with sensitivities and specificities of 87.5% and 100% respectively (212). Extracellular vesicles derived from either the cell membrane or the endosomal system and are rich in nucleic acids and those derived from CSF have been used in the diagnosis of GBM (209). Plasma samples were collected and sequenced for CXJ020 but due to the

COVID-19 pandemic, these could not be analysed. However, they represent options for longitudinal monitoring of the evolution of the tumour in response to treatment in terms of molecular changes or response to treatment.

CHAPTER 8 – General discussion; classification of infant glioma

8.1 Novel infant subgroups

Malignant glioma presenting in infancy represents a specific clinical challenge, involving diagnostic uncertainty and a hesitancy to aggressively treat given the reported superior outcomes compared with older children, coupled with the high risk of neurocognitive deficits (5). This is compounded by a lack of biological understanding due to the rarity of these tumours. My thesis sought to address this by bringing together a large international collaborative study with the largest collection of tumours originally reported as high-grade or diffuse gliomas in this age group.

This study uniquely includes methylation and gene expression data, and allows for refinement of subgroups within the malignant spectrum of disease with important clinical management implications; experience of clinical responses with targeted agents are also presented, even after progression on standard chemotherapies. It includes a histological review of the cases, helping to identify specific features which characterise these tumours, refining the diagnostic process. I have also undertaken a small longitudinal study of infant HGG, which to the best of our knowledge is the first of its kind, exploring the evolution of these tumours with both time and treatment. The overall study features several examples of case histories of fusion-positive infant HGG who have been referred and had their tumours profiled by myself and have been successfully treated with Trk inhibitors based on the work of this study. The findings of this study will have a significant clinical impact worldwide on the diagnosis, treatment and outcome for these very young patients.

Other studies of infant HGG are rare and feature far fewer cases than my study. Another recent multi-institutional study was predominantly comprised of low-grade tumours (n=104), with only 33 cases of HGG, and five cases displaying a mixed histological picture (9). They conducted a histological review of their cases, and tumour samples underwent molecular characterisation (targeted single nucleotide variant and fusion profiling, and copy number arrays), which identified three different subgroups. However, they did not use methylation profiling to further characterise the subgroups and relied on the histological assessment to make the diagnosis (9), which my study has shown is not reliable for both in terms of accuracy and as a predictor of prognosis. Prior to this, a study of 35 infants with diffuse HGG (featuring both GBM and AA cases) used multiplex ligation probe-dependent amplification (MLPA), immunohistochemistry and pyrosequencing of known glioma-associated genes; they showed a distinct absence of the most frequently HGG-associated genes and a reduced number of chromosomal alterations compared with older children (94). However, a detailed histological review was not undertaken and the identification of fusions within the cohort was not explored.

A classification of infant HGG has therefore long been needed to understand the apparent clinical differences. Existing classifications define subgroups based on tumour location and mutations; in the paper by Stucklin *et al* (2019), their classification encompasses both high- and low-grade infant gliomas and defines three subgroups. Specifically, these include tumours which are hemispheric RTK driven (group 1; including HGG cases, some LGG cases, and others difficult to determine by histology), hemispheric RAS/MAPK driven (group 2; comprising LGG tumours), and midline RAS/MAPK driven (group 3; comprising LGG) (9). Identifying the driving mutations is clearly important, and the group defined by the presence of RTK fusions is a significant finding and in keeping with my study, but relying on histology to determine the tumour type associated with the fusions creates diagnostic uncertainty, particularly for the group 1 cases with a mixed histological picture (9). Given that we have identified new infant subgroups in my study through methylation profiling and subsequent molecular characterisation, it is hypothesized that many of these fusion-positive cases would be classified as IHG, also supported by the lack of other known pHGG-associated somatic mutations in these cases. Methylation profiling has helped to define our infant HGG cohort further and provide a more detailed classification. This is very important as IHG tumours have subtle but characteristic architectural and cytological features by histology, but they also share many features of GBMs which also occur in the infant age group; a third of cases classified as well-established high or low grade tumour entities. They occur in children aged >1 year, in diverse locations within the CNS and are characterized by expected molecular findings, including pathognomic fusions (although far less frequently than other infant subgroups) and mutations. They are best regarded as examples of classic paediatric HGG and LGG entities occurring in the infant population. Using methylation profiling helps to make the diagnosis more accurate from the very beginning of the diagnostic pathway; our study has shown that treatment of fusion-positive infant HGG tumours should be different to the established protocols and so accurate diagnosis should be the target and will significantly impact on the future management of the patients. As a direct result of this and to highlight the importance of this work, I am proposing my own classification of infant HGG subgroups (**figure 8-1**).

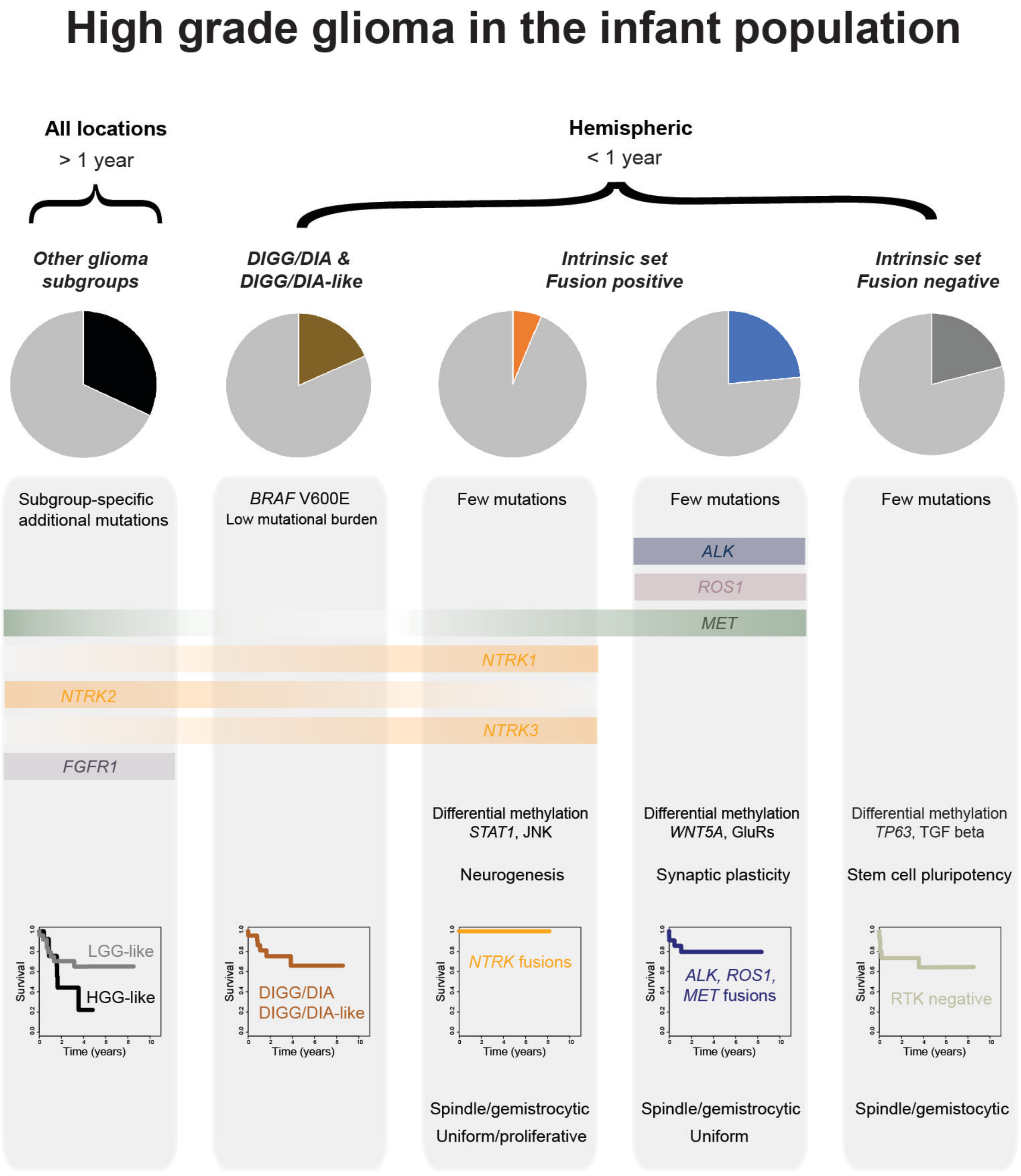

Figure 8-1. Classification of high grade glioma in the infant population. A classification of infant high grade gliomas showing the different subgroups identified by this study. The histological, molecular and clinical features of each subgroup are provided.

Four different subgroups (with a fifth group encompassing existing known HGG and LGG entities) are presented each of which are characterised by their clinical, histological and molecular features. Some are already well known including the well-characterised infantile tumour entity DIGG/DIA, which occur in infants aged <1 year and in hemispheric locations. As already mentioned, others classified as a member of the already established HGG and LGG entities with their characteristic molecular profiles. However, the remaining cases either classified as the relatively new tumour entity called IHG, or classified very poorly. The poor-scoring cases formed a continuum between the IHG and the DIGG/DIA groups on the t-SNE, and have therefore been termed ‘DIGG/DIA-like’. These cases are interesting as they do not fall into either of the established clusters but project between them. This could result from a number of explanations; it could be related to QC of the DNA, or the quantity impacted by the amount of material available for extraction. This would affect the processing (including quality of bisulfite conversion) and the output from the array. However, they passed our QC of the methylation array data and therefore remained in the cohort. Alternatively, these cases may represent a possible evolutionary trajectory between the two infant tumours; RTK fusions were found in this group (predominantly *NTRK*) with an absence of somatic mutations, and so they do show similarities to the molecular profile of IHG cases. It is hypothesised that the DIGG/DIA-like tumours represent an evolutionary link between the two. Further work is needed to explore these possibilities, including the acquisition of a great number of cases, a more extensive histological review, and clinical correlation. However, overall the DIGG/DIA, DIGG/DIA-like and IHG cases form the ‘intrinsic set’ of infant gliomas. The intrinsic set (found in infants aged <1 year and in hemispheric locations) are further divided into other novel subgroups based on histology, molecular features and survival.

8.2 Clinical characteristics

The signs and symptoms at presentation were not specific to the infant subgroup but are more appropriately discussed in terms of the age of the child. Brain tumours in infants aged <1 year, specifically those classed as congenital, were identified by ultrasound scan *in utero*. Others did not meet the expected developmental milestones or failed to thrive. Acute clinical presentations were also seen with reduced consciousness and signs of intracranial haemorrhage. Although not specific, children aged >1 year more frequently showed specific neurological signs including hemiparesis, seizure activity, eye signs, and more general symptoms including vomiting and irritability. The early presentation of these brain tumours (i.e. before birth) could argue for some form of screening. However, there are significant cost implications given the rarity of the tumour, but we already effectively screen for this using the 20 week anomaly ultrasound scan which is performed on every expectant mother in the UK and US. This will vary worldwide, and some tumours appear later, but given the logistical and financial constraints it is a useful early warning for the presence of these tumours. Further work looking at the specific developmental stage when these tumours develop would also be very useful and informative for diagnosis. However, if a tumour did develop in an infant after birth, studies have shown that the TDI is reduced for younger children (111) possibly related to more frequent interaction with healthcare professionals and observations by parents and family. Campaigns such as HeadSmart (110) provide parents with knowledge of signs and symptoms; further campaigns through engagement with nurseries and schools may help to ensure that these tumours are identified even earlier helping to prevent significant impact on the still-developing brain.

Radiological appearances varied according to tumour type; there were no reported differences between established tumour entities occurring in infants and older children. However, cases in the intrinsic set were characterised by a hemispheric location, large size and solid-cystic components. These are not specific to the intrinsic set and similar appearances are seen in HGG cases. Other studies have not reported unique radiological features for infant HGG cases (92), but individual published case reports often describe similar features to those found in this study (81,119,124,126). However, it should be noted that the IHG tumours are a relatively new subgroup and there may be subtle radiological features (similar to the histology) which would help radiologists to consider IHG tumours in their differential diagnosis. To the best of our knowledge, no studies of this nature have explored the specific radiological features of IHG tumours; with the acquisition of more cases (and the retrospective review of existing ones), this would also provide a valuable adjunct to the characterisation of this tumour and assist diagnosis. Histology has shown that these tumours frequently have a well-defined border without infiltration into the normal brain parenchyma. Therefore, if a radiologist can suggest that the tumour may be an IHG rather than a GBM (which should automatically be considered with reference to the age of the patient, tumour location, and general radiological appearance), then this may result in the surgeons taking a different strategy to maximise the chance of achieving a complete resection. Serial imaging is also crucial in these cases; after subtotal resection I describe cases where tumours did not progress and did not require further treatment, and so close monitoring of other such cases is important.

8.3 Histological characteristics

The need for careful scrutiny of the diagnostic pathway is demonstrated by the finding that 84% of the IHG cases are reported histologically as an HGG. Histological features overlap with HGG (including microvascular proliferation, palisading necrosis and frequent mitoses). These features in IHG cases can make diagnosis challenging due to the association of such features correlating with aggressive tumours and poor survival. However, histology still has an important role in their diagnosis; the architectural (increased cellularity and sheet-like monotony) and cytological features (spindle-shaped or gemistocytic-like cells, and occasional ganglion cell components) of the IHG and DIGG/DIA-like cases are useful characteristics for a neuropathologist to identify. Histology is also needed to assess the percentage of tumour cells, the cellularity of the tumour, and confirm if tumour is present to correctly interpret molecular results but can be inaccurate and requires training (213). The DIGG/DIA tumours are characterised by a spindle-shaped cell morphology but can also be composed of gemistocytic-shaped neoplastic astrocytes (13). I think that focal areas showing the described cytological features implies that they are evolving changes, particularly with the prominence of the spindled cell change and ganglionic cells seen in the longitudinal study, but more detailed and extensive reviews are needed to firmly establish which trajectory the changes are following and the molecular characteristics of these different cellular morphologies. Supporting the hypotheses drawn from the methylation profiling, the histological findings hint at a continuum or evolutionary link between the two groups, perhaps in relation to the cell(s) of origin. Further work is needed, particularly exploring more longitudinal cases to further understand the evolutionary trajectory of these tumours, aiming to establish a possible timeline; not all such cases showed a changing morphology and the reasons may be related to differing time periods between resections or molecular profiles. More cases are needed to provide answers to these questions.

Immunohistochemistry (other than Ki-67) formed a small part of the histological review performed as part of this study. However, its use in fusion identification is reported although not always reliable (214); for *ALK* fusion-positive tumours, expression levels of ALK protein are variable depending on tumour types (215) and protein expression is not always linked to a gene rearrangement (135,214). Therefore, the risk is that a case may be fusion-positive, but the fusion is missed if the results of immunohistochemistry are used in isolation. Antibodies exist which will detect *ALK* expression (even at low levels) and with good concordance with sequencing results (216) but even this may be impacted by existing protocols for the fixation of material. Molecular and proteomic results can be altered by sub-optimally processed FFPE material including differences in prefixation handling, tissue-to-fixative ratios, and paraffin embedding reagents (217). Differing fixative types and times can also lead to interpretive errors including detection of *ALK* overexpression by other mechanisms (135). For *NTRK* fusions, a pan-Trk antibody is required but sensitivity can vary with one study quoting only 75% of fusion-positive cases detected (150), and 45% of *NTRK3* fusion-positive cases (detected by sequencing) were negative by IHC (150) which is clinically significant and further supports the idea that immunohistochemistry should not be used in fusion detection.

Other panels of immunohistochemistry could have been explored (including stains such as GFAP, S100, Nestin, EMA and OLIG2 amongst others) similar to those described for other CNS tumours and detailed in the WHO classification (13). This would allow a characteristic immunohistochemical profile for the IHG cases to be attained. Fusion detection by immunohistochemistry could also have been explored. However, a careful balance is needed with the best use of material for both research and diagnosis. I would argue that for these infant cases, and especially for very small biopsies, extracting DNA from FFPE rolls, which can then undergo methylation profiling would be of more value than using many sections to explore the immunohistochemical profile (which may not give a definitive answer) and would leave very little material for further investigations such as fusion detection by sequencing. Some centres are now using methylation profiling and fusion panel sequencing on all their paediatric cases as standard.

The discrepancy between the high-grade histological features of the IHG cases versus the improved survival means that assigning a WHO grade for these tumours is not straightforward. The grading system is used to help predict the clinical course of a tumour and the overall prognosis (13,218). Most are being reported as WHO grade III or IV due to histological high-grade features, and are being managed in accordance with this. Ki-67 shows fusion-positive cases have a higher proliferative index (particularly *NTRK*) than fusion-negative cases with the fusion causing an overactivation of signal transduction pathways resulting in proliferation, differentiation, and the prevention of apoptosis thereby increasing cell survival in both neoplastic and non-neoplastic cells (95). A high proliferative index is also a high-grade feature (13,219) but this study has shown that these cases have a significantly better outcome than predicted by their histology. However, some cases do not have a good outcome succumbing to the disease within four years of diagnosis. Previously, this was related to the management approach of infant HGG; these tumours were biopsied and if confirmed to be an HGG by histology, they would not undergo further resection and best supportive/palliative care was the ceiling of treatment. These cases have subsequently been diagnosed as IHG in our study; given the improved survival of these tumours, accurate diagnosis and characterisation of infant tumours is essential to ensure that this does not happen in clinical practice. Although not related to the disease, another infant died as a result of haemorrhagic complications post biopsy (and given the high vascularity observed on the histology, this is an unsurprising risk). However, other IHG cases have shown clinical progression of the tumour with the patient dying due to disease. The value of WHO grading has recently been questioned, with cases from the HERBY trial showing that the assignment of a WHO grade has no prognostic value for these cases (93). Until more clinical data specifically related to the follow up of these cases is available, neuropathologists should not assign a grade and advise close monitoring and frequent clinical review, as recommended by the forthcoming WHO CNS Classification 2020 for the IHG tumours.

8.4 Molecular characteristics

Molecularly, the intrinsic set are characterised by the presence of RTK fusions (*ALK/NTRK/MET/ROS1*), at a significantly higher frequency than those seen in older children and the other glioma entities, with *ALK* fusions confined specifically to infants. They are identified via copy number changes, FISH and different sequencing modalities (Sanger, panel, whole genome and RNA). Each method has limitations; FISH, although more widely available than other techniques, requires design of specific probes, expert interpretation, varied sensitivity/specificity, and it will not confirm fusion expression. DNA-based NGS fusion panels need to be specifically designed to capture the required sequences; fusions detected also may not be in-frame or expressed (220). WGS allows the detection of a larger number of fusions because all intronic regions are sequenced in all genes but has a lower sensitivity, requires more computational/bioinformatical input for analysis and is more expensive (150). RNA sequencing will confirm if the fusion is expressed. However, RNA is more labile than DNA and the ability to detect low-level transcripts is very challenging (150). My recommendation would be for all cases to undergo methylation profiling; the copy number data derived from this can be screened for breakpoints in the RTK genes (**figure 8-2**). In addition, or where methylation profiling is not achievable, custom designed panel sequencing is recommended. Findings should be validated by RNA sequencing confirming the fusion but also providing expression data which may be important for the subsequent response to a Trk inhibitor. Alternatively, FISH could be used if RNA is not available (**figure 8-2**). Where possible, we attempted to validate the fusions using one of the methods listed above given the limitations of each method, and for decisions about treatment. However, this was not possible in all cases; some cases underwent only one form of fusion detection due to limited material or an absence of it; some fusions were identified via copy number alterations alone. However, these were scrutinised using validated fusion associated copy number changes so we feel confident in our interpretation. Also, the fusion panel did not feature sequences for the *ROS1* gene and so two fusion-negative cases were diagnosed with *ROS1* fusions after WGS. Recently, *ETV6:RET* fusions have been identified in other RTK fusion-associated tumours such as secretory carcinoma of the salivary glands (221) and given the close parallels between these tumour groups and infant HGG in terms of fusion incidence, it is possible that they will be detected in future cases of infant HGG. Future work should include updating our DNA fusion panel to include these important genes.

By running methylation-based gene ontology analysis on differentially methylated regions, we identified that *ALK* fusions are associated with dysregulation of genes associated with glutamate receptors and synapse plasticity whereas *NTRK* fusions and fusion-negative tumours are associated with genes controlling the signalling via the JNK cascade and neuronal differentiation, or the TGFβ pathway respectively. However, this aspect of the study was only exploratory due to the limited number of cases, and would require validation by an independent cohort to further support these findings. There is also reduced methylation of CpG sites governing expression of WNT5A in *ALK* fusion, and STAT1 in *NTRK* fusion-positive cases with differential expression reflecting this. Based on the evidence of my study, the data supports the idea that these fusions are the driving event in these tumours (with the example given of the work on *PPP1CB:ALK*), and the absence of the glioma-associated mutations in these cases. Similar findings have been seen in studies of other RTK positive tumours; lung adenocarcinomas which are positive for *RET, ALK* or *ROS1* fusions are also negative for *KRAS* mutations (which are usually a frequent finding in NSCLC) (222). However, fusion-positive cases are reported to occur with a background of *PDGFRA, TP53, EGFR, RBM10*, and *ERBB2* mutations (223). *NTRK* fusion-positive cancers can show greater variability; a study featuring 31 cases across different tumour types showed that only 29% of them contained a fusion in isolation, with the mutational burden varying between 1 – 37 somatic mutations per megabase, the most frequent of which were *TP53, PTEN* and *PIK3CA* (154). Although our longitudinal study did not identify any glioma-associated genes in either the primary or recurrence samples, different coding variants were identified in all cases, including the fusion-negative cases. However, no recurrent variants were identified and the significance of these needs to be explored.

In contrast to the high frequency of recurrent RTK fusions in the infant intrinsic set, the frequency of associated fusion partners was more variable, particularly for the *ALK* fusions with more frequent partners including *CCDC88A, PPP1CB,* and *EML4* and novel partners including *MAD1L1, MAP2, MSI2, SYNDIG1L, CLIP2,* and *ZC3H7A.* Only two partners were seen in *NTRK3* (*ETV6* and *EML4*) and only one for *NTRK1* (*TPM3*). The structure of the fusions predicted the retention of the tyrosine kinase domain of the RTK gene, consistent across all RTK fusions. The significance of the fusion partners in infant HGG needs to be explored, but studies of RTK fusions in other tumours have shown that the fusion partner impacts survival; NSCLC cases positive for *EML4:ALK* fusions respond better to ALK inhibitors and show an improved survival compared to fusion-negative cases and those with a different fusion partner (148). Also, clonal 3T3 cell lines expressing different *ALK* fusions with different fusion partners showed differing protein expression profiles (148). Further work looking at the importance of the RTK fusion partners in infant gliomas would help to explain why particular fusion types appear to have an improved survival. More fusion-positive cases with the same fusion partner are needed, but could also be engineered using CRISPR/Cas9 and cloning techniques (similar to those used to engineer *KCTD16:NTRK2* and *ETV6:NTRK3* fusion models in this study). Studies with *NTRK, ROS1, MET* and *ALK* fusions featuring the same and different fusion partners, and measuring their levels of fusion protein expression and responses to different Trk inhibitors would help to explore this further.

However, the fusion-negative cases present a contrasting group in this study; the absence of other mutations is very striking and they show epigenetic differences when compared to the fusion-positive cases with a potential immature progenitor cell phenotype with dysregulation of stem cell pluripotency gene networks. The question of what is driving these particular tumours, and whether this currently unknown molecular feature is shared with the fusion-positive cases is still to be answered. However, with the limitations of fusion detection already discussed, further analysis using RNA sequencing is critical to confirm that they are truly fusion-negative and identify any fusion-positive cases which have been missed; given that 60% of the intrinsic set of cases harbour a fusion, there is a high likelihood that they contain a fusion. Once completed, this will provide a more robust set of fusion-negative cases from which to look for other novel epigenetic or molecular drivers, possibly using ChIP-Seq to explore DNA-associated proteins, and also single cell RNA sequencing to look for clonal and cell population differences. With the caveat of limited clinical data, these cases show a worse survival compared to the fusion-positive cases; therefore whatever is driving these tumours could be impacting on outcome and therefore needs to be identified.

Given the young age at presentation, the associated fusions, and their concurrence with other infantile tumours including infantile fibrosarcoma the cell of origin is an important consideration; immunohistochemistry performed by referring institutions points to an astrocytic lineage (with GFAP positivity and lack of neuronal marker expression). However, the focal ganglion cell differentiation does not support this. Single cell sequencing may help to explore their lineage (I have just received data for three *NTRK* fusion-positive infant tumours and this is being explored); such data of 3321 cells from six H3K27M mutant glioma models showed that they predominantly contain cells that resemble oligodendrocyte-precursors which were found to have greater proliferative and tumour propagating potential, possibly related to *PDGFRA* signalling (98). A limitation of our retrospective study was that germline samples were not available to sequence alongside the tumour samples; which would have shown if the fusions were tumour-specific and also asked the question as to whether the tumour could be considered an abnormality of a development. To the best of my knowledge, other studies have not identified fusions in germline samples associated with infantile tumours. Germline samples for future studies will be very valuable in this regard, but also continuing to clinically monitor these children to identify the onset of secondary malignancies. Studies of paediatric, adolescent and young adult survivors of fusion-positive sarcomas show that they are at a two-fold greater risk of developing a secondary malignancy (solid tumours, lymphomas and leukaemias) and nearly three-fold greater in survivors of fusion-negative sarcoma, hinting at a possible germline driver alteration in these patients (224). Given the already close parallels between other infantile tumours, continued clinical follow up of infant HGG survivors will be needed to see if secondary tumours are a feature later in life.

We hold a collection of patient derived infant HGG cell culture models (n=5); HGG models can be challenging to establish in culture; general issues associated with culturing any sample include a risk of an infection or contamination, and any changes to established protocols should be minimal to avoid inducing changes to the molecular characteristics of the cells including the expression profile (170). Where possible, serial characterisation of cells at different passages is important to identify any deviation from the original culture and ensure the retention of molecular drivers (170). The three fusion-positive cell lines within my study that I was able to establish sufficiently (QCTB_INF_R077, QCTB_INF_R102 and CXJ-020) are sensitive to Trk inhibitors *in vitro*, consistent with the findings of our RTK fusion clinical case studies (OPBG_INF_035 and MSKC_INF_006). Sensitivity was also seen in the *ALK* fusion-positive case (DKFZ_INF_307). Given the existing evidence from this study that these fusions are the driving event in these tumours and with the evidence of clinical success seen so far, there does not appear to be a rationale for treating any other targets in these tumours currently. However, the fusion-negative cases represent an interesting group where the rationale for using a Trk inhibitor is not met. Exploring the *in vitro* sensitivity of a fusion-negative patient-derived model would show whether sensitivity to Trk inhibitors is a universal feature of all IHG cases, or just those which are fusion-positive. The principle of ‘precision medicine’ also describes the idea of adapting the treatment to the specific driving alterations assessed for each individual patient (225). At present, no known glioma-associated mutations have been found to occur in these patients and so potential combination therapies appear to be unnecessary. Prior to the use of targeted inhibitors in infantile fibrosarcoma, chemotherapy combinations were used including vincristine and dactinomycin with some success (226). Many of the fusion-positive IHG cases were also treated with combination chemotherapy in this study with good outcomes. However, whether the tumour is responsive to the chemotherapy or the improved prognosis is an inherent characteristic of the tumour (hinted at by the longitudinal study histological features of differentiation) remains to be conclusively confirmed. The principle of oncogene-induced senescence seen in tumours such as neuroblastoma and pilocytic astrocytomas, also may be relevant to fusion-positive infant HGG; longitudinal studies looking for differing expression of the fusions in recurrent samples would be helpful. The longitudinal study showed no evidence of acquired somatic glioma-associated mutations in the recurrent samples although new variants with increased allelic depth compared to the primary sample were identified; the small sample size and sparse clinical data related to chemotherapy treatments did not allow exploration as to whether these changes were significant or related to treatment. Existing trials have not evaluated the use of Trk inhibitors alongside other chemotherapy regimens. However, the forthcoming trial developed by the CONNECT Consortium to evaluate the use of larotrectinib for the treatment of newly diagnosed fusion-positive HGG contains an arm that will be explore the use of larotrectinib as a monotherapy and in combination with either Baby POG of HIT-SKK chemotherapy regimens (202). The data from this trial will be extremely valuable in exploring the chemo-sensitivity of these tumours.

The infant subgroup which encompasses other HGG and LGG glioma entities reflects the mutational burden and subgroup-specific mutations seen in older children including histone (*H3F3A* and *HIST1H3B*), *TP53, IDH1, FGFR1* and *ACVR1* mutations. In addition, *NTRK* fusions are identified in some of these cases, a feature well recognised in the literature with examples being reported in both HGG and LGG (227). *NTRK* fusions are found in 4% of paediatric gliomas overall. Studies quote 1.1 – 2.6% of glioblastomas contain an *NTRK* fusion, 4% of DIPGs and 2.3% of AA (227). Examples of *NTRK* fusions found in GBM include *BCAN:NTRK1, NFASC:NTRK1, CHTOP:NTRK1* and *TBC1D2:NTRK2*. One study looked at 237 WHO grade IV tumours and found four *NTRK* fusions (1.7%) and 10 *MET* fusions (4.2%) with a median age of 52 years for the fusion-positive cases. Although in adults, they did not report any co-existing mutations in these cases (82). However, another study showed that the *NTRK* fusions do not occur in isolation with reported *H3.3 K27M* mutations*, CDKN2A/B* deletions, *MET* amplifications, *TP53* mutations, and *CDK4/6* mutations also occurring alongside (74). Within my study, we found *H3F3A, PTEN,* and *CDKN2A/B* mutations alongside *NTRK* fusions, with the fusion conferring no obvious survival advantage in these cases. This is an important consideration clinically as these cases may not show such a positive response to Trk inhibitors compared to those that contain a fusion alone; this may be further explored by the CONNECT Consortium trial (202).

Preliminary analysis of the single cell RNA sequencing of three fusion-positive infant HGG cases highlighted the high proportion of microglia in the *NTRK2* fusion CXJ-020 sample. Studies have shown that microglia are a heterogenous population in terms of their expression profiles but also that both gender and age can be factors affecting this and their function, and that they display plasticity (228); this may be significant for the infant age group. The association with microglia both in terms of cell proportions and expression, and the possible lymphocyte aggregations seen in the longitudinal histology requires further exploration to see if the immune profile of these tumours is significant for their behaviour, evolution and outcome. The use of CIBERSORT in glioma research has utilised a more robust approach to analysing the immune profile of a tumour; the more traditional methods of using panels of IHC and flow cytometry have significant limitations in that the can miss immune populations and do not identify functional phenotypes such as resting or active lymphocytes (162). CIBERSORT can analyse both expression data and methylation data derived from bulk tumour samples against a validated signature matrix; this is then used to define different immune cell fractions within a tumour (162). With such an extensive cohort of infant HGG cases, all of which have undergone methylation profiling, it would be useful to analyse these using methyl CIBERSORT to see if they show a prominent immune profile (as suggested by the findings of CXJ-020) and whether this changes with time, as the histology of the longitudinal cases may suggest.

Further work on these data exploring the differences in malignant cells of each tumour will be important both in terms of understanding their heterogeneity and exploring more about the cell of origin; single cell sequencing has previously identified different cell states that drive the heterogeneity of malignant cells in glioblastoma, including oligodendrocyte progenitor cell-like (OPC-like), neural-progenitor cell-like (NPC-like), astrocyte-like (AC-like) and mesenchymal-like (MES-like) characterised by copy number amplifications of *CDK4, PDGFRA, EGFR* and *NF1* mutations (75). Single cell data can also be used to analyse RNA-velocity (a predictor of the future state of cells with a timescale of hours) (229) which may be very useful for longitudinal infant cases to identify any changes in cell state response to treatment and time.

8.5 Survival

With the caveat that very limited clinical data was available for the cohort, the IHG cases showed a significantly improved survival compared to the HGG infant cases, following a very similar survival curve to the LGG and DIGG/DIA cases. Considering 84% were reported as an HGG, and given the frequency of high-grade histological features seen in these cases, the clear discrepancy between the histology, WHO grading and prognosis for these patients is striking. Although not using established HGG entities as a comparator, other published datasets show that infant hemispheric RAS/MAPK driven tumours have the better outcome, with hemispheric RTK driven tumours showing an improved survival compared to midline RAS/MAPK driven tumours (9).

When looking at survival in relation to the presence of a fusion, the *ROS1* fusion cases show the best overall survival followed by *ALK* and *NTRK* fusion-positive cases. However, only very small numbers of cases featured and so this cannot be conclusively proven at this stage with the need for further cases to supplement the existing data. Published case reports of infant HGG cases surviving with *ALK, ROS1* and *NTRK* fusions support this finding (81,119,124,126). The fusion-negative IHG cases show a poorer outcome compared to the fusion-positive cases; similar findings are observed in other RTK fusion-positive tumours including congenital mesoblastic nephroma. One study reported no recurrences in *ETV6:NTRK3* fusion-positive cases where as the recurrence free survival for fusion-negative cases was 73% (230), and a case report of a fusion-negative infantile fibrosarcoma (metastatic and refractory to treatment) was subsequently found to contain an *LMNA:NTRK1* fusion rather than the characteristic *ETV6:NTRK3* fusion with a rapid response to larotrectinib (231); therefore our fusion-negative group may contain an as-yet undiscovered fusion. However, despite the unknown driving alteration, their survival was still significantly improved compared to other HGG entities, with some surviving up to 20 years post-diagnosis. Another study has shown differing outcomes to mine, with *ROS1* fusions doing poorly compared to *NTRK* and *ALK* fusions which have a better overall survival, but again with the caveat of very limited survival data available (9). However, isolated case studies report *ROS1* fusion survivors in HGG (81), and similar positive outcomes with case studies of *ALK* fusion-positive infant HGG (119). Also, it is known that *NTRK* and *ROS1* fusions can occur in the established HGG entities and existing studies have not separated these from the survival data (94,102). These differing and variable findings highlight the need for more fusion-positive cases with associated clinical data to better understand the survival differences, and also explore in more depth the reasons why some cases do not do as well.

Overall, the IHG cases show an improved survival compared to other HGG entities, and fusion-positive intrinsic set cases have an improved survival compared to the fusion-negative cases. Many fusion-positive cases have not been treated with a targeted inhibitor; some have been treated with conventional chemotherapy regimens or surgery alone. This therefore makes it very challenging to elucidate whether it is the response to the treatment or the biology of the tumour or both that are contributing to this positive outcome. However, as stated earlier, there are cases which do not do well and die within four years of diagnosis. The young age of these patients may also be a factor. To explore this in greater detail, more robust and extensive clinical follow-up data is needed; going forward this should include studies monitoring the response of children treated with Trk inhibitor monotherapy alongside those who are treated with both Trk inhibitors and chemotherapy, compared with the responses in infants who treated with conventional chemotherapy alone. Although our longitudinal study did not see the acquisition of glioma-associated mutations in the paired samples, a more extensive longitudinal study would be important to monitor changes in the tumour profile with these different treatment options, helping to improve the survival still further.

8.6 Therapeutics and management

Based on the clinical case studies and the study design and findings, I have created a flowchart demonstrating the management of HGG in the infant population (**figure 8-2**).

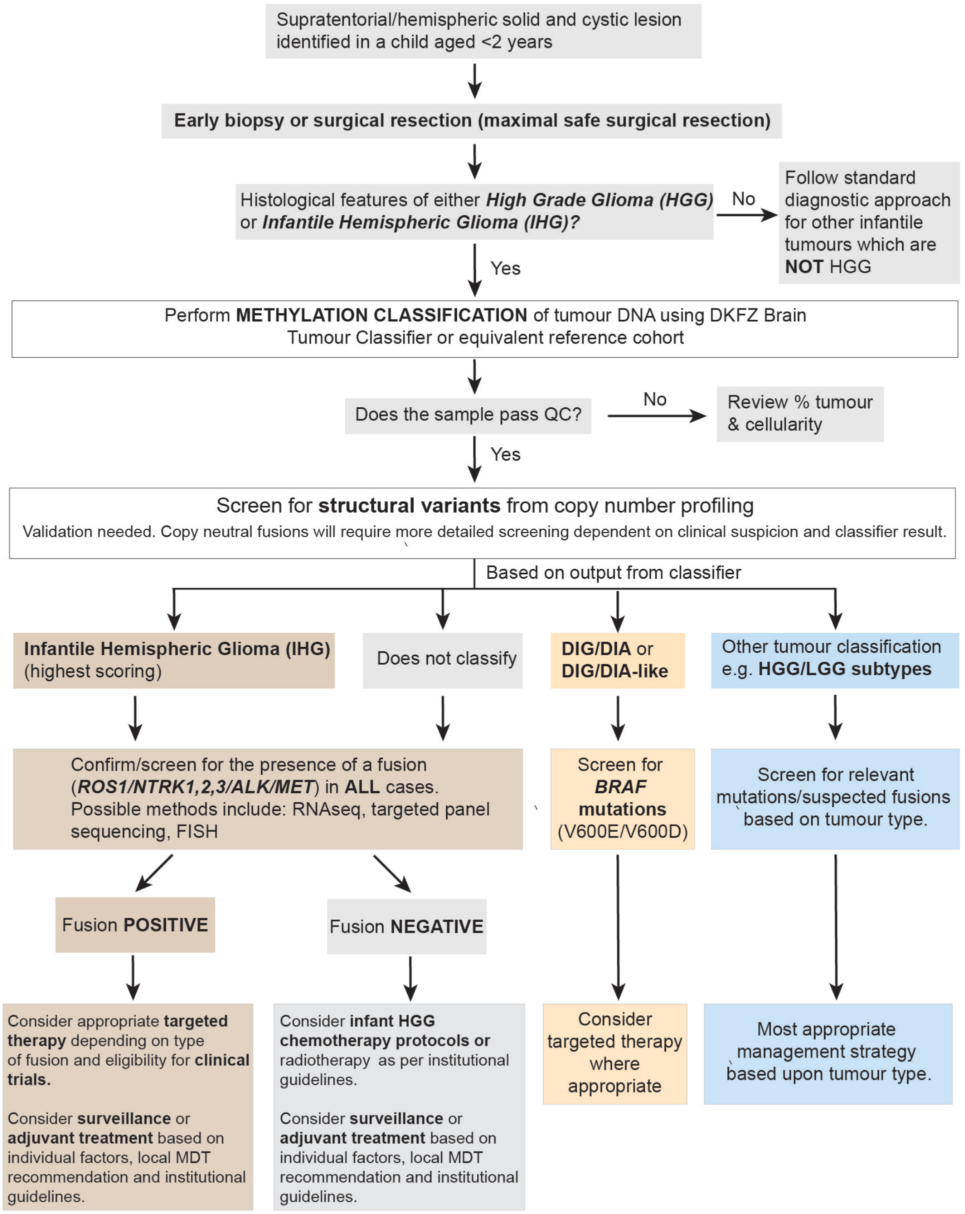

Figure 8-2. Management of high grade gliomas in the infant population. A flow chart that has been constructed based on the work of my study and in consultation with consultant paediatric oncologists, showing a diagnostic and management approach that could be used to guide clinical staff who are working with infant high grade gliomas.

The diagnosis of infant brain tumours begins with imaging which is generally MRI, but some cases are also first identified from *in utero* scans. The established entities such as DMG K27M-mutant and glioblastoma have typical appearances which aide the radiologist in giving a diagnosis (18). As mentioned, the IHG group do have recognisable radiological appearances but proper studies are needed to assess for more subtle defining features which are different to those seen in other HGG.

After imaging and MDT discussion, the child will proceed to biopsy (if a tissue diagnosis would alter management) or maximal safe surgical resection. This study has shown that well-established HGG and LGG occur in infants including gangliogliomas, PXA and glioblastomas. Therefore, an early tissue diagnosis (providing the opportunity for histological review and molecular testing) is very important for accuracy and treatment planning.

At histological review, if the tumour shows features that are not an HGG or IHG, the standard diagnostic approach for these cases should be followed. Current diagnostic protocols and reporting (stated by WHO classification 2016) require histological review, a WHO grade assignment and molecular investigations performed which assist diagnosis. This data is collated to form the ‘integrated diagnosis’ (13,18). The histological features that characterise the IHG cases are subtle and focal and could be easily missed. With the high frequency of high-grade histological features, the reporting neuropathologist is faced with a challenging decision and the potential for misdiagnosis is considerable.

Methylation profiling should be performed (if accessible) using the Illumina EPIC array and DKFZ brain tumour classifier (59) being careful to check that the sample passes the QC parameters. This would provide greater diagnostic certainty and allow a more informed decision regarding the appropriate use of targeted inhibitors, chemotherapy or radiotherapy. Also, a suboptimal calibrated score (i.e. a score <0.9 which would be considered non-diagnostic) can still provide useful information to correlate with the histological features, sequencing findings and clinical picture. For example, valuable copy number data can still be derived from cases with low calibrated scores, and if characteristic copy number changes are present, they can reliably support a particular diagnosis. A screen for structural variants can also be performed using copy number data derived from the methylation array, being careful to consider that some can appear copy neutral and so other screening methods (such as sequencing) should also be used.

IHG cases (or non-classifying tumours) should be rigorously screened for an RTK fusion (via copy number, FISH, targeted panel sequencing or RNA sequencing). Whether fusion-positive or negative, maximal safe surgical resection should be aimed for in all cases. However, if fusion-positive, targeted therapy or entry into a clinical trial may be considered rather than the conventional chemotherapy (187). However, careful surveillance or adjuvant treatment should be discussed based on individual clinical factors, local MDT recommendations and institutional guidelines. In addition for fusion-negative cases, infant HGG chemotherapy protocols (including Baby POG or HIT-SKK) as per local guidelines is an option. Overall, this will help to avoid unnecessary aggressive use of adjuvant therapies which have significant risk in infants, with evidence of cumulative cognitive decline (5).

For those cases which classify as a DIGG/DIA or DIGG/DIA-like case, they should be screened for *BRAF* mutations (V600E and V600E). Again, maximal safe surgical resection should be aimed for and targeted therapy using *BRAF* inhibitors can be considered (113). For cases which classify as other LGG or HGG entities, they should be screened for relevant mutations or fusions based on tumour type, perhaps using a targeted panel. After maximal safe surgical resection, the most appropriate management strategy based on tumour type can be followed.

Clinical trials with Trk inhibitors have shown very positive results; the phase 1/2 trial of larotrectinib featuring 55 patients aged from 4 months to 76 years with NTRK fusion-positive solid tumours (no CNS tumours) showed an overall response rate of 75%. Importantly it was deemed to be safe and tolerable with only 5% of patients experiencing grade 1 adverse events and the drug did not have to be discontinued in any cases (187). A 3 year old girl with an *ETV6:NTRK3* positive HGG with multiple failed therapies (including chemotherapy and radiotherapy), had a rapid clinical improvement as a result of larotrectinib; the response was near total resolution of both the primary and metastatic lesions, the first reported case of a fusion-positive glioma treated with a Trk inhibitor (126). Another very recently-published case report supports the efficacy of this drug in fusion-positive brain tumours; a GBM in an 18 month old female that was positive for an *ETV6:NTRK3* fusion was treated with larotrectinib at recurrence; 8 weeks later MRI scans showed significant tumour regression (186). I was also notified about a case (HMCI_INF_002) during the composition of my thesis and so full molecular profiling has not been possible at present. The child was referred from the Hadassah Medical Center, Israel and is a 1.3-year-old male who was diagnosed with a left-fronto-temporal-parietal lesion. The child subsequently underwent a subtotal resection. The tumour was diagnosed as an oligoastrocytoma (WHO grade III) based on histology. He was subsequently treated for three months with temozolomide but showed evidence of progression and underwent three further resections. The histology of the re-resections showed features of a high-grade neuroepithelial tumour possibly consistent with an anaplastic pleomorphic xanthoastrocytoma. Panel sequencing identified a *SPECC1L:NTRK2* fusion and the child has been treated with larotrectinib for nine months and is considered to be in complete remission. Interestingly, during this period the child had a two week break from larotrectinib; an MRI scan during this time showed evidence of relapse which resolved when the drug was restarted.

However, although targeted therapy has shown positive results, resistance mechanisms can develop. *ROS1*-rearranged NSCLC can acquire *KRAS* G12C, amplification of *KRAS* and *FGF3* leading to resistance to entrectinib (232). The larotrectinib trial showed that after treatment, mutations in *NTRK3* G623R and *NTRK1* G595R could be acquired, interfering with drug binding and therefore its inhibitory effect (187). Similarly, *NTRK1* F589L, *NTRK1* G667S and *NTRK3* G696A have been identified at progression (187). The ability to sequence cfDNA samples from either CSF or plasma, affords an exciting opportunity to be able to monitor the evolution and response of these tumours to treatment, including the acquisition of resistance mutations, in a less invasive way than through serial biopsies (211). Liquid biopsies will allow better monitoring of changes in the tumour molecular profile for future studies.

Trials with entrectinib have also shown positive outcomes; three trials (ALKA-372-001, STARTRK-1 and STARTRK-2) enrolled 54 patients who had *NTRK* fusion-positive solid tumours which were locally advanced or metastatic and aged >18 years. 54% had an objective response to the drug, with 7% complete responses and a further 50% with a partial response. Anaemia, weight gain and nervous system disorders were some of the serious adverse events reported by the studies, but they concluded that it was otherwise well tolerated with a manageable safety profile (203). The START-NG trial featured 13 patients with fusion-positive HGG, infantile fibrosarcoma and inflammatory myofibroblastic tumours, all of which had objective responses, with 2 complete responses in HGG cases with *NTRK3* fusions (233). These excellent outcomes provide further support for a clinical trial specifically focussed on the use of Trk inhibitors in infant fusion-positive HGG cases.

It is clear that infant HGGs harbour unique biology with associated clinicopathologic differences and should no longer be diagnosed or treated in the same way as their older counterparts. Maximal safe surgical resection remains the aim of treatment, regardless of subtype (5). However, our study has shown that RTK fusions can be found across all subgroups and so screening (initially via copy-number profiling with subsequent validation) will help to assess eligibility for targeted therapy or clinical trials. A more cautious approach, including ‘watchful waiting’ may be of value; targeted agents could be an option for fusion-positive cases but there may not be any urgency. Clinicians should aim to treat according to tumour behaviour. From the future work described in this chapter, it is hoped that a better understanding of how tumour progression and treatment response can be predicted will soon be forthcoming.

8.7 Implications of this study

As a result of the work and publication of this study, and others, the forthcoming WHO CNS tumour classification 2020 will feature a new chapter; infantile-type hemispheric glioma, H3-wild-type. To summarise the description in the chapter, the tumour is described as a cerebral hemispheric cellular astrocytoma that presents in early childhood and is characterised by a distinctive methylation profile and genetic alterations (typically fusions) including those in the *NTRK, ROS*, *ALK* and *MET* which define the different molecular subgroups. They are large masses located in the supratentorial compartment, often involving the leptomeninges with a presentation that is usually acute or non-specific. Their histology is described as cellular and well demarcated, with astrocytic spindled cells, mild-moderate pleomorphism, a uniform architecture and occasional gemistocytic-cell morphology. Essential and desired diagnostic criteria are a cellular astrocytoma, early childhood presentation, location in the cerebral hemispheres and the presence of an RTK abnormality and/or typical methylation profile. Due to the limited data available, a grade has not been assigned (13). The WHO classification is used by neuropathologists as a guide to assist diagnosis; the inclusion of this tumour in the classification is therefore of huge importance to ensuring that both the neuropathological and neuro-oncological community worldwide are aware of it and therefore can ensure it is diagnosed correctly and treated optimally.

As previously mentioned, the prominence of the RTK fusions within our study, and the success of Trk inhibitors in fusion-positive tumours both in clinical trials and in isolated case reports, has resulted in the design of a pilot and surgical study of larotrectinib for the treatment of newly diagnosed children with fusion-positive HGG by the CONNECT Consortium. It is expected to recruit 15 patients over 2.5 years, aiming to assess the disease control rate, characterise the tumour and plasma pharmacokinetics of larotrectinib, the safety profile of the different arms, the objective response rate and the progression free survival. This will also be compared to previous data derived from children treated with Baby POG and HIT-SKK chemotherapy regimens. Children aged 1 month to 21 years will be eligible. Children who are aged <3 years will be given two cycles of larotrectinib upon diagnosis followed by disease evaluation. If they have a complete response, they will continue with larotrectinib monotherapy. If it is a partial response with >50% tumour reduction, they will be given either Baby POG or HIT-SKK chemotherapy in combination with larotrectinib. However, if they show disease progression, they will stop larotrectinib and will be treated as per the discretion of their physician. Those children aged >3 will follow similar arms but if it is a partial response to monotherapy, radiotherapy (instead of chemotherapy) will be used alongside larotrectinib. Liquid biopsies (blood and CSF where appropriate) will be taken throughout to monitor the presence of the fusion and detect any resistance mutations. A small surgical study will also trial giving larotrectinib to patients who have been diagnosed via a biopsy/partial resection; these children will be given the drug for 3-5 days before further resection to evaluate the response (202). This is a very exciting proposal which will evaluate the use of the drug in paediatric and infant CNS tumours, leading to the use as part of the standard treatment practice of infant glioma. It will hopefully provide data about the variation in tumour response and the reasons behind this, exploring if there is optimal window for Trk inhibitor use in terms of tumour differentiation, and continued fusion detection and expression.

References

1. AMERICAN CANCER SOCIETY. Key Statistics for Childhood Cancers. 2016;2018. Available from: https://www.cancer.org/cancer/cancer-in-children/key-statistics.html
2. Plowman PN, Brada M. Paediatric brain tumours. Br Med Bull. 1996;52(4):802–17.
3. Hewitt M, Weiner SL, Simone J V, Cancer N, Board P. The National Academies Press. Vol. 12, Kartografija i Geoinformacije. 2013. 126–129 p.
4. Radhi M, Fulbright JM, Ginn KF, Guest EM. Childhood cancer for the primary care physician. Prim Care - Clin Off Pract. 2015;42(1):43–55.
5. Duffner PK, Horowitz ME, Krischer JP, Burger PC, Cohen ME, Sanford RA, et al. The treatment of malignant brain tumors in infants and very young children: An update of the Pediatric Oncology Group experience. Neuro Oncol. 1999;1(2):152–61.
6. Forrest SJ, Geoerger B, Janeway KA. Precision medicine in pediatric oncology. Curr Opin Pediatr. 2018;30(1):17–24.
7. Wilne SH, Dineen RA, Dommett RM, Chu TPC, Walker DA. Identifying brain tumours in children and young adults. BMJ [Internet]. 2013;347(7928):1–10. Available from: http://dx.doi.org/doi:10.1136/bmj.f5844
8. Ostrom QT, Cioffi G, Gittleman H, Patil N, Waite K, Kruchko C, et al. CBTRUS Statistical Report: Primary Brain and Other Central Nervous System Tumors Diagnosed in the United States in 2012-2016. Neuro Oncol. 2019;21:V1–100.
9. Guerreiro Stucklin AS, Ryall S, Fukuoka K, Zapotocky M, Lassaletta A, Li C, et al. Alterations in ALK/ROS1/NTRK/MET drive a group of infantile hemispheric gliomas. Nat Commun. 2019;10(1):1–13.
10. Gianno F, Antonelli M, Ferretti E, Massimino M, Arcella A, Giangaspero F. Pediatric high-grade glioma: A heterogeneous group of neoplasms with different molecular drivers. Glioma. 2018;1(4):117.
11. Jones C, Perryman L, Hargrave D. Paediatric and adult malignant glioma: Close relatives or distant cousins? Nat Rev Clin Oncol. 2012;9(7):400–13.
12. Doyle J, Khalafallah AM, Yang W, Sun Y, Bettegowda C, Mukherjee D. Association between extent of resection on survival in adult brainstem high-grade glioma patients. J Neurooncol. 2019;145(3):479–86.
13. Louis DN, Ohgaki H, Wiestler OD, Cavenee WK, Ellison DW, Figarella-Branger D, et al. WHO Classification of Tumours of the Central Nervous System. Revised 4t. International Agency for Research on Cancer; 2016.
14. Suwanwela N, Phanthumchinda K, Kaoropthum S. Headache in Brain Tumor: A Cross-Sectional Study. Headache J Head Face Pain. 1994;34(7):435–8.
15. Hamilton W, Kernick D. Clinical features of primary brain tumours: A case-control study using electronic primary care records. Br J Gen Pract. 2007;57(542):695–9.
16. Schwartzbaum J, Jonsson F, Ahlbom A, Preston-Martin S, Malmer B, Lönn S, et al. Prior hospitalization for epilepsy, diabetes, and stroke and subsequent glioma and meningioma risk. Cancer Epidemiol Biomarkers Prev. 2005;14(3):643–50.
17. Wilne SH, Ferris RC, Nathwani A, Kennedy CR. The presenting features

of brain tumours: A review of 200 cases. Arch Dis Child. 2006;91(6):502–6.

18. Louis DN, Perry A, Reifenberger G, von Deimling A, Figarella-Branger D, Cavenee WK, et al. The 2016 World Health Organization Classification of Tumors of the Central Nervous System: a summary. Acta Neuropathol. 2016;131(6):803–20.
19. Johung TB, Monje M. Current Neuropharmacology Send Orders for Reprints to reprints@benthamscience.ae Diffuse Intrinsic Pontine Glioma: New Pathophysiological Insights and Emerging Therapeutic Targets. Curr Neuropharmacol. 2017;15:88–97.
20. VLEESCHOUWER S DE, BERGERS G. Glioblastoma: To Target the Tumor Cell or the Microenvironment? Glioblastoma. 2017;(5):315–40.
21. Mackay A, Burford A, Carvalho D, Izquierdo E, Fazal-Salom J, Taylor KR, et al. Integrated Molecular Meta-Analysis of 1,000 Pediatric High-Grade and Diffuse Intrinsic Pontine Glioma. Cancer Cell. 2017;32(4):520-537.e5.
22. Seliger C, Luber C, Gerken M, Schaertl J, Proescholdt M, Riemenschneider MJ, et al. Use of metformin and survival of patients with high-grade glioma. Int J Cancer. 2019;144(2):273–80.
23. Maher EA, Bachoo RM. Glioblastoma. Rosenberg's Molecular and Genetic Basis of Neurological and Psychiatric Disease: Fifth Edition. 2014. 909–917 p.
24. Kline C, Felton E, Allen IE, Tahir P, Mueller S, Francisco S, et al. HHS Public Access. 2019;137(1):103–10.
25. Hervey-Jumper SL, Berger MS. Evidence for Improving Outcome Through Extent of Resection. Neurosurg Clin N Am. 2019;30(1):85–93.
26. Belsuzarri TAB, Araujo JFM, Catanoce AP, Neves MWF, Sola RAS, Navarro JN, et al. Giant cells glioblastoma: Case report and pathological analysis from this uncommon subtype of glioma. Rare Tumors. 2015;7(1):26–8.
27. Vizcaino MA, Palsgrove DN, Yuan M, Giannini C, Cabrera-Aldana EE, Pallavajjala A, et al. Granular cell astrocytoma: an aggressive IDH-wildtype diffuse glioma with molecular genetic features of primary glioblastoma. Brain Pathol. 2019;29(2):193–204.
28. Rodriguez FJ, Scheithauer BW, Giannini C, Bryant SC, Jenkins RB. Epithelial and pseudoepithelial differentiation in glioblastoma and gliosarcoma: A comparative morphologic and molecular genetic study. Cancer. 2008;113(10):2779–89.
29. Wippold FJ, Lämmle M, Anatelli F, Lennerz J, Perry A. Neuropathology for the neuroradiologist: Palisades and pseudopalisades. Am J Neuroradiol. 2006;27(10):2037–41.
30. Krishnatry R, Zhukova N, Guerreiro Stucklin AS, Pole JD, Mistry M, Fried I, et al. Clinical and treatment factors determining long-term outcomes for adult survivors of childhood low-grade glioma: A population-based study. Cancer. 2016;122(8):1261–9.
31. Blionas A, Giakoumettis D, Klonou A, Neromyliotis E, Karydakis P, Themistocleous MS. Paediatric gliomas: diagnosis, molecular biology and management. Ann Transl Med. 2018;6(12):251–251.
32. Hasselblatt M, Jaber M, Reuss D, Grauer O, Bibo A, Terwey S, et al. Diffuse astrocytoma, IDH-wildtype: A dissolving diagnosis. J Neuropathol Exp Neurol. 2018;77(6):422–5.
33. Gladson CL, Prayson RA, Liu WM. The pathobiology of glioma tumors.

Annu Rev Pathol Mech Dis. 2010;5(Cmv):33–50.

34. Lucas JT, Huang AJ, Mott RT, Lesser GJ, Tatter SB, Chan MD. Anaplastic ganglioglioma: a report of three cases and review of the literature. J Neurooncol. 2015;123(1):171–7.
35. Zanello M, Pages M, De-Espariat AT, Saffroy R, Puget S, Lacroix L, et al. Clinical, imaging, histopathological and molecular characterization of anaplastic ganglioglioma. J Neuropathol Exp Neurol. 2016;75(10):971–80.
36. Bender S, Tang Y, Lindroth AM, Hovestadt V, Jones DTW, Kool M, et al. Reduced H3K27me3 and DNA Hypomethylation Are Major Drivers of Gene Expression in K27M Mutant Pediatric High-Grade Gliomas. Cancer Cell. 2013;24(5):660–72.
37. Ragazzini R, Pérez-Palacios R, Baymaz IH, Diop S, Ancelin K, Zielinski D, et al. EZHIP constrains Polycomb Repressive Complex 2 activity in germ cells. Nat Commun. 2019;10(1):1–18.
38. Castel D, Kergrohen T, Tauziède-Espariat A, Mackay A, Ghermaoui S, Lechapt E, et al. Histone H3 wild-type DIPG/DMG overexpressing EZHIP extend the spectrum diffuse midline gliomas with PRC2 inhibition beyond H3-K27M mutation. Acta Neuropathol. 2020;139(6):1109–13.
39. Chourmouzi D, Papadopoulou E, Konstantinidis M, Syrris V, Kouskouras K, Haritanti A, et al. Manifestations of pilocytic astrocytoma: A pictorial review. Insights Imaging. 2014;5(3):387–402.
40. Collins VP, Jones DTW, Giannini C. Pilocytic astrocytoma: pathology, molecular mechanisms and markers. Acta Neuropathol [Internet]. 2015;129(6):775–88. Available from: http://dx.doi.org/10.1007/s00401-015-1410-7
41. Ida CM, Rodriguez FJ, Burger PC, Caron AA, Jenkins SM, Spears GM, et al. Pleomorphic xanthoastrocytoma: Natural history and long-term follow-up. Brain Pathol. 2015;25(5):575–86.
42. Greer A, Foreman NK, Donson A, Davies KD, Kleinschmidt-DeMasters BK. Desmoplastic infantile astrocytoma/ganglioglioma with rare BRAF V600D mutation. Pediatr Blood Cancer. 2017;64(6).
43. Peet AC, Arvanitis TN, Leach MO, Waldman AD. Functional imaging in adult and paediatric brain tumours. Nat Rev Clin Oncol. 2012;9(12):700–11.
44. Vanan MI, Eisenstat DD. DIPG in children - What can we learn from the past? Front Oncol. 2015;5(OCT).
45. Puget S, Beccaria K, Blauwblomme T, Roujeau T, James S, Grill J, et al. Biopsy in a series of 130 pediatric diffuse intrinsic Pontine gliomas. Child’s Nerv Syst. 2015;31(10):1773–80.
46. Description S. Biological Medicine for Di ff use Intrinsic Pontine Glioma (DIPG) Eradication (BIOMEDE). 2018;
47. Barthel FP, Johnson KC, Varn FS, Moskalik AD, Tanner G, Kocakavuk E, et al. Longitudinal molecular trajectories of diffuse glioma in adults. Nature [Internet]. 2019;576(7785):112–20. Available from: http://dx.doi.org/10.1038/s41586-019-1775-1
48. Wu G, Broniscer A, McEachron TA, Lu C, Paugh BS, Becksfort J, et al. Somatic histone H3 alterations in pediatric diffuse intrinsic pontine gliomas and non-brainstem glioblastomas. Nat Genet. 2012;44(3):251–3.
49. Vinci M, Burford A, Molinari V, Kessler K, Popov S, Clarke M, et al. Functional diversity and cooperativity between subclonal populations of

pediatric glioblastoma and diffuse intrinsic pontine glioma cells. Nat Med. 2018;24(8):1204–15.
50. Spunt SL, Vargas SO, Coffin CM, Skapek SX, Parham DM, Darling J, et al. The clinical, research, and social value of autopsy after any cancer death: A perspective from the Children's Oncology Group soft tissue sarcoma committee. Cancer. 2012;118(12):3002–9.
51. Fangusaro J. Pediatric high grade glioma: A review and update on tumor clinical characteristics and biology. Front Oncol. 2012;2 AUG.
52. Gottardo NG, Gajjar A. Chemotherapy for malignant brain tumors of childhood. J Child Neurol. 2008;23(10):1149–59.
53. Cohen KJ, Pollack IF, Zhou T, Buxton A, Holmes EJ, Burger PC, et al. Temozolomide in the treatment of high-grade gliomas in children: A report from the Children's Oncology Group. Neuro Oncol. 2011;13(3):317–23.
54. Mansouri A, Hachem LD, Mansouri S, Nassiri F, Laperriere NJ, Xia D, et al. MGMT promoter methylation status testing to guide therapy for glioblastoma: Refining the approach based on emerging evidence and current challenges. Neuro Oncol. 2019;21(2):167–78.
55. Jones C, Karajannis MA, Jones DTW, Kieran MW, Monje M, Baker SJ, et al. Pediatric high-grade glioma: Biologically and clinically in need of new thinking. Neuro Oncol. 2017;19(2):153–61.
56. Weber M, Hellmann I, Stadler MB, Ramos L, Pääbo S, Rebhan M, et al. Distribution, silencing potential and evolutionary impact of promoter DNA methylation in the human genome. Nat Genet. 2007;39(4):457–66.
57. Kumar R, Liu APY, Orr BA, Northcott PA, Robinson GW. Advances in the classification of pediatric brain tumors through DNA methylation profiling: From research tool to frontline diagnostic. Vol. 124, Cancer. 2018. p. 4168–80.
58. Esteller M. CpG island hypermethylation and tumor suppressor genes: A booming present, a brighter future. Oncogene. 2002;21(35 REV. ISS. 3):5427–40.
59. Capper D, Jones DTW, Sill M, Hovestadt V, Schrimpf D, Sturm D, et al. DNA methylation-based classification of central nervous system tumours. Nature. 2018;555(7697):469–74.
60. van der Maaten L, Hinton G. Visualizing Data using t-SNE. J Mach Learn Res. 2008;9:2579–605.
61. Jaunmuktane Z, Capper D, Jones DTW, Schrimpf D, Sill M, Dutt M, et al. Methylation array profiling of adult brain tumours: diagnostic outcomes in a large, single centre. Acta Neuropathol Commun. 2019;7(1):24.
62. Pickles JC, Fairchild AR, Stone TJ, Brownlee L, Merve A, Yasin SA, et al. DNA methylation-based profiling for paediatric CNS tumour diagnosis and treatment: a population-based study. Lancet Child Adolesc Heal. 2020;4(2):121–30.
63. Mackay A, Burford A, Molinari V, Jones DTW, Izquierdo E, Brouwer-Visser J, et al. Molecular, Pathological, Radiological, and Immune Profiling of Non-brainstem Pediatric High-Grade Glioma from the HERBY Phase II Randomized Trial. Cancer Cell. 2018;33(5):829-842.e5.
64. Korshunov A, Ryzhova M, Hovestadt V, Bender S, Sturm D, Capper D, et al. Integrated analysis of pediatric glioblastoma reveals a subset of biologically favorable tumors with associated molecular prognostic markers. Acta Neuropathol. 2015;129(5):669–78.
65. Lowe BR, Maxham LA, Hamey JJ, Wilkins MR, Partridge JF. Histone H3

mutations: An updated view of their role in chromatin deregulation and cancer. Cancers (Basel). 2019;11(5):1–24.
66. Kasper LH, Baker SJ. Invited Review: Emerging functions of histone H3 mutations in paediatric diffuse high-grade gliomas. Neuropathol Appl Neurobiol. 2020;46(1):73–85.
67. Schwartzentruber J, Korshunov A, Liu XY, Jones DTW, Pfaff E, Jacob K, et al. Driver mutations in histone H3.3 and chromatin remodelling genes in paediatric glioblastoma. Nature. 2012;482(7384):226–31.
68. Sturm D, Witt H, Hovestadt V, Khuong-Quang DA, Jones DTW, Konermann C, et al. Hotspot Mutations in H3F3A and IDH1 Define Distinct Epigenetic and Biological Subgroups of Glioblastoma. Cancer Cell. 2012;22(4):425–37.
69. Bjerke L, Mackay A, Nandhabalan M, Burford A, Jury A, Popov S, et al. Histone H3.3 mutations drive pediatric glioblastoma through upregulation of MYCN. Cancer Discov. 2013;3(5):512–9.
70. Carvalho D, Taylor KR, Olaciregui NG, Molinari V, Clarke M, Mackay A, et al. ALK2 inhibitors display beneficial effects in preclinical models of ACVR1 mutant diffuse intrinsic pontine glioma. Commun Biol. 2019;2(1):2–3.
71. Taylor KR, Mackay A, Truffaux N, Butterfield YS, Morozova O, Philippe C, et al. Recurrent activating ACVR1 mutations in diffuse intrinsic pontine glioma. Nat Genet. 2014;46(5):457–61.
72. Buczkowicz P, Hoeman C, Rakopoulos P, Pajovic S, Letourneau L, Dzamba M, et al. Genomic analysis of diffuse intrinsic pontine gliomas identifies three molecular subgroups and recurrent activating ACVR1 mutations. Nat Genet. 2014;46(5):451–6.
73. Jones DTW, Hutter B, Jäger N, Korshunov A, Kool M, Warnatz HJ, et al. Recurrent somatic alterations of FGFR1 and NTRK2 in pilocytic astrocytoma. Nat Genet. 2013;45(8):927–32.
74. Wu G, Diaz AK, Paugh BS, Rankin SL, Ju B, Li Y, et al. The genomic landscape of diffuse intrinsic pontine glioma and pediatric non-brainstem high-grade glioma. Nat Genet. 2014;46(5):444–50.
75. Neftel C, Laffy J, Filbin MG, Hara T, Shore ME, Rahme GJ, et al. An Integrative Model of Cellular States, Plasticity, and Genetics for Glioblastoma. Cell. 2019;178(4):835-849.e21.
76. Cimino PJ, McFerrin L, Wirsching HG, Arora S, Bolouri H, Rabadan R, et al. Copy number profiling across glioblastoma populations has implications for clinical trial design. Neuro Oncol. 2018;20(10):1368–73.
77. Jain P, Fierst TM, Han HJ, Smith TE, Vakil A, Storm PB, et al. CRAF gene fusions in pediatric low-grade gliomas define a distinct drug response based on dimerization profiles. Oncogene [Internet]. 2017;36(45):6348–58. Available from: http://dx.doi.org/10.1038/onc.2017.276
78. Sturm D, Orr BA, Toprak UH, Hovestadt V, Jones DTW, Capper D, et al. New Brain Tumor Entities Emerge from Molecular Classification of CNS-PNETs. Cell. 2016;164(5):1060–72.
79. Bender S, Gronych J, Warnatz HJ, Hutter B, Gröbner S, Ryzhova M, et al. Recurrent MET fusion genes represent a drug target in pediatric glioblastoma. Nat Med. 2016;22(11):1314–20.
80. Johnson A, Severson E, Gay L, Vergilio J, Elvin J, Suh J, et al. Comprehensive Genomic Profiling of 282 Pediatric Low- and High-Grade

Gliomas Reveals Genomic Drivers, Tumor Mutational Burden, and Hypermutation Signatures. Oncologist. 2017;22(12):1478–90.

81. Kiehna EN, Arnush MR, Tamrazi B, Cotter JA, Hawes D, Robison NJ, et al. Novel GOPC(FIG)-ROS1 fusion in a pediatric high-grade glioma survivor. J Neurosurg Pediatr. 2017;20(1):51–5.
82. Ferguson SD, Zhou S, Huse JT, de Groot JF, Xiu J, Subramaniam DS, et al. Targetable gene fusions associate with the IDH wild-type astrocytic lineage in adult gliomas. J Neuropathol Exp Neurol. 2018;77(6):437–42.
83. Di Stefano AL, Fucci A, Frattini V, Labussiere M, Mokhtari K, Zoppoli P, et al. Detection, characterization, and inhibition of FGFR-TACC fusions in IDH wild-type glioma. Clin Cancer Res. 2015;21(14):3307–17.
84. Lafay-Cousin L, Smith A, Chi SN, Wells E, Madden J, Margol A, et al. Clinical, Pathological, and Molecular Characterization of Infant Medulloblastomas Treated with Sequential High-Dose Chemotherapy. Pediatr Blood Cancer. 2016;63(9):1527–34.
85. Macy ME, Birks DK, Barton VN, Chan MH, Donson AM, Bemis LT, et al. of congenital glioblastoma. 2012;14(7):931–41.
86. Thompson WD, Kosnik EJ. Spontaneous regression of a diffuse brainstem lesion in the neonate: Report of two cases and review of the literature. J Neurosurg. 2005;102 PEDIAT(SUPPL. 1):65–71.
87. Schomerus L, Merkenschlager A, Kahn T, Hirsch W. Spontaneous remission of a diffuse brainstem lesion in a neonate. Pediatr Radiol. 2007;37(4):399–402.
88. Lenard HG. Complete remission of a diffuse pontine glioma. Neuropediatrics. 1998;29(6):328–30.
89. Suo-Palosaari M, Rantala H, Lehtinen S, Kumpulainen T, Salokorpi N. Long-term survival of an infant with diffuse brainstem lesion diagnosed by prenatal MRI: a case report and review of the literature. Child’s Nerv Syst. 2016;32(6):1163–8.
90. Takeshima H, Kawahara Y, Hirano H, Obara SI, Niiro M, Kuratsu JI, et al. Postoperative regression of desmoplastic infantile gangliogliomas: Report of two cases. Neurosurgery. 2003;53(4):979–84.
91. Haberler C, Slavc I, Czech T, Prayer D, Pirker C, Budka H, et al. Malignant predominantly minigemistocytic glioma in two infants: A distinctive glioma variant? Neuropathol Appl Neurobiol. 2007;33(2):169–78.
92. El-Ayadi M, Ansari M, Sturm D, Gielen GH, Warmuth-Metz M, Kramm CM, et al. High-grade glioma in very young children: A rare and particular patient population. Oncotarget. 2017;8(38):64564–78.
93. Varlet P, Le Teuff G, Le Deley MC, Giangaspero F, Haberler C, Jacques TS, et al. WHO grade has no prognostic value in the pediatric high-grade glioma included in the HERBY trial. Neuro Oncol. 2020;22(1):116–27.
94. Gielen GH, Gessi M, Buttarelli FR, Baldi C, Hammes J, Zur Muehlen A, et al. Genetic Analysis of Diffuse High-Grade Astrocytomas in Infancy Defines a Novel Molecular Entity. Brain Pathol. 2015;25(4):409–17.
95. Amatu A, Sartore-Bianchi A, Siena S. NTRK gene fusions as novel targets of cancer therapy across multiple tumour types. ESMO Open. 2016;1(2):1–9.
96. Qaddoumi I, Orisme W, Wen J, Santiago T, Gupta K, Dalton JD, et al. Genetic alterations in uncommon low-grade neuroepithelial tumors: BRAF, FGFR1, and MYB mutations occur at high frequency and align

with morphology. Acta Neuropathol. 2016;131(6):833–45.

97. Cook PJ, Thomas R, Kannan R, De Leon ES, Drilon A, Rosenblum MK, et al. Somatic chromosomal engineering identifies BCAN-NTRK1 as a potent glioma driver and therapeutic target. Nat Commun [Internet]. 2017;8(May 2017):1–10. Available from: http://dx.doi.org/10.1038/ncomms15987
98. Filbin MG, Tirosh I, Hovestadt V, Shaw ML, Escalante LE, Mathewson ND, et al. Developmental and oncogenic programs in H3K27M gliomas dissected by single-cell RNA-seq. Science (80-). 2018;360(6386):331–5.
99. La Manno G, Gyllborg D, Codeluppi S, Nishimura K, Salto C, Zeisel A, et al. Molecular Diversity of Midbrain Development in Mouse, Human, and Stem Cells. Cell. 2016;167(2):566-580.e19.
100. Kilkenny C, Browne WJ, Cuthill IC, Emerson M, Altman DG. Improving bioscience research reporting: The arrive guidelines for reporting animal research. PLoS Biol. 2010;8(6):19.
101. Workman P, Aboagye EO, Balkwill F, Balmain A, Bruder G, Chaplin DJ, et al. Guidelines for the welfare and use of animals in cancer research. Br J Cancer. 2010;102(11):1555–77.
102. Kramer ED, Donaldson M, Geyer JR. Survival of infants with malignant astrocytomas: A report from the childrens cancer group. Vol. 76, Cancer. 1995. p. 1685–6.
103. Dufour C, Grill J, Lellouch-Tubiana A, Puget S, Chastagner P, Frappaz D, et al. High-grade glioma in children under 5 years of age: A chemotherapy only approach with the BBSFOP protocol. Eur J Cancer. 2006;42(17):2939–45.
104. Grundy RG, Wilne SH, Robinson KJ, Ironside JW, Cox T, Chong WK, et al. Primary postoperative chemotherapy without radiotherapy for treatment of brain tumours other than ependymoma in children under 3 years: Results of the first UKCCSG/SIOP CNS 9204 trial. Eur J Cancer. 2010;46(1):120–33.
105. Schweizer L, Sieber L, Volckmann R, Versteeg R, Contributed KA. Molecular Classification of Ependymal Tumors across All CNS Compartments, Histopathological Grades, and Age Groups AUTHOR CONTRIBUTIONS to the design and conduct of experiments and to the writing HHS Public Access. Cancer Cell [Internet]. 2015;27(5):728–43. Available from: http://dx.doi.org/10.1016/j.ccell.2015.04.002.
106. Renner M, Wolf T, Meyer H, Hartmann W, Penzel R, Ulrich A, et al. Integrative DNA methylation and gene expression analysis in high-grade soft tissue sarcomas. Genome Biol. 2013;14(12).
107. Ahmad AS, Vasiljević N, Carter P, Berney DM, Møller H, Foster CS, et al. A novel DNA methylation score accurately predicts death from prostate cancer in men with low to intermediate clinical risk factors. Oncotarget. 2016;7(44):71833–40.
108. Vanaja DK, Ehrich M, Van Den Boom D, Cheville JC, Karnes RJ, Tindall DJ, et al. Hypermethylation of genes for diagnosis and risk stratification of prostate cancer. Cancer Invest. 2009;27(5):549–60.
109. Stiller CA, Bayne AM, Chakrabarty A, Kenny T, Chumas P. Incidence of childhood CNS tumours in Britain and variation in rates by definition of malignant behaviour: Population-based study. BMC Cancer. 2019;19(1):1–15.
110. Walker D, Wilne S, Grundy R, Kennedy C, Neil, Dickson A, et al. A new

clinical guideline from the Royal College of Paediatrics and Child Health with a national awareness campaign accelerates brain tumor diagnosis in UK children - “headSmart: Be Brain Tumour Aware.” Neuro Oncol. 2016;18(3):445–54.
111. Shanmugavadivel D, Liu JF, Murphy L, Wilne S, Walker D. Accelerating diagnosis for childhood brain tumours: An analysis of the HeadSmart UK population data. Arch Dis Child. 2020;105(4):355–62.
112. Chen F, Becker A, Loturco J, States U. Models and Their Utility in Drug Discovery. 2017;1–15.
113. van Tilburg CM, Selt F, Sahm F, Bächli H, Pfister SM, Witt O, et al. Response in a child with a BRAF V600E mutated desmoplastic infantile astrocytoma upon retreatment with vemurafenib. Pediatr Blood Cancer. 2018;65(3).
114. Jones C, Baker SJ. Unique genetic and epigenetic mechanisms driving paediatric diffuse high-grade glioma. Nat Rev Cancer. 2014;14(10):651–61.
115. Bouffet E, Larouche V, Campbell BB, Merico D, De Borja R, Aronson M, et al. Immune checkpoint inhibition for hypermutant glioblastoma multiforme resulting from germline biallelic mismatch repair deficiency. J Clin Oncol. 2016;34(19):2206–11.
116. Shlien A, Campbell BB, De Borja R, Alexandrov LB, Merico D, Wedge D, et al. Combined hereditary and somatic mutations of replication error repair genes result in rapid onset of ultra-hypermutated cancers. Nat Genet. 2015;47(3):257–62.
117. Anestis DM, Tsitsopoulos PP, Ble CA, Tsitouras V, Tsonidis CA. Congenital Glioblastoma Multiforme: An Unusual and Challenging Tumor. Neuropediatrics. 2017;48(6):403–12.
118. Wang AC, Jones DTW, Abecassis IJ, Cole BL, Leary SES, Lockwood CM, et al. Desmoplastic infantile ganglioglioma/astrocytoma (DIG/DIA) are distinct entities with frequent BRAFV600 mutations. Mol Cancer Res. 2018;16(10):1491–8.
119. Aghajan Y, Levy ML, Malicki DM, Crawford JR. Novel PPP1CB-ALK fusion protein in a high-grade glioma of infancy. BMJ Case Rep. 2016;2016:10–1.
120. Chmielecki J, Bailey M, He J, Elvin J, Vergilio JA, Ramkissoon S, et al. Genomic profiling of a large set of diverse pediatric cancers identifies known and novel mutations across tumor spectra. Cancer Res. 2017;77(2):509–19.
121. Coccé MC, Mardin BR, Bens S, Stütz AM, Lubieniecki F, Vater I, et al. Identification of ZCCHC8 as fusion partner of ROS1 in a case of congenital glioblastoma multiforme with a t(6;12)(q21;q24.3). Genes Chromosom Cancer. 2016;55(9):677–87.
122. Maruggi M, Malicki DM, Levy ML, Crawford JR. A novel KIF5B-ALK fusion in a child with an atypical central nervous system inflammatory myofibroblastic tumour. BMJ Case Rep. 2018;2018:19.
123. Nakano Y, Tomiyama A, Kohno T, Yoshida A, Yamasaki K, Ozawa T, et al. Identification of a novel KLC1–ROS1 fusion in a case of pediatric low-grade localized glioma. Brain Tumor Pathol. 2019;36(1):14–9.
124. Ng A, Levy ML, Malicki DM, Crawford JR. Unusual high-grade and low-grade glioma in an infant with PPP1CB-ALK gene fusion. BMJ Case Rep. 2019;12(2):2018–9.

125. Olsen TK, Panagopoulos I, Meling TR, Micci F, Gorunova L, Thorsen J, et al. Fusion genes with ALK as recurrent partner in ependymoma-like gliomas: A new brain tumor entity? Neuro Oncol. 2015;17(10):1365–73.
126. Ziegler DS, Wong M, Mayoh C, Kumar A, Tsoli M, Mould E, et al. Brief Report: Potent clinical and radiological response to larotrectinib in TRK fusion-driven high-grade glioma. Br J Cancer [Internet]. 2018;119(6):693–6. Available from: http://dx.doi.org/10.1038/s41416-018-0251-2
127. Menu M. Main Menu. 2011;0_1-0_1.
128. Church AJ, Calicchio ML, Nardi V, Skalova A, Pinto A, Dillon DA, et al. Recurrent EML4-NTRK3 fusions in infantile fibrosarcoma and congenital mesoblastic nephroma suggest a revised testing strategy. Mod Pathol [Internet]. 2018;31(3):463–73. Available from: http://dx.doi.org/10.1038/modpathol.2017.127
129. Torre M, Vasudevaraja V, Serrano J, Delorenzo M, Malinowski S, Blandin AF, et al. Molecular and clinicopathologic features of gliomas harboring NTRK fusions. Acta Neuropathol Commun. 2020;8(1):1–14.
130. Johannessen AL, Torp SH. The clinical value of Ki-67/MIB-1 labeling index in human astrocytomas. Pathol Oncol Res. 2006;12(3):143–7.
131. Charest A, Lane K, McMahon K, Park J, Preisinger E, Conroy H, et al. Fusion of FIG to the receptor tyrosine kinase ROS in a glioblastoma with an interstitial del(6)(q21q21). Genes Chromosom Cancer. 2003;37(1):58–71.
132. Young LC, Takeuchi K, Soda M, Inamura K, Togashi Y, Hatano S, et al. Identification of novel isoforms of the EML4-ALK transforming gene in non-small cell lung cancer. Cancer Res. 2008;68(13):4971–6.
133. Lipson D, Capelletti M, Yelensky R, Otto G, Parker A, Jarosz M, et al. Identification of new ALK and RET gene fusions from colorectal and lung cancer biopsies. Nat Med. 2012;18(3):382–4.
134. Debelenko L V., Arthur DC, Pack SD, Helman LJ, Schrump DS, Tsokos M. Identification of CARS-ALK fusion in primary and metastatic lesions of an inflammatory myofibroblastic tumor. Lab Investig. 2003;83(9):1255–65.
135. Rosenbaum JN, Bloom R, Forys JT, Hiken J, Armstrong JR, Branson J, et al. Genomic heterogeneity of ALK fusion breakpoints in non-small-cell lung cancer. Mod Pathol [Internet]. 2018;31(5):791–808. Available from: http://dx.doi.org/10.1038/modpathol.2017.181
136. Penzel R, Schirmacher P, Warth A. A novel EML4-ALK variant: Exon 6 of EML4 fused to exon 19 of ALK. J Thorac Oncol. 2012;7(7):1198–9.
137. McArthur GA, Laherty CD, Quéva C, Hurlin PJ, Loo L, James L, et al. The Mad protein family links transcriptional repression to cell differentiation. Cold Spring Harb Symp Quant Biol. 1998;63:423–33.
138. Gripp KW, Aldinger KA, Bennett JT, Baker L, Tusi J, Powell-Hamilton N, et al. A novel rasopathy caused by recurrent de novo missense mutations in PPP1CB closely resembles Noonan syndrome with loose anagen hair. Am J Med Genet Part A. 2016;170(9):2237–47.
139. Dehmelt L, Halpain S. The MAP2/Tau family of microtubule-associated proteins. Genome Biol. 2005;6(1).
140. Saadi I, Fowzan SA, Stephen SG, Goessling W, Cavallesco R, Turbe-Doan A, et al. Deficiency of the cytoskeletal protein SPECC1L leads to oblique facial clefting. Am J Hum Genet. 2011;89(1):44–55.
141. Wilson NR, Olm-Shipman AJ, Acevedo DS, Palaniyandi K, Hall EG, Kosa E, et al. SPECC1L deficiency results in increased adherens junction

stability and reduced cranial neural crest cell delamination. Sci Rep. 2016;6:1–3.

142. Kalashnikova E, Lorca RA, Kaur I, Barisone GA, Li B, Ishimaru T, et al. SynDIG1: An Activity-Regulated, AMPA- Receptor-Interacting Transmembrane Protein that Regulates Excitatory Synapse Development. Neuron. 2010;65(1):80–93.
143. Metzler M, Li B, Gan L, Georgiou J, Gutekunst CA, Wang Y, et al. Disruption of the endocytic protein HIP1 results in neurological deficits and decreased AMPA receptor trafficking. EMBO J. 2003;22(13):3254–66.
144. Nakai T, Nagai T, Tanaka M, Itoh N, Asai N, Enomoto A, et al. Girdin phosphorylation is crucial for synaptic plasticity and memory: A potential role in the interaction of BDNF/TrkB/ Akt signaling with NMDA receptor. J Neurosci. 2014;34(45):14995–5008.
145. Enomoto A, Murakami H, Asai N, Morone N, Watanabe T, Kawai K, et al. Akt/PKB regulates actin organization and cell motility via girdin/APE. Dev Cell. 2005;9(3):389–402.
146. Iwahara T, Fujimoto J, Wen D, Cupples R, Bucay N, Arakawa T, et al. Molecular characterization of ALK, a receptor tyrosine kinase expressed specifically in the nervous system. Oncogene. 1997;14(4):439–49.
147. Palmer RH, Vernersson E, Grabbe C, Hallberg B. Anaplastic lymphoma kinase: Signalling in development and disease. Biochem J. 2009;420(3):345–61.
148. Childress MA, Himmelberg SM, Chen H, Deng W, Davies MA, Lovly CM. ALK fusion partners impact response to ALK inhibition: Differential effects on sensitivity, cellular phenotypes, and biochemical properties. Mol Cancer Res. 2018;16(11):1724–36.
149. Singh D, Chan JM, Zoppoli P, Niola F, Castano A, Liu EM, et al. NIH Public Access. 2013;337(6099):1231–5.
150. Hsiao SJ, Zehir A, Sireci AN, Aisner DL. Detection of Tumor NTRK Gene Fusions to Identify Patients Who May Benefit from Tyrosine Kinase (TRK) Inhibitor Therapy. J Mol Diagnostics [Internet]. 2019;21(4):553–71. Available from: https://doi.org/10.1016/j.jmoldx.2019.03.008
151. Farago AF, Azzoli CG. Beyond ALK and ROS1: RET, NTRK, EGFR and BRAF gene rearrangements in non-small cell lung cancer. Transl Lung Cancer Res. 2017;6(5):550–9.
152. Pietrantonio F, Di Nicolantonio F, Schrock AB, Lee J, Tejpar S, Sartore-Bianchi A, et al. ALK, ROS1, and NTRK rearrangements in metastatic colorectal cancer. J Natl Cancer Inst. 2017;109(12):0–1.
153. Davare MA, Henderson JJ, Agarwal A, Wagner JP, Iyer SR, Shah N, et al. Rare but recurrent ROS1 fusions resulting from chromosome 6q22 microdeletions are targetable oncogenes in glioma. Clin Cancer Res. 2018;24(24):6471–82.
154. Gatalica Z, Xiu J, Swensen J, Vranic S. Molecular characterization of cancers with NTRK gene fusions. Mod Pathol [Internet]. 2019;32(1):147–53. Available from: http://dx.doi.org/10.1038/s41379-018-0118-3
155. Okamura R, Boichard A, Kato S, Sicklick JK, Bazhenova L, Kurzrock R. Analysis of NTRK Alterations in Pan-Cancer Adult and Pediatric Malignancies: Implications for NTRK-Targeted Therapeutics . JCO Precis Oncol. 2018;(2):1–20.
156. George SL, Izquierdo E, Campbell J, Koutroumanidou E, Proszek P,

Jamal S, et al. A tailored molecular profiling programme for children with cancer to identify clinically actionable genetic alterations. Eur J Cancer [Internet]. 2019;121:224–35. Available from: https://doi.org/10.1016/j.ejca.2019.07.027

157. Worst BC, van Tilburg CM, Balasubramanian GP, Fiesel P, Witt R, Freitag A, et al. Next-generation personalised medicine for high-risk paediatric cancer patients – The INFORM pilot study. Eur J Cancer. 2016;65:91–101.
158. Hao Z, Guo D. EGFR mutation: Novel prognostic factor associated with immune infiltration in lower-grade glioma; An exploratory study. BMC Cancer. 2019;19(1):1–13.
159. Berghoff AS, Kiesel B, Widhalm G, Wilhelm D, Rajky O, Kurscheid S, et al. Correlation of immune phenotype with IDH mutation in diffuse glioma. Neuro Oncol. 2017;19(11):1460–8.
160. Zhou W, Laird PW, Shen H. Comprehensive characterization, annotation and innovative use of Infinium DNA methylation BeadChip probes. Nucleic Acids Res. 2017;45(4):e22.
161. Ng A, Levy ML, Malicki DM, Crawford JR. Unusual high-grade and low-grade glioma in an infant with PPP1CB-ALK gene fusion. BMJ Case Rep. 2019;12(2):19.
162. Chen B, Khodadoust MS, Liu CL, Newman AM, Alizadeh AA. Profiling tumor infiltrating immune cells with CIBERSORT. Methods Mol Biol. 2018;1711(January):243–59.
163. Grabovska Y, Mackay A, O’Hare P, Crosier S, Finetti M, Schwalbe EC, et al. Pediatric pan-central nervous system tumor analysis of immune-cell infiltration identifies correlates of antitumor immunity. Nat Commun. 2020;11(1):1–2.
164. de Souza CF, Sabedot TS, Malta TM, Stetson L, Morozova O, Sokolov A, et al. A Distinct DNA Methylation Shift in a Subset of Glioma CpG Island Methylator Phenotypes during Tumor Recurrence. Cell Rep [Internet]. 2018;23(2):637–51. Available from: https://doi.org/10.1016/j.celrep.2018.03.107
165. Russo M, Misale S, Wei G, Siravegna G, Crisafulli G, Lazzari L, et al. Acquired resistance to the TRK inhibitor entrectinib in colorectal cancer. Cancer Discov. 2016;6(1):36–44.
166. Lezcano C, Shoushtari AN, Ariyan C, Hollmann TJ, Busam KJ. Primary and metastatic melanoma with NTRK fusions. Am J Surg Pathol. 2018;42(8):1052–8.
167. Burford A, Mackay A, Popov S, Vinci M, Carvalho D, Clarke M, et al. The ten-year evolutionary trajectory of a highly recurrent paediatric high grade neuroepithelial tumour with MN1:BEND2 fusion. Sci Rep [Internet]. 2018;8(1):1–10. Available from: http://dx.doi.org/10.1038/s41598-018-19389-9
168. Jiang J, Wu X, Tong X, Wei W, Chen A, Wang X, et al. GCC2-ALK as a targetable fusion in lung adenocarcinoma and its enduring clinical responses to ALK inhibitors. Lung Cancer. 2018;115:5–11.
169. Salloum R, McConechy MK, Mikael LG, Fuller C, Drissi R, DeWire M, et al. Characterizing temporal genomic heterogeneity in pediatric high-grade gliomas. Acta Neuropathol Commun. 2017;5(1):78.
170. Carvalho DM, Temelso S, Mackay A, Pemberton H, Rogers R, Kessler K, et al. Drug screening linked to molecular profiling identifies novel

dependencies in patient-derived primary cultures of paediatric high grade glioma and DIPG. Nat Commun.

171. Bax DA, Little SE, Gaspar N, Perryman L, Marshall L, Viana-Pereira M, et al. Molecular and phenotypic characterisation of paediatric glioma cell lines as models for preclinical drug development. PLoS One. 2009;4(4).
172. Pearce J, Khabra K, Nanji H, Stone J, Powell K, Martin D, et al. High Grade Gliomas in young children: the South Thames Neuro-Oncology Unit experience and review of recent advances. Unpublished.
173. Brabetz S, Leary SES, Gröbner SN, Nakamoto MW, Şeker-Cin H, Girard EJ, et al. A biobank of patient-derived pediatric brain tumor models. Nat Med. 2018;24(11):1752–61.
174. Vanoli F, Tomishima M, Feng W, Lamribet K, Babin L, Brunet E, et al. CRISPR-Cas9-guided oncogenic chromosomal translocations with conditional fusion protein expression in human mesenchymal cells. Proc Natl Acad Sci U S A. 2017;114(14):3696–701.
175. Maddalo D, Manchado E, Concepcion CP, Bonetti C, Vidigal JA, Han YC, et al. In vivo engineering of oncogenic chromosomal rearrangements with the CRISPR/Cas9 system. Nature. 2014;516(7531):423–8.
176. Ou SHI, Tan J, Yen Y, Soo RA. ROS1 as a “druggable” receptor tyrosine kinase: Lessons learned from inhibiting the ALK pathway. Expert Rev Anticancer Ther. 2012;12(4):447–56.
177. Clarke M, Mackay A, Ismer B, Pickles JC, Tatevossian RG, Newman S, et al. Infant High-Grade Gliomas Comprise Multiple Subgroups Characterized by Novel Targetable Gene Fusions and Favorable Outcomes. Cancer Discov. 2020;10(7):942–63.
178. Liscovitch N, Chechik G. Specialization of Gene Expression during Mouse Brain Development. PLoS Comput Biol. 2013;9(9).
179. Semple BD, Blomgren K, Gimlin K, Ferriero DM, Noble-Haeusslein LJ. Brain development in rodents and humans: Identifying benchmarks of maturation and vulnerability to injury across species. Prog Neurobiol. 2013;106–107:1–16.
180. Kim JY, Grunke SD, Levites Y, Golde TE, Jankowsky JL. Intracerebroventricular viral injection of the neonatal mouse brain for persistent and widespread neuronal transduction. J Vis Exp. 2014;(91):1–7.
181. Ambros IM, Zellner A, Roald B, Amann G, Ladenstein R, Printz D, et al. Role of ploidy, chromosome 1p, and Schwann cells in the maturation of neuroblastoma. N Engl J Med. 1996;334(23):1505–11.
182. Cozzi DA, Mele E, Ceccanti S, Natale F, Clerico A, Schiavetti A, et al. Long-term follow-up of the “wait and see” approach to localized perinatal adrenal neuroblastoma. World J Surg. 2013;37(2):459–65.
183. Jacob K, Quang-Khuong DA, Jones DTW, Witt H, Lambert S, Albrecht S, et al. Genetic aberrations leading to MAPK pathway activation mediate oncogene-induced senescence in sporadic pilocytic astrocytomas. Clin Cancer Res. 2011;17(14):4650–60.
184. Buhl JL, Selt F, Hielscher T, Guiho R, Ecker J, Sahm F, et al. The Senescence-associated Secretory Phenotype Mediates Oncogene-induced Senescence in Pediatric Pilocytic Astrocytoma. Clin Cancer Res. 2019;25(6):1851–66.
185. Jones TA, Jeyapalan JN, Forshew T, Tatevossian RG, Lawson ARJ, Patel SN, et al. Molecular analysis of pediatric brain tumors identifies

microRNAs in pilocytic astrocytomas that target the MAPK and NF-κB pathways. Acta Neuropathol Commun [Internet]. 2015;3:86. Available from: http://dx.doi.org/10.1186/s40478-015-0266-3

186. Alharbi M, Mobark NA, Balbaid AA, Alanazi F, Aljabarat W abdel R, Bakhsh E, et al. Regression of ETV6-NTRK3 Infantile Glioblastoma After First-Line Treatment With Larotrectinib. JCO Precis Oncol. 2020;(4):796–800.
187. Drilon A, Laetsch TW, Kummar S, Dubois SG, Lassen UN, Demetri GD, et al. Efficacy of larotrectinib in TRK fusion-positive cancers in adults and children. N Engl J Med. 2018;378(8):731–9.
188. Doebele RC, Davis LE, Vaishnavi A, Le AT, Estrada-Bernal A, Keysar S, et al. An oncogenic NTRK fusion in a patient with soft-tissue sarcoma with response to the tropomyosin-related kinase inhibitor LOXO-101. Cancer Discov. 2015;5(10):1049–57.
189. Almeida J, Costa J, Coelho P, Cea V, Galesio M, Noronha JP, et al. Adipocyte proteome and secretome influence inflammatory and hormone pathways in glioma. Metab Brain Dis. 2019;34(1):141–52.
190. Aftab Q, Mesnil M, Ojefua E, Poole A, Noordenbos J, Strale P-O, et al. Cx43-Associated Secretome and Interactome Reveal Synergistic Mechanisms for Glioma Migration and MMP3 Activation. Front Neurosci. 2019;13(March):1–20.
191. Ledur PF, Onzi GR, Zong H, Lenz G. Culture conditions defining glioblastoma cells behavior: what is the impact for novel discoveries? Oncotarget. 2017;8(40):69185–97.
192. Ledur PF, Liu C, He H, Harris AR, Minussi DC, Zhou HY, et al. Culture conditions tailored to the cell of origin are critical for maintaining native properties and tumorigenicity of glioma cells. Neuro Oncol. 2016;18(10):1413–24.
193. Sanders RP, Kocak M, Burger PC, Merchant TE, Gajjar A, Broniscer A. High-grade astrocytoma in very young children. Pediatr Blood Cancer. 2007;49(7):888–93.
194. Davis T, Doyle H, Tobias V, Ellison DW, Ziegler DS. Case report of spontaneous resolution of a congenital glioblastoma. Pediatrics. 2016;137(4).
195. Gelabert-Gonzalez M, Serramito-García R, Arcos-Algaba A. Desmoplastic infantile and non-infantile ganglioglioma. Review of the literature. Neurosurg Rev. 2011;34(2):151–8.
196. Lafay-Cousin L, Strother D. Current Treatment Approaches for Infants with Malignant Central Nervous System Tumors. Oncologist. 2009;14(4):433–44.
197. Laetsch TW, DuBois SG, Mascarenhas L, Turpin B, Federman N, Albert CM, et al. Larotrectinib for paediatric solid tumours harbouring NTRK gene fusions: phase 1 results from a multicentre, open-label, phase 1/2 study. Lancet Oncol. 2018;19(5):705–14.
198. Bielack SS, Cox MC, Nathrath M, Apel K, Blattmann C, Holl T, et al. Rapid, complete and sustained tumour response to the TRK inhibitor larotrectinib in an infant with recurrent, chemotherapy-refractory infantile fibrosarcoma carrying the characteristic ETV6-NTRK3 gene fusion. Ann Oncol. 2019;30(Supplement 8):VIII31–5.
199. DuBois SG, Laetsch TW, Federman N, Turpin BK, Albert CM, Nagasubramanian R, et al. The use of neoadjuvant larotrectinib in the

management of children with locally advanced TRK fusion sarcomas. Cancer. 2018;124(21):4241–7.

200. Hong DS, Bauer TM, Lee JJ, Dowlati A, Brose MS, Farago AF, et al. Larotrectinib in adult patients with solid tumours: A multi-centre, open-label, phase i dose-escalation study. Ann Oncol [Internet]. 2019;30(2):325–31. Available from: http://dx.doi.org/10.1093/annonc/mdy539
201. Izquierdo E, Proszek P, Temelso S, Clarke M, Carvalho DM, Mackay A, et al. ddPCR-based detection of circulating tumour DNA from paediatric high grade and diffuse midline glioma patients. Unpublished.
202. Consortium C. Study protocol: A Pilot and Surgical study of Larotrectinib for Treatment of Newly-Diagnosed Children with High-Grade Glioma with NTRK fusion. 2020.
203. Doebele RC, Drilon A, Paz-Ares L, Siena S, Shaw AT, Farago AF, et al. Entrectinib in patients with advanced or metastatic NTRK fusion-positive solid tumours: integrated analysis of three phase 1–2 trials. Lancet Oncol. 2020;21(2):271–82.
204. López GY, Van Ziffle J, Onodera C, Grenert JP, Yeh I, Bastian BC, et al. The genetic landscape of gliomas arising after therapeutic radiation. Acta Neuropathol. 2019;137(1):139–50.
205. Raabe EH, Lim KS, Kim JM, Meeker A, Mao XG, Nikkhah G, et al. BRAF activation induces transformation and then senescence in human neural stem cells: A pilocytic astrocytoma model. Clin Cancer Res. 2011;17(11):3590–9.
206. Wolff B, Ng A, Roth D, Parthey K, Warmuth-Metz M, Eyrich M, et al. Pediatric high grade glioma of the spinal cord: Results of the HIT-GBM database. J Neurooncol. 2012;107(1):139–46.
207. Kumar A, Rashid S, Singh S, Li R, Dure LS. Spinal Cord Diffuse Midline Glioma in a 4-Year-Old Boy. Child Neurol Open. 2019;6:2329048X1984245.
208. Konar SK, Bir SC, Maiti TK, Nanda A. A systematic review of overall survival in pediatric primary glioblastoma multiforme of the spinal cord. J Neurosurg Pediatr. 2017;19(2):239–48.
209. Hafeez U, Cher LM. Biomarkers and smart intracranial devices for the diagnosis, treatment, and monitoring of high-grade gliomas: a review of the literature and future prospects. Neuro-Oncology Adv. 2019;1(1):1–12.
210. Mouliere F, Mair R, Chandrananda D, Marass F, Smith CG, Su J, et al. Detection of cell-free DNA fragmentation and copy number alterations in cerebrospinal fluid from glioma patients . EMBO Mol Med. 2018;10(12):1–6.
211. Cheng AP, Burnham P, De Vlaminck I. Biopsy-free screening for glioma. EMBO Mol Med. 2018;10(12):4–6.
212. Huang TY, Piunti A, Lulla RR, Qi J, Horbinski CM, Tomita T, et al. Detection of Histone H3 mutations in cerebrospinal fluid-derived tumor DNA from children with diffuse midline glioma. Acta Neuropathol Commun. 2017;5(1):28.
213. Smits AJJ, Kummer JA, De Bruin PC, Bol M, Van Den Tweel JG, Seldenrijk KA, et al. The estimation of tumor cell percentage for molecular testing by pathologists is not accurate. Mod Pathol. 2014;27(2):168–74.
214. Vendrell JA, Taviaux S, Béganton B, Godreuil S, Audran P, Grand D, et al. Detection of known and novel ALK fusion transcripts in lung cancer

patients using next-generation sequencing approaches. Sci Rep. 2017;7(1):1–11.
215. Tennstedt P, Strobel G, Bölch C, Grob T, Minner S, Masser S, et al. Patterns of ALK expression in different human cancer types. J Clin Pathol. 2014;67(6):477–81.
216. Kim H, Chung JH. Overview of clinicopathologic features of ALK-rearranged lung adenocarcinoma and current diagnostic testing for ALK rearrangement. Transl Lung Cancer Res. 2015;4(2):149–55.
217. Bass BP, Engel KB, Greytak SR, Moore HM. A review of preanalytical factors affecting molecular, protein, and morphological analysis of Formalin-Fixed, Paraffin-Embedded (FFPE) tissue: How well do you know your FFPE specimen? Arch Pathol Lab Med. 2014;138(11):1520–30.
218. Lym RL, Ostrom QT, Kruchko C, Couce M, Brat DJ, Louis DN, et al. Completeness and concordancy of WHO grade assignment for brain and central nervous system tumors in the United States, 2004–2011. J Neurooncol. 2015;123(1):43–51.
219. Nielsen LAG, Bangsø JA, Lindahl KH, Dahlrot RH, Hjelmborg JVB, Hansen S, et al. Evaluation of the proliferation marker Ki-67 in gliomas: Interobserver variability and digital quantification. Diagn Pathol. 2018;13(1).
220. Latysheva NS, Babu MM. Discovering and understanding oncogenic gene fusions through data intensive computational approaches. Nucleic Acids Res. 2016;44(10):4487–503.
221. Guilmette J, Dias-Santagata D, Nosé V, Lennerz JK, Sadow PM. Novel gene fusions in secretory carcinoma of the salivary glands: enlarging the ETV6 family. Hum Pathol. 2019;83:50–8.
222. Takeuchi K, Soda M, Togashi Y, Suzuki R, Sakata S, Hatano S, et al. RET, ROS1 and ALK fusions in lung cancer. Nat Med. 2012;18(3):378–81.
223. Liu L, Liu J, Shao D, Deng Q, Tang H, Liu Z, et al. Comprehensive genomic profiling of lung cancer using a validated panel to explore therapeutic targets in East Asian patients. Cancer Sci. 2017;108(12):2487–94.
224. Lupo PJ, Brown AL, Hettmer S. Second malignancy risk among pediatric, adolescent, and young adult survivors of fusion-positive and fusion-negative sarcomas: Results from the SEER database, 1992 through 2012. Cancer. 2016;122(22):3492–500.
225. Nussinov R, Jang H, Tsai CJ, Cheng F. Correction: Review: Precision medicine and driver mutations: Computational methods, functional assays and conformational principles for interpreting cancer drivers (PLoS Comput Biol, (2019), 15, 3, 10.1371/journal.pcbi.1006658). Vol. 15, PLoS Computational Biology. 2019. 1–54 p.
226. Yoshihara H, Yoshimoto Y, Hosoya Y, Hasegawa D, Kawano T, Sakoda A, et al. Infantile fibrosarcoma treated with postoperative vincristine and dactinomycin. Vol. 59, Pediatrics International. 2017. p. 371–4.
227. Gambella A, Senetta R, Collemi G, Vallero SG, Monticelli M, Cofano F, et al. NTRK fusions in central nervous system tumors: A rare, but worthy target. Int J Mol Sci. 2020;21(3):1–24.
228. Masuda T, Sankowski R, Staszewski O, Prinz M. Microglia Heterogeneity in the Single-Cell Era. Cell Rep [Internet]. 2020;30(5):1271–81. Available from: https://doi.org/10.1016/j.celrep.2020.01.010

229. La Manno G, Soldatov R, Zeisel A, Braun E, Hochgerner H, Petukhov V, et al. RNA velocity of single cells. Nature. 2018;560(7719):494–8.
230. Vokuhl C, Nourkami-Tutdibi N, Furtwängler R, Gessler M, Graf N, Leuschner I. ETV6–NTRK3 in congenital mesoblastic nephroma: A report of the SIOP/GPOH nephroblastoma study. Pediatr Blood Cancer. 2018;65(4).
231. Nagasubramanian R, Wei J, Gordon P, Rastatter JC, Cox MC, Pappo A. Infantile Fibrosarcoma With NTRK3–ETV6 Fusion Successfully Treated With the Tropomyosin-Related Kinase Inhibitor LOXO-101. Pediatr Blood Cancer. 2016;63(8):1468–70.
232. Ku BM, Bae YH, Lee KY, Sun JM, Lee SH, Ahn JS, et al. Entrectinib resistance mechanisms in ROS1-rearranged non-small cell lung cancer. Invest New Drugs. 2020;38(2):360–8.
233. Entrectinib Shows Pediatric Potential. Cancer Discov [Internet]. 2019 Jul 1;9(7):OF4 LP-OF4. Available from: http://cancerdiscovery.aacrjournals.org/content/9/7/OF4.abstract

Appendix 1

Appendix figure 1. Fusion panel workflow. A flow diagram showing the preparatory workflow for both the library preparation and single capture that each sample underwent before being sequenced using the DNA fusion panel.

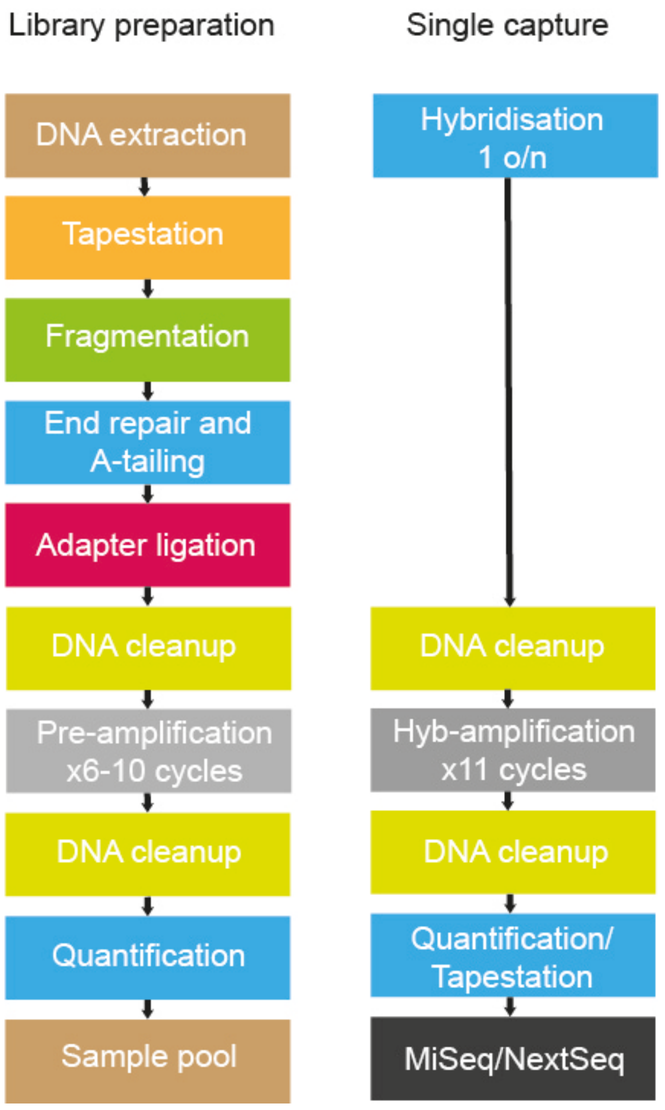

Appendix figure 2. 19ABHESP_pMA-T plasmids. Schematic representation of the 19ABHESP_pMA-T plasmids containing the respective fusions *KCTD16:NTRK2, ETV6:NTRK3 (1)* and *ETV6:NTRK3 (2)* with the v5 tag.

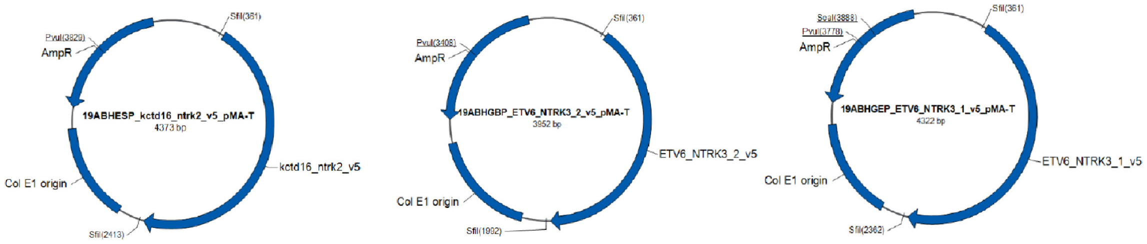

Appendix figure 3. AAVS1_Puro_PGK1_3xFLAG_Twin_Strep plasmid. Schematic representation of the AAVS1_Puro_PGK1_3xFLAG_Twin_Strep plasmid into which the fusions and v5 tag sequences were ligated. The location of the puromycin resistance gene is labelled 'PuroR' and shaded light green.

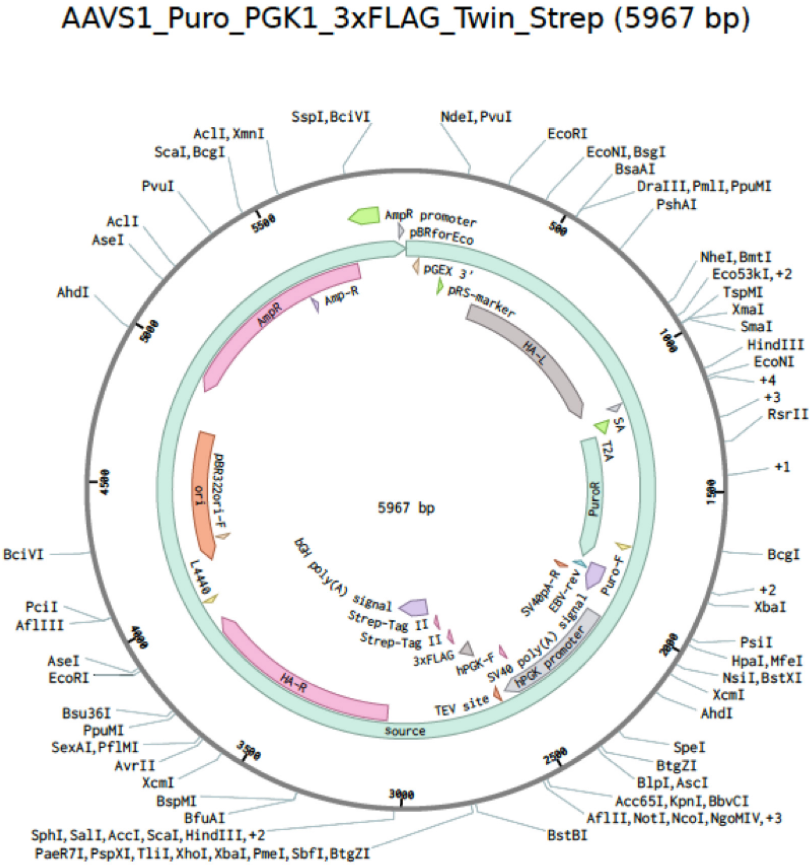

Appendix figure 4. PBCAG-eGFP plasmid. Schematic representation of the structure of the PBCAG-eGFP plasmid into which the fusions and v5 tag sequences were ligated. The EGFP sequence is labelled and coloured orange

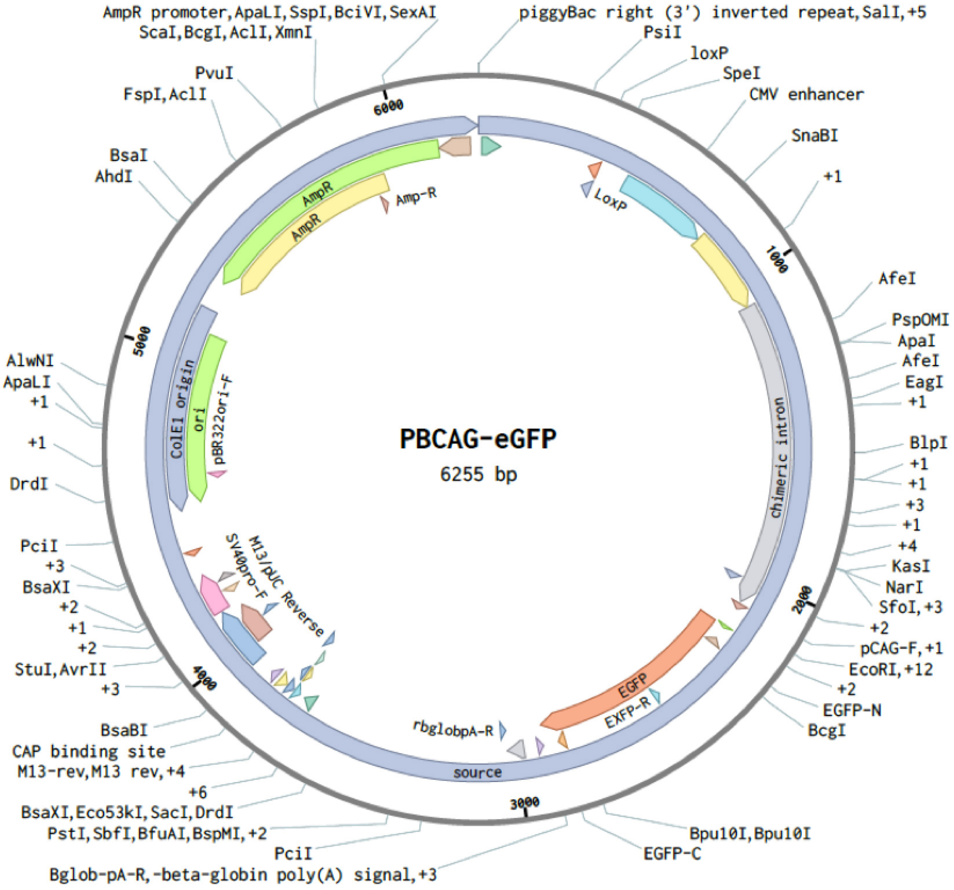

Appendix table 1. Primers for fusion validation. A table providing the forward and reverse primers used for the PCR validation of the fusions for each cases

Name	Sequence
QCTB INF R102 2F	GGTTACAGCCAACTTCCTGCTAT
QCTB INF R102 1R	GACTGCCCATTAACCATTAATCTC
OPBG INF 035 CELLS (1) 2F	GAGTGAGACTCCATCTCAAACAGA
OPBG INF 035 CELLS (1) 1R	CTTTGGGTAAATATGCCTCTCTTC
OPBG INF 035 CELLS (2) 1F	GAGTGAGACTCCATCTCAAACAGA
OPBG INF 035 CELLS (2) 2R	TTTCTATAGTGGCTTCCTTGGTTC
OPBG INF 035 CELLS (3) 2F	GAGTGAGACTCCATCTCAAACAGA
OPBG INF 035 CELLS (3) 1R	TGATTTCAGTAAACTGTCAGGTCAA
OPBG INF 036 1F	CCTGGGTAACAGAGAGACCTAGAC
OPBG INF 036 2R	TTTTTAGTAGGGTTTTGCCATGTT
OPBG INF 036 2F	GAGCTGGCTATGTCCATCTTTAAT
OPBG INF 036 1R	TGTCTGGCCAATTTAAACCTTAAT
OPBG INF 035 B 1F	GAGTGAGACTCCATCTCAAACAGA
OPBG INF 035 B 2R	TTTCTATAGTGGCTTCCTTGGTTC
OPBG INF 035 (1) 1F	GAGTGAGACTCCATCTCAAACAGA
OPBG INF 035 (1) 2R	TTTCTATAGTGGCTTCCTTGGTTC
OPBG INF 035 (2) 1F	CTGCTAGCCTCTCTGAGCTTCT
OPBG INF 035 (2) 2R	GGTGATTTGTCGTGATAGGTGAC
OPBG INF 020 2F	GTGCAATAACTCACTGCAACCTCT
OPBG INF 020 1R	AGTCAGGGTATCTTTGACCATAGC
OPBG INF 019 1F	GCTCTCAGTTTGTGTGCTTTCTAA
OPBG INF 019 2R	GTGAGTATCTGCACCACTTTTGTC
OPBG INF 019 2F	TCACGTAGACCTTTATCTTTGTGC
OPBG INF 019 1R	AAAACACACATTGAACATTTTTGG
NUTH INF 005 1F	AATGACCACCTCTTTTCCTTCTTA
NUTH INF 005 2R	TGCTTCAATTAAAGACACACCTTC
CHOW INF 001 1F	GCAGACTGTGTTGCAAGTATAACC
CHOW INF 001 2R	TATAACAACTGCTCAGAGCCCACT
CHOW INF 001 2F	TCTTAAACAGATTGACAGCCAAAA
CHOW INF 001 1R	GCTGAGCACAGCAGAAATACTAAG
KING INF 018 1F	CTCCCCTTAGAACAACTTTAGCAA
KING INF 018 2R	CATGGTAGAAAGGGTCTGAGAACT
KING INF 018 (2) 2F	GCTTTCTGTTCTTTTAGGTGGATT
KING INF 018 (2) 1R	TTTATTGTGGAATTGACTCTGCAT
GOSH INF 026 2F	CTGAGGCAAGATAATGGAGTGAAC
GOSH INF 026 1R	AAGGGAGAAAAGCTCTAATGTGTG
GOSH INF 014 2F	CCCTCACTCTACCCTTGCTAAAT
GOSH INF 014 1R	TCTGATAAATGGACACTGTTGAGG
GOSH INF 010 2F	CCTTAGCTTGCTCATACTCCATTT
GOSH INF 010 1R	AAACTTAAAGTCATGGCAGAAGGT
GOSH INF 005 2F	CTCTGGGTAATATGATGGGGTAAG
GOSH INF 005 1R	AGTTACCATCCCTGCCTACAGAG

CNMC INF 001 2F	AACCTGCAAGGATCAAAGTTTTAG
CNMC INF 001 1R	AGATAGTTTGGTCACCTCCAAATC
OPBG INF 005 (1) 1F	ACTTAAGCAAGGGATCAGATCAAC
OPBG INF 005 (1) 2R	AAGGCATGTTTGACAGGATAAAAG
SPHR INF 001 (4) 1F	TTGTTTCTTTTGAAAGCATTAGCA
SPHR INF 001 (4) 2R	GCTGAGCACAGCAGAAATACTAAG
SMHB INF 007C (2) 2F	TAATTATCTTTAGGCCAACCAAGC
SMHB INF 007C (2) 1R	GGAATTCGAGCCAGAGAATAAAG
OPBG INF 001 (1) 1F	TCGCAAACCAAGTAAATACAGATG
OPBG INF 001 (1) 2R	AATGCCAATACTAGGGGTCTTTCT
KIFN INF 001 2F	GCAGACTGTGTTGCAAGTATAACC
KIFN INF 001 1R	TTACATTTTAGGGTTGTGGAAGTG
CSMC INF 001 1F	GTAATTCAAGCATTTGTCATCTCC
CSMC INF 001 2R	TGGCAGTTCTCCAACTATAGGAA

Appendix table 2. pHGG panel genes. A table showing the 333 genes which form the pHGG panel. They are genes that are known to be associated with pHGG. Some of the infant cases in the cohort were sequenced using this panel to identify background somatic mutations.

PRKCZ
CHD5
RERE
MTOR
ID3
ARID1A
MAP3K6
AHDC1
PUM1
HDAC1
SF3A3
BMP8A
PTPRF
CDKN2C
FUBP1
NRAS
HIST2H2BF
HIST2H3D
HIST2H4A
HIST2H3C
HIST2H2AA3
HIST2H2AA4
HNRNPUL1
CIC
TEAD2
SCAF1
ATF5
SUV420H2
CENPB
MCM8
BMP2
ID1
PLAGL2
ASXL1
E2F1
RALGAPB
PLCG1
PTPRT
SALL4
RAB36
BCR
SMARCB1
CHEK2
NF2
ELMO3
FHOD1
SF3B3
FANCA
TP53
KDM6B
AURKB
PIK3R5
MAP2K4
TOP3A
MAPK7
ULK2
NF1
SUZ12
CDK12
ERBB2
IGFBP4
SMARCE1
BRCA1
RAD51C
PPM1D
BRIP1
CCND2
ATN1
ETV6
CDKN1B
PIK3C2G
KRAS
KMT2D
ESPL1
ERBB3
MARS
CDK4
MDM2
PTPN11
TBX3
SETD1B
FLT1
RXFP2
BRCA2
CCNA1
RB1
FANCM
MAX
EZH2
KMT2C
LPL
BMP1
STMN4
RAB11FIP1
FGFR1
CHD7
MYC
PARP10
SMARCA2
NFIB
CDKN2A
CDKN2B
FANCG
FBXO10
NTRK2
PTCH1
RET
KAT6B
PTEN
CCNJ
HIST1H2BK
HIST1H4I
HIST1H2BL
HIST1H2AI
HIST1H3H
HIST1H2AJ
HIST1H2BM
HIST1H4J
HIST1H4K
HIST1H2AK
HIST1H2BN
HIST1H2AL
HIST1H1B
HIST1H3I
HIST1H4L
HIST1H3J
HIST1H2AM
HIST1H2BO
MSH5
DAXX
PIM1
ROS1
WNT8A
KDM3B
CSF1R
GABRP
GNB2L1
HIST1H2AA
HIST1H2BA
HIST1H1A
HIST1H3A
HIST1H4A
HIST1H4B
HIST1H3B
HIST1H2AB
HIST1H2BB
HIST1H3C
HIST1H1C
HIST1H4C
HIST1H1T
HIST1H2BC
HIST1H2AC
HIST1H1E
HIST1H2BD
PMS1
SF3B1
IDH1
UNC80
ERBB4
VIL1
MLH1
CTNNB1
ZKSCAN7
SETD2
PTPN23
MAPKAPK3
POLQ
MCM2
PIK3CB
ATR
PIK3CA
EPHB3
MAP3K13
IGF2BP2
PDGFRA
KIT

HIST2H2AC
HIST2H2AB
NTRK1
KDM5B
PIK3C2B
MDM4
MAPKAPK2
TP53BP2
H3F3A
WNT9A
PXDN
ID2
MYCN
MSH2
MSH6
KDM3A
POLR1B
GLI2
ERCC3
ACVR1
SF3A1
DEPDC5
MCM5
SOX10
MAFF
APOBEC3H
PDGFB
WNT7B
TLR7
MAP3K15
BCOR
UBA1
CDK16
HDAC6
CCNB3
SHROOM4
HUWE1
AMER1
ATRX
STAG2
BPTF
CBX4
RPTOR
DSG1
SMAD7
SF3A2
CHAF1A
FEM1A
KDM4B
MAP2K7
SMARCA4
CC2D1A
BRD4
PIK3R2
CCNE1
KMT2B
AKT2
SHKBP1
AXL
IFIH1
MAP3K9
MLH3
DICER1
CCNK
WDR20
CDC42BPB
AKT1
PML
CSPG4
NTRK3
IDH2
BLM
IGF1R
CRAMP1L
TSC2
PALB2
INO80E
SRCAP
SETD1A
BCORL1
PIK3AP1
SUFU
TCF7L2
EIF3A
FGFR2
BUB3
MGMT
HRAS
CDKN1C
WEE1
PIK3C2A
SYVN1
SF3B2
SUV420H1
CCND1
WNT11
GAB2
ATM
CBL
PRKRA
ARID1B
MAP3K4
QKI
PDGFA
MAFK
PMS2
GLI3
HECW1
ADCY1
EGFR
PTPN12
CDK6
CNPY4
STAG3
TFR2
MET
WNT2
SMO
BRAF
RAD50
HIST1H2BE
HIST1H4D
HIST1H3D
HIST1H2AD
HIST1H2BF
HIST1H4E
HIST1H2BG
HIST1H2AE
HIST1H3E
HIST1H1D
HIST1H4F
HIST1H4G
HIST1H3F
HIST1H2BH
HIST1H3G
HIST1H2BI
HIST1H4H
HIST1H2BJ
HIST1H2AG
ATG12
KDR
IGFBP7
BMP2K
BMP3
SMARCA5
FBXW7
SORBS2
TERT
DROSHA
GOLPH3
HCN1
MAP3K1
PIK3R1
ENC1
POLK
RASGRF2
APC

Appendix table 3. Table of primer sequences. A table of primer sequences for the genes and fusions in AAVS1_Puro_PGK1 plasmids.

Name	**Sequence**
KCTD16+v5 in AAVS1_Puro_PGK1 FWD	ggtaccctcagccttaaggcAGGCATGGCTCTGAGTGG
KCTD16+v5 in AAVS1_Puro_PGK1 REV	actagaaggcacagcctgcaTTACGTAGAATCGAGACCGAG
NTRK2+v5 in AAVS1_Puro_PGK1 FWD	ggtaccctcagccttaaggcAGGCATGTCGTCCTGGATAAG
NTRK2+v5 in AAVS1_Puro_PGK1 REV	actagaaggcacagcctgcaCTACGTAGAATCGAGACCGAG
ETV6+v5 in AAVS1_Puro_PGK1 FWD	ggtaccctcagccttaaggcAGGCATGTCTGAGACTCC
ETV6+v5 in AAVS1_Puro_PGK1 REV	actagaaggcacagcctgcaTCACGTAGAATCGAGACC
NTRK3+v5 in AAVS1_Puro_PGK1 FWD	ggtaccctcagccttaaggcAGGCATGGATGTCTCTCTTTG
NTRK3+v5 in AAVS1_Puro_PGK1 REV	actagaaggcacagcctgcaTTACGTAGAATCGAGACCG
KCTD16:NTRK2 in AAVS1_Puro_PGK1 FWD	ggtaccctcagccttaaggcATGGCTCTGAGTGGAAACTG
KCTD16:NTRK2 in AAVS1_Puro_PGK1 REV	actagaaggcacagcctgcaCTACGTAGAATCGAGACCGAG
ETV6:NTRK3 1 in AAVS1_Puro_PGK1 FWD	ggtaccctcagccttaaggcATGTCTGAGACTCCTGCTC
ETV6:NTRK3 1 in AAVS1_Puro_PGK1 REV	actagaaggcacagcctgcaCTACGTAGAATCGAGACCG

Appendix table 4. Fusion detection and validation. A table showing all the tumour samples in which an RTK fusion was detected, and the different methods that were used for both fusion detection and validation in each case

Sample Name	Fusion	Copy number	Fusion panel	Whole genome	Sanger	RNA seq
CHOW_INF_001	*MAP2:ALK*		Yes	Yes	Yes	
CSMC_INF_001	*HIP1:ALK*	Yes	Yes		Yes	Yes
DKFZ_INF_301	*ETV6:NTRK3*	Yes				
DKFZ_INF_302	*MSI2:ALK*	Yes				Yes
DKFZ_INF_303	*ROS1*	Yes				
DKFZ_INF_307	*MAD1L1:ALK*	Yes				Yes
DKFZ_INF_308	*MET*	Yes				
DKFZ_INF_312	*MET*	Yes				
DKFZ_INF_313	*PPP1CB:ALK*	Yes				Yes
DKFZ_INF_314	*PPP1CB:ALK*	Yes				Yes
DKFZ_INF_315	*ALK*	Yes				
DKFZ_INF_317	*EML4:ALK*	Yes				
DKFZ_INF_318	*CCDC88A:ALK*	Yes				Yes
DKFZ_INF_324	*EML4:NTRK3*	Yes				
DKFZ_INF_326	*CCDC88A:ALK*	Yes				
DKFZ_INF_328	*ALK*	Yes				
DKFZ_INF_330	*ALK*	Yes				
DKFZ_INF_332	*PPP1CB:ALK*	Yes				Yes
DKFZ_INF_336	*PPP1CB:ALK*	Yes				
DKFZ_INF_338	*ROS1*	Yes				
DKFZ_INF_341	*ETV6:NTRK3*	Yes				

DKFZ_INF_344	*ALK*	Yes				
DKFZ_INF_345	*ALK*	Yes				
DKFZ_INF_348	*PPP1CB:ALK*	Yes				Yes
DKFZ_INF_351	*ALK*	Yes				
DKFZ_INF_356	*ROS1*	Yes				
DKFZ_INF_357	*ROS1*	Yes				
DKFZ_INF_361	*EML4:ALK*					Yes
DKFZ_INF_362	*EML4:ALK*					Yes
DKFZ_INF_366	*CHCHD3:ROS1*	Yes				Yes
DKFZ_INF_368	*ETV6:NTRK3*	Yes				Yes
DKFZ_INF_370	*CCDC88A:ALK*	Yes				Yes
DKFZ_INF_371	*PPP1CB:ALK*	Yes				Yes
DKFZ_INF_372	*GOPC:ROS1*	Yes				Yes
DKFZ_INF_373	*SPECC1L:ALK*	Yes				Yes
DKFZ_INF_G132	*NTRK2*	Yes				
DKFZ_INF_G135	*MET*	Yes				
DKFZ_INF_G170	*ROS1*	Yes				
DKFZ_INF_G179	*FGFR1:TACC1*	Yes				
DKFZ_INF_G251	*ROS1*	Yes				
DKFZ_INF_ICGC34	*NTRK2*	Yes				
EMUH_INF_001	*CCDC88A:ALK*	Yes				Yes
GOSH_INF_001	*ETV6:NTRK3*	Yes	Yes	Yes		Yes
GOSH_INF_002	*MET*	Yes		Yes		
GOSH_INF_004	*ETV6:NTRK3*	Yes	Yes			
GOSH_INF_005	*SPECC1L:ALK*	Yes	Yes	Yes	Yes	Yes

GOSH_INF_007	*ETV6:NTRK3*	Yes				
GOSH_INF_011	*HIP1:ALK*	Yes	Yes			
GOSH_INF_012	*FGFR3:TACC3*	Yes				
GOSH_INF_017	*PPP1CB:ALK*	Yes		Yes		
GOSH_INF_023	*ROS1*	Yes		Yes		
GOSH_INF_026	*ETV6:NTRK3*	Yes	Yes		Yes	Yes
GOSH_INF_028	*ROS1*			Yes		Yes
KIFN_INF_001	*ZC3H7A:ALK*	Yes	Yes		Yes	Yes
KING_INF_001	*FGFR1:TACC1*	Yes				
KING_INF_012	*MET*	Yes				
KING_INF_018	*KCTD16:NTRK2*	Yes	Yes		Yes	
MSKC_INF_001	*GOPC:ROS1*	Yes				Yes
MSKC_INF_006	*ETV6:NTRK3*					Yes
NUTH_INF_001	*AGBL4:NTRK2*		Yes			
NUTH_INF_005	*SYNDIG1L:ALK*	Yes	Yes		Yes	Yes
OHSU_INF_001	*CCDC88A:ALK*					Yes
OPBG_INF_001	*ETV6:NTRK3*		Yes			
OPBG_INF_005	*KCTD8:NTRK2*		Yes			
OPBG_INF_019	*KIF5B:NTRK2*	Yes	Yes		Yes	Yes
OPBG_INF_035	*ETV6:NTRK3*		Yes			
PMHK_INF_001	*ROS1*	Yes		Yes		Yes
QCTB_INF_R077	*ETV6:NTRK3*	Yes	Yes	Yes	Yes	
QCTB_INF_R102	*TPM3:NTRK1*		Yes			
SMHB_INF_002	*EML4:ALK*	Yes	Yes			
SMHB_INF_003	*CCDC88A:ALK*	Yes		Yes		

SMHB_INF_007	*EML4:NTRK3*		Yes			
SPHR_INF_001	*PRKAR2A:ALK*		Yes		Yes	
STJU_INF_001	*TPM3:NTRK1*			Yes		Yes
STJU_INF_005	*TPM3:NTRK1*			Yes		Yes
STJU_INF_006	*ETV6:NTRK3*			Yes		Yes
STJU_INF_013	*AGBL4:NTRK2*			Yes		Yes
STJU_INF_014	*PPP1CB:ALK*	Yes				
STJU_INF_015	*CLIP2:ALK*	Yes				
STJU_INF_016	*ALK*	Yes				
STJU_INF_017	*SPTBN1:ALK*	Yes				
UOLP_INF_001	*EML4:ALK*					Yes
WFSM_INF_001	*CCDC88A:ALK*					Yes

Appendix table 5. Histological review of intrinsic set cases. Table summarising the histological features identified in the IHG cases, including the Ki67 score. Each sample is also labelled with the respective RTK fusion they were found to contain.

Study ID	Ganglion cells	Pleomorphism	Spindle cells	Gemistocytic cells	Mitoses	Vascular proliferation	Uniform architecture	Necrosis	Ki67	Fusion
SMHB_INF_003	NA	NA	NA	NA	NA	NA	NA	NA	2.34	*CCDC88A:ALK*
UOLP_INF_001	YES	no	no	no	YES	YES	no	YES	18.10	*EML4:ALK*
GOSH_INF_011	no	no	no	YES	YES	YES	no	YES	NA	*HIP1:ALK*
CSMC_INF_001	no	YES	no	no	no	no	YES	YES	NA	*HIP1/UNC79:ALK*
CHOW_INF_001	no	no	YES	no	YES	no	YES	no	13.08	*MAP2:ALK*
SPHR_INF_001	no	no	YES	no	YES	YES	YES	YES	7.74	*PRKAR2A:ALK*
GOSH_INF_005	no	YES	no	YES	YES	YES	YES	YES	35.69	*SPECC1L1:ALK*
NUTH_INF_005	no	no	no	no	YES	YES	YES	YES	30.16	*SYNDIG1L:ALK*
KIFN_INF_001	no	YES	no	no	YES	no	YES	YES	NA	*ZC3H7A:ALK*
GOSH_INF_001	no	YES	no	no	YES	YES	no	YES	22.53	*ETV6:NTRK3*
GOSH_INF_004	no	no	no	YES	no	YES	YES	YES	13.42	*ETV6:NTRK3*
GOSH_INF_007	no	YES	YES	no	no	no	YES	YES	20.90	*ETV6:NTRK3*
OPBG_INF_035	no	YES	no	YES	no	no	no	YES	43.87	*ETV6:NTRK3*
QCTB_INF_R077	no	no	YES	YES	YES	no	YES	no	29.11	*ETV6:NTRK3*
GOSH_INF_002	no	YES	YES	no	YES	no	no	YES	13.37	*MET*
GOSH_INF_003	no	no	YES	YES	no	no	YES	no	25.38	None
GOSH_INF_008	no	no	no	YES	no	no	no	YES	14.66	None
KING_INF_014	no	no	no	YES	no	YES	no	YES	5.63	None
PMHK_INF_001	no	no	YES	no	no	no	no	YES	3.24	None
STGH_INF_001	no	no	no	YES	no	YES	no	no	NA	None
UKEH_INF_005	no	YES	YES	no	YES	no	no	no	2.49	None

Appendix 2

The following are the sequences of the three fusions that were used to construct the *NTRK* models. The fusion is indicated by ***:

KCTD16:NTRK2

```
ATGGCTCTGAGTGGAAACTGTAGTCGTTATTATCCTCGAGAACAAGGGTCCGCAGTTCCCAACTCCTTCC
CTGAGGTGGTAGAGCTGAATGTCGGGGGTCAAGTTTATTTTACTCGCCATTCCACATTGATAAGCATCCC
TCATTCCCTCCTGTGGAAAATGTTTTCCCCAAAGAGAGACACGGCTAATGATCTAGCCAAGGACTCCAAG
GGAAGGTTTTTCATTGACAGAGATGGATTCTTGTTCCGTTATATTCTGGACTATCTCAGGGACAGGCAGG
TGGTCCTGCCTGATCACTTTCCAGAAAAAGGAAGACTGAAAAGGGAAGCTGAATACTTCCAGCTCCCAGA
CTTGGTCAAACTCCTGACCCCCGATGAAATCAAGCAAAGCCCAGATGAATTCTGCCACAGTGACTTTGAA
GATGCCTCCCAAGGAAGCGACACAAGAATCTGCCCCCCTTCCTCCCTGCTCCCTGCCGACCGCAAGTGGG
GTTTCATTACTGTGGGTTACAGAGGATCCTGCACCTTGGGCAGAGAGGGACAGGCAGATGCCAAGTTTCG
GAGAGTTCCCCGGATTTTGGTTTGTGGAAGGATTTCCTTGGCAAAAGAAGTCTTTGGAGAAACTTTGAAT
GAAAGCAGAGACCCTGATCGAGCCCCAGAAAGATACACCTCCAGATTTTATCTCAAATTCAAGCACCTGG
AAAGGGCTTTTGATATGTTGTCAGAGTGTGGATTCCACATGGTGGCCTGTAACTCATCGGTGACAGCATC
TTTCATCAACCAATATACAGATGACAAGATCTGGTCAAGCTACACTGAATATGTCTTCTACC***ATTTC
TCATGGTTTGGATTTGGGAAAGTAAAATCAAGACAAGGTGTTGGCCCAGCCTCCGTTATCAGCAATGATG
ATGACTCTGCCAGCCCACTCCATCACATCTCCAATGGGAGTAACACTCCATCTTCTTCGGAAGGTGGCCC
AGATGCTGTCATTATTGGAATGACCAAGATCCCTGTCATTGAAAATCCCCAGTACTTTGGCATCACCAAC
AGTCAGCTCAAGCCAGACACATTTGTTCAGCACATCAAGCGACATAACATTGTTCTGAAAAGGGAGCTAG
GCGAAGGAGCCTTTGGAAAAGTGTTCCTAGCTGAATGCTATAACCTCTGTCCTGAGCAGGACAAGATCTT
GGTGGCAGTGAAGACCCTGAAGGATGCCAGTGACAATGCACGCAAGGACTTCCACCGTGAGGCCGAGCTC
CTGACCAACCTCCAGCATGAGCACATCGTCAAGTTCTATGGCGTCTGCGTGGAGGGCGACCCCCTCATCA
TGGTCTTTGAGTACATGAAGCATGGGGACCTCAACAAGTTCCTCAGGGCACACGGCCCTGATGCCGTGCT
GATGGCTGAGGGCAACCCGCCCACGGAACTGACGCAGTCGCAGATGCTGCATATAGCCCAGCAGATCGCC
GCGGGCATGGTCTACCTGGCGTCCCAGCACTTCGTGCACCGCGATTTGGCCACCAGGAACTGCCTGGTCG
GGGAGAACTTGCTGGTGAAAATCGGGGACTTTGGGATGTCCCGGGACGTGTACAGCACTGACTACTACAG
GGTCGGTGGCCACACAATGCTGCCCATTCGCTGGATGCCTCCAGAGAGCATCATGTACAGGAAATTCACG
ACGGAAAGCGACGTCTGGAGCCTGGGGGTCGTGTTGTGGGAGATTTTCACCTATGGCAAACAGCCCTGGT
ACCAGCTGTCAAACAATGAGGTGATAGAGTGTATCACTCAGGGCCGAGTCCTGCAGCGACCCCGCACGTG
CCCCCAGGAGGTGTATGAGCTGATGCTGGGGTGCTGGCAGCGAGAGCCCCACATGAGGAAGAACATCAAG
GGCATCCATACCCTCCTTCAGAACTTGGCCAAGGCATCTCCGGTCTACCTGGACATTCTAGGCTAG
```

ETV6:NTRK3 1

```
ATGTCTGAGACTCCTGCTCAGTGTAGCATTAAGCAGGAACGAATTTCATATACACCTCCAGAGAGCCCAG
TGCCGAGTTACGCTTCCTCGACGCCACTTCATGTTCCAGTGCCTCGAGCGCTCAGGATGGAGGAAGACTC
GATCCGCCTGCCTGCGCACCTGCGCTTGCAGCCAATTTACTGGAGCAGGGATGACGTAGCCCAGTGGCTC
AAGTGGGCTGAAAATGAGTTTTCTTTAAGGCCAATTGACAGCAACACGTTTGAAATGAATGGCAAAGCTC
TCCTGCTGCTGACCAAAGAGGACTTTCGCTATCGATCTCCTCATTCAGGTGATGTGCTCTATGAACTCCT
TCAGCATATTCTGAAGCAGAGGAAACCTCGGATTCTTTTTTCACCATTCTTCCACCCTGGAAACTCTATA
CACACACAGCCGGAGGTCATACTGCATCAGAACCATGAAGAAGATAACTGTGTCCAGAGGACCCCCAGGC
CATCCGTGGATAATGTGCACCATAACCCTCCCACCATTGAACTGTTGCACCGCTCCAGGTCACCTATCAC
GACAAATCACCGGCCTTCTCCTGACCCCGAGCAGCGGCCCCTCCGGTCCCCCCTGGACAACATGATCCGC
CGCCTCTCCCCGGCTGAGAGAGCTCAGGGACCCAGGCCGCACCAGGAGAACAACCACCAGGAGTCCTACC
CTCTGTCAGTGTCTCCCATGGAGAATAATCACTGCCCAGCGTCCTCCGAGTCCCACCCGAAGCCATCCAG
CCCCCGGCAGGAGAGCACACGCGTGATCCAGCTGATGCCCAGCCCCATCATGCACCCTCTGATCCTGAAC
CCCCGGCACTCCGTGGATTTCAAACAGTCCAGGCTCTCCGAGGACGGGCTGCATAGGGAAGGGAAGCCCA
TCAACCTCTCTCATCGGGAAGACCTGGCTTACATGAACCACATCATGGTCTCTGTCTCCCCGCCTGAAGA
GCACGCCATGCCCATTGGGAGAATAGCAG***ATGTGCAGCACATTAAGAGGAGAGACATCGTGCTGAAG
CGAGAACTGGGTGAGGGAGCCTTTGGAAAGGTCTTCCTGGCCGAGTGCTACAACCTCAGCCCGACCAAGG
ACAAGATGCTTGTGGCTGTGAAGGCCCTGAAGGATCCCACCCTGGCTGCCCGGAAGGATTTCCAGAGGGA
GGCCGAGCTGCTCACCAACCTGCAGCATGAGCACATTGTCAAGTTCTATGGAGTGTGCGGCGATGGGGAC
CCCCTCATCATGGTCTTTGAATACATGAAGCATGGAGACCTGAATAAGTTCCTCAGGGCCCATGGGCCAG
ATGCAATGATCCTTGTGGATGGACAGCCACGCCAGGCCAAGGGTGAGCTGGGGCTCTCCCAAATGCTCCA
CATTGCCAGTCAGATCGCCTCGGGTATGGTGTACCTGGCCTCCCAGCACTTTGTGCACCGAGACCTGGCC
```

ACCAGGAACTGCCTGGTTGGAGCGAATCTGCTAGTGAAGATTGGGGACTTCGGCATGTCCAGAGATGTCT
ACAGCACGGATTATTACAGGGTGGGAGGACACACCATGCTCCCCATTCGCTGGATGCCTCCTGAAAGCAT
CATGTACCGGAAGTTCACTACAGAGAGTGATGTATGGAGCTTCGGGGTGATCCTCTGGGAGATCTTCACC
TATGGAAAGCAGCCATGGTTCCAACTCTCAAACACGGAGGTCATTGAGTGCATTACCCAAGGTCGTGTTT
TGGAGCGGCCCCGAGTCTGCCCCAAAGAGGTGTACGATGTCATGCTGGGGTGCTGGCAGAGGGAACCACA
GCAGCGGTTGAACATCAAGGAGATCTACAAAATCCTCCATGCTTTGGGGAAGGCCACCCCAATCTACCTG
GACATTCTTGGCTAG

ETV6:NTRK3 2

ATGTCTGAGACTCCTGCTCAGTGTAGCATTAAGCAGGAACGAATTTCATATACACCTCCAGAGAGCCCAG
TGCCGAGTTACGCTTCCTCGACGCCACTTCATGTTCCAGTGCCTCGAGCGCTCAGGATGGAGGAAGACTC
GATCCGCCTGCCTGCGCACCTGCGCTTGCAGCCAATTTACTGGAGCAGGGATGACGTAGCCCAGTGGCTC
AAGTGGGCTGAAAATGAGTTTTCTTTAAGGCCAATTGACAGCAACACGTTTGAAATGAATGGCAAAGCTC
TCCTGCTGCTGACCAAAGAGGACTTTCGCTATCGATCTCCTCATTCAGGTGATGTGCTCTATGAACTCCT
TCAGCATATTCTGAAGCAGAGGAAACCTCGGATTCTTTTTTCACCATTCTTCCACCCTGGAAACTCTATA
CACACACAGCCGGAGGTCATACTGCATCAGAACC***GTCCCGTGGCTGTCATCAGTGGTGAGGAGGACT
CAGCCAGCCCACTGCACCACATCAACCACGGCATCACCACGCCCTCGTCACTGGATGCCGGGCCCGACAC
TGTGGTCATTGGCATGACTCGCATCCCTGTCATTGAGAACCCCCAGTACTTCCGTCAGGGACACAACTGC
CACAAGCCGGACACGTATGTGCAGCACATTAAGAGGAGAGACATCGTGCTGAAGCGAGAACTGGGTGAGG
GAGCCTTTGGAAAGGTCTTCCTGGCCGAGTGCTACAACCTCAGCCCGACCAAGGACAAGATGCTTGTGGC
TGTGAAGGCCCTGAAGGATCCCACCCTGGCTGCCCGGAAGGATTTCCAGAGGGAGGCCGAGCTGCTCACC
AACCTGCAGCATGAGCACATTGTCAAGTTCTATGGAGTGTGCGGCGATGGGGACCCCCTCATCATGGTCT
TTGAATACATGAAGCATGGAGACCTGAATAAGTTCCTCAGGGCCCATGGGCCAGATGCAATGATCCTTGT
GGATGGACAGCCACGCCAGGCCAAGGGTGAGCTGGGGCTCTCCCAAATGCTCCACATTGCCAGTCAGATC
GCCTCGGGTATGGTGTACCTGGCCTCCCAGCACTTTGTGCACCGAGACCTGGCCACCAGGAACTGCCTGG
TTGGAGCGAATCTGCTAGTGAAGATTGGGGACTTCGGCATGTCCAGAGATGTCTACAGCACGGATTATTA
CAGGGTGGGAGGACACACCATGCTCCCCATTCGCTGGATGCCTCCTGAAAGCATCATGTACCGGAAGTTC
ACTACAGAGAGTGATGTATGGAGCTTCGGGGTGATCCTCTGGGAGATCTTCACCTATGGAAAGCAGCCAT
GGTTCCAACTCTCAAACACGGAGGTCATTGAGTGCATTACCCAAGGTCGTGTTTTGGAGCGGCCCCGAGT
CTGCCCCAAAGAGGTGTACGATGTCATGCTGGGGTGCTGGCAGAGGGAACCACAGCAGCGGTTGAACATC
AAGGAGATCTACAAAATCCTCCATGCTTTGGGGAAGGCCACCCCAATCTACCTGGACATTCTTGGCTAG

Appendix 3

Novel *ALK* fusion mouse model

A *PPP1CB:ALK* fusion construct was cloned into either an RCAS or a pT2K vector using RNA from a human glioma sample as a template. After cDNA synthesis and PCR amplification, the ends of the product were cut with EcoRI and XhoI (for cloning into pT2K) or NotI and ClaI (for RCAS) and ligated into the target vector using the Takara Ligation mixture (Clontech). Bacterial amplification and QIAprep Spin Miniprep Kit (QIAGEN) were performed according to the manufacturer's instructions to isolate the cloned plasmid. The DNA was sequenced using Sanger Sequencing at GATC Biotech and protein expression was confirmed on Western blot after transfection of DF-1 cells with the vector.

In Utero Electroporation

After confirming that the expression vector contained the right inserts, embryos of CD1 mice were injected with plasmid into the fourth ventricle and electroporated in utero at E14.5. The *PPP1CB:ALK* fusion plasmid was used alone or in combination with CRISPR guide RNAs against Cdkn2a. Because of the incorporated IRES-Luciferase reporter on the pT2K vector, mice with successful integration of the transgene could be assessed at postnatal day 3 using bioluminescence imaging on an IVIS imager (PerkinElmer). Mice were sacrificed upon first signs of tumour-related symptoms according to humane endpoint criteria. H&E and IHC staining was performed according to standard protocols on 3µm sections.

RCAS

Four days before the calculated birth date, early-passage DF-1 fibroblasts for virus production were plated at 2–3 x 10^5 cells/T25 flask in 5 mL DMEM with 10% FCS + 1% penicillin/ streptomycin + 1% Glutamax at 5% CO2 at 39°C. One day after, the cells were transfected with the RCAS construct as follows: 4 µg of the RCAS plasmid was incubated in 200µL of room temperature OptiMEM and 10µL FuGene transfection reagent. After a 15-minute incubation time, this mixture was slowly added to the settled DF-1 cells, mixed well by gently moving the flask and placed back in the incubator. An RCAS-GFP plasmid was always run in parallel in a separate flask to check for transfection success. On the day of birth, the transfected DF-1 cells were harvested using 10x Trypsin-EDTA and counted using the automated cell counter TC20. Cells (4 x 10^5 in 1µL) were used for injection into newborn *Ntv-a;Cdkn2a−/−*;*Pten*$^{fl/fl}$ pups at p0. The required amount of cells, depending on the size of the litter, was eluted in DMEM culture medium. The pups were taken out of the cage in a sterile hood and injected into the striatum with 1µL of the DF-1 cell solution using a 10µL Hamilton syringe. Mice were sacrificed upon first signs of tumour-related symptoms according to humane endpoint criteria. All animal protocols were approved by the relevant authority (Regierungspr.sidium Karlsruhe) under registration numbers
G-212/16 and G-168/17.

In Vitro Culture and Compound Testing of Murine Tumour Cells

Murine *ALK* fusion–positive tumours were dissected immediately postmortem, mechanically dissociated, and then filtered through a 40µm cell strainer. Cells were then plated *in vitro* in 10-cm dishes and grown as spheres in a 1:1 mix of Neurobasal-A and DMEM/F-12 media containing 1% 1mol/L HEPES buffer solution, 1% 100mmol/L sodium pyruvate MEM, 1% 10mmol/L MEM nonessential amino acids solution, 1% GlutaMAX and 1% antibiotic–antimycotic supplemented with 2% B27, 2 μg/mL heparin solution, 10ng/mL H-PDGF-AA, 20 ng/mL recombinant human bFGF, and 20ng/mL recombinant human EGF. For splitting, cells were dissociated with Accumax at 37°C for 5 minutes.

For *in vitro* drug testing, primary sphere culture cells were plated at 1 x 10^4 cells/well in 80μL growth factor–containing medium/ well in 96-well plates. Triplicates per drug concentration (20μL total volume for each) were added 24 hours after seeding the cells. The drug concentrations ranged between 1nmol/L and 30μmol/L. Corresponding DMSO concentrations were plated as controls, to which the treated wells were normalised. The ALK inhibitors crizotinib, alectinib, ceritinib, and lorlatinib were used. All compounds were purchased from Selleck Chemicals and initially diluted in DMSO to either a 10 mmol/L or 1 mmol/L stock, which were stored at −80°C. A CellTiter-Glo assay (Promega) was used as a readout of compound efficacy. This assay was conducted 72 hours after drugs were added to the cells. For this purpose, 50μL of CellTiter-Glo substrate was added to each well using a multichannel pipette, and plates were incubated for 15 minutes while shaking in the dark. After that time, the luminescence signal per well was measured using a Mithras LB940 microplate reader. The respective DMSO control value was subtracted from the drug’s value to normalise the readout. The GI50 curves show the mean Å} SD of the triplicates per condition measured. Representative results from duplicate experiments are shown.

In Vivo Compound Testing

To test the effectiveness of ALK inhibition *in vivo*, 6-week-old CD1 mice were intracranially allografted with 5 x 10^5 mouse *PPP1CB:ALK* tumour cells (see above) to give a more standardised latency of tumour formation and to avoid having to administer treatment to very young animals. The chosen inhibitor was lorlatinib based on the *in vitro* results, as well as HCl and temozolomide as vehicle control and standard of care, respectively. Tumour growth was monitored using BLI on an IVIS imager (PerkinElmer). The tumours were allowed to develop for two weeks before animals were stratified into three treatment groups based on their luciferase signal (rank 1, 4, 7, etc., being assigned to lorlatinib, rank 2, 5, 8, etc., to temozolomide, and rank 3, 6, 9, etc., to vehicle control). Animals were monitored daily for symptoms or abnormal behavior and weighed three times a week, and were sacrificed upon first signs of tumour-related symptoms according to humane endpoint criteria